

**DYNAMIC ANALYSIS OF MULTIPLE-BODY FLOATING PLATFORMS
COUPLED WITH MOORING LINES AND RISERS**

A Dissertation

by

YOUNG-BOK KIM

Submitted to the Office of Graduate Studies of
Texas A&M University
in partial fulfillment of the requirements for the degree of

DOCTOR OF PHILOSOPHY

May 2003

Major Subject: Ocean Engineering

**DYNAMIC ANALYSIS OF MULTIPLE-BODY FLOATING PLATFORMS
COUPLED WITH MOORING LINES AND RISERS**

A Dissertation

by

YOUNG-BOK KIM

Submitted to the Office of Graduate Studies of
Texas A&M University
in partial fulfillment of the requirements for the degree of

DOCTOR OF PHILOSOPHY

Approved as to style and content by:

Moo-Hyun Kim
(Co-Chair of Committee)

Cheung H. Kim
(Co-Chair of Committee)

Jun Zhang
(Member)

Robert H. Stewart
(Member)

Paul N. Roschke
(Head of Department)

May 2003

Major Subject: Ocean Engineering

ABSTRACT

Dynamic Analysis of Multiple-Body Floating Platforms Coupled with Mooring

Lines and Risers. (May 2003)

Young-Bok Kim, B.S., Inha University;

M.S., Seoul National University

Co-Chairs of Advisory Committee: Dr. Moo-Hyun Kim

Dr. Cheung H. Kim

A computer program, WINPOST-MULT, is developed for the dynamic analysis of a multiple-body floating system coupled with mooring lines and risers in the presence of waves, winds and currents. The coupled dynamics program for a single platform is extended for analyzing multiple-body systems by including all the platforms, mooring lines and risers in a combined matrix equation in the time domain. Compared to the iteration method between multiple bodies, the combined matrix method can include the $6N \times 6N$ full hydrodynamic interactions among N bodies. The floating platform is modeled as a rigid body with six degrees of freedom. The first- and second-order wave forces, added mass coefficients, and radiation damping coefficients are calculated from the hydrodynamics program WAMIT for multiple bodies. Then, the time series of wave forces are generated in the time domain based on the two-term Volterra model. The wind forces are separately generated from the input wind spectrum and wind force formula. The current is included in Morison's drag force formula. In the case of FPSO, the wind and current forces are generated using the respective coefficients given in the OCIMF

data sheet. A finite element method is derived for the long elastic element of an arbitrary shape and material. This newly developed computer program is first applied to the system of a turret-moored FPSO and a shuttle tanker in tandem mooring. The dynamics of the turret-moored FPSO in waves, winds and currents are verified against independent computation and OTRC experiment. Then, the simulations for the FPSO-shuttle system with a hawser connection are carried out and the results are compared with the simplified methods without considering or partially including hydrodynamic interactions.

ACKNOWLEDGEMENTS

This work was completed only because of the financial support of the OTRC and JIP (Joint Industry Project) for over four years. I deeply thank the sponsors for this support. I would like to express my sincere gratitude to my advisors, Dr. M. H. Kim and Dr. C. H. Kim, for their continuous encouragement and guidance during my studies. I also would like to thank Dr. Zhihuang Ran (Alex) and Dr. Arcandra Tahar for sharing their efforts to review the programming and to discuss the problem. I greatly appreciate Dr. J. Zhang and Dr. R. H. Stewart for serving as advisory committee members, Dr. R. Mercier for releasing the OTRC experiment data, and Dr. E. B. Portis for supervising the procedure of the final defense as a GCR.

Finally, I would like to thank my wife, Deock-Seung Seo, for her support and encouragement during the period of this study.

This work could only be done under the merciful guidance and the tender love of God. I would like to devote this work to His Glory.

TABLE OF CONTENTS

| | Page |
|---|------|
| ABSTRACT | iii |
| ACKNOWLEDGEMENTS | v |
| TABLE OF CONTENTS | vi |
| LIST OF FIGURES | x |
| LIST OF TABLES | xiv |
| CHAPTER | |
| I INTRODUCTION | 1 |
| 1.1 Background..... | 1 |
| 1.2 Literature Review | 3 |
| 1.3 Objective and Scope | 5 |
| 1.4 Procedure | 7 |
| 1.4.1 Interpretation and Preparation of WAMIT Results and Wind/ Current Forces | 7 |
| 1.4.2 Developing the Coupled Dynamic Program | 8 |
| 1.4.3 Comparative Studies | 10 |
| II DYNAMICS OF THE FLOATING PLATFORM | 12 |
| 2.1 Introduction | 12 |
| 2.2 Formulation of Surface Wave | 12 |
| 2.2.1 Boundary Value Problem (BVP) of Surface Wave | 12 |
| 2.2.2 Wave Theory | 14 |
| 2.2.3 Diffraction and Radiation Theory | 16 |
| 2.2.3.1 First-Order Boundary Value Problem | 17 |
| 2.2.3.2 Second-Order Boundary Value Problem | 19 |
| 2.3 Hydrodynamic Forces | 23 |
| 2.3.1 The First-Order Hydrodynamic Forces and Moments | 23 |
| 2.3.2 The Second-Order Hydrodynamic Forces and Moments | 26 |
| 2.4 Multiple-Body Interaction of Fluid | 28 |
| 2.5 Boundary Element Method | 30 |
| 2.6 Motions of the Floating Platform | 33 |
| 2.6.1 Wave Loads | 33 |
| 2.6.2 Morison's Equation | 36 |

| CHAPTER | Page |
|--|-----------|
| 2.6.3 Single Body Motion | 37 |
| 2.6.4 Multiple Body Motion | 38 |
| 2.6.5 Time Domain Solution of the Platform Motions | 40 |
| III DYNAMICS OF MOORING LINES AND RISERS | 44 |
| 3.1 Introduction | 44 |
| 3.2 Theory of the Rod | 46 |
| 3.3 Finite Element Modeling | 50 |
| 3.4 Formulation of Static Problem | 55 |
| 3.5 Formulation for Dynamic Problem-Time Domain Integration | 59 |
| 3.6 Modeling of the Seafloor | 63 |
| IV COUPLED ANALYSIS OF INTEGRATED PLATFORM AND MOORING SYSTEM | 66 |
| 4.1 Introduction | 66 |
| 4.2 The Spring to Connect the Platform and the Mooring System..... | 67 |
| 4.2.1 Static Analysis | 69 |
| 4.2.2 Time-Domain Analysis | 71 |
| 4.3 Modeling of Damper on the Connection | 72 |
| 4.4 Modeling of Connection between Lines and Seafloor | 74 |
| 4.5 Formulation for the Multiple Body System | 75 |
| V CASE STUDY 1: DYNAMIC ANALYSIS OF A TANKER BASED FPSO | 79 |
| 5.1 Introduction | 79 |
| 5.2 Design Premise Data of FPSO and Mooring Systems | 80 |
| 5.3 Environmental Data | 85 |
| 5.3.1 Wave Force | 87 |
| 5.3.2 Wind Force | 88 |
| 5.3.3 Wind and Current Forces by OCIMF | 90 |
| 5.4 Hydrodynamic Coefficients | 93 |
| 5.5 Coupled Analysis of FPSO | 95 |
| 5.6 Results and Discussion | 98 |
| 5.6.1 Static Offset Test (in Calm Water without Current) | 99 |
| 5.6.2 Free-decay Tests (in Calm Water without Current) | 101 |
| 5.6.3 Time-domain Simulation for Hurricane Condition | 103 |
| 5.7 Summary and Conclusions | 106 |

| CHAPTER | Page |
|---------|--|
| VI | CASE STUDY 2: DYNAMIC ANALYSIS OF A TANKER BASED FPSO COMPARED WITH THE OTRC EXPERIMENT 108 |
| | 6.1 Introduction 108 |
| | 6.2 OTRC Experimental Results and Design Premise Data 109 |
| | 6.3 Environmental Data 114 |
| | 6.4 Re-generation of the Experimental Model 116 |
| | 6.5 Results and Discussion 119 |
| | 6.5.1 Static Offset Test with Re-generated Model Data 119 |
| | 6.5.2 Free-Decay Test with Re-generated Model Data 120 |
| | 6.5.3 Time Simulation Results 123 |
| | 6.6 Summary and Conclusions 125 |
| VII | CASE STUDY 3: CALCULATION OF HYDRODYNAMIC COEFFICIENTS FOR TWO BODY SYSTEM OF FPSO AND SHUTTLE TANKER 126 |
| | 7.1 Introduction 126 |
| | 7.2 Particulars of Models and Arrangements for the Tests 128 |
| | 7.3 Environmental Conditions 132 |
| | 7.4 Results and Discussion 133 |
| | 7.5 Summary and Conclusions 141 |
| VIII | CASE STUDY 4: DYNAMIC ANALYSIS FOR TWO-BODY SYSTEM COMPOSED OF SPAR AND SPAR 142 |
| | 8.1 Introduction 142 |
| | 8.2 Particulars of Models and Arrangements for the Analyses 143 |
| | 8.3 Environmental Conditions 146 |
| | 8.4 Calculation of Hydrodynamic Coefficients Using WAMIT 1 st and 2 nd Order 147 |
| | 8.5 Linear Spring Modeling 149 |
| | 8.6 Results and Discussion 149 |
| | 8.7 Summary and Conclusions 154 |
| IX | CASE STUDY 5: DYNAMIC ANALYSIS FOR TWO-BODY SYSTEM COMPOSED OF AN FPSO-FPSO AND AN FPSO-SHUTTLE TANKER 155 |
| | 9.1 Introduction 155 |
| | 9.2 Particulars of Models and Arrangements for the Analyses 156 |
| | 9.3 Environmental Conditions 160 |

| CHAPTER | Page |
|--|------|
| 9.4 Calculation of Hydrodynamic Coefficients Using WAMIT | 162 |
| 9.5 Two-Mass-Spring Modeling | 164 |
| 9.6 Results and Discussion | 174 |
| 9.7 Summary and Conclusions | 200 |
| X CONCLUSIONS FOR ALL CASE STUDIES | 201 |
| REFERENCES | 203 |
| VITA | 208 |

LIST OF FIGURES

| FIGURE | Page |
|---|------|
| 3.1 Coordinate system of rod | 46 |
| 5.1 The body plan and the isotropic view of FPSO 6,000 ft | 82 |
| 5.2 Arrangement of the mooring lines for FPSO 6,000 ft. | 84 |
| 5.3 Arrangement of the risers for FPSO 6,000 ft. | 85 |
| 5.4 JONSWAP wave spectrum | 88 |
| 5.5 API wind spectrum | 89 |
| 5.6 Modeling of body surface of FPSO | 94 |
| 5.7 Modeling of body surface and free surface of the water | 95 |
| 5.8 Hull drag damping coefficients (Wichers, 1996) | 97 |
| 5.9 Static offset test results for surge motion | 100 |
| 5.10 Free-decay test results for surge, heave and roll motions | 102 |
| 6.1 General arrangement and body plan of FPSO 6,000 ft | 110 |
| 6.2 Arrangement of mooring lines for turret-moored FPSO | 113 |
| 6.3 NPD wind spectrum curve | 115 |
| 6.4 Comparison of the static offset test results | 121 |
| 6.5 Hull drag coefficients proposed by Wichers (1998 & 2001) | 122 |
| 7.1 Configuration of the mooring system | 131 |
| 7.2 Rough-meshed numerical modeling for a LNG FPSO and a shuttle tanker | 132 |
| 7.3 Fine-meshed numerical modeling for a LNG FPSO and a shuttle tanker | 132 |

| FIGURE | Page |
|--|------|
| 7.4 Heave response operators of side-by-side moored vessels in the beam sea | 134 |
| 7.5 Roll response operators of side-by-side moored vessels in the beam sea | 135 |
| 7.6 Longitudinal wave drift force of tandem moored vessels in the head sea | 136 |
| 7.7 Longitudinal wave drift force of side-by-side moored vessels in the head sea ... | 137 |
| 7.8 The distance effect on the longitudinal wave drift force for a two-body and a single body model in the head sea | 138 |
| 7.9 Lateral wave drift force of side-by-side moored vessels in the head sea | 139 |
| 7.10 Lateral wave drift force of side-by-side moored vessels in the beam sea | 140 |
| 8.1 Configuration of the mooring system and the environmental loads (Tandem arrangement, $d=30\text{m}$)..... | 144 |
| 8.2 Configuration of the modeling of a single spar | 148 |
| 8.3 Configuration of the modeling of a two-body spar | 148 |
| 8.4.a Comparison of the surge motion RAOs | 151 |
| 8.4.b Comparison of the heave motion RAOs | 151 |
| 8.4.c Comparison of the roll motion RAOs | 152 |
| 8.5 Comparison of the surge drift force | 152 |
| 9.1 Configuration of the mooring systems (Tandem mooring system)..... | 158 |
| 9.2 Configuration of the arrangement of the mooring line groups | 159 |
| 9.3 Configuration of single-body, two-body models and the system | 163 |
| 9.4 Two-mass-spring model | 165 |
| 9.5 The diagram of the time simulation in SIMULINK of MATLAB | 168 |

| FIGURE | Page |
|--|------|
| 9.6 The surge motion of the FPSO and FPSO model by MATLAB for mass-spring model and by WINPOST-MULT for two-body model | 169 |
| 9.7 The time simulation results of the FPSO and shuttle tanker model | 172 |
| 9.8.a Time simulation for the two body model of the FPSO and shuttle tanker (at body #1=FPSO; tandem; without interaction effect) | 176 |
| 9.8.b Time simulation for the two body model of the FPSO and shuttle tanker (at body #2=shuttle tanker; tandem; without interaction effect) | 178 |
| 9.8.c Amplitude spectrum density curve of the motion responses for the two body model of the FPSO and shuttle tanker (at body #1=FPSO; tandem; without interaction effect) | 180 |
| 9.8.d Amplitude spectrum density curve of the motion responses for the two body model of the FPSO and shuttle tanker (at body #2=shuttle tanker; tandem; without interaction effect) | 182 |
| 9.9.a Time simulation for the two body model of the FPSO and shuttle tanker (at body #1=FPSO; tandem; with interaction effect and by iteration method).. | 184 |
| 9.9.b Time simulation for the two body model of the FPSO and shuttle tanker (at body #2=shuttle tanker; tandem; with interaction effect by iteration method) | 186 |
| 9.9.c Amplitude spectrum density curve of the motion responses for the two body model of FPSO and shuttle tanker (at body #1=FPSO; tandem; with interaction effect by iteration method) | 188 |
| 9.9.d Amplitude spectrum density curve of the motion responses for the two body model of FPSO and shuttle tanker (at body #2=shuttle tanker; tandem; with interaction effect by combined method) | 190 |
| 9.10.a Time simulation for the two body model of the FPSO and shuttle tanker (at body #1=FPSO; tandem; with interaction effect by combined method) ... | 192 |
| 9.10.b Time simulation for the two body model of the FPSO and shuttle tanker (at body #2=shuttle tanker; tandem; with interaction effect by combined method) | 194 |

| FIGURE | Page |
|--|------|
| 9.10.c Amplitude spectrum density curve of the motion responses for the two body model of the FPSO and shuttle tanker (at body #1=FPSO; tandem; with interaction effect by combined method) ... | 196 |
| 9.10.d Amplitude spectrum density curve of the motion responses for two body model of FPSO and shuttle tanker (at body #2=shuttle tanker; tandem; with interaction effect by combined method) | 198 |

LIST OF TABLES

| TABLE | Page |
|---|------|
| 5.1 Main particulars of the turret moored FPSO 6,000 ft | 81 |
| 5.2 Main particulars of mooring systems | 83 |
| 5.3 Hydrodynamic coefficients of the chain, rope and polyester | 83 |
| 5.4 Main particulars of risers | 84 |
| 5.5 Hydrodynamic coefficients of risers | 84 |
| 5.6 Azimuth angles of risers bounded on the earth | 85 |
| 5.7 Environmental loading condition | 86 |
| 5.8 Natural periods from free-decay tests | 103 |
| 5.9 Damping from free-decay tests estimated from the first 4 peaks assuming linear damping | 103 |
| 5.10 Time-domain simulation results | 104 |
| 5.11 The results of tensions on the mooring lines and risers | 105 |
| 6.1 Main particulars of the turret moored for the OTRC FPSO | 111 |
| 6.2 Main particulars of mooring systems for the OTRC FPSO | 112 |
| 6.3 Hydrodynamic coefficients of the chain, rope and wire for the OTRC FPSO | 112 |
| 6.4 Environmental loading condition for the OTRC FPSO | 114 |
| 6.5 WAMIT output and hand-calculation | 117 |
| 6.6 Re-estimated data from WAMIT output and hand-calculation | 119 |
| 6.7 Comparison of the free decay test results | 122 |

| TABLE | Page |
|--|------|
| 6.8 Comparison of time simulation results | 124 |
| 7.1 Main particulars of two vessels | 129 |
| 7.2 Free-decay test results for a LNG FPSO and a shuttle tanker (heave and roll) | 130 |
| 7.3 Comparison of the hydrodynamic coefficients obtained from the rough model and the fine models | 131 |
| 8.1 Main particulars of moored spar | 144 |
| 8.2 Particulars of the mooring systems | 145 |
| 8.3 Environmental conditions | 146 |
| 8.4 The analysis results for two-body model composed of two spars | 153 |
| 9.1 Main particulars of the turret moored FPSO | 157 |
| 9.2 Main particulars of the mooring systems | 158 |
| 9.3.a Environmental conditions (100-year storm condition at GoM) | 161 |
| 9.3.b Environmental conditions (west Africa sea condition) | 161 |
| 9.4 The system parameters for two-mass-spring model | 168 |
| 9.5 Analysis results of mass-spring model: displacement at mass #1 and #2 | 170 |
| 9.6 Summary of the analysis results for two body FPSO+FPSO | 171 |
| 9.7 Summary of the analysis results for the two-body FPSO+shuttle tanker | 173 |

CHAPTER I

INTRODUCTION

1.1 Background

Recently, floating structures have been invented and their installation has been attempted worldwide because of cost effectiveness, in an attempt to replace traditional fixed jacket platforms. These structures include the ship-shaped vessel called an FPSO(Floating Production Storage and Offloading Unit), the column stabilized semi-submergible platform, the spar platform, and the tension leg platform(TLP). The last two types have been designed and installed in the Gulf of Mexico(GoM) for the last decade. In the case of TLPs, there were several built and installed in GoM, of which Auger, Mars, Ursa, and Marlin were fixed in position by means of the mooring lines or risers in 2,800 ft to 4,000 ft of water depth. In the case of spars, Neptune, Genesis, and Diana were installed in 2,000 ft, 2,590 ft, 4,300 ft of water depth, respectively. These installations were made from 1996 to 1999. Nowadays, the truss spar is being considered more cost-effective. The recent trend in the installation of floating structures shows the water depth getting deeper and deeper since the oil and gas fields are expedited and discovered in the deeper sea. This means the more developed designs should be invented and studied realistically for the installation of the floating structures in deep water of 6,000 ft or more. Floating structures are more attractive to the industrial companies

This dissertation follows the style and the format of the *Journal of Fluid Mechanics*.

because they can allow for environmental conditions more flexibly than the fixed structures.

They have more advantages in that they have been designed under the concept of optimization and minimization against the responses to environmental conditions. For the spars, they have small water plane areas compared with other floating structures. This results in reducing the heave response by decreasing the vertical wave load and shifting the heave natural frequency in the low part far apart from the wave-dominant frequency. The surface-production trees and rigid risers are allowed due to the above-mentioned aspect of design, instead of the sub-sea trees and flexible risers that are more expensive. For the TLPs, the high-strength vertical tethers are normally used. It results in avoiding the resonance between the motion of TLPs and the wave excitations so that it is able to stay more stable while operating during oil or gas extraction, and it allows using the surface-production trees. For the floating structures in deep water, many researchers have proved that coupled dynamic analyses are indispensable to get more convincing results from the platform responses and the line tensions than those of conventional uncoupled analysis methods (Pauling and Webster, 1986; Kim et al., 1994; Ran and Kim, 1997; Ran, Kim and Zheng, 1999a; Ran, Kim and Zheng, 1999b; Ma et al., 2000). Since the ship-shaped floating structures called FPSOs have more advantages as the solutions to comparably large deck space, cost-saving problems and less risk of oil spills, they will have to be potentially attractive production systems in ultra deep water of the GOM. Nowadays, the Mineral Management System (MMS) has approved the installation of an FPSO under the condition that the vessel has the construction of a double hull tanker in

the GOM. The large storage capacity is the biggest advantage because no pipeline has to be laid out from the sea floor to the land. A kind of LNG carrier or oil shuttle tanker is substituted for the pipelines for the purpose of turning over the oil and gas. For the installation of FPSO in deep water such as GoM, the development of a coupled dynamic analysis code for solving the large yaw motion and the interaction problem of multiple-body system becomes indispensable.

1.2 Literature Review

The comprehensive studies about the viscous dampings for dynamic motion analysis of the turret-moored FPSO were performed by Wichers(1988). He derived the equation of the motions of a single-point-moored FPSO exposed to current, wind and long-crested irregular waves, and carried out the nonlinear analysis by uncoupled method, which solves the motions of body and mooring lines, separately. The coupling effects of the low frequency component of a viscous reaction force were studied by Wichers and Chunqun Ji (2000). By conducting a series of experimental studies, they examined the coupling terms due to the combined modes of motion in still water and in the current. They proved the viscous part in a normal direction contributes significantly to the hull dynamics, so that it cannot be neglected. In addition, the coupling effect of rigid body motion and the motions of the mooring lines and risers was investigated by Wichers and Devlin(2001). The fully coupled dynamic mathematical model is necessary to estimate realistic motion responses and line tensions.

The extreme response of a turret moored FPSO in GoM was studied by Baar et al. (2000). The dynamic motion of FPSO on collinear, non-collinear wind, the wave and current of a 100-year return period storm was investigated so that it was verified that the response of a turret FPSO is sensitive to non-collinear environmental conditions. Ward et al.(2001) presented the results of experiments conducted in OTRC(Offshore Technology of Research Center in Texas A&M University) for a turret-moored FPSO in collinear and non-collinear environmental conditions. The hull/mooring/riser coupled analyses of a tanker-based turret-moored FPSO was carried out by Arcandra et al. (2002) using a coupled dynamic analysis tool for floating structures, developed by him. They investigated two types of mooring system of the polyester mooring lines and buoy type mooring lines through the time simulation of FPSO 6,000 ft under the conditions of 100-year hurricane.

The aspects of the hydrodynamic characteristics of the multiple-body structure combined with a barge and a mini TLP were studied by Teigen (2000). He compared the hydrodynamic coefficients of the multiple-body and the single-body and also conducted the convergence tests according to the mesh size of the multiple body. He emphasized the importance of hydrodynamic interaction for the motion response of two bodies and indicated the fact that neglecting the fluid-coupling effect may result in an erroneous and non-conservative prediction. Using a three-dimensional source technique, Inoue et al. (2001) solved the drift force for a multiple-body system of the FPSO-LNG carrier in parallel arrangement with zero forward speed waves. By adding the viscous roll damping to the potential damping, the study was attempted to compare the effect on drift forces

with experimental results in regular and irregular waves. For a multi-body system with a side-by-side mooring of an FPSO and an LNG carrier, a linear potential solver was developed by Huijismans (2001), and the mean and low-frequency wave drift forces were calculated by using it. For the same model, Buchner et al. (2001) conducted the numerical simulation for the prediction of hydrodynamic responses of an LNG FPSO with alongside moored an LNG carrier. They used a free surface lid in this multiple-body diffraction analysis for the calculation of drift forces and a relative viscous damping in a horizontal plane, and the composition of the complete matrix of retardation function for the correct prediction of heave and pitch motions. The hydrodynamic interaction of forces and motions of the floating multiple-body was investigated using the WAMIT program (Clauss et al., 2002) and the higher-order boundary element method (Choi et al., 2002).

1.3 Objective and Scope

The main objective of this research is to develop a numerical program to analyze the hydrodynamic interaction responses of multiple bodies, mooring lines and risers based on the hull/mooring/riser coupled dynamic program called WINPOST-FPSO(Arcandra, 2001), using the hydrodynamic coefficients calculated by WAMIT (Lee, 1999) considering the interaction effects of the multiple-body.

The first stage consists of the evaluation and interpretation of the hydrodynamic interaction analysis results with WAMIT and the preparation of the wind and current force data (OCIMF, 1994) for performing the coupled dynamic analysis program newly

developed (WINPOST-MULT) for the ship-shaped multiple-body system (FPSO, LNG carrier etc.). The interpretation program (WAMPOST-MULT) of the WAMIT results will be made for the preparing the properly formatted data for WINPOST-MULTI. For the wind and current forces, a modification in some parts of the original program (WINPOST-FPSO) will be needed.

In the second stage of this research, the original program (WINPOST-FPSO) will be developed to be able to perform the hull/mooring/riser coupled dynamic analysis for general multiple floating bodies. In the new program, it will be considered that the multiple bodies can be laid in any relative position to the open sea. The wave heading angle will be considered separately for each body at every small degree of angle and the relative angles between multiple bodies will be considered at every span in the same manner as for the wave heading angle.

The third stage is to prove the validity of the newly developed program through carrying out the numerical simulation after the proper models are selected. Buchner's model (2001) and Choi's model (2002) may be used for a comparative study about the results to be obtained from WINPOST-MULT. The former has the characteristics to deal with the close proximity problem of a side-by-side off-loading system. The latter took two, same sized vessels of an FPSO and a shuttle tanker to tackle the problems of both cases of the side-by-side system and the tandem system, and used the higher-order boundary element method (HOBEM) while the constant panel method(CPM) was used in WAMIT. The coupled dynamic analysis scheme adopted in the program WINPOST-

MULT will be proved as the robust tool for analyzing the interaction problem of the multiple-body floating structure.

1.4 Procedure

1.4.1 Interpretation and Preparation of WAMIT Results and Wind/Current Forces

For the calculation of the hydrodynamic coefficients and wave forces, WAMIT (1999) will be used. WAMIT will give the results of $6 \times N$ degree of freedoms (DOFs) for N bodies in consideration of the N -body interaction. WAMIT should be run for each contacting angle between N bodies at every small angle. It will give the hydrodynamic interaction coefficients of added mass and damping and wave forces. The added mass and wave drift damping will be given as a matrix sized by ($NFREQ \times 6N \times 6N$), where $NFREQ$ means the number of frequencies of the wave. The wave forces will be given as the linear wave force transfer function (LTF), sized by ($NFREQ \times 6N$) and as the sum- and difference-frequency components sized by ($NFREQ \times NFREQ \times 6N$). WAMIT should be pre-run for each contacting angle between N -bodies at every small angle of wave heading and at every small amount angle of contact with each body for the expected positions. These results will be converted as the input data (each input data file will be named as data000.wv) for WINPOST-MULT. For the preparation of the input data, one converting program (WAMPOST-MULT) will be made.

The wind and current forces subject to any ship-shaped floating structures can be referred to the OCIMF (1994). For the full loading and the ballast condition, wind and

current forces and moments can be read from the tables in the booklet published by OCIMF (1994). They also will be prepared prior to running the WINPOST-MULT. In the WINPOST-MULT, the two data files will be read, and the real drafts of the subjected vessels will be recognized as the draft ratio to the full draft. During the running of the program WINPOST-MULT, the angles against wave headings and the relative angles between multiple bodies will be checked at every time step. If the angles exceed the initial angle, the wind/current forces and moments for the updated angle will be read from the files of the hydrodynamic coefficients pre-calculated for every 5 degree of yaw angle.

1.4.2 Developing the Coupled Dynamic Program

The back-born program, WINPOST-FPSO, is already developed by Arcandra(2001). For the N bodies, the dealing DOF number should be set up as $6N$ and the related subroutines should be modified. WINPOST-FPSO is a coupled dynamic program that can treat the body and rods(mooring lines and risers). For N bodies, the total equations of motion for the total system will be combined with the mooring line dynamic equations. For a single body system, the final equation of motion with a combination of the coupling terms of a single body and mooring lines/risers is obtained as:

$$\begin{bmatrix} \mathbf{K}^L & \mathbf{K}^C \\ (\mathbf{K}^C)^T & \mathbf{K}^B \end{bmatrix} \begin{Bmatrix} \mathbf{U}^L \\ \mathbf{U}^B \end{Bmatrix} = \begin{Bmatrix} \mathbf{F}^L \\ \mathbf{F}^B \end{Bmatrix}$$

where, subscripts of r , c and b mean the rod, the coupled term and the body, respectively.

If the total number of mooring lines and risers of the system is defined as n_L , the

matrices in the above equation, where the equations and figures in the parentheses after the matrix name mean the matrix size, are defined as follows:

$\mathbf{K}^L ((n_L \times [8 \times (n_E + 1) - 1]) \times (\text{bandwidth}))$ = the stiffness matrix of mooring lines and risers

$\mathbf{K}^C (n_L \times [8 \times (n_E + 1) - 1] \times (6 \times N))$ = the stiffness matrix coupled with the body and mooring lines/risers

$\mathbf{K}^B (6N \times 6N)$ = the motion matrix of the body

$\mathbf{U}^L ((n_L \times [8 \times (n_E + 1) - 1]) \times 1)$ = the motion vector of mooring lines and risers

$\mathbf{U}^B (6N \times 1)$ = the motion vector of the body

$\mathbf{F}^L ((n_L \times [8 \times (n_E + 1) - 1]) \times 1)$ = the external force vector subject to mooring lines and

risers

$\mathbf{F}^B (6N \times 1)$ = the external force vector subject to the body

where n_E is the number of elements per one line, the bandwidth is 15, and N denotes the number of bodies to be considered. For the multiple body system of N bodies, the rigid bodies are lumped at N points with $6N$ DOFs, which are connected with springs and dampers to the mooring lines and risers. The number of DOFs of \mathbf{U}^B will be enlarged to $6N$ as much as the number of DOFs for multiple bodies. Furthermore, the part of the program to deal with multiple-body systems needs to be modified for reading

the hydrodynamic coefficients and wave forces for the proper contacting angle at every time step, and for evaluating and assigning to the external forces of the wind and current forces for the loading conditions of the subject vessels. At every time step, the program will check the yaw angle for each body, so that if the angle exceeds a certain amount, the proper wave data file will be read and used for next time step.

The existing program is implemented to consider the connecting part of the vessel to the mooring lines and risers as stiff linear rotational springs, or dampers only at the position of starting points of mooring lines and risers. On the contrary, the ending points of the mooring lines and risers are to be regarded as jointing to the sea floor with assumed very huge stiffness of the sea-bed foundation. Some parts of the future-developed program will be modified so that the flexible connections at both ends of the mooring lines and risers are available. The program will use the existing output format of the previous program except extending the columns of output file for $6N$ DOF motions.

1.4.3 Comparative Studies

In this stage, the Buchner's model(2001) and Choi's model(2002) may be taken for the comparative study about the results to be obtained from WINPOST-MULT. The former is the multiple body system composed of the LNG FPSO tanker and the LNG carrier. The two vessels are located each at very close proximity to the other in the open sea. Buchner et al. (2001) has performed the calculation of hydrodynamic interaction coefficients, wave load coefficients with the linear potential program using a lid

technique and the motion analysis of a multiple-body system using the above results as input data. The results will be good for comparison with WINPOST-MULT's. The latter used the combining model of the FPSO and shuttle tanker located at close proximity with the side-by-side arrangement and also at a distance with the tandem arrangement. Choi et al. (2002) used the higher-order boundary element method not CPM(Constant Panel Method) used in WAMIT.

Some examples are taken for verification of the hull/mooring/riser coupled dynamic analyses of two-body system using the WINPOST-MULT program, for which two identical SPARs, two identical FPSOs and also an FPSO and a shuttle tanker are selected as the test models. The analysis results for those models are compared with the simplified spring-mass models. For the environmental conditions, the 100-year storm condition in GOM and the sea condition in West Africa are taken.

CHAPTER II

DYNAMICS OF THE FLOATING PLATFORM

2.1 Introduction

In this chapter, the wave loads and dynamic responses of floating structures are discussed. First, linear and second-order wave theories are reviewed in the consideration of the free surface boundary value problem, and then the boundary element method is discussed as one of the solution schemes for the free surface boundary value problem, and Morison's equation and the wave drift damping are considered. Finally, the multiple-body interaction of fluid is reviewed, and then the dynamic motions for single body and multiple body systems of the floating structure are described, sequentially.

2.2 Formulation of Surface Wave

2.2.1 Boundary Value Problem (BVP) of Surface Wave

The fluid in the region surrounding the free surface boundary can be expressed as a boundary value problem in the domain. The surface wave theory is derived from the solution of the BVP with the free surface. The fluid motion can be expressed by the Laplace equation of a velocity potential with the assumption of irrotational motion and an incompressible fluid.

$$\nabla u = 0 \quad (2.1)$$

or

$$\nabla^2 \Phi = \frac{\partial^2 \Phi}{\partial x^2} + \frac{\partial^2 \Phi}{\partial y^2} + \frac{\partial^2 \Phi}{\partial z^2} = 0 \quad (2.2)$$

where u is the velocity in x, y or z direction of fluid, so it becomes $\frac{\partial\Phi}{\partial x}\mathbf{i} + \frac{\partial\Phi}{\partial y}\mathbf{j} + \frac{\partial\Phi}{\partial z}\mathbf{k}$.

ϕ is the velocity potential. In order to solve the equation (2.2), the boundary condition should be considered, specifically. The bottom boundary condition is to be considered. In addition, there are two free surface conditions, which are the dynamic free surface condition and the kinematic free surface condition. The bottom boundary condition is given by the condition that the sea bed is impermeable:

$$\frac{\partial\Phi}{\partial z} = 0 \quad \text{at } z = -d \quad (2.3)$$

where d is the water depth. The kinematic condition is to represent that the fluid particle on the free surface at any instance retains at one position of the free surface. The equation of the kinematic free surface condition can be given by:

$$\frac{\partial\eta}{\partial t} + u\frac{\partial\eta}{\partial x} + v\frac{\partial\eta}{\partial y} - \frac{\partial\Phi}{\partial z} = 0 \quad \text{at } z = -\eta \quad (2.4)$$

where $\eta(x, y, t)$ is the displacement on the plane of the free surface to be varied in space and time. The dynamic free surface condition defines that the pressure on the free surface is constant as the equal value to the atmospheric pressure and normally the atmospheric pressure is assumed to be zero. Thus, the condition can be described as follows:

$$\frac{\partial\Phi}{\partial t} + \frac{1}{2}(\nabla\Phi \cdot \nabla\Phi) + gz = 0 \quad \text{at } z = -\eta \quad (2.5)$$

where g is the gravitational acceleration. The most popular approach to solve the equation (2.1) is known as the perturbation method under the assumption that the wave

amplitude is very small, which can give the approximated solution to satisfy partially the free surface boundary conditions. In the method, the wave elevation (wave particle displacement) and the velocity potential are to be taken as the power series forms a very small non-dimensional perturbation parameter. The linear wave and the second order or higher order wave can be derived from the perturbation formula of the wave equation, to be represented by the wave elevation and the velocity potential in terms of the perturbation parameter.

2.2.2 Wave Theory

The perturbation formulation of the BVP with the first- and second-order parameters can give the first-order solution and the second-order solution. The first-order solution leads the linear wave theory and the second-order solution leads the second order wave theory. The velocity potential is represented by the summation of all perturbation terms and the wave elevation by summation of the perturbative wave elevations. Finally, the total velocity potential and the wave elevation are written in the following forms:

$$\Phi = \sum \varepsilon^{(n)} \Phi^{(n)} \quad (2.6)$$

$$\eta = \sum \varepsilon^{(n)} \eta^{(n)} \quad (2.7)$$

The linear wave equations are obtained by solving the perturbation formulation formed with the velocity potential and that with the wave elevation are obtained by:

The first-order potential:

$$\Phi^{(1)} = \text{Re} \left[\frac{-igA \cosh k(z+d)}{\omega \cosh kd} e^{i(kx \cos \theta + ky \sin \theta - \omega t)} \right] \quad (2.8)$$

The first-order wave elevation:

$$\eta^{(1)} = A \cos(kx \cos \theta + ky \sin \theta - \omega t) \quad (2.9)$$

where k is the wave number expressed by $\frac{2\pi}{L}$ when L is the wave length, ω is the wave frequency, A is the wave amplitude, and θ is the incident wave angle. The second-order potential and the second-order wave elevation are obtained by solving the perturbation formulations formed with the second-order potential and the second-order wave elevation are obtained as follows:

The second-order potential:

$$\Phi^{(2)} = \text{Re} \left[\frac{3}{8} \omega A^2 \frac{\cosh 2k(z+d)}{\sinh^4 kd} e^{i(2kx \cos \theta + 2ky \sin \theta - 2\omega t)} \right] \quad (2.10)$$

The second-order wave elevation:

$$\eta^{(2)} = A^2 k \frac{\cosh kd}{\sinh^3 kd} (2 + \cosh 2kd) \cos(2kx \cos \theta + 2ky \sin \theta - 2\omega t) \quad (2.11)$$

In the real sea, the wave is irregular and random. A fully developed wave is normally modeled in terms of energy spectra combined with ensembles of wave trains generated by random phases. Well-known spectra in common usage, such as the Pierson- Moskowitz and the JONSWAP spectra, are established. The time series for a given input amplitude spectrum $S(\omega)$ is obtained by combining a reasonably large number N of linear wave components with random phases:

$$\eta(x, y, t) = \sum_{i=1}^N A_i \cos(k_i x \cos \theta + k_i y \sin \theta - \omega_i t + \varepsilon_i) = \text{Re} \left[\sum_{i=1}^N A_i e^{i(k_i x \cos \theta + k_i y \sin \theta - \omega_i t + \varepsilon_i)} \right] \quad (2.12)$$

where $A_i = \sqrt{2S(\omega_i)\Delta\omega}$ is the wave amplitude of the i -th wave, $\Delta\omega$ is the interval of wave frequency, and ε_i is the random phase angle. To avoid the increase of wave components and to increase the computational efficiency for a long time simulation, the following modified formula is used:

$$\eta(x, y, t) = \text{Re} \left[\sum_{j=1}^N A_j e^{i(k_j x \cos\theta + k_j y \sin\theta - \omega'_j t + \varepsilon_j)} \right] \quad (2.13)$$

where $\omega'_j = \omega_j + \delta\omega_j$ and $\delta\omega_j$ is a random perturbation number uniformly determined between $-\frac{\Delta\omega}{2}$ and $\frac{\Delta\omega}{2}$. The total potential and the wave elevation are given by adding every solution of each order equation, including the diffraction and the radiation.

2.2.3 Diffraction and Radiation Theory

The total velocity potential is decomposed into the incident potential Φ_I , the diffraction potential Φ_D , and the radiation potential Φ_R . By applying the perturbation method, the total potential can be written by:

$$\Phi = \sum \varepsilon^{(n)} (\Phi_I^{(n)} + \Phi_D^{(n)} + \Phi_R^{(n)}) \quad (2.14)$$

The diffraction wave force and the radiation wave force have a significant effect on a floating platform in deep water. The diffraction wave represents the scattered term from the fixed body due to the presence of the incident wave. On the other hand, the radiation wave means the wave to be propagated by the oscillating body in calm water. The forces

induced by them are evaluated by integration of the pressure around the surface of the floating structure using the diffraction and the radiation potential, which can be obtained by solving the BVPs of them.

2.2.3.1 First-Order Boundary Value Problem

By separation of variable for the first-order component, the first-order potential can be written by:

$$\begin{aligned}\Phi^{(1)} &= \varepsilon(\Phi_I^{(1)} + \Phi_D^{(1)} + \Phi_R^{(1)}) \\ &= \text{Re}\left[\{\phi_I^{(1)}(x, y, z) + \phi_D^{(1)}(x, y, z) + \phi_R^{(1)}(x, y, z)\} \cdot e^{-i\omega t}\right]\end{aligned}\quad (2.15)$$

By referring to the equation (2.8), the solution of incident wave velocity potential is inferred as follows:

$$\phi_I^{(1)} = \text{Re}\left[\frac{-igA \cosh k(z+d)}{\omega \cosh kd}\right]\quad (2.16)$$

The BVPs for the first-order potential of diffraction and radiation are defined as the following formula:

$$\nabla^2 \phi_{D,R}^{(1)} = 0 \quad \text{in the fluid } (z < 0) \quad (2.17)$$

$$\left(-\omega^2 + \frac{\partial}{\partial z}\right) \phi_{D,R}^{(1)} = 0 \quad \text{on the free surface } (z = 0) \quad (2.18)$$

$$\frac{\partial \phi_{D,R}^{(1)}}{\partial z} = 0 \quad \text{on the bottom } (z = -d) \quad (2.19)$$

$$\left. \begin{aligned}\frac{\partial \phi_D^{(1)}}{\partial n} &= -\frac{\partial \phi_I^{(1)}}{\partial n} \\ \frac{\partial \phi_R^{(1)}}{\partial n} &= -i\omega n \cdot (\xi^{(1)} + \alpha^{(1)} \times r)\end{aligned}\right\} \quad \text{on the body surface} \quad (2.20)$$

$$\lim_{\zeta \rightarrow \infty} \sqrt{r} \left(\frac{\partial}{\partial \zeta} \pm ik \right) \phi_{D,R}^{(1)} = 0 \quad \text{at far field} \quad (2.21)$$

where \mathbf{r} is the position vector on the body surface, R is the radial distance from the origin ($r^2 = x^2 + y^2$), $\mathbf{n} = (n_x, n_y, n_z)$ is the outward unit normal vector on the body surface, $\Xi^{(1)}$ is the first-order translational motion of the body, and $A^{(1)}$ is the first-order rotational motion of body. The $\Xi^{(1)}$ and $A^{(1)}$ can be expressed as follows:

$$\Xi^{(1)} = \text{Re}[\xi e^{-i\alpha}], \quad \Xi^{(1)} = (\xi_1^{(1)}, \xi_2^{(1)}, \xi_3^{(1)}) \quad (2.22)$$

$$A^{(1)} = \text{Re}[\alpha e^{-i\alpha}], \quad \alpha^{(1)} = (\alpha_1^{(1)}, \alpha_2^{(1)}, \alpha_3^{(1)}) \quad (2.23)$$

where 1,2,3 means the x -, y -, z - axis, respectively. Thus, $\xi_1^{(1)}, \xi_2^{(1)}, \xi_3^{(1)}$ are defined as the amplitude of surge, sway and heave motion, while $\alpha_1^{(1)}, \alpha_2^{(1)}, \alpha_3^{(1)}$ are defined as the amplitude of roll, pitch and yaw motion. The six degrees of freedom of the first order motion are rewritten as:

$$\zeta_j = \begin{cases} \xi_j^{(1)} & \text{for } j = 1,2,3 \\ \alpha_{j-3}^{(1)} & \text{for } j = 4,5,6 \end{cases} \quad (2.24)$$

The radiation potential can be decomposed as follows:

$$\phi_R^{(1)} = \sum_{j=1}^6 \zeta_j \phi_j^{(1)} \quad (2.25)$$

where $\phi_j^{(1)}$ represents the velocity potential of rigid body motion with unit amplitude in the j th mode when the incident wave does not exist. Equation (2.25) should satisfy the boundary conditions of equation (2.18) to (2.21). The body boundary condition of $\phi_j^{(1)}$ is written as:

$$\frac{\partial \phi_j^{(1)}}{\partial n} = -i\omega n_j \quad \text{for } j = 1,2,3 \quad (2.26)$$

$$\frac{\partial \phi_j^{(1)}}{\partial n} = -i\omega(\mathbf{r} \times \mathbf{n})_{j-3} \quad \text{for } j = 4,5,6 \quad (2.27)$$

These boundary conditions are valid on the body surface. The diffraction potential problem, equation (2.17), can be solved numerically in consideration of the boundary conditions (equation (2.18)-(2.21)).

2.2.3.2 Second-Order Boundary Value Problem

The second-order boundary value problem is made by considering the interaction of bichromatic incident waves of frequency ω_m and ω_n with a floating body. The Volterra series method will be applied to solve the second-order BVP. If the second-order terms are taken from the perturbation formulation (2.14) and the separation of variable is applied, the second-order potential is derived by:

$$\begin{aligned} \Phi^{(2)}(x, y, z, t) &= \varepsilon^2 (\Phi_I^{(2)} + \Phi_D^{(2)} + \Phi_R^{(2)}) \\ &= \text{Re} \left[\left\{ \phi_I^-(x, y, z) + \phi_D^-(x, y, z) + \phi_R^-(x, y, z) \right\} \cdot e^{-i\omega^- t} \right. \\ &\quad \left. + \left\{ \phi_I^+(x, y, z) + \phi_D^+(x, y, z) + \phi_R^+(x, y, z) \right\} \cdot e^{-i\omega^+ t} \right] \end{aligned} \quad (2.28)$$

where $\omega^- = \omega_m - \omega_n$ is the difference-frequency, $\omega^+ = \omega_m + \omega_n$ is the sum frequency, ϕ^- is the difference-frequency potential, and ϕ^+ is the sum-frequency potential. The difference-potential and sum-frequency potential can be solved independently. The governing equation (2.1) or (2.2) can be solved for each potential component of equation (2.28) considering the boundary conditions, equation (2.3) to (2.5) as follows:

$$\phi_I^+ = \frac{1}{2}(\gamma_{mn}^+ + \gamma_{nm}^+) \frac{\cosh k^+(z+d)}{\cosh k^+d} e^{ik^+x} \quad (2.29)$$

$$\phi_I^- = \frac{1}{2}(\gamma_{mn}^- + \gamma_{nm}^{-*}) \frac{\cosh k^-(z+d)}{\cosh k^-d} e^{ik^-x} \quad (2.30)$$

where

$$\gamma_{mn}^+ = -\frac{igA_m A_n k_m^2 (1 - \tanh^2 k_m d) + 2k_m k_n (1 - \tanh k_m d \tanh k_n d)}{2\omega_m \nu^+ - k^+ \tanh k^+ d} \quad (2.31)$$

and

$$\gamma_{mn}^{-*} = -\frac{igA_m A_n^* k_m^2 (1 - \tanh^2 k_m d) - 2k_m k_n (1 + \tanh k_m d \tanh k_n d)}{2\omega_m \nu^- - k^- \tanh k^- d} \quad (2.32)$$

and the asterisk represents a complex conjugate, and ν^\pm and k^\pm are defined respectively by:

$$\nu^\pm = \frac{(\omega^\pm)^2}{g}, \quad k^\pm = k_m \pm k_n \quad (2.33)$$

The second-order diffraction and radiation potential, $\phi_{D,R}^{(2)}$, deal with the second interaction of plane bichromatic incident waves. The second-order diffraction potential, $\phi_D^{(2)}$, contains the contributions of the second-order incident potential and the first-order potential. The governing equation of the second-order radiation potential is only expressed by the outgoing waves propagated by the second-order body motion. Thus, the governing equation of the second-order diffraction potential is defined by:

$$\nabla^2 \phi_D^\pm = 0 \quad \text{in the quiescent fluid volume } (z < 0) \quad (2.34)$$

$$\left[-(\omega^\pm)^2 + g \frac{\partial}{\partial z} \right] \phi_D^\pm = Q^\pm \quad \text{on the free surface } (z = 0) \quad (2.35)$$

$$\frac{\partial \phi_D^\pm}{\partial z} = 0 \quad \text{on the bottom } (z = -d) \quad (2.36)$$

$$\frac{\partial \phi_D^\pm}{\partial n} = -\frac{\partial \phi_I^\pm}{\partial n} + B^\pm \quad \text{on the body surface} \quad (2.37)$$

$$\text{Boundary condition at far field} \quad (2.38)$$

where Q^\pm are the sum and difference frequency components of the free surface force and B^\pm are the sum and difference frequency components of the body surface force. The Q^\pm are symmetric and expressed as follows:

$$Q^+ = \frac{1}{2}(q_{mn}^+ + q_{nm}^+), \quad Q^- = \frac{1}{2}(q_{mn}^- + q_{nm}^{-*}) \quad (2.39)$$

and,

$$q_{mn}^+ = -\frac{i\omega_m}{g}\phi_n^{(1)}\left(-\omega^2\frac{\partial\phi_m^{(1)}}{\partial z} + g\frac{\partial^2\phi_m^{(1)}}{\partial z^2}\right) + i\omega_n\nabla\phi_m^{(1)}\nabla\phi_n^{(1)} - q_{ll}^+ \quad (2.40)$$

$$q_{mn}^- = -\frac{i\omega_m}{g}\phi_n^{(1)*}\left(-\omega^2\frac{\partial\phi_m^{(1)}}{\partial z} + g\frac{\partial^2\phi_m^{(1)}}{\partial z^2}\right) + i\omega_n\nabla\phi_m^{(1)}\nabla\phi_n^{(1)*} - q_{ll}^- \quad (2.41)$$

The B^\pm are also symmetric and expressed as follows:

$$B^+ = \frac{1}{2}(b_{mn}^+ + b_{nm}^+), \quad B^- = \frac{1}{2}(b_{mn}^- + b_{nm}^{-*}) \quad (2.42)$$

and,

$$b_{mn}^+ = -\frac{1}{2}\mathbf{n} \cdot (\boldsymbol{\zeta}_n^{(1)} \cdot \nabla) \nabla \phi_m^{(1)} \quad (2.43)$$

$$b_{mn}^- = -\frac{1}{2}\mathbf{n} \cdot (\boldsymbol{\zeta}_n^{(1)*} \cdot \nabla) \nabla \phi_m^{(1)} \quad (2.44)$$

The boundary condition (2.37) for the second-order diffraction potential needs to be applied to the decomposed diffraction potential into a homogenous term and a particular solution term due to the complication. The homogeneous term of the second-order diffraction potential has the far-field propagating behavior, while the free surface force Q^\pm are dominant in the particular equation term.

The governing equation and boundary conditions for the second-order radiation potential ϕ_R^\pm are defined as the first-order radiation BVP, since the boundary conditions for the radiation potential do not contain any other potentials:

$$\nabla^2 \phi_R^\pm = 0 \quad \text{in the fluid } (z < 0) \quad (2.45)$$

$$\left(-\omega^2 + \frac{\partial}{\partial z} \right) \phi_R^\pm = 0 \quad \text{on the free surface } (z = 0) \quad (2.46)$$

$$\frac{\partial \phi_R^\pm}{\partial z} = 0 \quad \text{on the bottom } (z = -d) \quad (2.47)$$

$$\frac{\partial \phi_R^\pm}{\partial n} = -i\omega \mathbf{n} \cdot (\xi^\pm + \alpha^\pm \times \mathbf{r}) \quad \text{on the body surface} \quad (2.48)$$

$$\lim_{R \rightarrow \infty} \sqrt{R} \left(\frac{\partial}{\partial R} \pm ik \right) \phi_R^\pm = 0 \quad \text{at far field} \quad (2.49)$$

where ξ^\pm and α^\pm are the second order translations and rotational motions of the body at the sum and difference frequencies. Therefore, the second-order radiation potential has the same formula as the first-order radiation potential.

2.3 Hydrodynamic Forces

2.3.1 The First-Order Hydrodynamic Forces and Moments

If all of the potentials are solved, the first-order force and moment can be obtained from the integration over the whole surface pressure on the body. The pressure on the body surface ($\partial\Omega_B$) is obtained from the potential as follows:

$$P^{(1)} = -\rho \left(\frac{\partial\Phi^{(1)}}{\partial t} + gz \right) \quad (2.50)$$

where ρ is the fluid density. The six components of forces and moments are calculated as follows:

$$F_j^{(1)}(t) = -\rho g \iint_{\partial\Omega_B} z n_j dS - \rho \operatorname{Re} \left[i\omega \zeta_j e^{-i\omega t} \iint_{\partial\Omega_B} \phi_j n_j dS \right] - \rho \operatorname{Re} \left[i\omega A e^{-i\omega t} \iint_{\partial\Omega_B} (\phi_I + \phi_D) n_j dS \right], \quad j = 1 \dots 6 \quad (2.51)$$

where,

$$\mathbf{n} = \begin{cases} (n_1, n_2, n_3) & \text{for } j = 1, 2, 3 \\ (n_4, n_5, n_6) = \mathbf{r} \times \mathbf{n} & \text{for } j = 4, 5, 6 \end{cases} \quad (2.52)$$

In the above equation (2.51), the three terms represent the different contributions to the body forces and moments. The first term ($F_s^{(1)}$) is the hydrostatic restoring force, the second term ($F_R^{(1)}$) is the force term due to the radiation potential, and the last term ($F_E^{(1)}$) is the exciting forces generated by the incident and the diffraction potentials. The hydrostatic restoring forces are defined as the multiplication of the restoring stiffness and the motion responses, and the components of restoring stiffness are defined as the

following surface-integral form over the wetted body surface at the mean position

($\partial\Omega_B$):

$$F_s^{(1)} = -[K]\{\zeta^{(1)}\} \quad (2.53)$$

where

$$\begin{aligned} K_{33} &= \rho g \iint_{\partial\Omega_B} n_3 dS = \rho g A_{wp} \\ K_{34} &= \rho g \iint_{\partial\Omega_B} y n_3 dS = \rho g A_{wp} y_f \\ K_{35} &= -\rho g \iint_{\partial\Omega_B} x n_3 dS = \rho g A_{wp} x_f \\ K_{44} &= \rho g \iint_{\partial\Omega_B} y^2 n_3 dS + \rho g \nabla z_b - mg z_{cg} \\ K_{45} &= -\rho g \iint_{\partial\Omega_B} x y n_3 dS \\ K_{46} &= -\rho g \nabla x_b + mg x_{cg} \\ K_{55} &= \rho g \iint_{\partial\Omega_B} x^2 n_3 dS + \rho g \nabla z_b - mg z_{cg} \\ K_{56} &= -\rho g \nabla y_b + mg y_{cg} \end{aligned} \quad (2.54)$$

where $K_{mn} = K_{nm}$ for all m and n , A_{wp} is the water plane area, x_f and y_f are the distances from the center of the water plane area to the center of gravity in x-direction and in y-direction, respectively, ∇ is the buoyancy of the body, (x_{cg}, y_{cg}, z_{cg}) is the center of gravity, and (x_b, y_b, z_b) is the center of buoyancy of the body.

The hydrostatic restoring stiffness will be used for the motion analysis of the floating body. The radiation potential forces and moments corresponding to the second term of the equation (2.51) can be rewritten as the form:

$$\begin{aligned}
F_R^{(1)} &= -\rho \operatorname{Re} \left[\zeta_j e^{-i\omega t} \iint_{\partial\Omega_B} \frac{\partial\phi_j}{\partial n} \phi_j dS \right] \\
&= \operatorname{Re} \left(M^a \ddot{\zeta}^{(1)} + C \dot{\zeta}^{(1)} \right) = \operatorname{Re} \left[(-\omega^2 M^a - i\omega C) \zeta_j e^{-i\omega t} \right]
\end{aligned} \tag{2.55}$$

where M^a is the added mass coefficients, C is the radiation damping coefficients, and $\zeta = \zeta e^{-i\omega t}$ are the body motions of six degrees of freedom. They can be represented as follows:

$$M^a = \rho \operatorname{Re} \left[\iint_{\partial\Omega_B} \frac{\partial\phi_j}{\partial n} \phi_j dS \right] \tag{2.56}$$

$$C = \rho \operatorname{Im} \left[\iint_{\partial\Omega_B} \frac{\partial\phi_j}{\partial n} \phi_j dS \right] \tag{2.57}$$

They are symmetric and dependent on the frequency of the body motion.

The last term of the equation (2.51) corresponds to the linear wave exciting force, and it can be rewritten as the form:

$$F_E^{(1)} = -\rho \operatorname{Re} \left[A e^{-i\omega t} \iint_{\partial\Omega_B} (\phi_l + \phi_D) \frac{\partial\phi_j}{\partial n} dS \right] \tag{2.58}$$

Therefore, the equation of motion is formed as:

$$M \ddot{\zeta}^{(1)} = F_S^{(1)} + F_R^{(1)} + F_E^{(1)} = -K \zeta - (M^a \ddot{\zeta} + C \dot{\zeta}) + F_E^{(1)} \tag{2.59}$$

where M is the mass matrix of the body, which is described as:

$$M = \begin{bmatrix} m & 0 & 0 & 0 & mz_{cg} & -my_{cg} \\ 0 & m & 0 & -mz_{cg} & 0 & mx_{cg} \\ 0 & 0 & m & my_{cg} & -mx_{cg} & 0 \\ 0 & -mz_{cg} & my_{cg} & I_{11} & I_{12} & I_{13} \\ mz_{cg} & 0 & -mx_{cg} & I_{21} & I_{22} & I_{23} \\ -my_{cg} & mx_{cg} & 0 & I_{31} & I_{32} & I_{33} \end{bmatrix} \tag{2.60}$$

where V represents the body volume, $m = \iiint_V \rho_B dV$ is the body mass,

$I_{mn} = \iiint_V \rho_B (x \cdot x \delta_{mn} - x_m x_n) dV$ is the moment of inertia, ρ_B is the density of the body,

and δ_{mn} is the Kronecker delta function.

2.3.2 The Second-Order Hydrodynamic Forces and Moments

The second-order wave forces and moments on the body can be obtained by direct integration of the hydrodynamic pressure over the wetted surface of the body at the instantaneous time step. The second-order pressure is defined as:

$$P^{(2)} = -\rho \frac{\partial \Phi^{(2)}}{\partial t} - \frac{1}{2} \rho (\nabla \Phi^{(1)})^2 \quad (2.61)$$

In consideration of the bichromatic wave, the second-order pressure is modified as:

$$P^{(2)} = \text{Re} \sum_{m=1}^2 \sum_{n=1}^2 \left[A_m A_n p_{mn}^+ e^{-i\omega^+ t} + A_m A_n^* p_{mn}^- e^{-i\omega^- t} \right] \quad (2.62)$$

where p_{mn}^\pm are defined as the sum and difference frequency quadratic transfer functions for the second-order pressure. The second-order forces and moments are defined as:

$$\mathbf{F}^{(2)} = \mathbf{F}_S^{(2)} + \mathbf{F}_R^{(2)} + \mathbf{F}_E^{(2)} \quad (2.63)$$

where $\mathbf{F}_S^{(2)}$ represents the second-order hydrostatic force, $\mathbf{F}_E^{(2)} = \mathbf{F}_p^{(2)} + \mathbf{F}_q^{(2)}$ is the second-order wave exciting force, and $\mathbf{F}_R^{(2)}$ is the radiation potential force. The components of $\mathbf{F}_E^{(2)}$ are defined as $\mathbf{F}_p^{(2)} = \mathbf{F}_I^{(2)} + \mathbf{F}_D^{(2)}$, which denotes the incident and diffraction potential

forces, and $F_q^{(2)}$ denotes the quadratic product of the first-order forces. The component forces are derived in the integration forms of potentials as follows:

$$F_S^{(2)} = \rho g A_{wp} (\xi_z^{(2)} + y_f \alpha_x^{(2)} - x_f \alpha_y^{(2)}) k \quad (2.64)$$

$$F_R^{(2)} = \rho \iint_{\partial\Omega_B} \frac{\partial\Phi_R^{(2)}}{\partial t} n dS \quad (2.65)$$

$$F_{I,D}^{(2)} = \rho \iint_{\partial\Omega_B} \frac{\partial\Phi_{I,D}^{(2)}}{\partial t} n dS \quad (2.66)$$

$$F_E^{(2)} = \text{Re} \sum_{m=1}^2 \sum_{n=1}^2 [A_m A_n f_{mn}^+ e^{-i\omega^+ t} + A_m A_n^* f_{mn}^- e^{-i\omega^- t}] \quad (2.67)$$

where f_{mn}^\pm denote the quadratic transfer function (QTF) of the sum and difference frequency exciting force. QTF is obtained by the addition of h_{mn}^\pm and g_{mn}^\pm , where h_{mn}^\pm are the contribution of first-order quadratic transfer function and g_{mn}^\pm are the summation of the quadratic transfer function of the sum and difference frequency exciting force due to the incident potential and the diffraction potential. Each component of the QTF is defined as:

$$f_{mn}^\pm = h_{mn}^\pm + g_{mn}^\pm \quad (2.68)$$

$$h_{mn}^+ = \left[-\frac{\rho}{4} \iint_{\partial\Omega_B} (\nabla\phi_m^{(1)} \cdot \nabla\phi_n^{(1)}) n dS - \frac{\rho\omega_m\omega_n}{4g} \int_{L_w} \phi_m^{(1)}\phi_n^{(1)} N dL \right] / A_m A_n \quad (2.69)$$

$$h_{mn}^- = \left[-\frac{\rho}{4} \iint_{\partial\Omega_B} (\nabla\phi_m^{(1)} \cdot \nabla\phi_n^{(1)*}) n dS - \frac{\rho\omega_m\omega_n}{4g} \int_{L_w} \phi_m^{(1)}\phi_n^{(1)*} N dL \right] / A_m A_n^* \quad (2.70)$$

$$g_{mn}^\pm = \left[\rho i \omega^\pm \iint_{\partial\Omega_B} (\phi_I^\pm + \phi_D^\pm) n dS \right] / (A_m A_n, A_m A_n^*) \quad (2.71)$$

where $N = n/\sqrt{(1-n_z^2)}$, and k is the unit vector in the z -direction.

2.4 Multiple Body Interaction of Fluid

The boundary value problem of the multiple body interaction of fluid is explained that the effects of the incident potential and the scattered potential on the main body and the adjacent body are investigated. For the single body system, the radiation potential and the incident potential are obtained as described in the above sections. The diffraction problem for the isolated body can be defined by the incident potential as follows:

$$\frac{\partial \phi_7^I}{\partial n} = -\frac{\partial \phi_I}{\partial n} \quad \text{on } S_I \quad (2.72)$$

$$\frac{\partial \phi_7^{II}}{\partial n} = -\frac{\partial \phi_I}{\partial n} \quad \text{on } S_{II} \quad (2.73)$$

where S_I, S_{II} denotes the wetted surface of the isolated body I and II , respectively, ϕ_7^I, ϕ_7^{II} denotes the scattered potential to the isolated body I and II , respectively, and ϕ_I represents the incident wave potential of the isolated body. The radiation potential for the isolated body can be decomposed in the similar manner to the equation (2.25) as follows:

$$\phi_R^I = \sum_{j=1}^6 \zeta_j \phi_j^I \quad (2.74)$$

$$\phi_R^{II} = \sum_{j=1}^6 \zeta_j \phi_j^{II} \quad (2.75)$$

The radiation problem for the isolated body I and II can be given by:

$$\frac{\partial \phi_j^I}{\partial n} = n_j^I \quad \text{on } S_I \quad (j = 1, 2, \dots, 6) \quad (2.76)$$

$$\frac{\partial \phi_j^{II}}{\partial n} = n_j^{II} \quad \text{on } S_{II} \quad (j = 1, 2, \dots, 6) \quad (2.77)$$

where ϕ_j^I, ϕ_j^{II} denotes the decomposed radiation potential components for the isolated body I and II , respectively, and $n_j^{I,II}$ is a unit normal vector for the six degree of freedom for the isolated body I and II , respectively. In equation (2.76) and (2.77), $n_j^{I,II}$ is given by:

$$\mathbf{n}^{I,II} = \begin{cases} (n_1, n_2, n_3)^{I,II} & \text{for } j = 1, 2, 3 \\ (n_4, n_5, n_6)^{I,II} = \tilde{\mathbf{r}} \times \mathbf{n}^{I,II} & \text{for } j = 4, 5, 6 \end{cases} \quad (2.78)$$

where $\tilde{\mathbf{r}}$ denotes the relative distance from the origin to each body center.

The boundary-value equation and the boundary condition for each body of the interaction problem is defined in the form of the radiation/scatter potential and the derivative as follows:

Interaction problem – radiation/scatter from I near II:

$$\frac{\partial \hat{\phi}_j^I}{\partial n} = -\frac{\partial \phi_j^I}{\partial n} \quad \text{on } S_I \quad (j = 1, 2, \dots, 7) \quad (2.79)$$

$$\frac{\partial \hat{\phi}_j^I}{\partial n} = 0 \quad \text{on } S_{II} \quad (j = 1, 2, \dots, 7) \quad (2.80)$$

Interaction problem – radiation/scatter from II near I:

$$\frac{\partial \hat{\phi}_j^{II}}{\partial n} = -\frac{\partial \phi_j^{II}}{\partial n} \quad \text{on } S_{II} \quad (j = 1, 2, \dots, 7) \quad (2.81)$$

$$\frac{\partial \hat{\phi}_j^{I,II}}{\partial n} = 0 \quad \text{on } S_I \quad (j = 1, 2, \dots, 7) \quad (2.82)$$

where $\hat{\phi}_j^{I,II}$ denotes the interaction potential affected by radiation/scatter potential from the body I to the body II , and vice versa, respectively. The potential when $j = 7$ means the scatter term. If the first-order radiation/scatter potential is used when the above BVP is solved, the resultant potential would be the first-order interaction potential, while the second-order radiation/scatter potential leads the second-order interaction potential.

2.5 Boundary Element Method

The boundary element method is proper for solving the boundary value problem of the fluid potential around the floating body since there is no analytic solution except for some special geometric bodies. BEM is generally called the inverse formulation, since the solution to satisfy all of the boundary conditions, except the body boundary condition for the first-order potential and the body boundary condition and the free surface condition for the second-order potential, is used as a weighting function. It is also based on Green-Lagrange's Identity given by:

$$\iiint_{\Omega} (G \nabla^2 \phi - \phi \nabla^2 G) d\Omega = \iint_{\partial\Omega} \left(G \frac{\partial \phi}{\partial n} - \phi \frac{\partial G}{\partial n} \right) dS \quad (2.83)$$

where G is the Green function to satisfy all of the boundary conditions, Ω denotes the fluid domain, and $\partial\Omega$ denotes the boundary of the domain. ϕ is the exact solution of potential and G satisfies the following equation:

$$\nabla^2 G = \delta(\mathbf{x}) \quad (2.84)$$

where δ is Dirac delta function, and \mathbf{x} means the position coordinates. Since ϕ and G satisfy all of the boundary conditions except the body or the free surface, the right hand side of the equation (2.83) becomes:

$$c(\mathbf{x})\phi(\mathbf{x}) = \iint_{\partial\Omega_B} \left(G \frac{\partial\phi}{\partial n} - \phi \frac{\partial G}{\partial n} \right) dS + \iint_{\partial\Omega_F} \left(G \frac{\partial\phi}{\partial n} - \phi \frac{\partial G}{\partial n} \right) dS \quad (2.85)$$

where $c(\mathbf{x})$ means a shape factor depending on the body geometry, $\partial\Omega_B$ represents the body boundary, and $\partial\Omega_F$ is the free surface boundary. If the body geometry has a smooth surface, $c(\mathbf{x})$ becomes 2π . The equation (2.85) is a fundamental equation called the Inverse Formulation.

If the formulation is applied to the first-order diffraction potential problem for the smooth surface of body, the equation (2.85) becomes a second kind of Fredholm integral equation such as:

$$2\pi\phi_D^{(1)}(\mathbf{x}) + \iint_{\partial\Omega_B} \phi_D^{(1)}(\xi) \frac{\partial G(\xi; \mathbf{x})}{\partial n} dS(\xi) = \iint_{\partial\Omega_B} G(\xi; \mathbf{x}) \left(-\frac{\partial\phi_r^{(1)}(\xi)}{\partial n} \right) dS(\xi) \quad (2.86)$$

where ξ denotes the source point coordinates. If it is applied to the first-order radiation potential problem, it becomes as:

$$2\pi\phi_R^{(1)}(\mathbf{x}) + \iint_{\partial\Omega_B} \phi_R^{(1)}(\xi) \frac{\partial G(\xi; \mathbf{x})}{\partial n} dS(\xi) = \begin{cases} \iint_{\partial\Omega_B} G(\xi; \mathbf{x}) n_k dS(\xi) & \text{for } k = 1, 2, 3 \\ \iint_{\partial\Omega_B} G(\xi; \mathbf{x}) (\mathbf{r} \times \mathbf{n})_{k-3} dS(\xi) & \text{for } k = 4, 5, 6 \end{cases} \quad (2.87)$$

If the formulation is applied to the second-order diffraction potential problem for the flat surface of body, it becomes as:

$$2\pi\phi_D^\pm + \iint_{\partial\Omega_B} \phi_D^\pm \frac{\partial G^\pm}{\partial n} dS = \iint_{\partial\Omega_B} G^\pm \left(B^\pm - \frac{\partial\phi_I^\pm}{\partial n} \right) dS + \frac{1}{g} \iint_{\partial\Omega_F} Q^\pm G^\pm dS \quad (2.88)$$

If it is applied to the second-order radiation potential problem for a far field, it becomes

as:

$$2\pi\phi_R^\pm + \iint_{\partial\Omega_B} \phi_R^\pm \frac{\partial G^\pm}{\partial n} dS = \begin{cases} \iint_{\partial\Omega_B} G^\pm n_k dS + \iint_{\partial\Omega_F} \left(\omega^2 G^\pm \phi_R^\pm \mp \lim_{R \rightarrow \infty} ik\sqrt{R} \phi_R^\pm \right) dS & \text{for } k = 1,2,3 \\ \iint_{\partial\Omega_B} G^\pm (\mathbf{r} \times \mathbf{n})_{k-3} dS + \iint_{\partial\Omega_F} \left(\omega^2 G^\pm \phi_R^\pm \mp \lim_{R \rightarrow \infty} ik\sqrt{R} \phi_R^\pm \right) dS & \text{for } k = 4,5,6 \end{cases} \quad (2.89)$$

In this formulation, it is noted that the integration term for the free surface remains. If the Constant Panel Method (CPM) of BEM is taken, the simplest form is shown as:

$$2\pi\phi(\mathbf{x}) + \iint_{\partial\Omega_B} \phi(\xi) \frac{\partial G(\xi, \mathbf{x})}{\partial n(\xi)} dS(\xi) = \iint_{\partial\Omega_B} G(\xi, \mathbf{x}) \frac{\partial \phi(\xi)}{\partial n(\xi)} dS(\xi) \quad (2.90)$$

If the equation is applied for the discretized model, it is modified as:

$$\phi(\xi) = \sum_{j=1}^L N_j(x_1, x_2) \phi_j, \quad L = 1, 2, \dots, (\text{No. of Interpolation points}) \quad (2.91)$$

$$\sum_{j=1}^M H_{ij} \phi_j = \sum_{j=1}^M G_{ij} \left(\frac{\partial \phi}{\partial n} \right)_j, \quad M = 1, 2, \dots, (\text{No of pannels}) \quad (2.92)$$

where N_j is the shape function, (x_1, x_2) is the local coordinate, and H_{ij} and G_{ij} are as

follows:

$$H_{ij} = \frac{1}{2} \delta_{ij} + \frac{1}{4\pi} \iint_{\partial\Omega_B, j \neq i} \frac{\partial G(\xi, \mathbf{x})}{\partial n(\xi)} dS(\xi) \quad (2.93)$$

$$G_{ij} = \frac{1}{4\pi} \iint_{\partial\Omega_B, j \neq i} G(\xi, \mathbf{x}) dS(\xi) \quad (2.94)$$

In the equations of (2.92) and (2.94), $\frac{\partial \phi}{\partial n}$ is given by the equation (2.20) and

$G(\xi, \mathbf{x}), \frac{\partial G(\xi, \mathbf{x})}{\partial n(\xi)}$ are known as the exact forms. Thus, the equation (2.92) can be solved

for the whole panels.

For the BEM program, the WAMIT (Lee et al, 1991) of CPM is well known in this field. the WAMIT can be applied to the first-order and second-order diffraction/radiation potential problem. In this study, the WAMIT will be taken for solving the fluid interaction problem of the multiple-body system.

2.6 Motions of the Floating Platform

2.6.1 Wave Loads

The linear wave forces are calculated in the frequency domain, and the second-order sum and difference frequency wave loads are computed by considering the bichromatic wave interactions. The real sea is made of random waves, so that it is essential to make the random waves for applying the external wave loads to the floating body.

The linear and the second-order hydrodynamic forces can be rewritten as the form of a two-term Volterra series in time domain:

$$F^{(1)}(t) + F^{(2)}(t) = \int_{-\infty}^{\infty} h_1(\tau) \eta(t - \tau) d\tau + \int_{-\infty}^{\infty} \int_{-\infty}^{\infty} h_2(\tau_1, \tau_2) \eta(t - \tau_1) \eta(t - \tau_2) d\tau_1 d\tau_2 \quad (2.95)$$

where $h_1(\tau)$ is the linear impulse response function, and $h_2(\tau_1, \tau_2)$ is the quadratic impulse response function, i.e., the second-order exciting force at time t for the two

different unit amplitude inputs at time τ_1 and τ_2 . $\eta(t)$ is the ambient wave free surface elevation at a reference position. Since $\eta(t)$, $h_1(\tau)$ and $h_2(\tau_1, \tau_2)$ can be expressed in the functions of frequency, the unidirectional wave exciting forces induced by the incident potential and the diffraction potential to have the similar form of the equation (2.95) can be rewritten in the form of the summation of the frequency components as follows:

$$F_i^{(1)}(t) = \text{Re} \left[\sum_{j=1}^N A_j q_L(\omega_j) e^{i\omega t} \right] \quad (2.96)$$

$$F_i^{(2)}(t) = \text{Re} \left[\sum_{j=1}^N \sum_{k=1}^N A_j A_k^* q_D(\omega_j, -\omega_k) e^{i\omega^- t} + \sum_{j=1}^N \sum_{k=1}^N A_j A_k q_S(\omega_j, \omega_k) e^{i\omega^+ t} \right] \quad (2.97)$$

where $q_L(\omega_j)$ represents the linear force transfer function (LTF), and $q_D(\omega_j, -\omega_k)$ and $q_S(\omega_j, \omega_k)$ are the difference and the sum frequency quadratic transfer functions (QTF), respectively. Using the Fourier transform, the equation (2.96) and (2.97) can be easily changed into the energy spectra given by:

$$S_F^{(1)}(\omega) = S_\eta(\omega) |q_L(\omega)|^2 \quad (2.98)$$

$$S_F^-(\omega) = 8 \int_0^\infty |q_D(\mu, \omega - \mu)|^2 S_\eta(\mu) S_\eta(\omega - \mu) dS_\eta(\mu) \quad (2.99)$$

$$S_F^+(\omega) = 8 \int_0^{\omega/2} \left| q_S\left(\frac{\omega}{2} + \mu, \frac{\omega}{2} - \mu\right) \right|^2 S_\eta\left(\frac{\omega}{2} + \mu\right) S_\eta\left(\frac{\omega}{2} - \mu\right) dS_\eta(\mu) \quad (2.100)$$

where $S_\eta(\omega)$ is the wave spectrum, $S_F^{(1)}(\omega)$ is the linear wave force spectrum, and $S_F^-(\omega)$ and $S_F^+(\omega)$ are the second-order sum- and difference-frequency wave force spectrum, respectively.

The first- and second-order radiation potential forces are calculated by the following formula:

$$F_R(t) = \left(M^a(\omega) - \int_0^\infty R(t) \cos \omega t dt \right) \ddot{\zeta}(t) - \int_{-\infty}^t R(t-\tau) \dot{\zeta}(\tau) d\tau \quad (2.101)$$

where $M^a(\omega)$ is the added mass coefficient as defined in the equation (2.55) at frequency ω , and $R(t)$ is called a retardation function as defined below:

$$R(t) = \frac{2}{\pi} \int_0^\infty C(\omega) \frac{\sin \omega t}{\omega} d\omega \quad (2.102)$$

where $C(\omega)$ is the radiation damping coefficient in the equation (2.56) at frequency ω .

The total wave forces and moments can be obtained by summation of the equation (2.96), (2.97) and (2.101) as the same form as the summation of the equation (2.59) and (2.63) as follows:

$$F_T = F_I + F_c + \tilde{F}_R \quad (2.103)$$

where $F_T = F^{(1)} + F^{(2)}$ is the total wave exciting force, $F_I = F_I^{(1)} + F_I^{(2)}$ is the sum of the equation (2.96) and (2.97), F_c is the last term of the right hand side of the equation (2.101), and \tilde{F}_R is the first term of the equation (2.101).

2.6.2 Morison's Equation

For the slender cylindrical floating structure, the inertia and added mass effect and the damping effect of the drag force on the slow drift motion can be evaluated by using Morison's equation. Morison et al. (1950) proposed that the total force is the sum of drag force and inertia force as follows:

$$F_m = C_m \rho V \dot{u}_n - C_a \rho V \ddot{\zeta}_n + \frac{1}{2} \rho C_D D_s (u_n - \dot{\zeta}_n) |u_n - \dot{\zeta}_n| \quad (2.104)$$

where F_m denotes Morison's force, $V = \frac{\pi D^2}{4}$ is the volume per unit length of the structure, D is the diameter of the slender body, $C_m = 1 + C_a$ is the inertia coefficient, C_a is the added mass coefficient, C_D is the drag coefficient, D_s is the breadth or diameter of the structure, \dot{u}_n and u_n are the acceleration and the velocity of the fluid normal to the body, respectively, and $\ddot{\zeta}_n$ and $\dot{\zeta}_n$ are the acceleration and the velocity of the body, respectively. In the above equation, the first term is called Froude-Krylov force, the second term the added mass effect, and the last term the drag force. The drag force on the floating structure cannot be neglected, because the slenderness ratio of the structure (the ratio of breadth or diameter to the length of the structure) is small compared to the wavelength so that the viscous effect cannot be negligible. The derived force by the equation (2.104) is added to the wave forces of the equation (2.103) to get the total force.

2.6.3 Single Body Motion

The equilibrium equation using Newton's second law called the momentum equation for the floating structure can be given as:

$$\mathbf{M} \frac{d^2 \mathbf{x}_{cg}}{dt^2} = \mathbf{f} \quad (2.105)$$

$$\mathbf{I} \frac{d\boldsymbol{\varphi}}{dt} + \boldsymbol{\varphi} \times (\mathbf{I} \boldsymbol{\varphi}) = \mathbf{m} \quad (2.106)$$

where \mathbf{M} is the mass of the floating structure, \mathbf{x}_{cg} is the coordinates of the center of gravity of the floating body, \mathbf{I} is the moment of inertia, and $\boldsymbol{\varphi}$ is the angular velocity, \mathbf{f} and \mathbf{m} are the external force and moment. The second term of the left-hand side of the equation (2.104) and the relative angular motion of the body to the wave motion are nonlinear. If the rotation is assumed to be small, the equation (2.106) becomes a linear equation as follows:

$$\mathbf{M} \ddot{\boldsymbol{\zeta}} = \mathbf{F}(t) \quad (2.107)$$

where $\ddot{\boldsymbol{\zeta}}$ is the normal acceleration of body motion, \mathbf{M} is the 6×6 body mass matrix to be the same as equation (2.59) and $\mathbf{F}(t)$ is the external force vector. In the time domain, the above equation is expanded as:

$$\left[\mathbf{M} + \mathbf{M}^a(\infty) \right] \ddot{\boldsymbol{\zeta}} + \mathbf{K} \boldsymbol{\zeta} = \mathbf{F}_l(t) + \mathbf{F}_c(\dot{\boldsymbol{\zeta}}, t) + \mathbf{F}_m(\dot{\boldsymbol{\zeta}}, t) \quad (2.108)$$

where $\mathbf{M}^a(\infty)$ is a constant, equivalent added mass of the body at the infinite frequency and can be expressed by :

$$\mathbf{M}^a(\infty) = \mathbf{M}^a(\omega) - \int_0^{\infty} \mathbf{R}(t) \cos \omega t dt \quad (2.109)$$

where $\mathbf{M}^a(\omega)$ is the same as defined in the equation (2.56). \mathbf{F}_c is the same as the second term of the equation (2.103) and defined as:

$$\mathbf{F}_c(\dot{\zeta}, t) = - \int_{-\infty}^t \mathbf{R}(t-\tau) \dot{\zeta} d\tau \quad (2.110)$$

\mathbf{F}_l is the same as the equation (2.96) and (2.97), and \mathbf{F}_m is the force by Morison's equation such as the equation (2.104). $\dot{\zeta}$ is the normal velocity of the body.

2.6.4 Multiple Body Motion

For the multiple body system, the number of the degrees of freedom of the mass matrix, the body motion vector and the force vector in the equation (2.106) are changed to $6N \times 6N$, $6N$ and $6N$, N of which is the number of bodies. And also in the total system equation (2.106), the matrix sizes are extended accordingly. For the formulation of motion, the local coordinate system is used for each body. After forming the equation of motion for each body, the coordinate transformation is needed. Finally, the total equation of motion in the global coordinate system is assembled for the combined system. The hydrodynamic coefficients are pre-made in consideration of the fluid-interaction terms influenced on each body by using WAMIT. The hydrodynamic coefficients are solved in the sequence as follows:

- 1) The radiation/diffraction problem for each body in isolation
- 2) The interaction problem resulting from radiation/scatter from body I in the presence of body II, and radiation/scatter from body II in the presence of body I.

Where body I and II represent one pair of bodies which interact hydrodynamically. If there are several bodies, the two-body problem should be addressed for each unique pair of bodies. The boundary-value problem is formed differently due to the different kinematic boundary condition on the immersed surface of bodies, but other boundary conditions for the bodies are the same as those in the isolated body.

The boundary–value problem of fluid interaction is solved using the equation (2.81) and (2.82) in the section 2.4 in the form of an excitation force coefficient as follows:

$$C_j^{I,I} = -\int_{S_i} a \hat{\phi}_j^I n_j dS, \quad (j = 1, 2, \dots, 6) \quad (2.111)$$

$$C_j^{II,II} = -\int_{S_i} a \hat{\phi}_j^{II} n_j dS, \quad (j = 1, 2, \dots, 6) \quad (2.112)$$

$$C_j^{I,II} = -\int_{S_i} a (\hat{\phi}_j^{II} + \phi_j^{II}) n_j dS, \quad (j = 1, 2, \dots, 6) \quad (2.113)$$

$$C_j^{II,I} = -\int_{S_{ii}} a (\hat{\phi}_j^I + \phi_j^I) n_j dS, \quad (j = 1, 2, \dots, 6) \quad (2.114)$$

where the superscript *I* and *II* represent the body I and II. If the coefficients are written in the form of equation (2.109), the hydrodynamic coefficients are obtained by:

$$M^{a^{I,I}}(\infty) = -\int_{S_i} \hat{\phi}_j^I n_i dS, \quad i, j = 1, 2, \dots, 6 \quad (2.115)$$

$$M^{a^{II,II}}(\infty) = -\int_{S_{ii}} \hat{\phi}_j^{II} n_i dS, \quad i, j = 1, 2, \dots, 6 \quad (2.116)$$

$$M^{a^{I,II}}(\infty) = -\int_{S_i} (\hat{\phi}_j^{II} + \phi_j^{II}) n_i dS, \quad i, j = 1, 2, \dots, 6 \quad (2.117)$$

$$M^{a^{II,I}}(\infty) = -\int_{S_{ii}} (\hat{\phi}_j^I + \phi_j^I) n_i dS, \quad i, j = 1, 2, \dots, 6 \quad (2.118)$$

Then, for the two-body problem, the equation (2.113) to equation (2.116) are replaced for the equation (2.107), and the replaced equations mean the matrix $\mathbf{M}^a(\infty)$ in the equation (2.106). In the equation (2.106), the other matrices contain the terms for two bodies. Thus,

$$\mathbf{M} = \begin{bmatrix} \mathbf{M}^I & 0 \\ 0 & \mathbf{M}^{II} \end{bmatrix}, \quad (2.119)$$

$$\mathbf{K} = \begin{bmatrix} \mathbf{K}^{I,I} & \mathbf{K}^{I,II} \\ \mathbf{K}^{II,I} & \mathbf{K}^{II,II} \end{bmatrix}, \quad (2.120)$$

$$\mathbf{F}_I = \begin{bmatrix} \mathbf{F}_I^I \\ \mathbf{F}_I^{II} \end{bmatrix}, \quad (2.121)$$

$$\mathbf{F}_C = \begin{bmatrix} \mathbf{F}_C^I \\ \mathbf{F}_C^{II} \end{bmatrix}, \quad (2.122)$$

$$\mathbf{F}_m = \begin{bmatrix} \mathbf{F}_m^I \\ \mathbf{F}_m^{II} \end{bmatrix}, \quad (2.223)$$

where the superscript I and II represent the body I and II. The total equation of motion of the system has the same form of equation (2.106), but for the N-body with 6 DOF for each body, the matrices are of the size of $6N \times 6N$.

2.6.5 Time Domain Solution of the Platform Motions

Since the system contains the nonlinear effect, the numerical scheme of the iterative procedure in the time domain is commonly used. The equation of motion in time domain for a single-body system and/or a two-body system is expressed as the

equation (2.108) with the equation (2.109) and (2.110). For the numerical integration in the time domain, there are several kinds of implicit methods developed, such as the Newmark-Beta method, Runge-Kuta method and the Adams-Moulton method (or mid-point method). The last is used for the purpose of the guarantee of the second-order accuracy. Another reason to use it is that the method has the merit to solve together the coupled equations of the platform motion and mooring line motions at each time step. Furthermore, the Adams-Bashforth method is also used for the time integration of the nonlinear force.

In the first step, the equation (2.108) is de-rated to the first order differential equation:

$$\tilde{\mathbf{M}}\dot{\eta} = \mathbf{F}_l(t) + \mathbf{F}_c(t, \zeta) + \mathbf{F}_m(t, \zeta) - \mathbf{K}\zeta \quad (2.124)$$

$$\eta = \dot{\zeta} \quad (2.125)$$

where $\tilde{\mathbf{M}} = \mathbf{M} + \mathbf{M}^a(\infty)$ denotes the virtual mass matrix. If the integration from time step $t^{(n)}$ to $t^{(n+1)}$ is performed, the following equation is obtained:

$$\tilde{\mathbf{M}}\eta^{(n+1)} = \tilde{\mathbf{M}}\eta^{(n)} + \int_{t^{(n)}}^{t^{(n+1)}} (\mathbf{F}_l + \mathbf{F}_c + \mathbf{F}_m)dt - \int_{t^{(n)}}^{t^{(n+1)}} \mathbf{K}\zeta dt \quad (2.126)$$

$$\zeta^{(n+1)} = \zeta^{(n)} + \int_{t^{(n)}}^{t^{(n+1)}} \eta dt \quad (2.127)$$

If the Adam-Moulton method is applied to the equation (2.126) and (2.127), the following equation is obtained after the resultant equation re-arranged:

$$\tilde{\mathbf{M}}\eta^{(n+1)} = \tilde{\mathbf{M}}\eta^{(n)} + \frac{\Delta t}{2}(\mathbf{F}_l^{(n+1)} + \mathbf{F}_c^{(n+1)} + \mathbf{F}_m^{(n+1)} + \mathbf{F}_l^{(n)} + \mathbf{F}_c^{(n)} + \mathbf{F}_m^{(n)}) - \frac{\Delta t}{2}\mathbf{K}(\zeta^{(n+1)} + \zeta^{(n)}) \quad (2.228)$$

$$\eta^{(n+1)} = \frac{2}{\Delta t}(\zeta^{(n+1)} - \zeta^{(n)}) - \eta^{(n)} \quad (2.229)$$

The equations (2.228) and (2.229) are the combination of two linear algebraic equations with the unknowns of $\eta^{(n+1)}$ and $\zeta^{(n+1)}$. To solve the above equations, the assumption of the first terms is needed. It means that the time integration may have an error term due to the arbitrary adoption of the first term. For the evaluation of the first terms of time varying unknowns to avoid the above-mentioned problem, the Adams-Bashforth scheme is used. Thus, the time integration of the nonlinear term of radiation damping force is as follows:

$$\int_{t^{(n)}}^{t^{(n+1)}} \mathbf{F}_c dt = \frac{\Delta t}{2}(3\mathbf{F}_c^{(n)} - \mathbf{F}_c^{(n-1)}) \quad (2.230)$$

$$\int_{t^{(n)}}^{t^{(n+1)}} \mathbf{F}_c dt = \Delta t \mathbf{F}_c^{(0)} \quad \text{for } n = 0 \quad (2.231)$$

In the same sense, the time integration of the nonlinear term of drag force in Morison's formulation is as follows:

$$\int_{t^{(n)}}^{t^{(n+1)}} \mathbf{F}_m dt = \frac{\Delta t}{2}(3\mathbf{F}_m^{(n)} - \mathbf{F}_m^{(n-1)}) \quad (2.232)$$

$$\int_{t^{(n)}}^{t^{(n+1)}} \mathbf{F}_m dt = \Delta t \mathbf{F}_m^{(0)} \quad \text{for } n = 0 \quad (2.233)$$

Eventually, the equation (2.124) and (2.125) are derived as follows:

$$\begin{aligned} \left[\frac{4}{\Delta t^2} \tilde{\mathbf{M}} + \mathbf{K} \right] \Delta \zeta = & \frac{4}{\Delta t} \tilde{\mathbf{M}} \eta^{(n)} + (\mathbf{F}_l^{(n+1)} + \mathbf{F}_l^{(n)}) + (3\mathbf{F}_c^{(n)} - \mathbf{F}_c^{(n-1)}) \\ & + (3\mathbf{F}_m^{(n)} - \mathbf{F}_m^{(n-1)}) - 2\mathbf{K} \zeta^{(n)} + 2\mathbf{F}_0 \end{aligned} \quad (2.234)$$

$$\Delta \zeta = \zeta^{(n+1)} - \zeta^{(n)} \quad (2.235)$$

where \mathbf{F}_0 represents the net buoyancy force for balancing the system. Firstly, the equation (2.234) is solved for the unknown of $\Delta\zeta$. Then, $\eta^{(n+1)}$ and $\zeta^{(n+1)}$ can be obtained from the equation (2.229) and (2.235). To obtain the stability and the accuracy of the solution, the time interval of Δt may be small enough to solve the mooring line dynamics, since the mooring line shows a stronger nonlinear behavior than the platform movement.

CHAPTER III

DYNAMICS OF MOORING LINES AND RISERS

3.1 Introduction

In this chapter, the theory and the numerical method for the dynamic analysis of the mooring lines and risers are explained.

The platform is considered as a single-point floating system when the behavior of the mooring line is taken into account. To maintain the sea keeping, several types and different materials of mooring lines have been installed. A steel wire rope with chains at both ends has been used for SPAR platform in deep water. There are also taut vertical mooring lines and tethers made of several vertical steel pipes, usually intended to be installed in the TLP. Synthetic mooring lines made of polyester are now considered as a more efficient solution. For the sea keeping for FPSOs, the attempt is to use synthetic mooring lines for fixing those structures in very deep water(over 6,000 ft). Sometimes FPSOs are needed to construct the mooring lines and risers, and to be connected to the TLP, the Single Point Mooring System (SPM) and the shuttle tankers with hawsers or fluid transfer lines(FTLs). The multiple body interaction problems are caused by those kinds of system arrangements. The interaction problem between the floating platforms is the matter to be pre-solved before planning the deep water installation of FPSOs.

For exporting and importing gas and water, and for the production of gas, risers are taken into account. The main purpose of risers is not to fix the floating structure in

the station keeping position, but to act the roles. It tends that the steel catenary risers are used more and more because they are inexpensive. Both mooring lines and risers are the same from the viewpoint of the installation, in that they don't have bending stiffness and are the slender members. The restoring forces of both lines result from gravitational forces, geometries and line tensions. But, the bending stiffness of the tendon and the riser in a TLP has a restoring effect. In the mooring lines and risers, the geometric nonlinearity is dominant on the line behavior.

The analysis of line dynamics is developed on the basis of the theories of behaviors of slender structures. The static position and the line tension are obtained by using the catenary equation. In the catenary equation, no hydrodynamic force on the line is considered. For the consideration of the hydrodynamic force on the line, the tensioned string theory is used, but in the theory the structural strain and stress contribution are missing. The strain and the stress of a structure with geometric nonlinearity can be solved with the beam theory using the updated Lagrangian approach. Therefore, in the program, the tensioned string theory using the string modeled as the beam elements is adopted for its rigorous analysis. It is called the elastic rod theory, and the formula was derived by Nordgen(1974) and Garret(1982). The finite difference method was applied to this problem by the former. Here the FEM technique suggested by the latter is taken. Garret proved line dynamics could be solved more accurately by the FEM.

In this study, a three-dimensional elastic rod theory containing line stretching and bending behavior is adopted. The advantage of the elastic rod theory is that the governing equation, including the geometric nonlinearity, can be treated in the global

coordinate system without transforming the coordinate system. In this chapter, the governing equation of the static equilibrium and the dynamic problem of the body and lines is constructed in a form of weak formulation based on the Galerkin method to apply the Finite Element Method.

3.2 Theory of the Rod

The behavior of a slender rod can be expressed in terms of the variation of the position of the rod centerline. A position vector $r(s,t)$ is the function of the arc length s of the rod and time t . The space curve can be defined by the position vector r . The unit tangential vector of the space curve is expressed as r' , the principal normal vector as r'' , and the bi-normal as $r' \times r''$, where the prime means the derivative with respect to the arc-length s . Figure 3.1 shows the coordinate system of the rod.

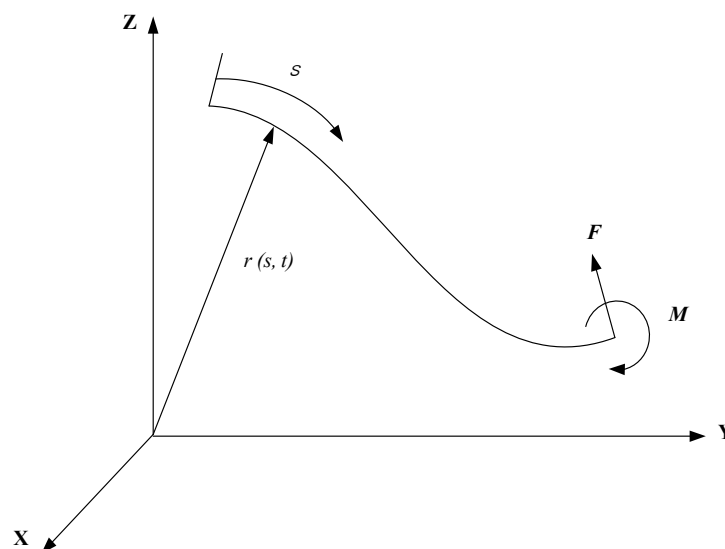


Figure 3.1 Coordinate system of the rod

$$\vec{F}' + \vec{q} = \rho \vec{\ddot{r}} \quad (3.1)$$

$$\vec{M}' + \vec{r}' \times \vec{F} + \vec{m} = \vec{0} \quad (3.2)$$

where

\vec{F} = resultant force acting along the centerline

\vec{M} = resultant moment acting along the centerline

\vec{q} = applied force per unit length

ρ = mass per unit length of the rod

\vec{m} = applied moment per unit length

The dot denotes the time derivative. For the moment equilibrium, the bending moment and the curvature has the relationship as:

$$\vec{M} = \vec{r}' \times EI\vec{r}'' + H\vec{r}' \quad (3.3)$$

where EI is the bending stiffness, and H is the torque. Equation (3.2) and (3.3) can be combined as follows:

$$\vec{r}' \times \left[\left(EI\vec{r}'' \right)' + \vec{F} \right] + H'\vec{r}' + H\vec{r}'' + \vec{m} = \vec{0} \quad (3.4)$$

The scalar product with \vec{r}' for the equation (3.4) yields

$$H' + \vec{m} \cdot \vec{r}' = 0 \quad (3.5)$$

where $\vec{m} \cdot \vec{r}'$ is the distributed torsional moment. Since there is no distributed torsional moment, $\vec{m} \cdot \vec{r}' = 0$ and $H' = 0$. This means that the torque is independent on the arclength s . Furthermore, the torque in the line is usually small enough to be negligible.

Here the torque H and the applied moment \vec{m} on the line are assumed to be zero. Thus, the equation (3.4) can be rewritten in the reduced form:

$$\vec{r}' \times \left[\left(EI \vec{r}'' \right)' + \vec{F} \right] = \vec{0} \quad (3.6)$$

If a scalar function, $\lambda(s, t)$, which is also called Lagrangian multiplier, is introduced to the equation (3.6) and the product with \vec{r}' is taken, then the following formula is obtained:

$$\vec{F} = - \left(EI \vec{r}'' \right)' + \lambda \vec{r}' \quad (3.7)$$

where λ is the Lagrangian multiplier. \vec{r}' should satisfy the inextensibility condition:

$$\vec{r}' \cdot \vec{r}' = 1 \quad (3.8)$$

Applying dot product with \vec{r}' to (3.7) using the relation of (3.8),

$$\lambda = \vec{F} \cdot \vec{r}' + \left(EI \vec{r}'' \right)' \cdot \vec{r}' \quad (3.9)$$

or

$$\lambda = T - EI \kappa^2 \quad (3.10)$$

If the equation (3.7) is substituted into (3.1), the following equation of motion is obtained:

$$- \left(EI \vec{r}'' \right)'' + \left(\lambda \vec{r}' \right)' + \vec{q} = \rho \vec{\ddot{r}} \quad (3.11)$$

If the stretch of rod is assumed to be linear and small, the inextensibility condition (3.8) can be approximated as:

$$\frac{1}{2} (\vec{r}' \cdot \vec{r}' - 1) = \frac{T}{AE} \approx \frac{\lambda}{AE} \quad (3.12)$$

In the floating platforms, the applied force on the rod comes from hydrostatic and hydrodynamic forces caused by the environmental excitation by the surrounding fluid, and the gravitational force on the rod. Thus, \vec{q} may be rewritten by:

$$\vec{q} = \vec{w} + \vec{F}^s + \vec{F}^d \quad (3.13)$$

where \vec{w} is the weight of the rod per unit length, \vec{F}^s is the hydrostatic force on the rod per unit length, and \vec{F}^d is the hydrodynamic force on the rod per unit length. The hydrostatic force can be defined by:

$$\vec{F}^s = \vec{B} - (P\vec{r}') \quad (3.14)$$

where \vec{B} is the buoyancy force on the rod per unit length, and P is the hydrostatic pressure at the point \vec{r}' on the rod. The hydrodynamic force on the rod can be derived from the Morison formula as:

$$\begin{aligned} \vec{F}^d &= -C_A \ddot{\vec{r}}^n + C_M \ddot{\vec{V}}^n + C_D \left| \dot{\vec{V}}^n - \dot{\vec{r}}^n \right| \left(\dot{\vec{V}}^n - \dot{\vec{r}}^n \right) \\ &= -C_A \ddot{\vec{r}}^n + \vec{F}^d \end{aligned} \quad (3.15)$$

where C_A is the added mass coefficient (added mass per unit length), C_M is the inertia coefficient (inertia force per unit length per unit normal acceleration of rod), C_D is the drag coefficient (drag force per unit length per unit normal velocity), \vec{V}^n is the normal velocity to the rod centerline, $\ddot{\vec{V}}^n$ is the normal acceleration to the rod centerline, $\dot{\vec{r}}^n$ is the component of the rod velocity normal to the rod centerline, and $\ddot{\vec{r}}^n$ is the component of the rod acceleration normal to the rod centerline. The velocity and acceleration of the

rod can be derived from the fluid velocity vector, the line tangential vector, and their derivatives.

$$\vec{V}^n = (\vec{V} - \dot{\vec{r}}) - [(\vec{V} - \dot{\vec{r}}) \cdot \vec{r}'] \vec{r}' \quad (3.16)$$

$$\vec{V}^n = \vec{V} - (\vec{V} \cdot \vec{r}') \vec{r}' \quad (3.17)$$

$$\dot{\vec{r}}^n = \dot{\vec{r}} - (\dot{\vec{r}} \cdot \vec{r}') \vec{r}' \quad (3.18)$$

$$\ddot{\vec{r}}^n = \ddot{\vec{r}} - (\ddot{\vec{r}} \cdot \vec{r}') \vec{r}' \quad (3.19)$$

When the above equation (3.13), (3.14) and (3.15) are used, then the equation (3.11) can be rewritten as:

$$\rho \ddot{\vec{r}} + C_a \rho_w \ddot{\vec{r}}^n + (EI r''')'' - (\tilde{\lambda} r')' = \vec{w} + \vec{F}_d \quad (3.20)$$

where

$$\tilde{\lambda} = T + P - EI\kappa^2 = \tilde{T} - EI\kappa^2 \quad (3.21)$$

$$\vec{w} = \vec{w} + \vec{B} \quad (3.22)$$

$$\tilde{T} = T + P \quad (3.23)$$

\tilde{T} is the effective tension in the rod, and \vec{w} is the effective weight or the wet weight of the rod. The equation (3.20) with the equation (3.12) is the fundamental equation of motion for the elastic rod to be applied to the FEM formulation.

3.3 Finite Element Modeling

The governing equation (3.20) is nonlinear, and can be solved except for special cases with particular conditions. Nordgren (1974) applied the finite difference method

to the governing equation and the inextensibility condition. His analysis results showed satisfactorily the dynamic behavior of the pipe on the sea floor. In this study, the FEM technique is taken due to its various merits. The application of the FEM starts from describing the equation in the form of tensor such as:

$$-\rho\ddot{r}_i - C_A\ddot{r}_i^n - (EI r_i'')'' + (\tilde{\lambda} r_i')' + \tilde{w}_i + \tilde{F}_i^d = 0 \quad (3.24)$$

and

$$\frac{1}{2}(r_r' r_r' - 1) - \frac{\lambda}{AE} = 0 \quad (3.25)$$

Here the unknown variable r, λ can be approximated as:

$$r_i(s, t) = A_l(s) U_{il}(t) \quad (3.26)$$

$$\lambda(s, t) = P_m(s) \lambda_m(t) \quad (3.27)$$

where, $0 \leq s \leq L$, A_l, P_m are the interpolation(shape) functions, and U_{il}, λ_m are the unknown coefficients. By introducing shape functions for the solution, the weak formulations for applying the FEM technique are written by multiplying the weighting function of δr_i as follows:

$$\int_0^L \delta r_i \left[-\rho\ddot{r}_i - C_A\ddot{r}_i^n - (EI r_i'')'' + (\tilde{\lambda} r_i')' + \tilde{w}_i + \tilde{F}_i^d \right] ds = 0 \quad (3.28)$$

$$\int_0^L \delta \lambda \left[\frac{1}{2}(r_r' r_r' - 1) - \frac{\lambda}{AE} \right] ds = 0 \quad (3.29)$$

The following cubic shape functions for A_l and quadratic shape functions for P_m are used on the basis of the relation of $\delta r_i = A_l \delta U_{il}(t)$ and $\delta \lambda = P_m \lambda \delta_m$ such as equation (3.26) and (3.27):

$$\begin{aligned}
A_1 &= 1 - 3\xi^2 + 2\xi^3 \\
A_2 &= L \cdot (\xi - 2\xi^2 + \xi^3) \\
A_3 &= 3\xi^2 - 2\xi \\
A_4 &= L \cdot (-\xi^2 + \xi^3)
\end{aligned} \tag{3.30}$$

$$\begin{aligned}
P_1 &= 1 - 3\xi + 2\xi^2 \\
P_2 &= 4\xi(1 - \xi) \\
P_3 &= \xi(2\xi - 1)
\end{aligned} \tag{3.31}$$

where $\xi = \frac{s}{L}$.

$$\begin{aligned}
U_{i1} &= r_i(0, t), & U_{i2} &= r_i'(0, t), \\
U_{i3} &= r_i(L, t), & U_{i4} &= r_i'(L, t)
\end{aligned} \tag{3.32}$$

$$\lambda_1 = \lambda(0, t), \quad \lambda_2 = \lambda\left(\frac{L}{2}, t\right), \quad \lambda_3 = \lambda(L, t) \tag{3.33}$$

Thus, the equation (3.30) and (3.31) can be extended in term by term as follows:

$$\int_0^L \delta r_i (\rho \ddot{r}_i + C_A \ddot{r}_i^n) ds = \int_0^L (\rho \ddot{r}_i + C_A \ddot{r}_i^n) A_l \delta U_{il} ds \tag{3.34}$$

$$\begin{aligned}
\int_0^L \delta r_i (EI r_i'') ds &= \int_0^L (EI r_i'') A_l \delta U_{il} ds \\
&= \left[(EI r_i'') A_l \Big|_0^L - EI r_i'' A_l' \Big|_0^L + \int_0^L EIA_l'' r_i'' ds \right] \delta U_{il}
\end{aligned} \tag{3.35}$$

$$\begin{aligned}
\int_0^L \delta r_i (\tilde{\lambda} r_i') ds &= \int_0^L (\tilde{\lambda} r_i') A_l \delta U_{il} ds \\
&= \left[(\tilde{\lambda} r_i' A_l) \Big|_0^L - \int_0^L \tilde{\lambda} r_i' A_l' ds \right] \delta U_{il}
\end{aligned} \tag{3.36}$$

$$\int_0^L \delta r_i [\tilde{w}_i + \tilde{F}_i^d] ds = \left(\int_0^L (\tilde{w}_i + \tilde{F}_i^d) A_l ds \right) \delta U_{il} \quad (3.37)$$

$$\int_0^L \delta \lambda \left[\frac{1}{2} (r'_r r'_r - 1) - \frac{\lambda}{AE} \right] ds = \int_0^L P_m \left[\frac{1}{2} (r'_r r'_r - 1) - \frac{\lambda}{AE} \right] ds \delta \lambda_m \quad (3.38)$$

If the equation (3.34) to (3.37) are assembled and the term of δU_{il} is canceled out in both sides of the above equations, the following equation is obtained:

$$\begin{aligned} \int_0^L \left\{ A_l (\rho \ddot{r}_i + C_A \ddot{r}_i^n) + E I A_l'' r'' + \tilde{\lambda} A_l' r' - A_l (\tilde{w}_i + \tilde{F}_i^d) \right\} ds \\ = - E I r_i'' A_l' \Big|_0^L + \left[\tilde{\lambda} r_i' + (E I r_i'')' \right] A_l \Big|_0^L \end{aligned} \quad (3.39)$$

If the same operation is done for the equation (3.38), and $\delta \lambda_m$ is removed from both sides of the equation (3.38), the equation (3.38) becomes as:

$$\int_0^L P_m \left\{ \frac{1}{2} (r'_r r'_r - 1) - \frac{\lambda}{AE} \right\} ds = 0 \quad (3.40)$$

If the partial integrations are applied twice term by term for the equation (3.39) and (3.40), and the boundary conditions satisfy the equation (3.39), then the following equations are obtained:

$$\int_0^L \rho A_l \ddot{r}_i ds = \int_0^L \rho A_l A_k \delta_{ij} ds \ddot{U}_{jk} \quad (3.41)$$

$$\int_0^L A_l (C_A \ddot{r}_i^n) ds = C_A \left[\int_0^L A_l A_k \delta_{ij} ds - \int_0^L (A_l A_k A_s' A_t') U_{it} U_{js} \delta_{ij} ds \right] \ddot{U}_{jk} \quad (3.42)$$

$$\int_0^L E I A_l'' r_i'' ds = \int E I A_l'' A_k'' \delta_{ij} ds U_{jk} \quad (3.43)$$

$$\int_0^{\tilde{L}} \tilde{\lambda} A_l' r' ds = \lambda_n \int_0^L P_n A_l' A_k' \delta_{ij} ds \quad (3.44)$$

$$\int_0^L P_m \frac{1}{2} r_r' r_r' ds = \frac{1}{2} \int_0^L P_m A_l' A_k' ds U_{jl} U_{jk} \quad (3.45)$$

$$\int_0^L P_m \frac{\lambda}{AE} ds = \frac{1}{AE} \int_0^L \lambda_n P_m P_n ds \quad (3.46)$$

Using the equation (3.41) to (3.46), the equation (3.39) and (3.40) can be rewritten in a matrix form as follows:

$$(M_{ijkl} + M_{ijkl}^a) \ddot{U}_{jk} + (K_{ijkl}^1 + \lambda_n K_{nijlk}^2) U_{jk} - F_{il} = 0 \quad (3.47)$$

$$G_m = A_{mil} U_{kl} U_{ki} - B_m - C_{mn} \lambda_n = 0 \quad (3.48)$$

where,

$$M_{ijkl} = \int \rho A_l A_k \delta_{ij} ds \quad (3.49)$$

$$M_{ijkl}^a = C_A \left[\int_0^L A_l A_k \delta_{ij} ds - \left(\int_0^L A_l A_k A_s' A_t' ds \right) U_{it} U_{js} \delta_{ij} \right] \quad (3.50)$$

$$K_{ijkl}^1 = \int_0^L E I A_l'' A_k'' \delta_{ij} ds \quad (3.51)$$

$$K_{nijlk}^2 = \int_0^L P_n A_l' A_k' \delta_{ij} ds \quad (3.52)$$

$$F_{il} = \int_0^L (\tilde{w}_i + \tilde{F}_i^d) A_l ds \quad (3.53)$$

and

$$A_{mil} = \frac{1}{2} \int_0^L P_m A_i' A_l' ds \quad (3.54)$$

$$B_m = \frac{1}{2} \int_0^L P_m ds \quad (3.55)$$

$$C_{mn} = \frac{1}{AE} \int_0^L P_m P_n ds \quad (3.56)$$

and δ_{ij} is the Kronecker Delta function. The equation (3.47) and (3.48) are used for solving the rod dynamics. The program is implemented for calculating the equation (3.49) to (3.56), using the system parameters and the integration of the shape functions. Since the force vector, F_{il} , contains nonlinear terms, the total equations are nonlinear. So, in addition to the above manipulation, some numerical approaches for solving the nonlinear time-domain problem in time domain are needed. In the following sections, these schemes are introduced and explained.

3.4 Formation of Static Problem

The equations (3.47) and (3.48) can be called the equilibrium equation of the system energy and the equation of the extensible conditions in the FEM. If the residuals are taken from the system energy equation and the inextensibility equation, they should be zero. Thus, the total force and the stretching force are described as R_{il} and G_m as:

$$R_{il} = 0 \quad (3.57)$$

$$G_m = 0 \quad (3.58)$$

In the static problem, the dynamic term is removed in the equation (3.36). It becomes as:

$$R_{il} = (K_{ijlk}^1 + \lambda_n K_{nijlk}^2) U_{jk} - F_{il} \quad (3.59)$$

where F_{il} is a static forcing term formed by gravity force, drag force and uniform current and the other applied static force on the line. It is a nonlinear force vector. For solving the equation, Newton-Raphson's iterative method is used. Using the Taylor series expansion, the equation (3.57) and (3.58), with neglecting the higher order terms, can be expressed by:

$$R_{il}^{(n+1)} = R_{il}^{(n)} + \frac{\partial R_{il}}{\partial U_{jk}} (\Delta U_{jk}) + \frac{\partial R_{il}}{\partial \lambda_n} (\Delta \lambda_n) = 0 \quad (3.60)$$

$$G_m^{(n+1)} = G_m^{(n)} + \frac{\partial G_m}{\partial U_{jk}} (\Delta U_{jk}) + \frac{\partial G_m}{\partial \lambda_n} (\Delta \lambda_n) = 0 \quad (3.61)$$

And,

$$\frac{\partial R_{il}}{\partial U_{jk}} = K_{ijlk}^1 + \lambda_n K_{nijlk}^2 \quad (3.62)$$

$$\frac{\partial R_{il}}{\partial \lambda_n} = K_{nijlk}^2 U_{jk} \quad (3.63)$$

$$\frac{\partial G_m}{\partial U_{jk}} = 2 A_{mkl} U_{jk} \quad (3.64)$$

$$\frac{\partial G_m}{\partial \lambda_n} = -C_{mn} \quad (3.65)$$

If the equation (3.60) and (3.61) is rearranged by replacing the equation (3.62) to (3.65) and is rewritten, they are given by:

$$(K_{ijlk}^1 + \lambda_n K_{nijlk}^2)(\Delta U_{jk}) + (K_{nijlk}^2 U_{jl})(\Delta \lambda_n) = -R_{il}^{(n)} \quad (3.66)$$

$$2A_{mkl}U_{jl}(\Delta U_{jk}) - C_{mn}(\Delta \lambda_n) = -G_m^{(n)} \quad (3.67)$$

They can be rewritten in matrix form as follows:

$$\begin{bmatrix} K_{ijlk}^{t0(n)} & K_{i\ln}^{t1(n)} \\ D_{mjk}^{t0(n)} & D_{mn}^{t1(n)} \end{bmatrix} \begin{Bmatrix} \Delta U_{jk} \\ \Delta \lambda_n \end{Bmatrix} = \begin{Bmatrix} -R_{il}^{(n)} \\ -G_m^{(n)} \end{Bmatrix} \quad (3.68)$$

where,

$$K_{ijlk}^{t0(n)} = K_{ijlk}^1 + \lambda_n^{(n)} K_{nijlk}^2 \quad (3.69)$$

$$K_{i\ln}^{t1(n)} = K_{nijlk}^2 U_{jk}^{(n)} = \left(\int_0^L P_n A_l' A_k' ds \right) U_{jk}^{(n)} \quad (3.70)$$

$$D_{mjk}^{t0(n)} = A_{mkp} U_{jp}^{(n)} = \left(\int_0^L P_m A_k' A_p' ds \right) U_{jp}^{(n)} \quad (3.71)$$

$$D_{mn}^{t1(n)} = -C_{mn} = -\frac{1}{AE} \int_0^L P_m P_n ds \quad (3.72)$$

$$R_{il}^{(n)} = (K_{ijlk}^1 + \lambda_n K_{nijlk}^2) U_{jk}^{(n)} - F_{il} \quad (3.73)$$

$$G_m^{(n)} = A_{mil} U_{ki}^{(n)} U_{kl}^{(n)} - B_m - C_{mn} \lambda_n^{(n)} = 0 \quad (3.74)$$

After renumbering, the assembly equation in matrix form is given by:

$$\mathbf{K}^{(n)} (\Delta \mathbf{y}) = \mathbf{F}^{(n)} \quad (3.75)$$

where,

$$\mathbf{F}^r = \begin{bmatrix} -[\lambda r'_1 + (Br_1'')']A_l|_{s=0} \\ [EIr_1'']A_l'|_{s=0} \\ -[\lambda r'_2 + (Br_2'')']A_l|_{s=0} \\ [EIr_2'']A_l'|_{s=0} \\ -[\lambda r'_3 + (Br_3'')']A_l|_{s=0} \\ [EIr_3'']A_l'|_{s=0} \\ 0 \\ 0 \\ [\lambda r'_1 + (Br_1'')']A_l|_{s=L} \\ -[EIr_1'']A_l'|_{s=L} \\ [\lambda r'_2 + (Br_2'')']A_l|_{s=L} \\ -[EIr_2'']A_l'|_{s=L} \\ [\lambda r'_3 + (Br_3'')']A_l|_{s=L} \\ -[EIr_3'']A_l'|_{s=L} \\ 0 \end{bmatrix} = \begin{bmatrix} -N_1^{[1]} \\ -L_1^{[1]} \\ -N_2^{[1]} \\ -L_2^{[1]} \\ -N_3^{[1]} \\ -L_3^{[1]} \\ 0 \\ 0 \\ N_1^{[2]} \\ L_1^{[2]} \\ N_2^{[2]} \\ L_2^{[2]} \\ N_3^{[2]} \\ L_3^{[2]} \\ 0 \end{bmatrix} \quad (3.76)$$

$$\mathbf{y}^T = [U_{11} \ U_{12} \ U_{21} \ U_{22} \ U_{31} \ U_{32} \ \lambda_1 \ \lambda_2 \ U_{13} \ U_{14} \ U_{23} \ U_{24} \ U_{33} \ U_{34} \ \lambda_3] \quad (3.77)$$

$$\mathbf{F}^T = [-R_{11} \ -R_{12} \ -R_{21} \ -R_{22} \ -R_{31} \ -R_{32} \ -G_1 \ -G_2 \ -R_{13} \ -R_{14} \ -R_{23} \ -R_{24} \ -R_{33} \ -R_{34} \ -G_3] \quad (3.78)$$

$$\mathbf{y}^{(n+1)} = \mathbf{y}^{(n)} + \Delta \mathbf{y} \quad (3.79)$$

where [1] denotes the first end of element, and [2] the second end of element,

$N = \{N_1 \ N_2 \ N_3\}^T$ is the nodal resultant force, $L = \{L_1 \ L_2 \ L_3\}^T$ is the force relating to the

nodal resultant moment, and $M = L \times r'$ is the nodal resultant moment.

In every time step, the stiffness \mathbf{K} and the force vector \mathbf{F} are recalculated to solve $\Delta \mathbf{y}$. The bandwidth of the assembled stiffness matrix is 15, and the total number of equations is $(N + 1) \times 8 - 1$, where N is the number of elements for a line. The stiffness matrix is the symmetric and banded matrix. The Gauss elimination method for solving

the equation (3.75) conforming the symmetry and band is used. In addition, the iterative solution scheme is used to get Δy until it becomes smaller than a given tolerance. The resultant force can be obtained from force vector \mathbf{F}^r .

$$\mathbf{F}^r = -\mathbf{F}^{(n+1)} \quad (3.80)$$

3.5 Formulation for Dynamic Problem-Time Domain Integration

The equation of motion, (3.47) and the stretch condition (3.48) can be rearranged.

$$\begin{aligned} \hat{M}_{ijkl} \ddot{U}_{jk} &= -(K_{ijkl}^1 + \lambda_n K_{nijlk}^2) U_{jk} + F_{il} \\ &= \hat{F}_{il} \end{aligned} \quad (3.81)$$

$$G_m = A_{mil} U_{kl} U_{ki} - B_m - C_{mn} \lambda_n = 0 \quad (3.82)$$

where,

$$\begin{aligned} \hat{M}_{ijkl} &= M_{ijkl} + M_{ijkl}^a \\ \hat{F}_{il} &= -F_{il}^1 - F_{il}^2 + F_{il} \\ F_{il}^1 &= K_{ijkl}^1 U_{jk} \\ F_{il}^2 &= \lambda_n K_{nijlk}^2 U_{jk} \end{aligned} \quad (3.83)$$

The equation (3.81) is the second order differential equation, and the equation (3.82) is an algebraic equation. The order of the equation (3.81) is derated using the first derivative of the displacement of the rod, so that the equation results in two first order differential equations as follows:

$$\hat{M}_{ijkl} \dot{V}_{jk} = \hat{F}_{il} \quad (3.84)$$

$$\dot{U}_{jk} = V_{jk} \quad (3.85)$$

If the two equations are integrated, then they are given by:

$$\int_{t^{(n)}}^{t^{(n+1)}} \hat{M}_{ijkl} \dot{V}_{jk} dt = \int_{t^{(n)}}^{t^{(n+1)}} \hat{F}_{jl} dt \quad (3.86)$$

$$\int_{t^{(n)}}^{t^{(n+1)}} \dot{U}_{jk} dt = \int_{t^{(n)}}^{t^{(n+1)}} V_{jk} dt \quad (3.87)$$

In the equation (3.86), \hat{M}_{ijkl} is not a constant with respect to the time, since it includes the added mass term. In order that the time integration is possible, a constant mass is newly introduced. $\hat{M}_{ijkl}^{(n+\frac{1}{2})}$ is the mass at time $t^{(n+\frac{1}{2})} = t^{(n)} + \frac{\Delta t}{2}$ and a constant mass.

When the time step is $(n+1)$, $\hat{M}_{ijkl}^{(n+\frac{1}{2})}$ can be used for the integration of the equation (3.86). Then the integration is achieved with the 2nd order accuracy:

$$\hat{M}_{ijkl}^{(n+\frac{1}{2})} V_{jk}^{(n+1)} - \hat{M}_{ijkl}^{(n+\frac{1}{2})} V_{jk}^{(n)} = \int_{t^{(n)}}^{t^{(n+1)}} \hat{F}_{jl} dt \quad (3.88)$$

The $V_{jk}^{(n+1)}$ of the equation (3.87) is obtained from the following sequential calculations:

$$U_{jk}^{(n+1)} = U_{jk}^{(n)} + \frac{\Delta t}{2} (V_{jk}^{(n+1)} + V_{jk}^{(n)}) \quad (3.89)$$

$$\Delta U_{jk} = U_{jk}^{(n+1)} - U_{jk}^{(n)} = \frac{\Delta t}{2} (V_{jk}^{(n+1)} + V_{jk}^{(n)}) \quad (3.90)$$

$$V_{jk}^{(n+1)} = \frac{2}{\Delta t} (\Delta U_{jk}) - V_{jk}^{(n)} \quad (3.91)$$

Using the equation (3.91) and multiplying $\frac{2}{\Delta t}$ to both sides, the equation (3.88) can be

rewritten as:

$$\frac{4}{\Delta t^2} \hat{M}_{ijkl}^{(n+\frac{1}{2})} (\Delta U_{jk}) = \frac{4}{\Delta t} \hat{M}_{ijkl}^{(n+\frac{1}{2})} V_{jk}^{(n)} + \frac{2}{\Delta t} \int_{t^{(n)}}^{t^{(n+1)}} \hat{F}_{jl} dt \quad (3.92)$$

The integration of the right hand side of the equation (3.92) consists of three parts of integration:

$$\int_{t^{(n)}}^{t^{(n+1)}} \hat{F}_{jl} dt = - \int_{t^{(n)}}^{t^{(n+1)}} F_{il}^1 dt - \int_{t^{(n)}}^{t^{(n+1)}} F_{il}^2 dt + \int_{t^{(n)}}^{t^{(n+1)}} F_{jl} dt \quad (3.93)$$

If the trapezoidal integration rule is applied, each term of the equation (3.93) is given by:

$$\begin{aligned} \int_{t^{(n)}}^{t^{(n+1)}} F_{il}^1 dt &= \frac{\Delta t}{2} (F_{il}^{1(n+1)} + F_{il}^{1(n)}) \\ &= \frac{\Delta t}{2} [K_{ijkl}^1 (\Delta U_{jk}) + 2K_{ijkl}^1 U_{jk}^{(n)}] \end{aligned} \quad (3.94)$$

$$\begin{aligned} \int_{t^{(n)}}^{t^{(n+1)}} F_{il}^2 dt &= \frac{\Delta t}{2} (F_{il}^{2(n+1)} + F_{il}^{2(n)}) \\ &= \frac{\Delta t}{2} [\lambda_n^{(n+1)} K_{nijlk}^2 U_{jk}^{(n+1)} + \lambda_n^{(n)} K_{nijlk}^2 U_{jk}^{(n)}] \\ &\approx \frac{\Delta t}{2} \left[\lambda_n^{(n+\frac{1}{2})} K_{nijlk}^2 U_{jk}^{(n+1)} + \lambda_n^{(n+\frac{1}{2})} K_{nijlk}^2 U_{jk}^{(n)} \right] \\ &= \frac{\Delta t}{2} \left[2\lambda_n^{(n-\frac{1}{2})} K_{nijlk}^2 U_{jk}^{(n)} + 2K_{nijlk}^2 U_{jk}^{(n)} (\Delta\lambda_n) + \lambda_n^{(n-\frac{1}{2})} K_{nijlk}^2 (\Delta U_{jk}) \right] \end{aligned} \quad (3.95)$$

where, $\Delta\lambda_n = \lambda_n^{(n+\frac{1}{2})} - \lambda_n^{(n-\frac{1}{2})}$. The third term of the right hand side of the equation

(3.93) is the gravitational force and the hydrodynamic force. The gravitational force is a

constant with time. The hydrodynamic force can be calculated by applying Morison's formula and the Adam-Bashforth explicit integration scheme:

$$\int_{t^{(n)}}^{t^{(n+1)}} F_{il} dt = \begin{cases} \Delta t F_{il}^{(0)}, & \text{for step 1} \\ \frac{\Delta t}{2} (3F_{il}^{(n)} - F_{il}^{(n-1)}) & \text{for other steps} \end{cases} \quad (3.96)$$

The integration of force can be obtained by replacing the equations from (3.94) to (3.96) into the equation (3.93). The time integration of the equation (3.92) is represented by:

$$\begin{aligned} & \left[\frac{4}{\Delta t^2} \hat{M}_{ijkl}^{(n+\frac{1}{2})} + K_{ijkl}^1 + \lambda_n^{(n-\frac{1}{2})} K_{nijlk}^2 \right] (\Delta U_{jk}) + 2K_{nijlk}^2 U_{jk}^{(n)} (\Delta \lambda_n) \\ & = \frac{4}{\Delta t} \hat{M}_{ijkl}^{(n+\frac{1}{2})} V_{jk}^{(n)} + (3F_{il}^{(n)} - F_{il}^{(n-1)}) - 2K_{ijlk}^1 U_{jk}^{(n)} - 2\lambda_n^{(n-\frac{1}{2})} K_{nijlk}^2 U_{jk}^{(n)} \end{aligned} \quad (3.97)$$

The mass at time $t^{(n+\frac{1}{2})} = t^{(n)} + \frac{\Delta t}{2}$ is approximated using the Adam-Bashforth method by:

$$\hat{M}_{ijkl}^{(n+\frac{1}{2})} = \frac{1}{2} (3\hat{M}_{ijkl}^{(n)} - \hat{M}_{ijkl}^{(n-1)}) \quad (3.98)$$

By applying Taylor expansion to the stretching condition of the equation (3.82):

$$\begin{aligned} 0 &= 2G_m^{(n+1)} \approx 2G_m^{(n)} + 2 \frac{\partial G_m^{(n)}}{\partial U_{jk}} (\Delta U_{jk}) + 2 \frac{\partial G_m^{(n)}}{\partial \lambda_n} (\Delta \lambda_n) \\ &= 2G_m^{(n)} + 2K_{mijk}^2 U_{il} (\Delta U_{jk}) - 2C_{mn} (\Delta \lambda_n) \\ &= 2G_m^{(n)} + \hat{D}_{mjk}^{t0(n)} (\Delta U_{jk}) + 2D_{mn}^{t1(n)} (\Delta \lambda_n) \end{aligned} \quad (3.99)$$

Using the equation (3.97) and (3.99), the equation of motion and the stretching condition can be written as follows,

$$\hat{K}_{ijlk}^{t0(n)} (\Delta U_{jk}) + \hat{K}_{lin}^{t1(n)} (\Delta \lambda_n) = -\hat{R}_{il}^{(n)} \quad (3.100)$$

$$\hat{D}_{mjk}^{t0(n)}(\Delta U_{jk}) + \hat{D}_{mn}^{t1(n)}(\Delta \lambda_n) = -\hat{G}_m^{(n)} \quad (3.101)$$

If the equation is written in matrix form, it gives:

$$\begin{bmatrix} \hat{K}_{ijlk}^{t0(n)} & \hat{K}_{lin}^{t1(n)} \\ \hat{D}_{mjk}^{t0(n)} & \hat{D}_{mn}^{t1(n)} \end{bmatrix} \begin{Bmatrix} \Delta U_{jk} \\ \Delta \lambda_n \end{Bmatrix} = \begin{Bmatrix} -\hat{R}_{il}^{(n)} \\ -\hat{G}_m^{(n)} \end{Bmatrix} \quad (3.102)$$

where,

$$\hat{K}_{ijlk}^{t0(n)} = \frac{2}{\Delta t^2} (3\hat{M}_{ijlk}^{(n)} - \hat{M}_{ijlk}^{(n-1)}) + K_{ijlk}^1 + \lambda_n^{(n-\frac{1}{2})} K_{nijlk}^2 \quad (3.103)$$

$$\hat{K}_{lin}^{t1(n)} = 2K_{nijlk}^2 U_{jk}^{(n)} \quad (3.104)$$

$$\hat{D}_{mjk}^{t0(n)} = 2K_{nijlk}^2 U_{il}^{(n)} = 2D_{mjk}^{t0(n)} \quad (3.105)$$

$$\hat{D}_{mn}^{t1(n)} = -2C_{mn} = 2D_{mn}^{t1(n)} \quad (3.106)$$

$$\begin{aligned} \hat{R}_{il}^{(n)} = & \frac{2}{\Delta t} (3\hat{M}_{ijlk}^{(n)} - \hat{M}_{ijlk}^{(n-1)}) V_{jk}^{(n)} + (3F_{il}^{(n)} - F_{il}^{(n-1)}) \\ & - 2K_{ijlk}^1 U_{jk}^{(n)} - 2\lambda_n^{(n-\frac{1}{2})} K_{nijlk}^2 U_{jk}^{(n)} \end{aligned} \quad (3.107)$$

$$\hat{G}_m^{(n)} = 2G_m^{(n)} \quad (3.108)$$

The total equation in matrix form is written by:

$$\hat{\mathbf{K}}(\Delta \mathbf{y}) = \hat{\mathbf{F}} \quad \text{at time step } n \quad (3.109)$$

$$\mathbf{F}^r = -\hat{\mathbf{F}}^{(n+1)} \quad (3.110)$$

3.6 Modeling of the Seafloor

The anchors are used for fixing the mooring lines and risers on the sea floor. The interaction effect between the line and seafloor acts the important role on the line

movement. Thus, in the program, the seafloor is modeled as an elastic foundation, and the friction force is not considered. With the origin of the coordinate system located on the mean water surface and z -axis pointing upwards, the interaction force f on the line from the sea floor can be expressed as;

$$f_1 = 0, \quad f_2 = 0, \quad f_3 = \begin{cases} c(r_3 - D)^2, & \text{for } r_3 - D < 0 \\ 0, & \text{for } r_3 - D \geq 0 \end{cases} \quad (3.111)$$

where D is the water depth or vertical distance between the sea floor and the origin of the coordinate, and r_3 is the z -component of the line position vector r .

When the force from the sea floor is added, the equation of motion is re-written by;

$$(M_{ijkl} + M_{ijkl}^a) \ddot{U}_{jk} + (K_{ijkl}^1 + \lambda_n K_{nijlk}^2) U_{jk} = F_{il}^f + F_{il} \quad (3.112)$$

where

$$F_{il}^f = \int_0^L A_l f_i ds = \begin{cases} \int_0^L A_l \delta_{i3} c (r_3 - D)^2 ds, & \text{for } r_3 - D < 0 \\ 0, & \text{for } r_3 - D \geq 0 \end{cases} \quad (3.113)$$

$$= \begin{cases} \int_0^L A_l \delta_{i3} c (\delta_{i3} A_k U_{jk} - D)^2 ds, & \text{for } r_3 - D < 0 \\ 0, & \text{for } r_3 - D \geq 0 \end{cases}$$

and,

$$\delta_{i3} = \begin{cases} 1, & \text{for } i = 3 \\ 0, & \text{otherwise} \end{cases} \quad (\text{Kronecker Delta}) \quad (3.114)$$

In the static analysis using Newton's method, the dynamic stiffness matrix is modified as:

$$\begin{aligned}
K_{ijkl}^3 &= \frac{\partial F_{il}^f}{\partial U_{jk}} \\
&= \begin{cases} \int_0^L 2A_l \delta_{i3} c \delta_{j3} A_k (\delta_{m3} A_n U_{mn}^{(n)} - D) ds, & \text{for } \delta_{m3} A_n U_{mn}^{(n)} - D < 0 \\ 0, & \text{for } \delta_{m3} A_n U_{mn}^{(n)} - D \geq 0 \end{cases} \quad (3.115)
\end{aligned}$$

This K_{ijkl}^3 is added to K_{ijkl}^{t0} in order to form the tangential stiffness matrix in the equation (3.69). In time domain analysis using the trapezoidal rule, the dynamic stiffness matrix is modified as:

$$\begin{aligned}
\int_{t^{(n)}}^{t^{(n+1)}} F_{il}^f &= \frac{\Delta t}{2} (F_{il}^{f(n+1)} + F_{il}^{f(n)}) \\
&\approx \frac{\Delta t}{2} [K_{ijkl}^3 (\Delta U_{jk}) + 2F_{il}^{f(n)}] \quad (3.116)
\end{aligned}$$

The first term in the RHS of the above equation is added to the LHS of the equation (3.97), and it is finally combined into \tilde{K}_{ijkl}^{t0} . The second term in RHS of the equation (3.116) is added to the RHS of the equation (3.97). Thus,

$$\begin{aligned}
&\left[\frac{4}{\Delta t^2} \hat{M}_{ijkl}^{(n+\frac{1}{2})} + K_{ijkl}^1 + \lambda_n^{(n-\frac{1}{2})} K_{nijlk}^2 - K_{ijkl}^3 \right] (\Delta U_{jk}) + 2K_{nijlk}^2 U_{jk}^{(n)} (\Delta \lambda_n) \\
&= \frac{4}{\Delta t} \hat{M}_{ijkl}^{(n+\frac{1}{2})} V_{jk}^{(n)} + \left(3F_{il}^{(n)} - F_{il}^{(n-1)} + 2F_{il}^{f(n)} \right) - 2 \left(K_{ijkl}^1 + \lambda_n^{(n-\frac{1}{2})} K_{nijlk}^2 \right) U_{jk}^{(n)} \quad (3.117)
\end{aligned}$$

CHAPTER IV

COUPLED ANALYSIS OF INTEGRATED PLATFORM AND MOORING SYSTEM

4.1 Introduction

The statics and dynamics of the mooring lines and risers can be solved with the given data and the boundary conditions. At both ends of the lines, different boundary conditions are applied. The upper ends or the upper/lower ends, if the cable is installed for the connection of the vessel to vessel (for the multiple body interaction problem), of the lines are connected to the platform with strong springs. Thus, the end nodes are moved with almost the same displacements as the floating platform. The other ends of the lines are connected to the anchors on the seafloor and constrained with the fixed conditions in six degrees of freedom. The platform is concentrated as a single point on the center of the global coordinate and moved as a rigid body. It has six degrees of freedom. The body behavior is greatly influenced by the movement of the mooring lines and risers.

In the quasi-static analysis, the mooring lines and risers are treated separately to the body motion. The motion of the body is solved first, and then, in the post-processing, the dynamics of the mooring lines and risers are analyzed with the motions of the end nodes that are assumed to be the same amount as the body motion. The coupling effect of the body and the lines can be considered, since the system matrices of body and lines are assembled and solved together. But, the pre-obtained body motion cannot be evaluated

properly to consider the inertia effects and the hydrodynamic loads on the lines, because the body motion is analyzed separately without considering the line dynamics.

On the contrary, in the coupled analysis, the body and lines are analyzed at the same time. All dynamic effects of body and lines are included in system matrices, and solved together. As the water depth gets deeper and deeper, the inertia effect increases. So, the interaction effect greatly influences body and line motions. The coupled analysis is to be an essential tool for solving the floating platform motion and line dynamics in ultra deep water over 8,000 ft. in depth. The coupling effects were studied by Ran(2000). He developed the mathematical formulation to be applied to solving the coupled system. In his study, for static analysis, Newton-Raphson's iterative scheme was used. But, for the time-domain analysis, the Adam-Bashforth method was adopted as an explicit numerical scheme. In this study, the above numerical methods are also adopted as a numerical tool of the main solver, and the scheme is extended to the interaction problem of multiple body systems of floating platforms.

4.2 The Spring to Connect the Platform and the Mooring System

The end connection is modeled numerically by the translational and rotational springs between the body and lines. The stiffness should be considered strong enough so that the body reacts with the same amount of motion as the lines' in six DOFs (degrees of freedom). If the spring is strong enough, the applied force and moment to come from lines directly affects the body. If the angular motion is assumed small, the formulations of the forces and moments to be transferred to the body from the lines is given by:

$$N_i^S = K_i^L (X_i + p_i + \theta_j \times p_k - r_i) \quad (4.1)$$

$$L_i^S = K^\theta \left(e_i + \theta_j \times e_k - \frac{r_i'}{(r_m' r_m')^{1/2}} - \frac{r_i' r_j'}{(r_n' r_n')^{3/2}} \right) \quad (4.2)$$

where $N_i^S = [N_1^S N_2^S N_3^S]^T$ and $L_i^S = [L_1^S L_2^S L_3^S]$ are the nodal resultant forces and moments on the end node of the line, $K_i^L = [K_1^L K_2^L K_3^L]$ and $K_i^\theta = [K_1^\theta K_2^\theta K_3^\theta]$ are the translational and the rotational spring constants in the x, y, z direction and in the $\theta_x, \theta_y, \theta_z$ direction, X_i and θ_j are the translational and rotational motions of the body, p_i is the position vector of the node of the body connected to the spring, r_i is the position vector of the ending or the starting node of the line attached by the spring to the body, r_i' is the space derivative of the position vector r_i , and e_i is a unit vector of the reference direction of the rotational spring. The r_i vector at the end node of the line is defined as:

When the connection point is the starting point of the line:

$$r_1 = U_{11}, \quad r_2 = U_{21}, \quad r_3 = U_{31} \quad (4.3)$$

$$r_1' = U_{12}, \quad r_2' = U_{22}, \quad r_3' = U_{32} \quad (4.4)$$

When the connection point is the ending point of the line:

$$r_1 = U_{13}, \quad r_2 = U_{23}, \quad r_3 = U_{33} \quad (4.5)$$

$$r_1' = U_{14}, \quad r_2' = U_{24}, \quad r_3' = U_{34} \quad (4.6)$$

C_{ji} and D_{ji} are defined to make easy the numerical manipulation of the vector product with the position vector p_i and the unit vector e_i as:

$$[C] = \begin{bmatrix} 0 & -p_3 & p_2 \\ -p_3 & 0 & -p_1 \\ p_2 & -p_1 & 0 \end{bmatrix} \quad (4.7)$$

$$[D] = \begin{bmatrix} 0 & -e_3 & e_2 \\ -e_3 & 0 & -e_1 \\ e_2 & -e_1 & 0 \end{bmatrix} \quad (4.8)$$

If the equations (4.7) and (4.8) are used in equations (4.1) and (4.2), the equations are rewritten as:

$$N_i^S = K_i^L (X_i + p_i + \theta_j C_{ji} - r_i) \quad (4.1')$$

$$L_i^S = K^\theta \left(e_i + \theta_j D_{ji} - \frac{r_i'}{(r_m' r_m')^{1/2}} - \frac{r_i' r_j'}{(r_n' r_n')^{3/2}} \right) \quad (4.2')$$

The resultant force F_i^S and moment M_i^S transferred to the body are defined as follows:

$$F_i^S = -N_i^S \quad (4.9)$$

$$\begin{aligned} M_i^S &= M_i^L + M_i^\theta \\ &= N_k^S C_{ki} + L_k^S D_{ki} \end{aligned} \quad (4.10)$$

where $M_i^L = N_k^S \times p_j$ is the moment resulting from the linear spring, and $M_i^\theta = L_k^S \times e_j$ is the moment resulting from the rotational spring. The force F_i^S and the moment M_i^S act on the body.

4.2.1 Static Analysis

The connector force and moment on the end node of the line are included in the equation of motion of the integrated system as external forces. In the static analysis, the

Newton-Raphson method is applied, so that the force and moment in $(n+1)$ iteration are approximated as follows:

$$\text{For } r_i: \quad N_i^{S(n+1)} = N_i^{S(n)} + K_{ij}^{rr} \Delta r_j + K_{ij}^{rX} \Delta X_j + K_{ij}^{\theta\theta} \Delta \theta_j \quad (4.11)$$

$$\text{For } r'_i: \quad L_i^{S(n+1)} = L_i^{S(n)} + K_{ij}^{r'r'} \Delta r'_j + K_{ij}^{r'\theta} \Delta \theta_j \quad (4.12)$$

Where,

$$\begin{aligned} K_{ij}^{rr} &= -\frac{\partial N_i^S}{\partial r_j} = K_i^L \delta_{ij} \\ K_{ij}^{rX} &= -\frac{\partial N_i^S}{\partial X_j} = -K_i^L \delta_{ij} \\ K_{ij}^{r\theta} &= -\frac{\partial N_i^S}{\partial \theta_j} = -K_i^L C_{ij} \\ K_{ij}^{r'r'} &= -\frac{\partial L_i^S}{\partial r'_j} = K_i^\theta \left[\frac{\delta_{ij}}{(r'_m r'_m)^{1/2}} - \frac{r'_i r'_j}{(r'_n r'_n)^{3/2}} \right] \\ K_{ij}^{\theta\theta} &= -\frac{\partial L_i^S}{\partial \theta_j} = -K_i^\theta D_{ij} \end{aligned} \quad (4.13)$$

These equations that shows forces and moments will be expressed with the coupled terms between body and line motions.

Similarly, the connector force and moment on the rigid body at iteration $(n+1)$ are approximated as follows using Newton's method:

$$\text{For } X_i: \quad F_i^{(n+1)} = F_i^{(n)} + K_{ij}^{Xr} \Delta r_j + K_{ij}^{XX} \Delta X_j + K_{ij}^{X\theta} \Delta \theta_j \quad (4.14)$$

$$\text{For } \theta_i: \quad M_i^{(n+1)} = M_i^{(n)} + K_{ij}^{\theta r} \Delta r_j + K_{ij}^{\theta r'} \Delta r'_j + K_{ij}^{\theta\theta} \Delta \theta_j \quad (4.15)$$

Where,

$$\begin{aligned}
K_{ij}^{Xr} &= -\frac{\partial F_i}{\partial r_j} = K_i^L \delta_{ij} \\
K_{ij}^{XX} &= -\frac{\partial F_i}{\partial X_j} = -K_i^L \delta_{ij} \\
K_{ij}^{X\theta} &= -\frac{\partial F_i}{\partial \theta_j} = -K_i^L C_{ij} \\
K_{ij}^{\theta r} &= -\frac{\partial M_i}{\partial r_j} = K_j^\theta C_{ji} \\
K_{ij}^{\theta r'} &= -\frac{\partial M_i}{\partial r'_j} = K_j^\theta \left[\frac{\delta_{ij}}{(r'_m r'_m)^{1/2}} - \frac{r'_i r'_j}{(r'_n r'_n)^{3/2}} \right] D_{ji} \\
K_{ij}^{\theta\theta} &= -\frac{\partial M_i}{\partial \theta_j} = -[K_j^L C_{ki} C_{kj} + K_j^\theta D_{ki} D_{kj}]
\end{aligned} \tag{4.16}$$

The stiffness coefficients K_{ij}^{rr} and $K_{ij}^{r'r'}$ are added the stiffness matrix of elements. K_{ij}^{XX} , $K_{ij}^{X\theta}$ and $K_{ij}^{\theta\theta}$ are included in the stiffness matrix of the platform. The other terms, K_{ij}^{rX} , $K_{ij}^{r\theta}$, $K_{ij}^{r'\theta}$, $K_{ij}^{\theta r}$, and $K_{ij}^{\theta r'}$, form the coupling terms in the assembled system matrix as the symmetric matrices. At each iteration step, the coupled assembly system equations are solved to obtain the behaviors for the body and lines simultaneously, and the iteration continues until the norms of the solutions reach a specified tolerance.

4.2.2 Time-Domain Analysis

The integrations from time $t^{(n)}$ to $t^{(n+1)}$ of the connector forces and moments on the end node of the lines are expressed by applying Newton's method as:

$$\begin{aligned}
\text{For } r_i : \quad \int_{t^{(n)}}^{t^{(n+1)}} N_i^S dt &= \frac{\Delta t}{2} \left(N_i^{S(n+1)} + N_i^{S(n)} \right) \\
&= \frac{\Delta t}{2} \left(-K_{ij}^{rr} \Delta r_j - K_{ij}^{rX} \Delta X_j - K_{ij}^{r\theta} \Delta \theta_j + 2N_i^{S(n)} \right)
\end{aligned} \tag{4.17}$$

$$\begin{aligned}
\text{For } r_i' : \quad \int_{t^{(n)}}^{t^{(n+1)}} L_i^S dt &= \frac{\Delta t}{2} \left(L_i^{S(n+1)} + L_i^{S(n)} \right) \\
&= \frac{\Delta t}{2} \left(-K_{ij}^{r'r'} \Delta r_j' - K_{ij}^{r'\theta} \Delta \theta_j + 2L_i^{S(n)} \right)
\end{aligned} \tag{4.18}$$

The integrations from time $t^{(n)}$ to $t^{(n+1)}$ of the connector forces and moments on the rigid body are expressed as:

$$\begin{aligned}
\text{For } X_i : \quad \int_{t^{(n)}}^{t^{(n+1)}} F_i dt &= \frac{\Delta t}{2} \left(F_i^{(n+1)} + F_i^{(n)} \right) \\
&= \frac{\Delta t}{2} \left(-K_{ij}^{Xr} \Delta r_j - K_{ij}^{XX} \Delta X_j - K_{ij}^{X\theta} \Delta \theta_j + 2F_i^{(n)} \right)
\end{aligned} \tag{4.19}$$

$$\begin{aligned}
\text{For } \theta_i : \quad \int_{t^{(n)}}^{t^{(n+1)}} M_i dt &= \frac{\Delta t}{2} \left(M_i^{(n+1)} + M_i^{(n)} \right) \\
&= \frac{\Delta t}{2} \left(-K_{ij}^{\theta r} \Delta r_j - K_{ij}^{\theta r'} \Delta r_j' - K_{ij}^{\theta\theta} \Delta \theta_j + 2M_i^{(n)} \right)
\end{aligned} \tag{4.20}$$

Where the notations and the expressions for the K matrices follow the same convention as the equations (4.13) and (4.16) in the static analysis.

4.3 Modeling of the Damper on the Connection

The damper on the connector is used for controlling the excessive resonance of the high frequency vibration of the tensioned line like the tether or the riser in the TLP. The damper is modeled as a linear damping force proportional to the vibratory velocity of the

line on the top connection node of the body and the line. The damping force, N_i^D , on the connection node of the line is given by:

$$N_i^D = C_d (\dot{X}_i + \dot{\theta}_j \times p_k - \dot{r}_i) \quad (4.21)$$

where C_d is the damping coefficient, \dot{X} and $\dot{\theta}$ are the translational and rotational velocity of the rigid body, \dot{r} is the velocity of the attached node of the line to the body. p_k is the position vector of the attached node of the line at the connection point, and the vector product of the $\dot{\theta}_j$ and p_k can be rewritten in the tensor form as $\dot{\theta}_j \times p_k = \dot{\theta}_j C_{ji}$, as shown in the equation (4.1'). So, the equation (4.21) becomes:

$$N_i^D = C_d (\dot{X}_i + \dot{\theta}_j C_{ji} - \dot{r}_i) \quad (4.21')$$

It acts on the rigid body as reaction force by:

$$F_i^D = -N_i^D \quad (4.22)$$

In the time domain analysis, the integration from time $t^{(n+1)}$ to $t^{(n)}$ is obtained as:

$$\begin{aligned} \text{For } r_i : \quad \int_{t^{(n)}}^{t^{(n+1)}} N_i^D dt &= \int_{t^{(n)}}^{t^{(n+1)}} C_d (\dot{X}_i + \dot{\theta}_j C_{ji} - \dot{r}_i) dt \\ &= C_d \Delta X_i + C_d C_{ji} \Delta \theta_j - C_d \Delta r_i \end{aligned} \quad (4.23)$$

$$\begin{aligned} \text{For } X_i : \quad \int_{t^{(n)}}^{t^{(n+1)}} F_i^D dt &= \int_{t^{(n)}}^{t^{(n+1)}} C_d (-\dot{X}_i - \dot{\theta}_j C_{ji} + \dot{r}_i) dt \\ &= -C_d \Delta X_i - C_d C_{ji} \Delta \theta_j + C_d \Delta r_i \end{aligned} \quad (4.24)$$

The equations of (4.23) and (4.24) show the terms of the geometric stiffness matrix of the system. There are coupled terms with the body and the lines on the connection point. The coupled terms can be solved together for body and line motions in the assembled system matrix equations.

4.4 Modeling the Connection between Lines and Seafloor

The lower ends of the mooring lines and risers are normally connected to the seafloor. The formulation for the connection part of the lines and the seafloor are very similar to the modeling of the connection part of the body and the line. If the end connection of the line consists of the anchor, the clamped or hinged boundary condition is needed, and then it can be obviously replaced by considering a proper spring so that the spring constant in the corresponding direction is to be large enough to hold the rigidity of the anchor or the hinged boundary sufficiently. The connector force N_i^F and moment L_i^F are defined by:

$$N_i^F = K_i^L (p_i^F - r_i) \quad (4.25)$$

$$L_i^F = K_i^\theta \left(e_i^F - \frac{r_i'}{(r_m' r_m')^{1/2}} - \frac{r_i' r_j'}{(r_n' r_n')^{3/2}} \right) \quad (4.26)$$

The damping force is defined as:

$$N_i^{Fd} = -K_i^L \dot{r}_i \quad (4.27)$$

where p_i^F is the position vector of the attached point of the seafloor, e_i^F is the reference direction vector of the rotational spring fixed on the seafloor, and r_i and r_i' are the position vector and the tangential vector of the attached node to the seafloor. Since the numbering of the lines starts from the seafloor when the line is attached to the seafloor, the position vector is assigned as:

$$r_1 = U_{11}, \quad r_2 = U_{21}, \quad r_3 = U_{31} \quad (4.28)$$

$$r_1' = U_{12}, \quad r_2' = U_{22}, \quad r_3' = U_{32} \quad (4.29)$$

4.5 Formulation for the Multiple Body System

The equation of motion and the equation of the stretching condition for the multiple body system combined with any types of vessels can be derived in the same way as the equation (3.47) and (3.48) for a single body system.

$$(M_{ijkl} + M_{ijkl}^a)\ddot{U}_{jk} + (K_{ijkl}^1 + \lambda_n K_{ijkl}^2)U_{jk} - F_{il} = 0 \quad (3.48)$$

$$G_m = A_{mil}U_{kl}U_{ki} - B_m - C_{mn}\lambda_n = 0 \quad (3.49)$$

The two equations for a multiple-body system has the same form, and they can be simplified as follows:

$$\mathbf{M}\ddot{\mathbf{U}} + \mathbf{K}\mathbf{U} = \mathbf{F} \quad (4.30)$$

$$\mathbf{A}\mathbf{U}^2 - \mathbf{B} - \mathbf{C}\boldsymbol{\lambda} = \mathbf{0} \quad (4.31)$$

The $[\mathbf{M}]$, $[\mathbf{K}]$, $[\mathbf{A}]$ and $[\mathbf{C}]$ have the size of rows $N_L \times [8 \times (N_E + 1) - 1]$ and the bandwidth of 15, and $[\mathbf{B}]$, $\{\ddot{\mathbf{U}}\}$, $\{\mathbf{U}\}$, $\{\mathbf{U}^2\}$, $\{\mathbf{F}\}$ and $\{\boldsymbol{\lambda}\}$ are the vectors of the size of $N_L \times [8 \times (N_E + 1) - 1]$, where N_L is the total number of lines and N_E is the number of elements per each line. The global coordinate is used for composing each matrix, regardless of the body to which the line is connected. In the next step, the matrix of equations for the lines is combined with the matrix for the body motion including the coupled terms in the stiffness matrix, and the assembled matrix and system equations are dealt with in the next section.

After applying the Taylor expansion, the Adams-Moulton method, and the Adams-Bashforth method, and the Newton method of static and dynamic analysis, the equations can be expressed in the matrix form as:

In static analysis:

$$\begin{bmatrix} K_{ijkl}^{t0(n)} & K_{iln}^{t1(n)} \\ D_{mjk}^{t0(n)} & D_{mn}^{t1(n)} \end{bmatrix} \begin{Bmatrix} \Delta U_{jk} \\ \Delta \lambda_n \end{Bmatrix} = \begin{Bmatrix} -R_{il}^{(n)} \\ -G_m^{(n)} \end{Bmatrix} \quad (4.32)$$

where,

$$\begin{aligned} K_{ijkl}^{t0(n)} &= K_{ijkl}^1 + \lambda_n^{(n)} K_{nijlk}^2 \\ K_{iln}^{t1(n)} &= K_{nijlk}^2 U_{jk}^{(n)} \\ D_{mjk}^{t0(n)} &= A_{mkp} U_{jp}^{(n)} \\ D_{mn}^{t1(n)} &= -C_{mn} \\ R_{il}^{(n)} &= (K_{ijkl}^1 + \lambda_n K_{nijlk}^2) U_{jk}^{(n)} - F_{il} \\ G_m^{(n)} &= 0 \end{aligned} \quad (4.33)$$

In the dynamic analysis in time domain:

$$\begin{bmatrix} \hat{K}_{ijkl}^{t0(n)} & \hat{K}_{iln}^{t1(n)} \\ \hat{D}_{mjk}^{t0(n)} & \hat{D}_{mn}^{t1(n)} \end{bmatrix} \begin{Bmatrix} \Delta U_{jk} \\ \Delta \lambda_n \end{Bmatrix} = \begin{Bmatrix} -\hat{R}_{il}^{(n)} \\ -\hat{G}_m^{(n)} \end{Bmatrix} \quad (4.34)$$

where,

$$\begin{aligned} \hat{K}_{ijkl}^{t0(n)} &= \frac{2}{\Delta t^2} \left(3\hat{M}_{ijkl}^{(n)} - \hat{M}_{ijkl}^{(n-1)} \right) + K_{ijkl}^1 + \lambda_n^{(n-\frac{1}{2})} K_{nijlk}^2 \\ \hat{K}_{iln}^{t1(n)} &= 2K_{nijlk}^2 U_{jk}^{(n)} \\ \hat{D}_{mjk}^{t0(n)} &= 2K_{nijlk}^2 U_{il}^{(n)} = 2D_{mjk}^{t0(n)} \\ \hat{D}_{mn}^{t1(n)} &= -2C_{mn} = 2D_{mn}^{t1(n)} \\ \hat{R}_{il}^{(n)} &= \frac{2}{\Delta t} \left(3\hat{M}_{ijkl}^{(n)} - \hat{M}_{ijkl}^{(n-1)} \right) U_{jk}^{(n)} + \left(3F_{il}^{(n)} - F_{il}^{(n-1)} \right) \\ &\quad - 2K_{ijkl}^1 U_{jk}^{(n)} - 2\lambda_n^{(n-\frac{1}{2})} K_{nijlk}^2 U_{jk}^{(n)} \\ \hat{G}_m^{(n)} &= 2G_m^{(n)} \end{aligned} \quad (4.35)$$

The assembled equation of the coupled system of the rigid body and the lines can be expressed as:

$$\begin{bmatrix} [\mathbf{K}^L] & [\mathbf{K}^C] \\ \hline [(\mathbf{K}^C)^T] & [\mathbf{K}^B] \end{bmatrix} \begin{Bmatrix} \mathbf{U}^L \\ \mathbf{U}^B \end{Bmatrix} = \begin{Bmatrix} \mathbf{F}^L \\ \mathbf{F}^B \end{Bmatrix} \quad (4.36)$$

where $[\mathbf{K}^L]$ is composed with the stiffness matrix of the lines and the connector springs, $[\mathbf{K}^B]$ is the stiffness matrix of the rigid body, $[\mathbf{K}^C]$ and $[(\mathbf{K}^C)^T]$ are the coupled stiffness matrices and its transpose matrix including the coupling terms of the rigid body and the lines. $[\mathbf{U}^L]$ and $[\mathbf{U}^B]$ denote the displacement matrices of the lines and the body, and $[\mathbf{F}^L]$ and $[\mathbf{F}^B]$ are the force and moment terms acting on the lines and the body. The size of $[\mathbf{K}^B]$ is 6×6 for a single body system, but for the multiple-body system $6N \times 6N$, where N is the number of the multiple bodies. For a single-body system, $[\mathbf{K}^C]$ has the size of $[8 \times (n_E + 1) - 1]$ rows and 6 columns per line. It has nontrivial terms of the size of 7×6 at the last end rows of the matrix, and the remaining terms subtracting the nontrivial terms from $[\mathbf{K}^C]$ are filled with zeros. The matrix $[(\mathbf{K}^C)^T]$ is the transpose matrix of $[\mathbf{K}^C]$. When the multiple-body system is considered, and the hawser or the fluid transfer line (FTL) between one body and another body is connected to body, the total number of rows of the matrix $[\mathbf{K}^C]$ becomes $[8 \times (n_E + 1) - 1]$ rows and $6 \times N$ columns per connecting line, where n_E is the number of elements per line. It makes two coupled terms on the starting node and the ending node of the connecting line.

Thus, it has the nontrivial terms twice of $7 \times 6N$ in size, and the remaining terms except the nontrivial terms are filled with zeros like those in a single body. The displacement vector $[\mathbf{U}^B]$ and the force vector $[\mathbf{F}^B]$ for the rigid body have the size of $6N \times 1$. The stiffness matrix, $[\mathbf{K}^L]$, of the lines has $n_L \times [8 \times (n_E + 1) - 1]$ rows and the bandwidth of 15, where n_L is the total number of lines. The matrix equation of total system explicitly has the sparse matrix form. It means that a special consideration should be required to solve it. Nowadays, some updated sparse matrix solvers are developed and announced by many mathematical researchers. For this study, the forward and backward Gauss elimination method as the rigorous and traditional solver is used, and modified slightly for the purpose of treating the sparseness of the system matrix effectively. After the forward elimination process is performed in the first step for solving the system matrix, the backward substitution follows it next.

CHAPTER V
CASE STUDY 1:
DYNAMIC ANALYSIS OF A TANKER BASED FPSO

5.1 Introduction

As mentioned in the previous chapter, the hull/mooring line/riser coupled analysis program for solving the two-body interaction problem was developed. Using this program, the following case studies were performed for verification of the program. For the first case, a tanker-based FPSO is taken. The tanker-based FPSO is designed for the purpose of installation in the sea at the water depth of 6,000 ft. The environmental conditions of the GoM (Gulf of Mexico) are used for the design.

The FPSO has a large, rotational movement during operation in the sea. In general, due to this kind of specific large yaw rotation, the current and the wind force coefficients are specially considered, and the experimental data of many years, based on many VLCCs investigated and developed by Oil Company International Marine Forum (OCIMF) is used. The wave loads induced by potential velocities are calculated by using WAMIT that is a program to solve the potential problem of the fluid interaction.

The test model is selected as a turret moored FPSO in 6,000 ft. of water depth, where the environmental conditions are the extreme hurricane conditions in the Gulf of Mexico. The mooring system is a semi-taut steel wire system. The results of the analysis are compared with MARIN's experimental results.

5.2 Design Premise Data of FPSO and Mooring Systems

The design premise data is described in this section. The vessel for this study is an FPSO in 6,000 ft of the water depth. The capacity of the vessel storage is 1,440,000 bbls, and the production level is 120,000 bpd. The dead weight of this vessel is 200 kDWT. This vessel has an LBP of 310 meters, a molded breadth of 47.17 meters, and a depth of 28.04 meters as the main dimensions. In the full load condition, the draft is 18.9 meters and the displacement is 240,869 MT. The turret is located at 63.55 meters aft of the forward perpendicular of the vessel. The details of the design premise data are shown in Table 5.1. The body plan and the isotropic view of the vessel are shown in Figure 5.1. In the figure, the bow of the vessel is heading toward the east.

The mooring lines and risers are spread from the turret. There are 12 combined mooring lines with chain, wire and chain, and 13 steel wire risers. Table 5.2 shows the main particulars of mooring lines. Table 5.3 gives the hydrodynamic coefficients for mooring lines. The main particulars of risers are shown in Table 5.4, and the hydrodynamic coefficients are depicted in Table 5.5. The schematic plot of the arrangement for mooring lines is shown in Figure 5.2. There are 4 groups of mooring lines, each of which is normal to the other group. Each group is composed of 3 mooring lines 5 degree apart from each mooring line in the group. The center of the first group is heading the true East, and so the second group is toward the true North. Each mooring line has a studless chain anchor of grade K4.

On the contrary, for the riser system, 19 lines are used in the prototype FPSO, but for the simulation, only 13 risers among them are modeled equivalently as to what

MARIN did in their experimental tests. The risers are arranged non-symmetrically with respect to the x-axis (the axis toward the East). With respect to the y-axis (the axis toward the North), the arrangement is also not symmetrical. But the risers are almost balanced in the viewpoint of top tension with respect to both axes. The top view of the arrangement of risers is shown in Table 5.6 and Figure 5.3 on the horizontal plane based on the earth. In this study, the riser bending stiffness is not considered.

Table 5.1 Main particulars of the turret moored FPSO 6,000 ft

| Description | Symbol | Unit | Quantity |
|--|------------------|-----------------------|-----------|
| Production level | | <i>bpd</i> | 120,000 |
| Storage | | <i>bbls</i> | 1,440,000 |
| Vessel size | | <i>kDWT</i> | 200 |
| Length between perpendicular | L _{pp} | <i>m</i> | 310.0 |
| Breadth | B | <i>m</i> | 47.17 |
| Depth | H | <i>m</i> | 28.04 |
| Draft (in full load) | T | <i>m</i> | 18.09 |
| Diaplacement (in full load) | | <i>MT</i> | 240,869 |
| Length-beam ratio | L/B | | 6.57 |
| Beam-draft ratio | B/T | | 2.5 |
| Block coefficient | C _b | | 0.85 |
| Center of buoyancy forward section 10 | FB | <i>m</i> | 6.6 |
| Water plane area | A | <i>m</i> ² | 13,400 |
| Water plane coefficient | C _w | | 0.9164 |
| Center of water plane area forward section 10 | FA | <i>m</i> | 1.0 |
| Center of gravity above keel | KG | <i>m</i> | 13.32 |
| Transverse metacentric height | M _{Gt} | <i>m</i> | 5.78 |
| Longitudinal metacentric height | M _{Gl} | <i>m</i> | 403.83 |
| Roll radius of gyration in air | R _{xx} | <i>m</i> | 14.77 |
| Pitch radius of gyration in air | R _{yy} | <i>m</i> | 77.47 |
| Yaw radius of gyration in air | R _{zz} | <i>m</i> | 79.30 |
| Frontal wind area | A _f | <i>m</i> ² | 1,012 |
| Transverse wind area | A _b | <i>m</i> ² | 3,772 |
| Turret in center line behind F _{pp} (20.5 % L _{pp}) | X _{tur} | <i>m</i> | 63.55 |
| Turret elevation below tanker base | Z _{tur} | <i>m</i> | 1.52 |
| Turret diameter | | <i>m</i> | 15.85 |

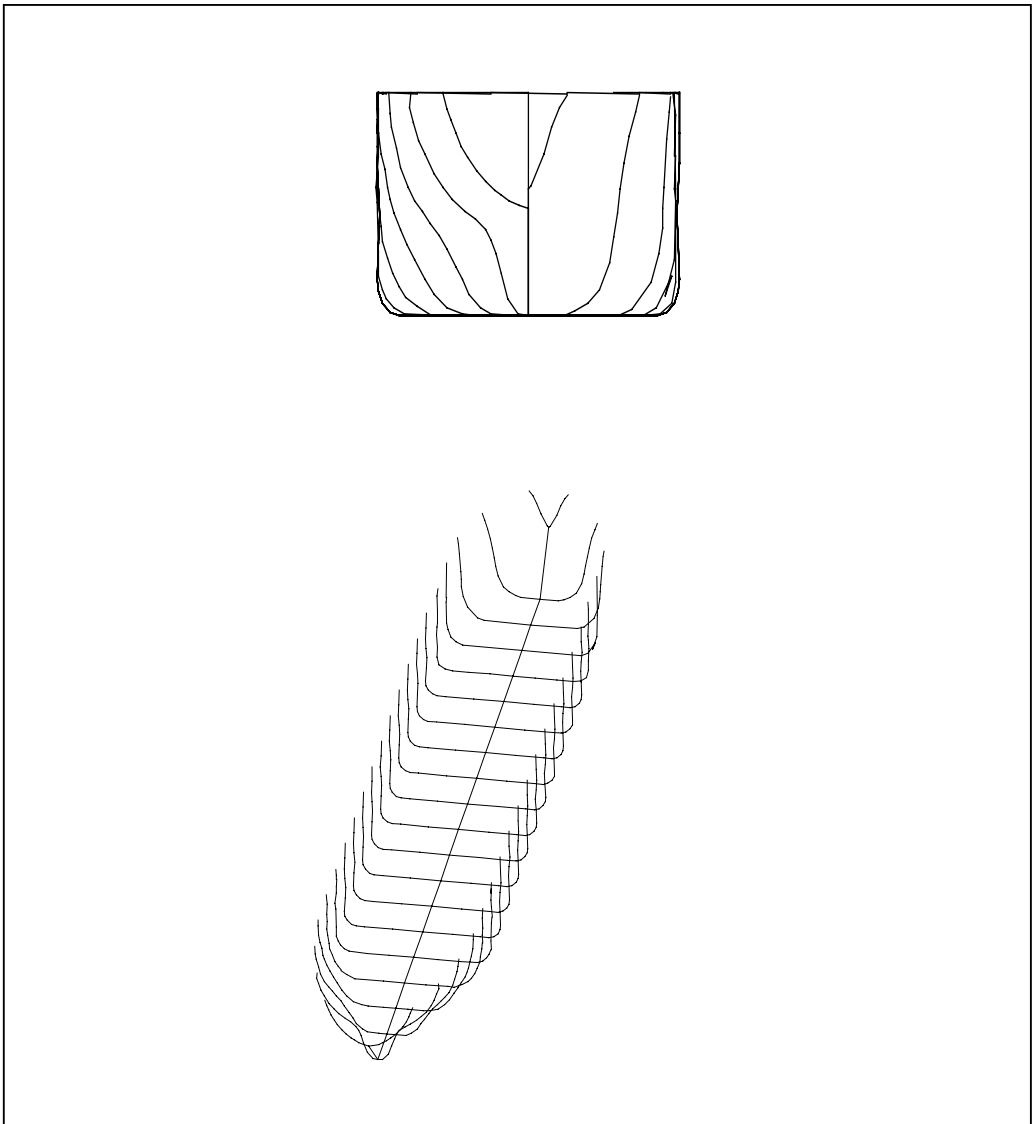


Figure 5.1 The body plan and the isotropic view of FPSO 6,000 ft

Table 5.2 Main particulars of mooring systems

| Description | Unit | Quantity |
|--|-------------|-----------------|
| Pretension | <i>kN</i> | 1,201 |
| Number of lines | | 4*3 |
| Degrees between 3 lines | <i>deg</i> | 5 |
| Length of mooring line | <i>m</i> | 2,087.9 |
| Radius of location of chain stoppers on turn table | <i>m</i> | 7.0 |
| Segment 1 (ground position): chain | | |
| Length at anchor point | <i>m</i> | 914.4 |
| Diameter | <i>mm</i> | 88.9 |
| Weight in air | <i>kg/m</i> | 164.9 |
| Weight in water | <i>kg/m</i> | 143.4 |
| Stiffness, AE | <i>kN</i> | 794,841 |
| Mean breaking load, MBL | <i>kN</i> | 6,515 |
| Segment 2: Polyester | | |
| Length | <i>m</i> | 1127.8 |
| Diameter | <i>mm</i> | 107.9 |
| Weight in air | <i>kg/m</i> | 42.0 |
| Weight in water | <i>kg/m</i> | 35.7 |
| Stiffness, AE | <i>kN</i> | 690,168 |
| Mean breaking load, MBL | <i>kN</i> | 6,421 |
| Segment 3 (hang-off position): chain | | |
| Length | <i>m</i> | 45.7 |
| Diameter | <i>mm</i> | 88.9 |
| Weight in air | <i>kg/m</i> | 164.9 |
| Weight in water | <i>kg/m</i> | 143.4 |
| Stiffness, AE | <i>kN</i> | 794,841 |
| Mean breaking load, MBL | <i>kN</i> | 6,515 |

Table 5.3 Hydrodynamic coefficients of the chain, rope and polyester

| Hydrodynamic Coefficients | Symbol | Chain | Rope/Poly |
|--------------------------------------|---------------|--------------|------------------|
| Normal drag | C_{dn} | 2.45 | 1.2 |
| Tangential drag | C_{dt} | 0.65 | 0.3 |
| Normal added inertia coefficient | C_{in} | 2.00 | 1.15 |
| Tangential added inertia coefficient | C_{it} | 0.50 | 0.2 |
| Coulomb friction over seabed | F | 1.0 | 0.6 |

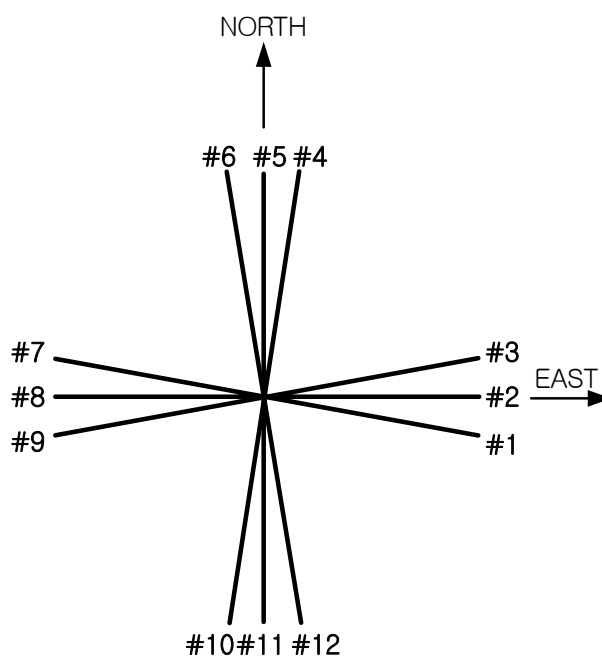


Figure 5.2 Arrangement of the mooring lines for FPSO 6,000 ft

Table 5.4 Main particulars of risers

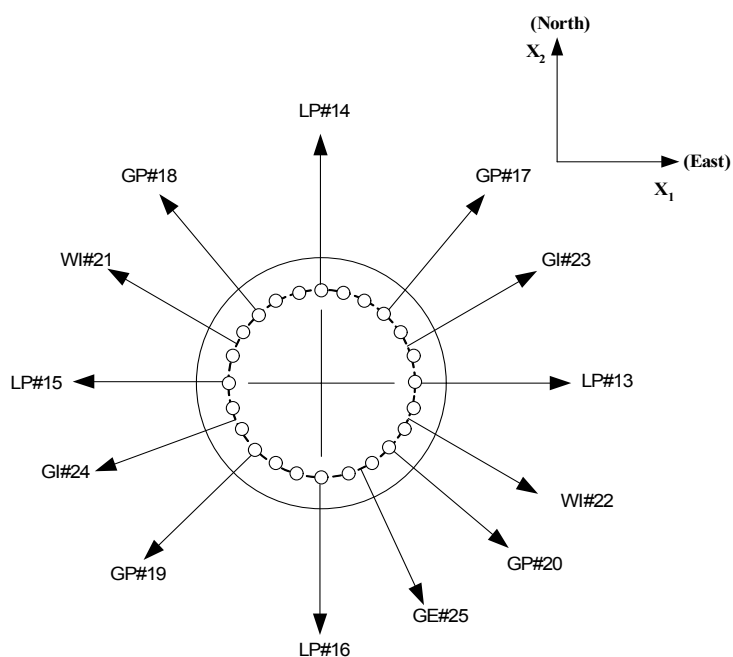
| Description | No. | Top tension kN | Out diameter mm | Stiffness, AE kN | Mass kg/m | Dry weight/ wet weight N/m | C _{dn} | Radius of riser connection | | |
|-------------------|-----|-------------------|--------------------|---------------------|--------------|----------------------------------|-----------------|----------------------------|-----------------------|-------------------|
| | | | | | | | | Points on turnable m | Connection level m | Total length m |
| Liquid production | 4 | 1112.5 | 444.5 | 1.83E+07 | 196.4 | 1927/1037 | 1.0 | 4.88 | 1.52 | 1829 |
| Gas production | 4 | 609.7 | 386.1 | 1.08E+07 | 174.1 | 1708/526 | 1.0 | 4.88 | 1.52 | 1829 |
| Water injection | 2 | 2020.0 | 530.9 | 1.86E+07 | 285.7 | 2803/1898 | 1.414 | 4.88 | 1.52 | 1829 |
| Gas injection | 2 | 1352.8 | 287.0 | 3.14E+07 | 184.5 | 1810/1168 | 1.414 | 4.88 | 1.52 | 1829 |
| Gas export | 1 | 453.9 | 342.9 | 8.60E+06 | 138.4 | 1358/423 | 1.0 | 4.88 | 1.52 | 1829 |

Table 5.5 Hydrodynamic coefficients of risers

| Description | Symbol | Coefficients |
|----------------------------------|-----------------|--------------|
| Normal drag | C _{dn} | 1.0 |
| Tangential drag | C _{dt} | 0.4 |
| Normal added inertia coefficient | C _{in} | 1.0 |
| Coulomb friction over seabed | F | 0.6 |

Table 5.6 Azimuth angles of risers bounded on the earth

| Description | Azimuth angle of riser | | | |
|------------------------|------------------------|-------|-----|-----|
| | #1 | #2 | #3 | #4 |
| Liquid production (LP) | 0 | 90 | 180 | 270 |
| Gas production (GP) | 45 | 135 | 225 | 315 |
| Water injection (WI) | 165 | 337.5 | | |
| Gas injection (GI) | 30 | 210 | | |
| Gas export (GE) | 300 | | | |

**Figure 5.3 Arrangement of the risers for FPSO 6,000 ft**

5.3 Environmental Data

For the loading condition for the analysis, the 100-year extreme hurricane condition at the GoM is used, which is one of the severest in the world. The wave condition is composed of the significant wave height of 12 m, the peak period of 14 sec, and the overshooting parameter of 2.5. The wind spectrum of API formulae is taken as

the design condition. The mean wind velocity at the reference height of 10 m for one hour sustained is 41.12 m/s. The current is mainly induced by the storm. The velocity of current at the sea surface is 1.0668 m/s, and it keeps until 60.96 m under the sea surface. From 60.96 m to 91.44 m under the sea surface, the current speed is varied from 1.0668 m/s to 0.05 m/s. For the intermediate region between 60.96 m to 91.44 m, the current profile is determined by the linear interpolation. The current speed is uniformly kept 0.05 m/s from 91.44 m under the surface to the sea bottom.

While the storm wave and wind arise, the current is assumed as a one-directional current. But, when the GoM environmental condition is applied to the platform design, the loop current in the GoM should be considered as a design loading condition. In this study, however, the loop-current condition will not be applied, since the hurricane condition is more severe than the loop current case. The summary of the environmental condition for this study is shown in Table 5.7.

Table 5.7 Environmental loading condition

| Description | Unit | Quantity |
|--------------------------------|--|-------------------|
| Wave | | |
| Significant wave height, H_s | <i>m</i> | 12.19 |
| Peak period, T_p | <i>sec</i> | 14 |
| Wave spectrum | <i>JONSWAP ($\gamma=2.5$)</i> | |
| Direction | <i>deg</i> | 180 ¹⁾ |
| Wind | | |
| Velocity | <i>m/s</i> | 41.12 m/s @ 10m |
| Spectrum | <i>API RP 2A-WSD</i> | |
| Direction | <i>deg</i> | 210 ¹⁾ |
| Current | | |
| Profile | | |
| at free surface (0 m) | <i>m/s</i> | 1.0668 |
| at 60.96 m | <i>m/s</i> | 1.0668 |
| at 91.44 m | <i>m/s</i> | 0.0914 |
| on the sea bottom | <i>m/s</i> | 0.0914 |
| Direction | <i>deg</i> | 150 ¹⁾ |

Remark: 1) The angle is measured counterclockwise from the x-axis (the East).

5.3.1 Wave Force

The JONSWAP spectrum was developed to define the wave by Hasselman, *et al.* (1973) for the Joint North Sea Wave Project. The formula is to be derived from the modified Pierson-Moskowitz spectrum formula. The formula is given by:

$$S(\omega) = \alpha g^2 \omega^{-5} \exp \left[-1.25 \left(\frac{\omega}{\omega_0} \right)^{-4} \right] \gamma \exp \left[-\frac{(\omega - \omega_0)^2}{2\tau^2 \omega_0^2} \right] \quad (5.1)$$

where α is a parameter related to the prevailing wind field with the wind velocity of U_w and a fetch length of X , g is the gravitational acceleration, γ is the overshooting or peakness parameter, and τ is the shape parameter. The α , γ and ω_0 are determined by the following formulae:

$$\alpha = 0.076(X_0)^{-0.22} \quad (5.2)$$

$$\tau = \begin{cases} 0.07 & \text{for } \omega \leq \omega_0 \\ 0.09 & \text{for } \omega > \omega_0 \end{cases} \quad (5.3)$$

$$\omega_0 = 2\pi \left(\frac{g}{U_w} \right) (X_0)^{-0.33} \quad (5.4)$$

where, $X_0 = g \frac{X}{U_w^2}$. When X is unknown, α is taken as 0.0081. In this study, the wave

frequencies are considered to be between in 0.2 rad/s and 1.5 rad/s. Figure 5.4 shows the wave spectrum with the given data.

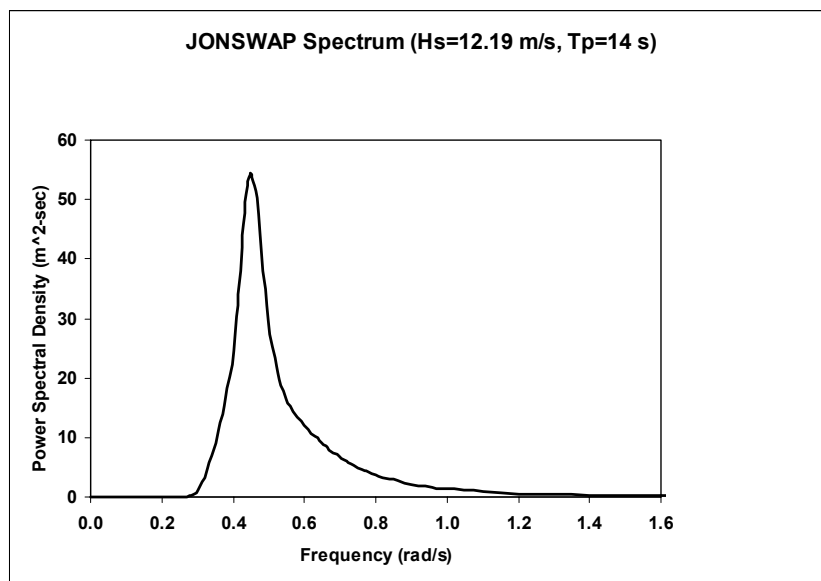


Figure 5.4 JONSWAP wave spectrum

5.3.2 Wind Force

The formulae of API wind spectrum is as follows:

$$S_{uu}(f) = \frac{f/f_p}{[1 + 1.5f/f_p]^{5/3}} \sigma(z)^2 \quad (5.5)$$

where:

$S_{uu}(f)$ = the spectral energy density at elevation z .

f = the frequency in hertz.

$f_p = 0.025V_z/z$ = the average value of the frequencies of the measured wind

spectra

$\sigma(z)$ = the standard deviation of wind speed, i.e.

$$\sigma(z) = \frac{I(z)}{V_z} \quad (5.6)$$

$V_z = V_H (z/H)^{0.125}$ = the mean wind speed at elevation z for one hour

V_H = the mean wind speed at elevation 10 m for one hour

$$I(z) = \frac{\sigma(z)}{V_z} = \begin{cases} 0.15(z/z_s)^{-0.125} & \text{for } z \leq z_s \\ 0.15(z/z_s)^{-0.275} & \text{for } z > z_s \end{cases} \quad (5.7)$$

= turbulence intensity over one hour

where $z_s = 20$ m is the thickness of the surface layer.

Figure 5.5 shows the API wind spectrum of the given wind speed at the reference elevation. After the normal wind force is calculated using the above wind spectrum, the actual wind force varying with the weathervaning angle (yaw) of the vessel should be re-estimated by considering the force coefficients of the wind and the current in the OCIMF booklet.

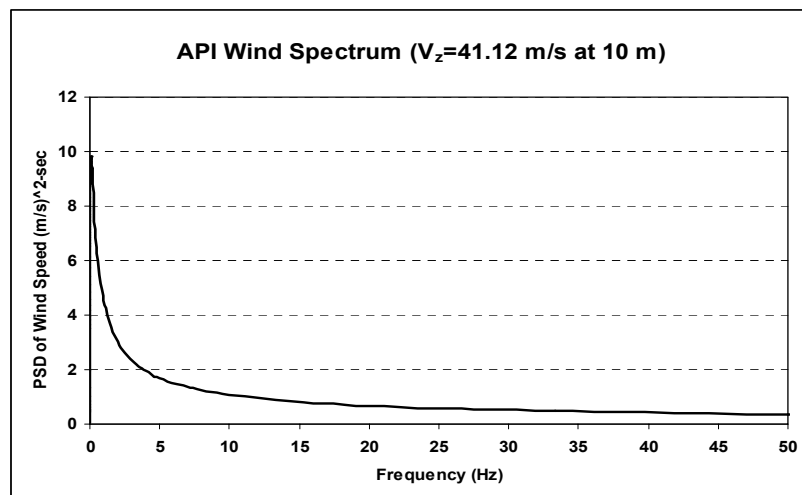


Figure 5.5 API wind spectrum

5.3.3 Wind and Current Forces by OCIMF

The FPSO is a kind of tanker-based vessel. The OCIMF is the international research committee that has been investigated the wind and current foresee subjected on VLCC. In this study, the OCIMF booklet published in 1998 is referred to for calculating the wind and current force coefficients. They suggest the following formula of the wind and current force coefficients:

$$F_{xw} = \frac{1}{2} C_{xw} \rho_w V_w^2 A_T \quad (5.8)$$

$$F_{yw} = \frac{1}{2} C_{yw} \rho_w V_w^2 A_L \quad (5.9)$$

$$M_{xyw} = \frac{1}{2} C_{xyw} \rho_w V_w^2 A_L L_{PP} \quad (5.10)$$

$$F_{xc} = \frac{1}{2} C_{xc} \rho_c V_c^2 L_{PP} T \quad (5.11)$$

$$F_{yc} = \frac{1}{2} C_{yc} \rho_c V_c^2 L_{PP} T \quad (5.12)$$

$$M_{xyc} = \frac{1}{2} C_{xyc} \rho_c V_c^2 L_{PP}^2 T \quad (5.13)$$

where F_{xw} and F_{yw} are the surge and sway wind forces, M_{xyw} is the yaw wind moment, F_{xc} and F_{yc} are the surge and sway current forces, and M_{xyc} is the current yaw moment. C_{xw} , C_{yw} and C_{xyw} are the wind force and moment coefficients, and C_{xc} , C_{yc} and C_{xyc} are the current force and moment coefficients. ρ_w and ρ_c are the densities of air and fluid, and V_w and V_c are the wind velocity and current speed at the free surface. A_T , A_L ,

T and L_{PP} are the transverse area, the longitudinal area, the draft and the length between perpendiculars of the vessel, respectively. They surveyed the force and moment coefficients on the varying attack angle, for the two loading conditions, and for two kinds of bow shapes. The attack angle is measured from 180 degree on the bow to 0 degree on the stern. The considered loading conditions are ballast and full load conditions. For the bow shape, the cylindrical bow and the conventional bulbous bow are taken. In the OCIMF booklet, the force and moment coefficients are shown in the variation of the attack angle with parameters of the loading condition and the bow configuration. For the current force coefficients, the water depth to draft ratio is also taken as a parameter.

In this study, the tanker area and drag coefficients are assumed unchanged during the time simulation. But, the coefficient for every 5 degree of attack angle is prepared in advance, and at every time step during analyzing the yaw angle is swept. Whenever the angle exceeds 5 degree, the wind and current force coefficients are re-calculated using the pre-made coefficient data files. The OCIMF formula for the wind and current forces are to be expressed with respect to the center of the vessel, which is located near the mid-ship. Thus, the forces and moments give the localized components acting on the vessel-wise coordinate. The subject vessel is a turret-moored tanker, so the center of the vessel movement should be the center of turret position, not the center of the vessel. Therefore, to calculate the global motions of the vessel, the forces and moments are transferred to the global coordinate components according to the yaw angle at every time

step during simulation. The force and moment are transferred by the inverse of rotation matrix as follows:

$$\text{Rotational matrix: } \mathbf{T} = \begin{bmatrix} \cos \theta & \sin \theta & 0 \\ -\sin \theta & \cos \theta & 0 \\ 0 & 0 & 1 \end{bmatrix} \quad (5.14)$$

$$\text{Inverse of rotational matrix: } \mathbf{T}^{-1} = \begin{bmatrix} \cos \theta & -\sin \theta & 0 \\ \sin \theta & \cos \theta & 0 \\ 0 & 0 & 1 \end{bmatrix} \quad (5.15)$$

Coordinate transformation of force vector:

$$\text{- Global force vectors: } \mathbf{F} = \begin{Bmatrix} F_x \\ F_y \\ M_{XY} \end{Bmatrix} \quad (5.16)$$

$$\text{- Local force vectors: } \mathbf{f} = \begin{Bmatrix} F_{xw} + F_{xc} \\ F_{yw} + F_{yc} \\ M_{xyw} + M_{xyc} \end{Bmatrix} = \begin{Bmatrix} F_x \\ F_y \\ M_{xy} \end{Bmatrix} \quad (5.17)$$

$$\mathbf{F} = \mathbf{T}^{-1} \mathbf{f} = \begin{bmatrix} \cos \theta & -\sin \theta & 0 \\ \sin \theta & \cos \theta & 0 \\ 0 & 0 & 1 \end{bmatrix} \begin{Bmatrix} F_x \\ F_y \\ M_{xy} \end{Bmatrix} \quad (5.18)$$

Considering the translation of turret position:

$$M_{XY} = F_y x_{turret} + M_{xy} \quad (5.19)$$

Resultant force vectors:

$$\mathbf{F} = \mathbf{T}^{-1} \mathbf{f} = \begin{bmatrix} \cos \theta & -\sin \theta & 0 \\ \sin \theta & \cos \theta & 0 \\ 0 & x_{turret} & 1 \end{bmatrix} \begin{Bmatrix} F_x \\ F_y \\ M_{xy} \end{Bmatrix} \quad (5.20)$$

where θ is the yaw rotation angle of the vessel and x_{turret} is the x -coordinate of the turret position in the body (local) coordinate system.

5.4 Hydrodynamic Coefficients

The hydrodynamic coefficients are calculated by using WAMIT, which can solve the diffraction/radiation and the interaction problem of fluid and the platform structure. The WAMIT is the program to solve the velocity potential on the wetted surface around the floating structure based on the potential theory by means of the Boundary Element Method (BEM) using the 3-dimensional panel elements. BEM is the numerical technique for considering only the wetted body surface and/or the water free surface instead of considering the whole fluid domain. Taking Green's function to satisfy all other boundary conditions in the fluid domain as the weighting function in the integral equation of motion makes it possible to solve the potential in the fluid domain.

In the linear theory, the added mass and linear damping coefficients, exciting forces by diffraction potential, and mean drift forces can be obtained from the WAMIT. By using the second order WAMIT, the quadratic transfer functions corresponding to the second-order difference frequency forces and the second-order sum frequency forces can be withdrawn. The modeling of the subject vessel is shown in Figures 5.6 and 5.7. Only the port side of the vessel is modeled, and the symmetric condition is used for the potential calculation in WAMIT. In the numerical model, the number of elements on the body is 1870. Several models with other sized numberings are selected for convergence

study. Through the convergence study, the determined model was proved to be proper for the analysis.

For the hydrodynamic coefficients, Newman's (1974) approximation method is used. In this method, the different frequency components are replaced by the mean part of the linear transfer function (LTF). It is well known that the difference frequency component of the quadratic transfer function is not sensitive to the frequency when two frequencies are close. When two frequencies are quite large, the different frequency is also large. Then, the frequency is far away from the natural frequency of the body or mooring system. So, it also does not have much influence on the body or on the mooring system.

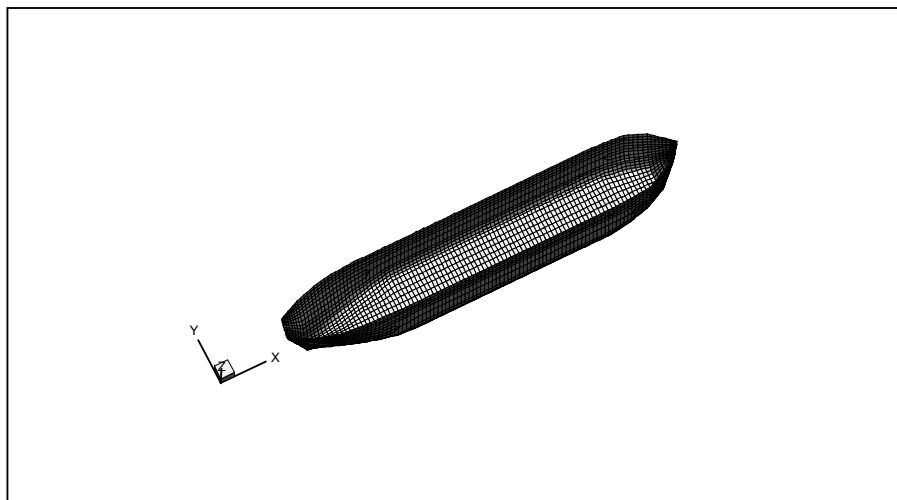


Figure 5.6 Modeling of body surface of FPSO

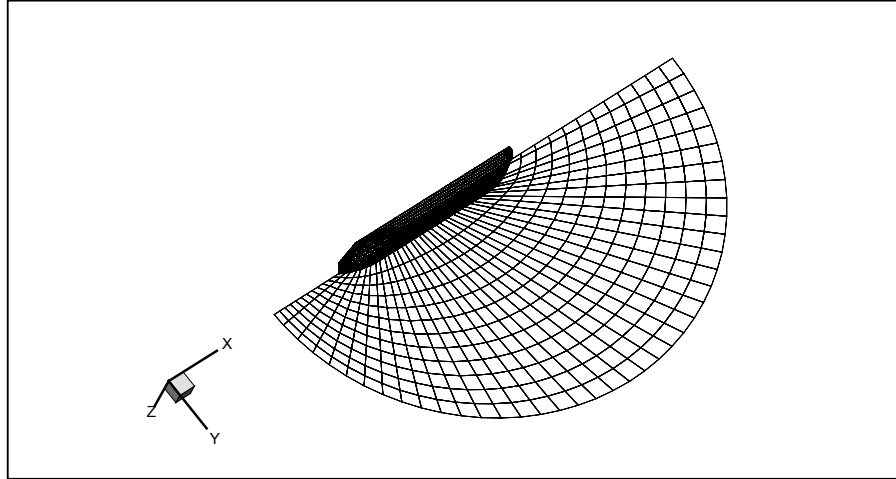


Figure 5.7 Modeling of body surface and free surface of the water

5.5 Coupled Analysis of FPSO

In this study, the analysis case is explained for the turret-moored FPSO mentioned in the previous section. The water depth is 6,000 ft (about 1828.8 m). The hydrodynamic coefficients are calculated at every 5 degree of yaw angle by WAMIT, and WIMPOST-FPSO is used for the coupled analysis. The results are compared with MARIN's. The mooring lines and risers are modeled for preparing the input data of WINPOST-FPSO.

The mooring lines consisted of three parts, i.e., a chain anchor part, a wire part of mid and a hang-off chain part. The first part is divided into 5 elements, the mid-part (wire) into eight elements, and the last chain part for the connection to the turret into 1 element. The connection boundary to the turret is modeled as a hinged joint. So, the

rotations are free, but no translation movement is allowed on that point. At the first node of mooring line on the sea bed, the Dirichlet boundary condition is applied.

All Risers are treated as Steel Catenary Risers (SCRs). The risers are divided uniformly into 12 elements. The boundary conditions for risers are the same as those for mooring lines. The input data for wind, current force and wave loading are described in Table 5.7.

Before the coupling dynamic analysis is performed, a static and dynamic balancing test should be provided. Through these tests, the stiffness and system parameters such as natural frequencies and damping factors of the numerical model can be judged whether they are equivalent to the real system or not.

Firstly, the static offset test is carried out for the surge motion. During this test, the FPSO is kept heading to 0 degree. From this test, the static weight balance with the top tension of mooring lines and risers, the vessel weight and the buoyancy are checked. Until a well-balanced state is obtained, the footprints of mooring lines and risers are adjusted back and forth. The stiffness of the combined system with the body and mooring system is reviewed as well. To review the surge stiffness is a measure to judge whether the vessel combined with mooring system is properly modeled or not.

Secondly, the free decay test is conducted for the surge, sway, heave, roll, pitch and yaw motion in the calm water and in the 0 degree heading angle of the vessel. The initial external force in the direction of the surge motion is set as $2.0E+07$ N. The time interval is defined as 0.02 sec. The surge external force is increased up to the initial force

level during four time steps, and then is released for 2,000 seconds. This test gives the critical damping coefficients in the still water.

Finally, the coupled analysis in the time domain is carried out in irregular waves. 51 wave components are combined to generate the time series wave data with random phases. The first-order and also the second-order wave forces are calculated using the concept of a two-term Volterra series model. The frequency range for this combination is 0.15 rad/s to 1.2 rad/s. These are corresponding to 42 sec and to 5.2 sec, respectively. Additional hull drag damping forces in the irregular state due to the current and waves are evaluated with reference to the paper produced by Wichers(1996). The damping coefficients for the hull drag forces are depicted in Figure 5.8. For the time simulation, the time interval is set to 0.02 sec, and the total time to 3 hours. In the beginning part of time duration, the ramping function is adopted to smoothly increase for 200 sec in order to avoid the peculiar transient state.

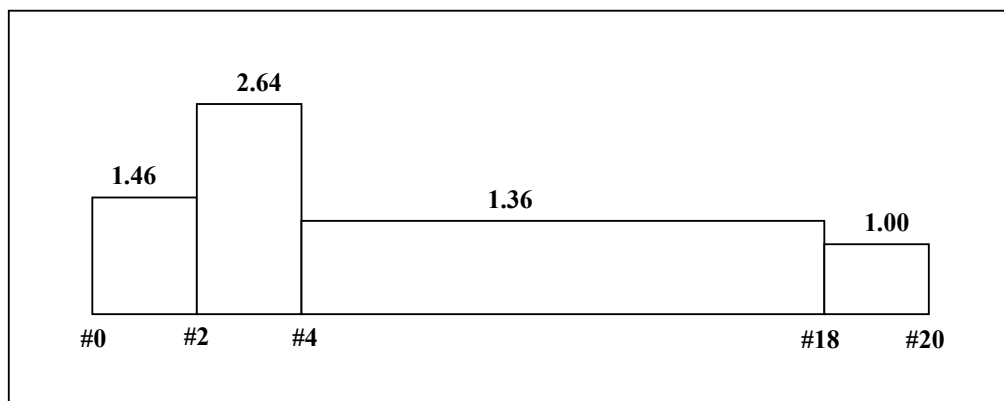


Figure 5.8 Hull drag damping coefficients (Wichers, 1996)

5.6 Results and Discussion

The added mass and radiation damping, first-order wave-frequency forces, and second-order mean and difference-frequency forces are calculated from the second-order diffraction/radiation program WAMIT (Lee et al, 1991). Figure 5.9 shows the distribution of panels on the body surface and free surface. Taking advantage of symmetry, only half domain is discretized (1684 panels for hull and 480 panels for free surface). All the hydrodynamic coefficients were calculated in the frequency domain, and then the corresponding forces were converted to the time domain using two-term Volterra series expansion (Ran and Kim, 1997). The frequency-dependent radiation damping was included in the form of convolution integral to the time domain equation. The wave drift damping was expected to be small and thus not included in the ensuing analysis.

The methodology for hull/mooring/riser coupled statics/dynamics is similar to that of Ran and Kim, 1997 and Kim et al., 1999. The mooring lines are assumed hinged at the turret and anchor position. The near-vertical riser is also hinged at the turret, and therefore, riser tension is included in the vertical static equilibrium of the hull. The calculated platform mass for the given condition is 2.3686×10^8 kg at 62-ft draft. The empirical coefficients for the viscous damping of the same FPSO hull in normal direction were obtained from the model test by Wichers(2000a).

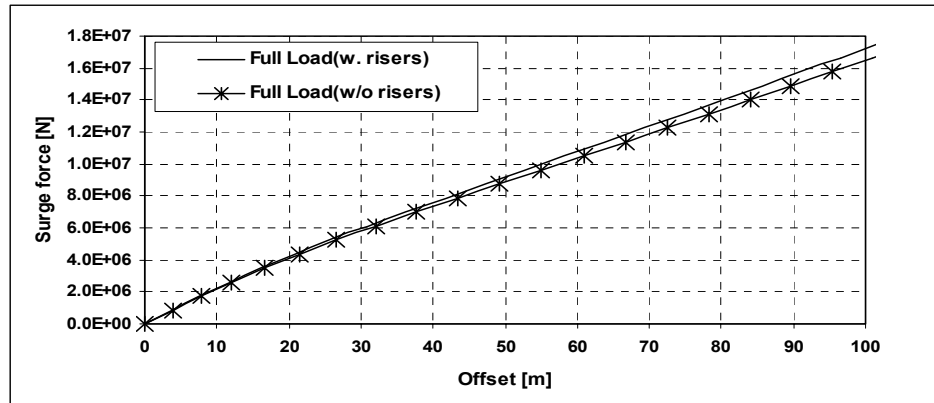
The wave force quadratic transfer functions are computed for 9 wave frequencies, ranging from 0.24 to 1.8 rad/sec and the intermediate values for other frequencies are interpolated. The hydrodynamic coefficients and wave forces are expected to vary

appreciably with large yaw angles and the effects should be taken into consideration for the reliable prediction of FPSO global motions. Therefore, they are calculated in advance for various yaw angles with a 5-degree interval and the data are then tabulated as inputs. The second-order diffraction/radiation computation for a 3D body is computationally very intensive especially when it has to be run for various yaw angles. Therefore, many researchers avoided such a complex procedure and have instead used simpler approach called Newman's approximation (Faltinsen, 1998) i.e. the off-diagonal components of the second-order difference-frequency QTFs are approximated by their diagonal values (mean drift forces and moments). This approximation can be justified only when the relevant natural frequency is very small and the slope of QTFs near the diagonal is not large. In this paper, the full QTFs are calculated and the validity of Newman's approximation is tested against more accurate results with complete QTFs. The wind and current force coefficients on the vessel are read from OCIMF data. The dynamic wind loading was generated from the wind velocities obtained from the API wind spectrum. The yaw wind moments are increased by 15% considering the effects of superstructures.

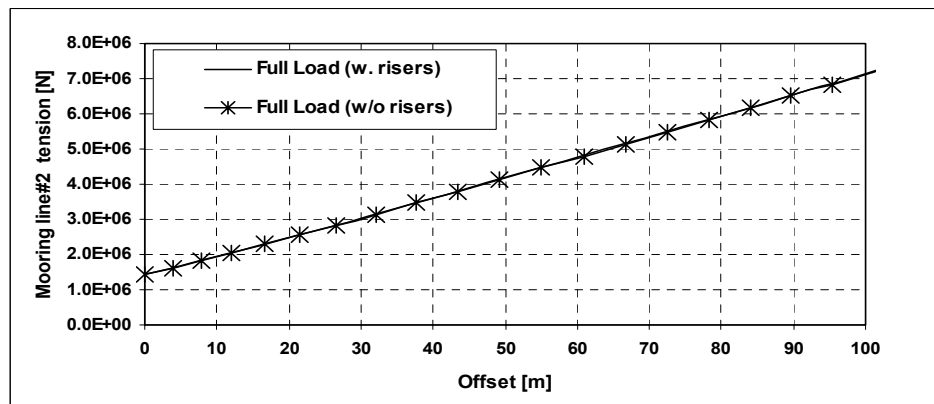
5.6.1 Static Offset Test (in Calm Water without Current)

The surge static offset test was conducted by pulling the VCG (Vertical Center of Gravity) in the horizontal direction in calm water. Typical results for surge offsets are shown in Figure 5.9. The surge static-offset test shows a weakly softening trend, which is contrary to the typical hardening behavior of catenary lines. The surge static offset

curves with risers are in general greater than those without risers due to the contribution of riser tension. On the other hand, the effects of risers on individual mooring tension are less appreciable. The results are shown in Figure 5.9.

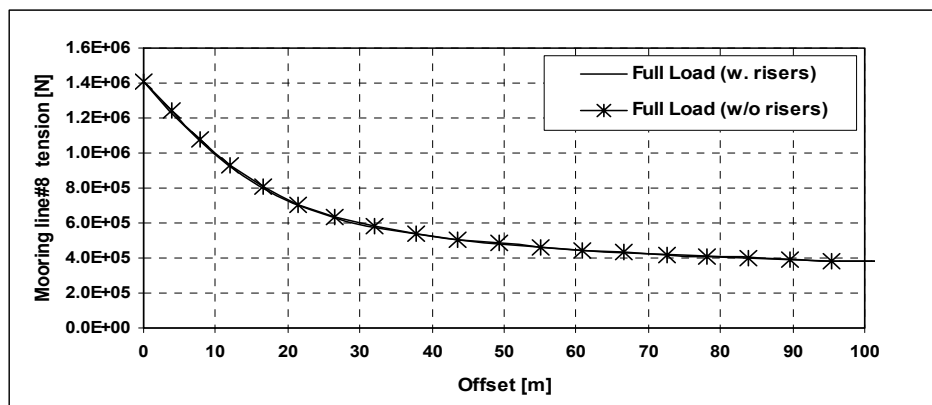


(a) Static offset test results for surge motion



(b) Static offset test results of #2 mooring line in the surge direction

Figure 5.9 Static offset test results for surge motion

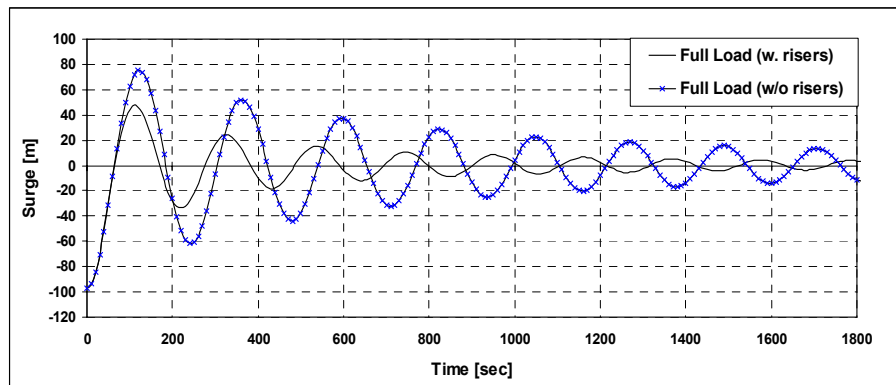


(c) Static offset test results of #8 mooring line in the surge direction

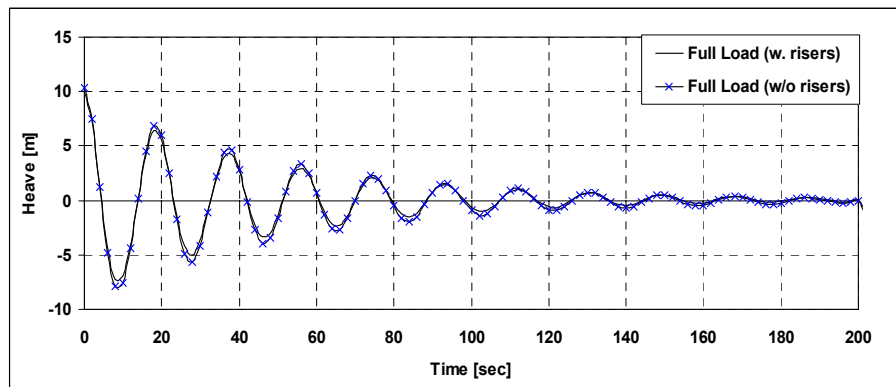
Figure 5.9 Continued

5.6.2 Free-decay Tests (in Calm Water without Current)

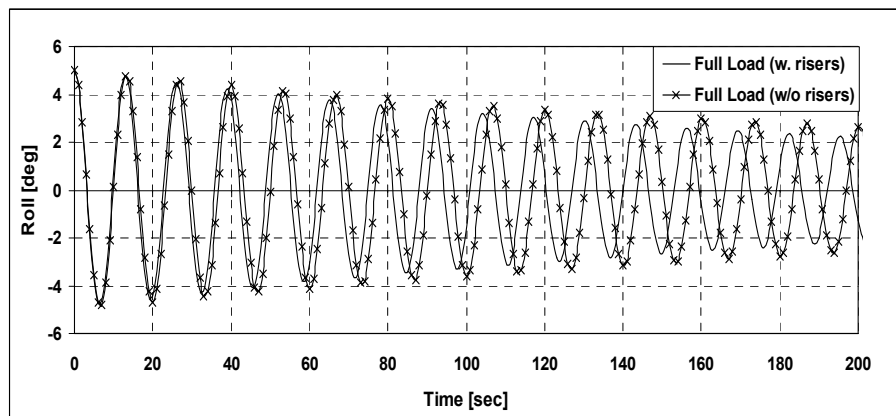
To see the effects of risers (mostly the amount of damping from risers) in the free-decay tests more clearly, a simpler riser model was developed i.e. all the 13 risers are replaced by a single equivalent massless riser at the center with the same total tension. The resulting surge/sway stiffness at the turret is then approximately calculated and added to the hydrostatic matrix. Figure 5.10 shows typical free-decay test results for surge, heave, roll, and pitch modes. The natural frequency and the damping coefficients obtained from the free decay test are summarized in Table 5.8 and Table 5.9.



(a) Free decay test for surge motion



(b) Free decay test for heave motion



(c) Free decay test for roll motion

Figure 5.10 Free-decay test results for surge, heave and roll motions

Table 5.8 Natural periods from free-decay tests

| | Surge | Heave | Roll | Pitch |
|-----------------------------|---------|--------|--------|--------|
| Full draft (with risers) | 209.8 s | 18.7 s | 13.0 s | 18.6 s |
| Full draft (w/o risers) | 225.9 s | 18.7 s | 13.4 s | 18.6 s |

Table 5.9 Damping from free-decay tests estimated from the first 4 peaks assuming linear damping

| | Surge | Heave | Roll | Pitch |
|--------------------------|-----------------------------|-------------------------|-------------------------|------------------------|
| Full draft (with risers) | 11.0 % (-97.5 ~ -12.2 m) | 6.5 % (10.9 ~ 3.2 m) | 0.86 % (5 ~ 4.2 deg) | 6.7 % (5 ~ 1.4 deg) |
| Full draft (w/o risers) | 5.8 % (-96.7 ~ -32.7 m) | 6.1 % (10.4 ~ 3.3 m) | 0.68 % (5 ~ 4.4 deg) | 6.0 % (5 ~ 1.6 deg) |

5.6.3 Time-domain Simulation for Hurricane Condition

The current is assumed to be steady and the irregular wave uni-directional. A JONSWAP spectrum of significant wave height $H_s = 12.192$ m, peak period $T_p = 14$ s, and overshoot parameter $\gamma = 2.5$ was selected to represent a typical 100-yr storm in the Gulf of Mexico. The storm induced current flows from 30-deg. right of wave direction. The current velocity is assumed to be 3.5ft/s between 0-200ft and reduced to 0.3ft/s at 300ft-3000ft. The wind speed used is [92mph@10m](#) and its direction is 30-deg. left of waves. The API wind spectrum is used for the generation of time-varying wind forces. The drag coefficients for wave forces are 1.0 for mooring lines, 1.0 to 1.414 for risers. The low- and wave-frequency regions are defined as 0-0.2 rad/s and 0.2-1.3 rad/s, respectively. The time-domain simulation results are summarized in Table 5.10.

Table 5.10 Time-domain simulation results (unit: m , deg.)

| | Condition | Mean | Low-freq. RMS | Wave-freq. RMS | Total RMS | Max |
|--------------|--------------------------------|-------|---------------|----------------|-----------|-------|
| Surge (m) | Newman's Approx. (with risers) | -13.9 | 6.98 | 0.49 | 7.0 | -34.6 |
| | Newman's Approx. (w/o risers) | -13.9 | 10.32 | 0.44 | 10.3 | -46.7 |
| | Full QTF (with risers) | -14.7 | 8.42 | 0.44 | 8.4 | -39.5 |
| Sway (m) | Newman's Approx. (with risers) | 4.7 | 2.50 | 0.49 | 2.5 | 13.4 |
| | Newman's Approx. (w/o risers) | 4.6 | 2.84 | 0.45 | 2.8 | 13.8 |
| | Full QTF (with risers) | 4.8 | 3.04 | 0.46 | 3.1 | 16.9 |
| Heave (m) | Newman's Approx. (with risers) | 0 | 0.04 | 3.36 | 3.4 | 10.9 |
| | Newman's Approx. (w/o risers) | 0 | 0.03 | 3.46 | 3.5 | -12.1 |
| | Full QTF (with risers) | 0.1 | 0.07 | 3.37 | 3.4 | 11.1 |
| Roll (deg.) | Newman's Approx. (with risers) | 0.2 | 0.16 | 0.98 | 1.0 | 3.5 |
| | Newman's Approx. (w/o risers) | 0.2 | 0.15 | 1.26 | 1.3 | 4.3 |
| | Full QTF (with risers) | 0.1 | 0.38 | 1.22 | 1.3 | 5.5 |
| Pitch (deg.) | Newman's Approx. (with risers) | 0.0 | 0.02 | 1.33 | 1.3 | -4.3 |
| | Newman's Approx. (w/o risers) | 0.0 | 0.02 | 1.39 | 1.4 | 4.7 |
| | Full QTF (with risers) | 0.0 | 0.04 | 1.34 | 1.3 | -4.5 |
| Yaw (deg.) | Newman's Approx. (with risers) | 15.3 | 2.74 | 0.28 | 2.6 | 22.7 |
| | Newman's Approx. (w/o risers) | 13.7 | 2.57 | 0.31 | 2.7 | 22.3 |
| | Full QTF (with risers) | 15.1 | 3.86 | 0.28 | 3.9 | 24.3 |

From this result, it is clearly seen that slowly varying components are dominant in horizontal-plane motions (surge, sway, yaw), while wave-frequency responses are more important in vertical-plane motions (heave, roll, pitch). It is also found that the effect of riser damping is very important in the surge, particularly its slowly varying component.

When riser damping is absent, the surge rms and maximum values are overestimated by about 47% and 35%, respectively. For the other modes, the effect of riser damping is less significant. If riser damping is not accounted for, the total rms

tension values on taut(#2) and slack(#8) mooring lines are overestimated by 38% and 40%, respectively. The simulation results for mooring lines and risers are summarized in Table 5.11. There also exist significant differences in rms and maximum tension of individual risers, which indirectly shows the importance of fully coupled analysis.

Table 5.11 The results of tensions on the mooring lines and risers (unit: kN)

| | Condition | Mean | Total RMS | Max |
|-----------------------------|--------------------------------|------|-----------|------|
| Mooring Line #2 | Newman's Approx. (with risers) | 2160 | 424 | 3529 |
| | Newman's Approx. (w/o risers) | 2157 | 583 | 4252 |
| | Full QTF (with risers) | 2201 | 479 | 3639 |
| Mooring Line #8 | Newman's Approx. (with risers) | 903 | 249 | 1860 |
| | Newman's Approx. (w/o risers) | 943 | 349 | 2319 |
| | Full QTF (with risers) | 901 | 296 | 2077 |
| Liquid production riser #13 | Newman's Approx. (with risers) | 2345 | 272 | 4941 |
| | Full QTF (with risers) | 2343 | 262 | 5393 |
| Gas production riser #20 | Newman's Approx. (with risers) | 1253 | 278 | 3509 |
| | Full QTF (with risers) | 1254 | 265 | 3213 |
| Water injection riser #22 | Newman's Approx. (with risers) | 4284 | 403 | 7629 |
| | Full QTF (with risers) | 4383 | 391 | 6923 |
| Gas injection riser #23 | Newman's Approx. (with risers) | 2744 | 234 | 4082 |
| | Full QTF (with risers) | 2746 | 227 | 4054 |
| Gas export riser #25 | Newman's Approx. (with risers) | 960 | 166 | 1804 |
| | Full QTF (with risers) | 961 | 166 | 1781 |

In Table 3 and 4, the comparison between Newman's approximation and the full QTF is also shown. As expected, only horizontal-plane motions are appreciably affected. In general, the horizontal-plane motion amplitudes (slowly varying parts) are underestimated by using Newman's approximation, but the differences are not large. The error caused by mass-less riser modeling appears to be much more serious than that caused by Newman's approximation in this example.

5.7 Summary and Conclusions

The global motions of a turret-moored FPSO with 12 chain-polyester-chain mooring lines and 13 steel catenary risers in a non-parallel wind-wave-current environment are investigated in the time domain using a fully coupled hull/mooring/riser dynamic analysis program. This case is similar to the relevant study in DEEPSTAR Offshore Industry Consortium and the overall comparison looks reasonable.

In horizontal-plane motions, slowly varying components are dominant, and therefore, the reliable estimation of the second-order mean and slowly varying wave forces and the magnitude of total system damping is very important. For vertical-plane motions, wave-frequency responses are dominant and even the first-order potential-based theory can do a good job in heave and pitch. The coupling effects are also minimal in vertical-plane motions.

In the present study, we particularly addressed two points, the effects of riser coupling/damping and the validity of Newman's approximation. The riser damping is found to be important in surge/sway modes, particularly in surge. The use of Newman's

approximation slightly under-estimates the actual horizontal-plane motions but seems to be adequate in practical applications. However, when an input wave spectrum is not narrow-banded or double-peaked, care should be taken.

In a fully coupled simulation in the time domain, the behaviors of vessel, risers, and mooring lines can be directly seen on the screen through graphics-animation software, which will greatly enhance the understanding of the relevant physics and the overall-performance assessment of the system.

CHAPTER VI
CASE STUDY 2:
DYNAMIC ANALYSIS OF A TANKER BASED FPSO
COMPARED WITH THE OTRC EXPERIMENT

6.1 Introduction

In this study, the tanker based FPSO designed for the water depth of 6,000 ft and tested in the OTRC basin is adopted for the verification of the WINPOST-FPSO program. This FPSO is also a tanker-based and turret-moored vessel. The GoM environmental conditions for wave, wind and current force are used in the analysis as what the OTRC used in the experiment. The numerical model is made based on the experimental model conducted in the OTRC basin. The principle data is the same as the FPSO introduced in the previous chapter, but the loading condition is different, and the turret position is moved forward to the bow. So, the draft is changed to 15.121 m, which corresponds to 80 % loading of full load. The x coordinate of the turret position is 116.27 m along the ship's center line, which is positioned at 38.734 meters aft of the forward perpendicular of the vessel.

For the wind and current forces, the OCIMF data is used. The force coefficients are taken for the full load and ballast loading. The force coefficients for 80 % loading are interpolated automatically in the program using both data. The wave loads in the consideration of the different loading with the previous vessel are calculated by using WAMIT.

6.2 OTRC Experimental Results and Design Premise Data

Here the OTRC experimental results in the published paper in ISOPE 2001 will be used for comparison with the analysis results by WINPOST-FPSO. The paper contains the experimental results of the static offset test, the free decay test and some time simulation. Due to the change of draft for the different loading conditions, many design premise data should be changed. With the given draft, the principle data of vessel and mooring line are estimated by some hand calculations and rechecked by some numerical calculations.

The design premise data is basically the same as this in the previous chapter, except for the draft and turret position. Using this basic design data and the OTRC experimental results, the attempt to find the model data and the experimental condition data is tried. The top tension of mooring lines is assumed to be the same as that of the original FPSO. On the basis of this starting point, the weight balance is checked. The displacement can be evaluated with the different loading condition data and corresponding draft. In this loading condition, the draft is given as 15.121 meters. The displacement can be expected to be 80 % of that of full load, so it will be 192,625 MT.

The details of the design premise data are shown in Table 6.1. The general arrangement and body plan of the vessel are shown in Figure 6.1. As shown in the above Figure, the vessel is toward the East (the bow is heading the East).

The mooring lines and risers are spread from the turret. In the original design data there are 12 combined mooring lines with chain, wire and chain, and 13 steel wire risers. There are 4 groups of mooring lines, each of which is normal to other group. Each group

is composed of 3 mooring lines 5 degrees apart from each mooring line in the group. The center of the first group is heading the true East, and so the second group is toward the true North. Each mooring line has a studless chain anchor of Grade K4.

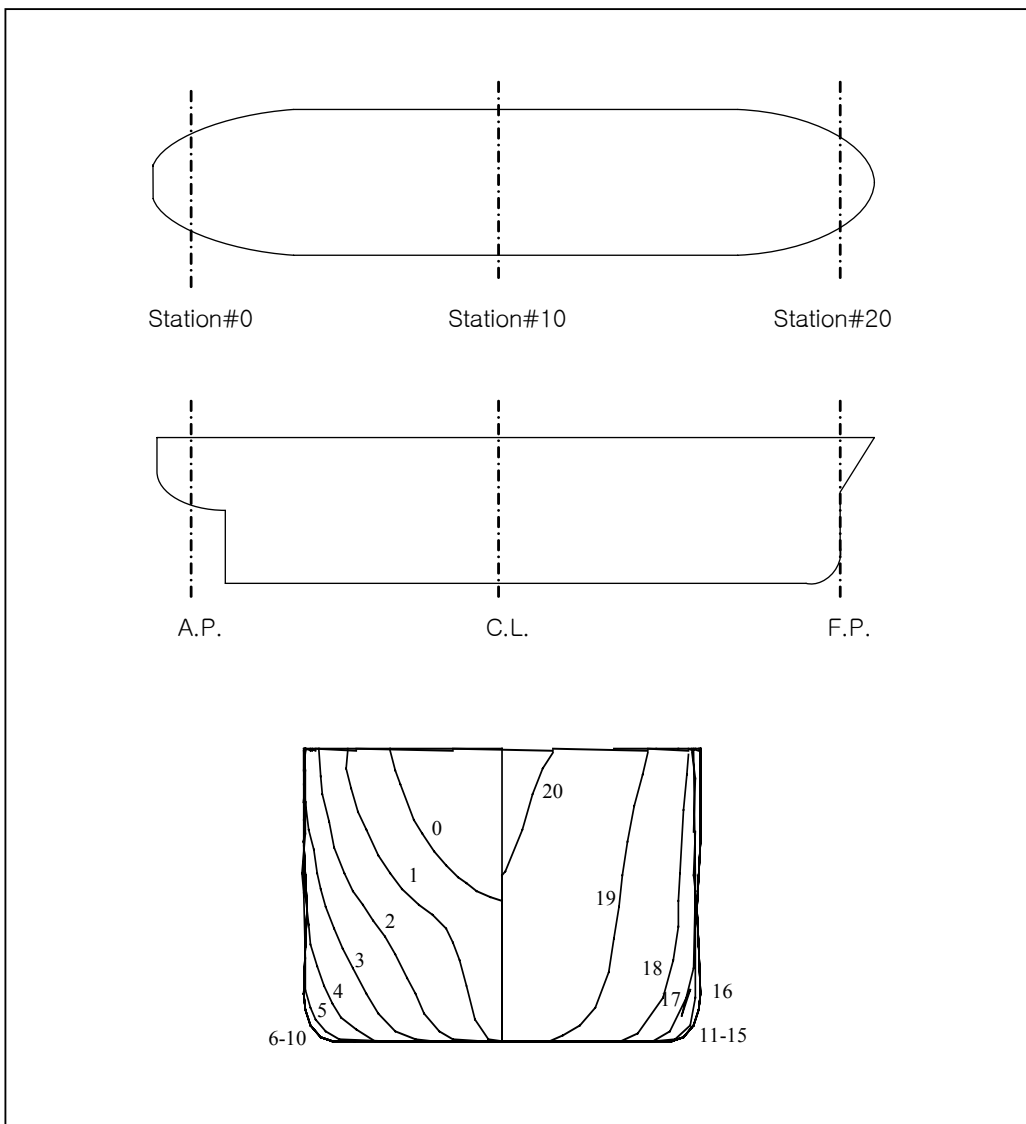


Figure 6.1 General arrangement and body plan of FPSO 6,000 ft

Table 6.1 Main particulars of the turret moored for the OTRC FPSO

| Description | Symbol | Unit | Quantity |
|---|-----------------|----------------------|-----------|
| Production level | | <i>bpd</i> | 120,000 |
| Storage | | <i>bbls</i> | 1,440,000 |
| Vessel size | | <i>kDWT</i> | 200 |
| Length between perpendicular | Lpp | <i>m</i> | 310.0 |
| Breadth | B | <i>m</i> | 47.17 |
| Depth | H | <i>m</i> | 28.04 |
| Draft (in full load) | T | <i>m</i> | 15.121 |
| Diaplacement (in full load) | | <i>MT</i> | 240,869 |
| Length-beam ratio | L/B | | 6.57 |
| Beam-draft ratio | B/T | | 3.12 |
| Block coefficient | Cb | | 0.85 |
| Center of buoyancy forward section 10 | FB | <i>m</i> | 6.6 |
| Water plane area | A | <i>m²</i> | 12,878 |
| Water plane coefficient | Cw | | 0.9164 |
| Center of water plane area forward section 10 | FA | <i>m</i> | 1.0 |
| Center of gravity above keel | KG | <i>m</i> | 13.32 |
| Transverse metacentric height | MGt | <i>m</i> | 5.78 |
| Longitudinal metacentric height | MGI | <i>m</i> | 403.83 |
| Roll raius of gyration in air | R _{xx} | <i>m</i> | - |
| Pitch raius of gyration in air | R _{yy} | <i>m</i> | - |
| Yaw radius of gyration in air | R _{zz} | <i>m</i> | - |
| Frontal wind area | Af | <i>m²</i> | - |
| Transverse wind area | Ab | <i>m²</i> | - |
| Turret in center line behind Fpp (12.5 % Lpp) | Xtur | <i>m</i> | 38.73 |
| Turret elevation below tanker base | Ztur | <i>m</i> | 1.52 |
| Turret diameter | | <i>m</i> | 15.85 |

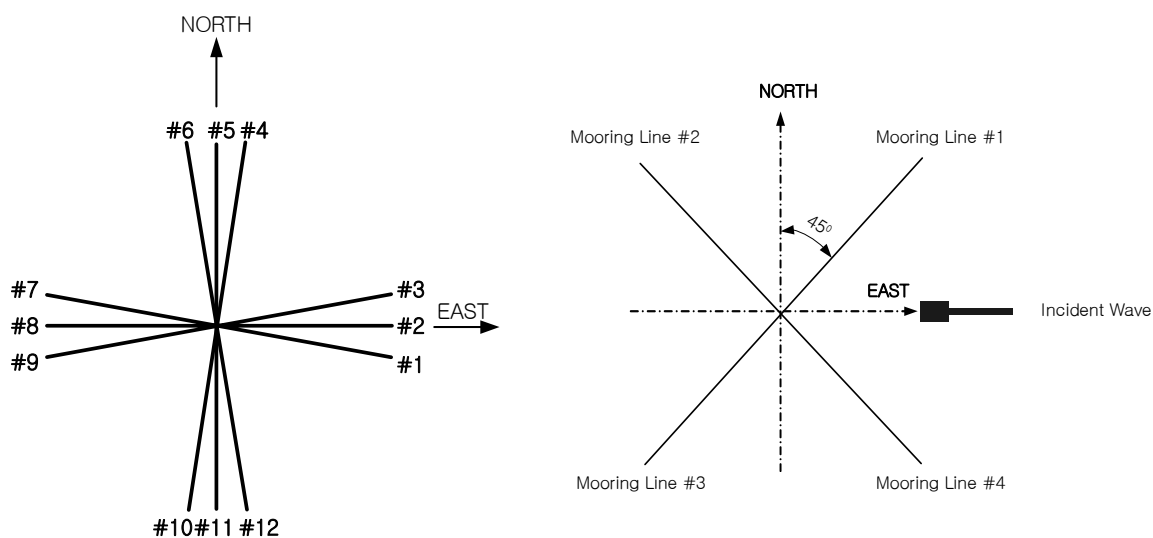
Table 6.2 Main particulars of mooring systems for the OTRC FPSO

| Description | Unit | Quantity |
|--|-------------|----------|
| Pretension | <i>kN</i> | 1,201 |
| Number of lines | | 4*3 |
| Degrees between 3 lines | <i>deg</i> | 5 |
| Length of mooring line | <i>m</i> | 2,087.9 |
| Radius of location of chain stoppers on turn table | <i>m</i> | 7.0 |
| Segment 1 (ground position): chain | | |
| Length at anchor point | <i>m</i> | 914.4 |
| Diameter | <i>mm</i> | 88.9 |
| Weight in air | <i>kg/m</i> | 164.9 |
| Weight in water | <i>kg/m</i> | 143.4 |
| Stiffness, AE | <i>kN</i> | 794,841 |
| Mean breaking load, MBL | <i>kN</i> | 6,515 |
| Segment 2: Polyester | | |
| Length | <i>m</i> | 1127.8 |
| Diameter | <i>mm</i> | 107.9 |
| Weight in air | <i>kg/m</i> | 42.0 |
| Weight in water | <i>kg/m</i> | 35.7 |
| Stiffness, AE | <i>kN</i> | 690,168 |
| Mean breaking load, MBL | <i>kN</i> | 6,421 |
| Segment 3 (hang-off position): chain | | |
| Length | <i>m</i> | 45.7 |
| Diameter | <i>mm</i> | 88.9 |
| Weight in air | <i>kg/m</i> | 164.9 |
| Weight in water | <i>kg/m</i> | 143.4 |
| Stiffness, AE | <i>kN</i> | 794,841 |
| Mean breaking load, MBL | <i>kN</i> | 6,515 |

Table 6.3 Hydrodynamic coefficients of the chain, rope and wire for the OTRC FPSO

| Hydrodynamic Coefficients | Symbol | Chain | Rope/Poly |
|--------------------------------------|----------|-------|-----------|
| Normal drag | C_{dn} | 2.45 | 1.2 |
| Tangential drag | C_{dt} | 0.65 | 0.3 |
| Normal added inertia coefficient | C_{in} | 2.00 | 1.15 |
| Tangential added inertia coefficient | C_{it} | 0.50 | 0.2 |
| Coulomb friction over seabed | F | 1.0 | 0.6 |

However, in ORTC model, only four equivalent mooring lines were used without risers. One equivalent mooring line is combined with 3 mooring lines. Table 6.2 shows the main particulars of equivalent mooring lines. Table 6.3 gives the hydrodynamic coefficients for mooring lines. The equivalent mooring lines are spread 90 degrees apart from the adjacent mooring lines. #1 equivalent mooring line goes to 45 degrees apart from the true East. So, #2 equivalent mooring line is spread toward 135 degrees apart from the true East. The schematic plot of the arrangement for mooring lines is shown in Figure 6.2. With respect to the x- and y-axis (the x-axis toward the East and the y-axis toward the North), the mooring lines are arranged symmetrically. In the numerical model for this study, the equivalent mooring system is used.



(a) Mooring system of the original FPSO (b) Mooring system of the ORTC experiment

Figure 6.2 Arrangement of mooring lines for turret-moored FPSO

6.3 Environmental Data

For the loading condition for the analysis, the 100-year extreme hurricane condition at the Gulf of Mexico (GoM) is used as the same as in the previous case. The wave condition is composed of the significant wave height of 12 m, the peak period of 14 sec, and the overshooting parameter of 2.5. The wind spectrum of NPD formulae is taken as the design condition, which spectrum is shown in Figure 6.3. The mean wind velocity at the reference height of 10 m for one hour sustained is 41.12 m/s. The current is mainly induced by the storm. The wind direction is applied differently with the original FPSO case in Chapter V. The velocity of current at the sea surface is 0.9144 m/s, and it keeps until 60.96 m under the sea surface. From 60.96 m to 91.44 m under the sea surface, the current speed is varied from 0.9144 m/s to 0.09144 m/s.

Table 6.4 Environmental loading condition for the OTRC FPSO

| Description | Unit | Quantity |
|--------------------------------|--|-------------------|
| Wave | | |
| Significant wave height, H_s | <i>m</i> | 12.19 |
| Peak period, T_p | <i>sec</i> | 14 |
| Wave spectrum | <i>JONSWAP ($\gamma=2.5$)</i> | |
| Direction | <i>deg</i> | 180 ¹⁾ |
| Wind | | |
| Velocity | <i>m/s</i> | 41.12 m/s @ 10m |
| Spectrum | <i>API RP 2A-WSD</i> | |
| Direction | <i>deg</i> | 150 ¹⁾ |
| Current | | |
| Profile | | |
| at free surface (0 m) | <i>m/s</i> | 0.9144 |
| at 60.96 m | <i>m/s</i> | 0.9144 |
| at 91.44 m | <i>m/s</i> | 0.0914 |
| on the sea bottom | <i>m/s</i> | 0.0914 |
| Direction | <i>deg</i> | 210 ¹⁾ |

Remark: 1) The angle is measured counterclockwise from the x-axis (the East).

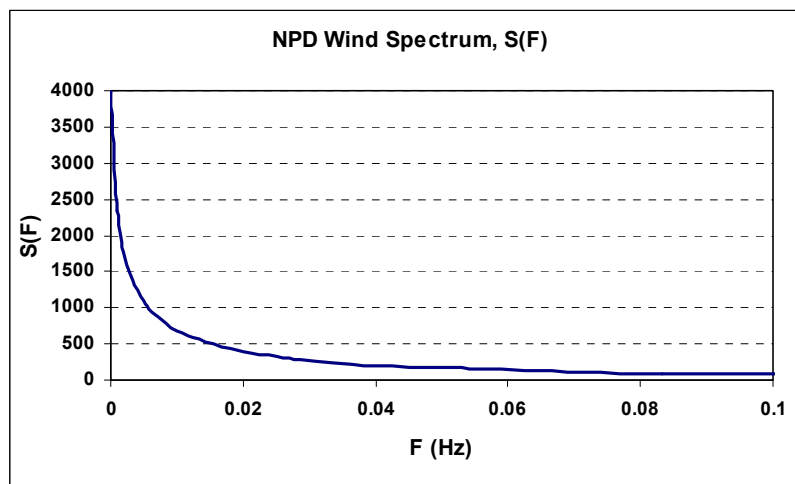


Figure 6.3 NPD wind spectrum curve

For the intermediate region between 60.96 m to 91.44 m, the current profile is determined by the linear interpolation. The current speed is uniformly kept 0.09144 m/s from 91.44 m under the surface to the sea bottom. While the storm wave and wind arise, the current is assumed as one directional current. But, when the GoM environmental condition is applied to the platform design, the loop current in the GoM should be considered as a design loading condition. In this study, however, the loop-current condition will not be applied, since the hurricane condition is severer than the loop current case. The summary of the environmental conditions for this study is shown in Table 6.4.

The current speed and direction in the OTRC experiment were set up differently with the original FPSO case. In the original data, the current speed at the free surface is 1.07 m/s, and the direction is 150° from the x-axis (true East). But, in the OTRC

experiment, the current speed was applied at the free surface of 0.9144 m/s, and the direction of 210° .

6.4 Re-generation of the Experimental Model

The design data are re-estimated to match the experimental model condition. The natural frequencies obtained from the free decay test in the OTRC experiment are known in a published paper (2001). The given data are $L \times B \times D$, T , KG , the turret position, and the top tension of mooring lines as shown in Table 6.1. Using the experimental model data and results, the required data should be newly estimated.

First, the hydrodynamic coefficients can be calculated by making the hydrodynamic modeling and by using WAMIT (the fluid interaction software to get the hydrodynamic coefficients), since the data of $L \times B \times D$, T and the body plan are given. The numerical modeling for WAMIT is very similar to the FPSO model in the previous chapter except the draft. From the WAMIT output, the displacement volume, the center of buoyancy and the restoring coefficients can be obtained. The obtained data from the WAMIT output is summarized in Table 6.5. Based on these data the weight of the model can be derived from the static equilibrium condition that the sum of the line top tensions and the weight is to be equal to the buoyancy. That's the reason why the top tension is called the net buoyancy:

Static equilibrium:

$$B = W + \frac{T}{g} \quad (6.1)$$

where B is the buoyancy, W denotes the weight of the body in mass unit, $\frac{T}{g}$ is the mass tension or the net buoyancy, and so T and g mean the top tension of mooring lines and the gravitational constant, respectively.

Table 6.5 WAMIT output and hand-calculation

| Description | Symbol | Unit | Quantity | Reference |
|------------------------|----------------|-------------|------------|-------------------------|
| Displaced volume | \forall | m^3 | 182,499 | WAMIT |
| Buoyancy | B | $m.ton$ | 187,060 | $\forall \times \rho_w$ |
| Total top tension | T | kN | 11,649 | Given data |
| Weight in mass | W | $m.ton$ | 185,870 | Static equilibrium |
| Center of gravity | x_g | m | -109.670 | Given data |
| | z_g | m | -1.801 | |
| Center of buoyancy | x_b | m | -89.086 | WAMIT |
| | z_b | m | -7.401 | |
| Restoring coefficients | \bar{C}_{33} | | 56.3226 | WAMIT |
| | \bar{C}_{44} | | 22.3251 | |
| | \bar{C}_{55} | | 4688.27 | |
| Added mass/moment | M_{a33} | $m.ton$ | 1.9566E+05 | WAMIT |
| | M_{a44} | $m.ton-m^2$ | 1.1018E+07 | |
| | M_{a55} | $m.ton-m^2$ | 3.5189E+09 | |

The relations between the natural frequency, and the restoring coefficients and the masses are defined as follows:

$$f = \frac{1}{2\pi} \sqrt{\frac{C_{ij}}{M_{vij}}} \quad (1/\text{sec or Hz}) \quad (i, j = 1, 2, \dots, 6) \quad (6.2)$$

where f is the natural frequency, C_{ij} is the restoring coefficients in which i and j can be any combination of six DOF, and M_{vij} ($= M_{aij} + m_{ij}$) is the virtual mass in which M_{aij} is the added mass and m_{ij} is the mass of the body in the i and j direction. The relationship between m_{ij} and W are as follows:

$$m_{33} = W \quad (6.3)$$

$$m_{44} = W(R_{xx}^2 + z_g^2 + y_g^2) \quad (6.4)$$

$$m_{55} = W(R_{yy}^2 + z_g^2 + x_g^2) \quad (6.5)$$

where (x_g, y_g, z_g) is the center of the gravity, and R_{xx}, R_{yy} are the radii of gyrations for roll and pitch motions. From the WAMIT output, M_{vij} can be obtained. These data are also summarized in Table 6.5. The restoring coefficients are defined by:

$$C_{33} = \rho_w g A_w, \quad \bar{C}_{33} = \frac{C_{33}}{\rho_w g L_R^2} \quad (6.6)$$

$$C_{44} = \rho_w g \iint_{A_w} y^2 n_3 ds + \rho_w g \nabla z_b - mgz_g = \rho_w g \nabla M_{Gl}, \quad \bar{C}_{44} = \frac{C_{44}}{\rho_w g L_R^4} \quad (6.7)$$

$$C_{55} = \rho_w g \iint_{A_w} x^2 n_3 ds + \rho_w g \nabla z_b - mgz_g = \rho_w g \nabla M_{Gl}, \quad \bar{C}_{55} = \frac{C_{55}}{\rho_w g L_R^4} \quad (6.8)$$

where \bar{C}_{33} , \bar{C}_{44} and \bar{C}_{55} are the non-dimensionalized restoring coefficients, ρ_w and A_w are the water density and the water plane area, ∇ is the displaced volume, z_b is the z-coordinate of the center of buoyancy, m is the mass of the body to be the same as W , and L_R is the referenced length that is taken as the depth or the breadth of the vessel.

Here, M_{Gt} and M_{Gl} denotes the transverse and longitudinal metacentric heights and n_3 represents the directional cosine in z-direction. Therefore, if the data in Table 6.6 and the equation (6.3) to (6.8) are taken advantage of, the radii of gyrations, restoring coefficients, and metacentric heights can be derived. The acquired data will be used as the analysis model data, and are summarized in Table 6.6.

Next, using the equation (6.2) and the experimental results in Table 6.7, the data are verified. It is the process to clarify whether the data obtained from the above equations are acceptable for the numerical calculation on behalf of the experimental model.

Table 6.6 Re-estimated data from WAMIT output and hand-calculation

| Description | Symbol | Unit | Quantity |
|---------------------------------|----------|-------|----------|
| Water plane area | A_w | m^2 | 12,878 |
| Radius of roll gyration | R_{xx} | m | 14.036 |
| Radius of pitch gyration | R_{yy} | m | 79.674 |
| Radius of yaw gyration | R_{zz} | m | 81.400 |
| Transverse metacentric height | M_{Gt} | m | 11.950 |
| Longitudinal metacentric height | M_{Gl} | m | 1349.0 |

6.5 Results and Discussion

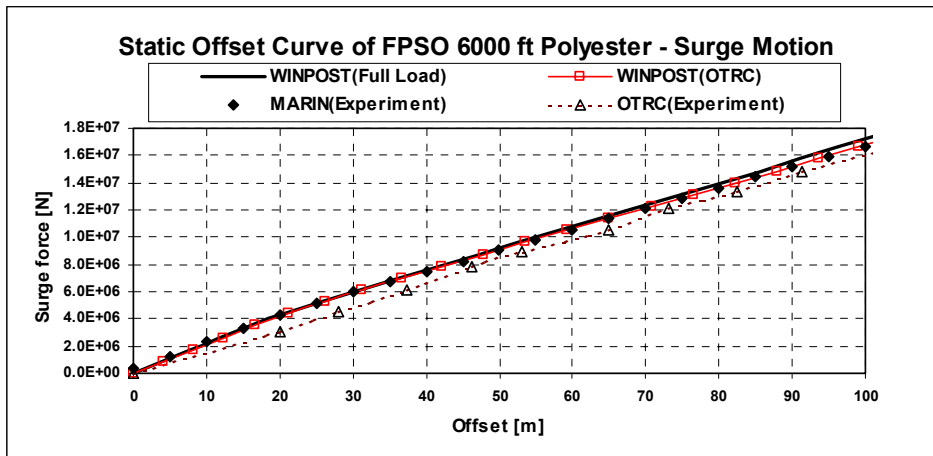
6.5.1 Static Offset Test with Re-generated Model Data

The static offset tests are performed with the data obtained above by WINPOST-FPSO. The test results are depicted in Figure 6.4. They show the stiffness of the re-

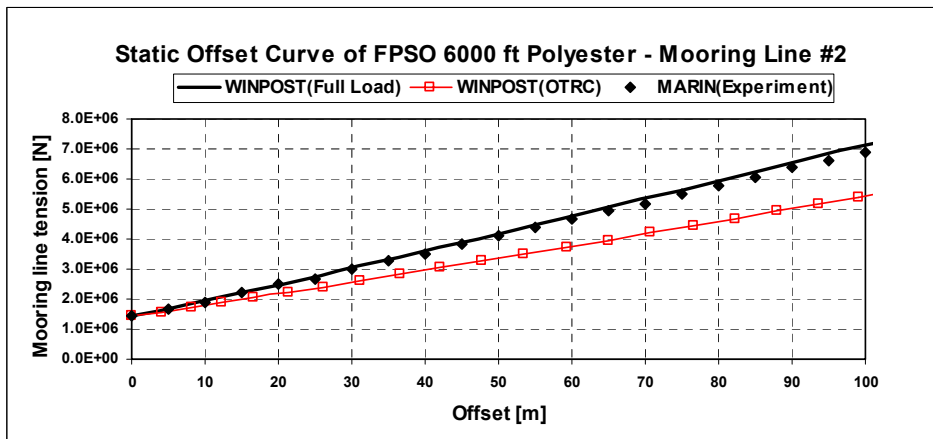
estimated model is well matched with that of the OTRC model. Only a small difference is shown in the initial point. It results from the fact that the OTRC experiment started with the initial setting of the experimental instruments after a standing position in the calm water at a certain moment was set as the static equilibrium state. But, it is hard to say that moment is the same instant as the time when the model reached static equilibrium position. The line tensions at #1 mooring line and #3 mooring line show a slight difference from the experiments. It can make the difference in surge motion.

6.5.2 Free Decay Test with Re-generated Model Data

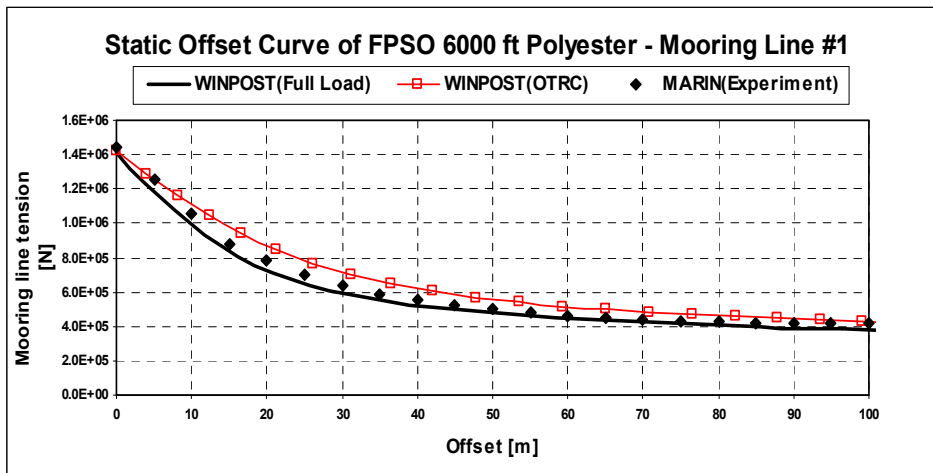
The proportional hull damping coefficients can be obtained from the free decay tests and the results are compared with the OTRC experiments. With the re-generated data, it is impossible and cannot be expected to get the same results once in the numerical calculation. Fortunately, very similar results were obtained. After small modification of the restoring coefficients, the compatible results for the natural periods are obtained as in Table 6.7. The reason to adjust the restoring coefficients for matching with the experimental is why the mooring line stiffness may contribute to the restoring forces of the system.



(a) Static offset curves for surge motion obtained by experiments and WINPOST-FPSO

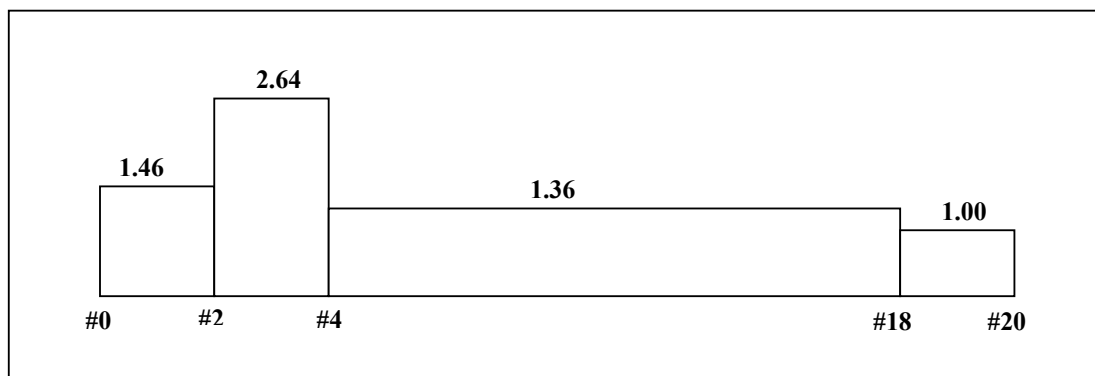


(b) Static offset test result of #2 mooring line in the surge direction

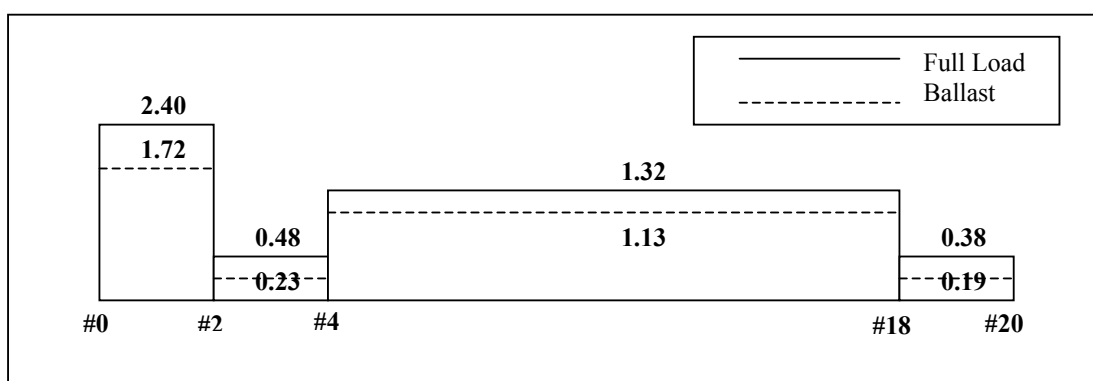


(c) Static offset test result of #1 mooring line in the surge direction

Figure 6.4 Comparison of the static offset test results



(a) Hull drag coefficients not in consideration of the current effect



(b) Hull drag coefficients in consideration of the current effect

Figure 6.5 Hull drag coefficients proposed by Wichers (1998 & 2001)**Table 6.7 Comparison of the free decay test results**

| | OTRC Experiment (4 equiv. Mooring lines) | | WINPOST | | | | | |
|-------------|--|------------|--------------------------------|------------|--------------------------------|------------|-------------------------------------|------------|
| | | | 12 mooring lines +13 risers | | 4 equiv. moorings + 1 riser | | 4 equiv. mooring lines w/o riser | |
| | period(sec) | damping(%) | period(sec) | damping(%) | period(sec) | damping(%) | period(sec) | damping(%) |
| surge (m) | 206.8 | 3.0 | 182.5 | 5.8 | 181.5 | 5.5 | 193.8 | 4.9 |
| heave (m) | 10.7 | 13.9 | 8.2 | 6.0 | 10.4 | 5.1 | 10.9 | 5.1 |
| roll (deg) | 12.7 | 4.4 | 13.4 | 0.9 | 12.7 | 1.1 | 12.6 | 0.8 |
| pitch (deg) | 10.5 | 16.5 | 13.9 | 6.0 | 10.8 | 8.5 | 10.9 | 8.5 |

6.5.3 Time Simulation Results

The comparison of the OTRC experiment and the WINPOST-FPSO analysis is shown in Table 6.8. In the table, the hull drag coefficients proposed by Wichers (1998, 2001) are used in this study as shown in Figure 6.5. The first column in the table is the case to use the hull drag coefficients without considering the current. In cases illustrated in the second and third column of the table, the hull drag coefficients considering the current in sway and/or surge direction are used. When the drag coefficients considering the current effect are used, the analysis results have the trend to follow the experiment in sway and roll. But, in surge and yaw motion, there are still rather big differences between the experiment and the numerical simulation results. The frontal wind area is 20 % larger, and the lateral area is 30 % larger than that of the full load case. The difference in the projected wind areas can result in the difference of statistically calculated values of motions. It can be caused by taking the mooring line truncation in the experiment due to the depth limitation of the OTRC basin and the difference of the mooring lines between the experimental model and the real vessel. Normally, the linear steel springs are used for the implementation of the steel wiring mooring lines in the experiments. As is well known, the spring has no static and dynamic mass. For the last test among four different cases, the frontal areas in surge and sway direction are used as the same as those in full load condition, and the drag coefficients in surge are multiplied by 2.5 for reviewing the drag force effect.

Table 6.8 Comparison of time simulation results

| | | OTRC Experiment | WINPOST (with 4-equiv. line model) | | | |
|-------------------------|------|--------------------|------------------------------------|--------------------------|--|---|
| | | | Old Sway Cd (1.5 hrs) | New Sway Cd (1.5 hrs) | New Sway Cd and Surge Cd (1.5 hrs) | New Sway and Surge Cd*2.5+old wind area (3 hrs) |
| Motion | | | | | | |
| surge (m) | mean | -22.92 | -25.22 | -20.26 | -19.39 | -20.89 |
| | min. | -61.26 | -83.10 | -83.33 | -78.64 | -88.72 |
| | max. | 2.29 | 21.31 | 22.67 | 18.94 | 24.49 |
| | rms. | 9.72 | 24.13 | 23.18 | 21.02 | 18.84 |
| sway (m) | mean | -0.09 | 4.76 | 2.99 | 2.90 | 3.66 |
| | min. | -21.43 | -8.17 | -8.21 | -7.15 | -12.14 |
| | max. | 13.08 | 22.96 | 21.67 | 21.18 | 31.75 |
| | rms. | 4.57 | 6.48 | 5.44 | 5.16 | 5.96 |
| heave (m) | mean | 0.14 | -0.39 | -0.38 | -0.38 | -0.38 |
| | min. | -11.31 | -5.05 | -3.91 | -4.11 | -5.58 |
| | max. | 10.91 | 4.28 | 3.28 | 3.26 | 5.15 |
| | rms. | 3.08 | 1.51 | 1.32 | 1.31 | 1.42 |
| roll (deg) | mean | -0.10 | -0.72 | -0.59 | -0.54 | -0.38 |
| | min. | -3.60 | -11.41 | -11.91 | -11.70 | -14.95 |
| | max. | 3.50 | 8.89 | 9.20 | 8.47 | 9.58 |
| | rms. | 0.90 | 3.52 | 3.73 | 3.27 | 3.68 |
| pitch (deg) | mean | 0.01 | -0.06 | -0.04 | -0.03 | -0.05 |
| | min. | -4.99 | -2.09 | -2.01 | -2.02 | -2.29 |
| | max. | 4.45 | 1.35 | 1.35 | 1.46 | 1.64 |
| | rms. | 1.31 | 0.59 | 0.53 | 0.53 | 0.56 |
| yaw (deg) | mean | -16.00 | -10.25 | -14.81 | -16.16 | -11.02 |
| | min. | -24.60 | -20.23 | -22.95 | -22.61 | -24.07 |
| | max. | -3.40 | -1.49 | -6.67 | -7.79 | 5.55 |
| | rms. | 3.80 | 4.18 | 3.11 | 2.84 | 5.48 |
| Mooring Tension | | | | | | |
| Mooring line #1 (kN) | mean | 5,907 | 6,403 | 6,487 | 6,440 | 7,757 |
| | min. | 3,679 | 1,230 | 1,218 | 1,566 | 2,447 |
| | max. | 10,360 | 14,600 | 14,893 | 14,173 | 16,783 |
| | rms. | 827 | 2,688 | 2,735 | 2,565 | 2,359 |
| Mooring line #2 (kN) | mean | | 2,400 | 2,379 | 2,333 | 3,457 |
| | min. | | 197 | 202 | 204 | 511 |
| | max. | | 7,883 | 7,853 | 7,537 | 9,537 |
| | rms. | | 2,046 | 2,036 | 1,931 | 1,506 |
| Mooring line #3 (kN) | mean | | 2,644 | 2,593 | 2,562 | 3,657 |
| | min. | | 630 | 530 | 782 | 1,163 |
| | max. | | 7,540 | 7,543 | 7,067 | 9,233 |
| | rms. | | 1,893 | 1,898 | 1,796 | 1,346 |
| Mooring line #4 (kN) | mean | 5,600 | 7,597 | 7,643 | 7,590 | 8,803 |
| | min. | 2,927 | 802 | 827 | 1,041 | 2,511 |
| | max. | 8,127 | 13,333 | 13,600 | 12,800 | 23,697 |
| | rms. | 801 | 2,020 | 2,047 | 1,870 | 3,560 |

In addition, it has no lateral stiffness, so it can react only in line. They can make the difference in the surge and the yaw motions. The difference in the line tension as

shown in the static offset tests in Table 6.3 (b) and (c) may be the reason for the discrepancy. The new sway hull drag coefficients are used as shown in Table 6.5. Furthermore, the surge drag force is newly considered ($C_d=1.0$). The analysis results are rather close to the experiments in viewpoint of overall trend. But, the yaw and surge motion still has a little large difference compared to the experiment.

For the consistency, Newman's approximation scheme is used for evaluating the wave forces applied to the single body model and also to the two-body model.

6.6 Summary and Conclusions

In this study, some efforts are exerted to re-generate the experimental results by the OTRC. To find the model parameters, the experimental static offset curve and the free decay test results are used. With the numerical model to be matched to the experimental model, some analyses are conducted with the WINPOST program. When the hull drag coefficients are applied in consideration of the current effect, the trends in sway and roll motion may well follow the experimental results, but those in surge and yaw motion show no good agreement. Some reasons for these differences can be imagined, such as the wind force generation, the current profile control, the mooring line truncation and the usage of springs for the steel wiring mooring lines. There are still many uncertainties for the reasons for the differences between the experiment and the numerical analysis results. For example, the investigation of the wind and current generated in the basin might give some clues.

CHAPTER VII

CASE STUDY 3:

CALCULATION OF HYDRODYNAMIC COEFFICIENTS FOR TWO BODY SYSTEM OF FPSO AND SHUTTLE TANKER

7.1 Introduction

In this study, the hydrodynamic coefficients for the two-body system are performed and compared with the experimental results of other institutes (KRISO, 2002). The multiple body system is composed of an LNG FPSO and a shuttle tanker. In many cases of the conventional tandem mooring of the FPSO and shuttle tanker, the hydrodynamic interaction between the two bodies has been ignored since the interaction is not considered large enough to be taken account of. It has resulted in conservative estimates for the behaviors of two bodies.

In this study, the interaction characteristics for the tandem and side-by-side moored vessels are investigated and compared with the experiments carried out for a two-body tanker model with different arrangements in regular waves. Motions and drift forces are mainly reviewed with the numerical calculations by the WAMIT (Wave Analysis program, developed by MIT using Boundary Element Method) program and experiments. This program has the module to solve the interaction problem based on the multiple body interaction theory. The changes of the distances between two vessels and the mooring types are used as parameters for investigation of the interaction characteristics.

There are several research works on this matter. Garrison (2000) developed the numerical tool for the time-domain analysis of the hydrodynamic loads and motions for a very large multi-body floating structure (VLFS) using the panel method based on the time-dependent Green's function. Inoue and Islam (2001) investigated the roll motion effect on wave drift force for the side-by-side moored vessels. Huijsmans, Pinkster and Wilde (2001) tried to obtain the numerical approach to solve the diffraction and the radiation potential problem for a very close multi-body system. For the same topic, Buchner, Dijk and Wilde (2001) developed the numerical time simulation solver to predict the hydrodynamic response of alongside moored vessels.

Here, as the conventional mooring pattern, the tandem mooring is taken into account since this type of mooring system has been used for the offloading operation in the way that the shuttle tanker is located behind FPSO. On the situation, the distances are kept between $\frac{1}{4}$ to $\frac{1}{3}$ of the ship's length. As another mooring system, side-by-side mooring is being considered since the offloading operations are sometimes preferred under the parallel position in relatively calm seas. In such a case, the distance between the two is very close, and so the hydrodynamic interaction and mooring design are very important. For the test models, an LNG FPSO and a shuttle tanker are taken. For two types of moorings and two different distances between the LNG FPSO and the shuttle tanker, parametric studies of the interaction effects on the drift forces and vessel behaviors are being performed in this study.

7.2 Particulars of Models and Arrangements for the Tests

Both models are tanker type vessels, of which the FPSO is fully loaded and the other is ballast loaded. The main particulars, including the principle data of the vessels, are listed in Table 7.1. The arrangements of tandem and side-by-side mooring are shown in Figure 7.1. The distances between the two vessels in tandem mooring are taken as 30 m and 50 m. On the other hand, the distances for side-by-side mooring are determined as 4 m and 10 m. Steel springs for the mooring systems are used, and the stiffness of the springs is set to 320 kN/m . The mooring lines modeled as springs are posted at the posts located at the end of the mooring lines. For the calculation of the hydrodynamic coefficients, the springs are not considered since the stiffness of the spring is too small and so their hydrodynamic effects can be negligible. For the validity of the numerical modeling for the two vessels, the natural frequencies are compared with each other. According to the experiment by KRISO (2002), the roll natural period of the LNG FPSO is 15.7 sec, and that of the shuttle tanker 9.97 sec. The free decay tests are conducted with the numerical models, and according to the test results, the roll natural period of 15.8 for LNG FPSO, and of 10.1 sec for shuttle tanker. Table 7.2 shows the free decay test results. The test reveals that the numerical model is good enough to use for the numerical calculation. In Figure 7.2, the numerical models are shown. In Figure 7.3, the fine-meshed numerical models are shown, which is made for a sensitivity study. It has 4 times number of elements of the rough-meshed model. Consequently, it was proved that the model size, i.e., the number of elements was not very sensitive to the results. In

Table 7.3, the comparison of the hydrodynamic coefficients obtained from the rough model and the fine model is shown.

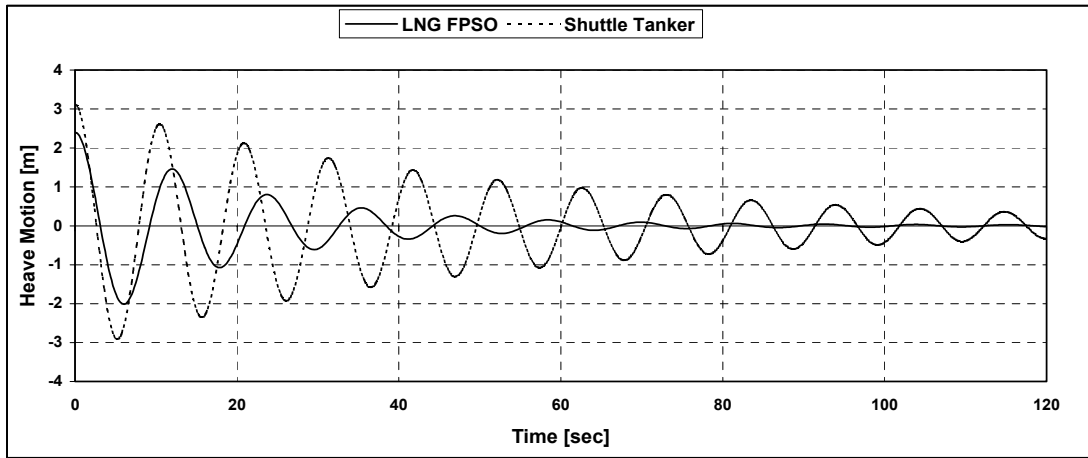
Table 7.1 Main particulars of two vessels

| Description | Symbol | Unit | LNG FPSO | Shuttle Tanker |
|--------------------------------|-----------|-------|----------|----------------|
| Length b/w perpendiculars | L_{pp} | m | 239 | 223 |
| Bredth | B | m | 45.82 | 42 |
| Draft at FP | T_{FP} | m | 15.82 | 6.8 |
| Draft at midship | T_{MID} | m | 15.82 | 7.65 |
| Draft at AP | T_{AP} | m | 15.82 | 8.5 |
| Displacement | ∇ | m^3 | 139,585 | 53,743.20 |
| Longitudinal center of gravity | LCG | m | 9.636 | 8.152 |
| Vertical center of gravity | KG | m | 14.54 | 9.577 |
| Metacentric height | GM | m | 6.028 | 12.888 |
| Radius of roll gyration | K_{xx} | m | 16.04 | 14.7 |
| Radius of pitch gyration | K_{yy} | m | 59.75 | 55.75 |
| Radius of yaw gyration | K_{zz} | m | 59.75 | 55.75 |

Table 7.2 Free-decay test results for a LNG FPSO and a shuttle tanker (heave and roll)

| LNG FPSO | | | | | |
|----------------|--------------|-------------|-------------|--------------|------------|
| Time(s) | Period(s) | Heave(m) | ln(x1/x2) | Damp. Ratio | 1st 3 Ave. |
| 0.0 | 0.0 | 2.399 | | | |
| 12.0 | 12.0 | 1.459 | 0.50 | 7.91% | |
| 23.6 | 11.6 | 0.801 | 0.60 | 9.54% | |
| 35.4 | 11.8 | 0.46 | 0.55 | 8.83% | 8.76% |
| 47.0 | 11.6 | 0.258 | 0.58 | 9.20% | |
| 58.4 | 11.4 | 0.152 | 0.53 | 8.42% | |
| 69.8 | 11.4 | 0.092 | 0.50 | 7.99% | |
| 81.2 | 11.4 | 0.06 | 0.43 | 6.80% | |
| 92.4 | 11.2 | 0.042 | 0.36 | 5.68% | |
| Average | 11.55 | 0.42 | 0.51 | 8.07% | |

| SHUTTLE TANKER | | | | | |
|----------------|--------------|-------------|-------------|--------------|------------|
| Time(s) | Period(s) | Heave(m) | ln(x1/x2) | Damp. Ratio | 1st 3 Ave. |
| 0.0 | 0.0 | 3.118 | | | |
| 10.4 | 10.4 | 2.608 | 0.18 | 2.84% | |
| 20.8 | 10.4 | 2.122 | 0.21 | 3.28% | |
| 31.2 | 10.4 | 1.739 | 0.20 | 3.17% | 3.10% |
| 41.8 | 10.6 | 1.434 | 0.19 | 3.07% | |
| 52.2 | 10.4 | 1.183 | 0.19 | 3.06% | |
| 62.6 | 10.4 | 0.976 | 0.19 | 3.06% | |
| 73.0 | 10.4 | 0.802 | 0.20 | 3.13% | |
| 83.4 | 10.4 | 0.657 | 0.20 | 3.17% | |
| Average | 10.43 | 1.44 | 0.19 | 3.13% | |



| LNG FPSO | | | | | |
|----------------|-------------|-------------|-------------|--------------|------------|
| Time(s) | Period(s) | Roll(deg) | ln(x1/x2) | Damp. Ratio | 1st 3 Ave. |
| 0.0 | 0.0 | 1.808 | | | |
| 15.8 | 15.8 | 1.792 | 0.01 | 0.14% | |
| 31.6 | 15.8 | 1.777 | 0.01 | 0.13% | |
| 47.4 | 15.8 | 1.762 | 0.01 | 0.13% | 0.14% |
| 63.2 | 15.8 | 1.747 | 0.01 | 0.14% | |
| 79.0 | 15.8 | 1.732 | 0.01 | 0.14% | |
| 94.8 | 15.8 | 1.717 | 0.01 | 0.14% | |
| 110.6 | 15.8 | 1.703 | 0.01 | 0.13% | |
| 126.6 | 16.0 | 1.689 | 0.01 | 0.13% | |
| Average | 15.8 | 1.74 | 0.01 | 0.13% | |

| SHUTTLE TANKER | | | | | |
|----------------|-------------|-------------|-------------|--------------|------------|
| Time(s) | Period(s) | Roll(deg) | ln(x1/x2) | Damp. Ratio | 1st 3 Ave. |
| 0.0 | 0.0 | 1.808 | | | |
| 10.0 | 10.0 | 1.798 | 0.01 | 0.09% | |
| 20.0 | 10.0 | 1.786 | 0.01 | 0.11% | |
| 30.2 | 10.2 | 1.784 | 0.00 | 0.02% | 0.07% |
| 40.2 | 10.0 | 1.779 | 0.00 | 0.04% | |
| 50.2 | 10.0 | 1.765 | 0.01 | 0.13% | |
| 60.2 | 10.0 | 1.756 | 0.01 | 0.08% | |
| 70.4 | 10.2 | 1.75 | 0.00 | 0.05% | |
| 80.4 | 10.0 | 1.738 | 0.01 | 0.11% | |
| Average | 10.1 | 1.77 | 0.00 | 0.08% | |

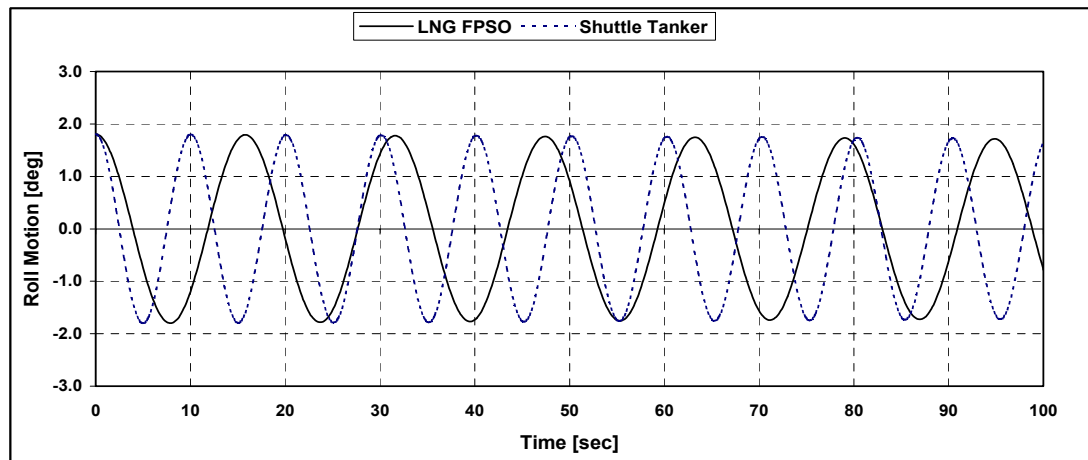


Table 7.3 Comparison of the hydrodynamic coefficients obtained from the rough model and the fine models

| Hydrodynamic coefficients | Symbol | LNG FPSO | | Shuttle tanker | |
|--|-----------|--------------|----------------|----------------|----------------|
| | | Simple model | Extended model | Simple model | Extended model |
| Added mass | Ma_{11} | 2.9242E+06 | 2.9253E+06 | 7.0029E+05 | 7.1139E+05 |
| | Ma_{22} | 3.7754E+07 | 3.7570E+07 | 9.1748E+06 | 9.1447E+06 |
| | Ma_{33} | 1.2637E+08 | 1.2623E+08 | 9.4537E+07 | 9.4468E+07 |
| | Ma_{44} | 1.2937E+09 | 1.2794E+09 | 4.3208E+06 | 4.3145E+06 |
| | Ma_{55} | 1.2265E+11 | 1.2282E+11 | 2.8218E+08 | 2.8210E+08 |
| | Ma_{66} | 5.2205E+10 | 5.2050E+10 | 4.4606E+07 | 4.4853E+07 |
| Max. difference in added masses | | 1.0% | | 1.6% | |
| Radiation damping | Fd_{11} | 1.8793E+02 | 1.8811E+02 | 2.7447E+01 | 2.7347E+01 |
| | Fd_{22} | 5.1766E+02 | 5.1563E+02 | 4.2727E+01 | 4.2678E+01 |
| | Fd_{33} | 1.4782E+06 | 1.4776E+06 | 8.9999E+05 | 8.9963E+05 |
| | Fd_{44} | 1.0976E+03 | 1.1462E+03 | 1.4176E+01 | 1.4379E+01 |
| | Fd_{55} | 8.9999E+06 | 9.0734E+06 | 1.3147E+05 | 1.3179E+05 |
| | Fd_{66} | 1.9093E+04 | 1.8971E+04 | 2.8058E+00 | 2.6910E+00 |
| Max. difference in radiation dampings | | 4.2% | | 4.3% | |

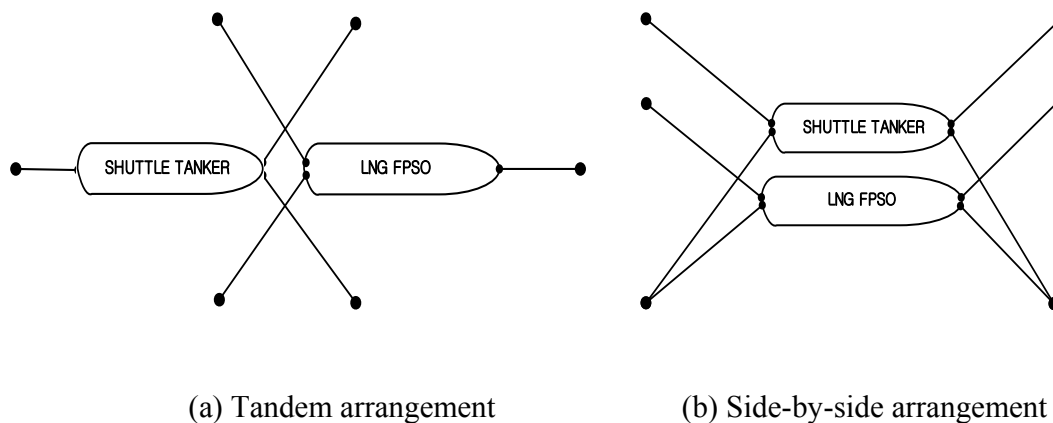
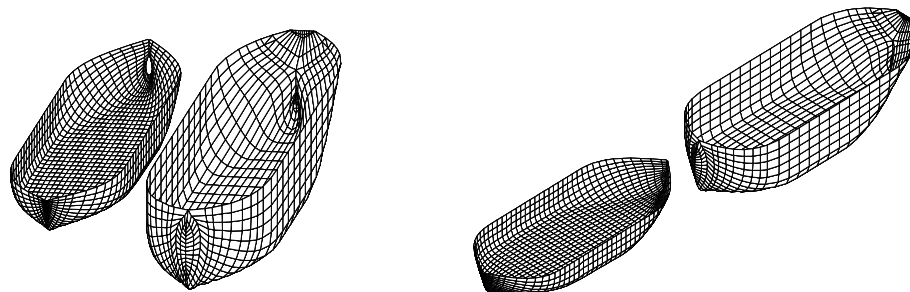


Figure 7.1 Configuration of the mooring system



(a) the side-by-side mooring arrangement

(b) the tandem mooring arrangement

Figure 7.2 Rough-meshed numerical modeling for a LNG FPSO and a shuttle tanker



(a) the side-by-side mooring

(b) the tandem mooring

Figure 7.3 Fine-meshed numerical modeling for a LNG FPSO and a shuttle tanker

7.3 Environmental Conditions

Regular waves are taken for the calculation of the beam sea and head sea conditions. Only head sea conditions are considered for the tandem moored case. On the contrary, for the side-by-side moored vessels, both beam sea and head sea conditions are

considered. The range of the wave frequencies is from 0.4 rad/s to 1.2 rad/s with 50 intermediate intervals.

7.4 Results and Discussion

The analysis results and the experiments can now be compared. The distances for the side-by-side mooring are taken as 4 and 10 meter as the parameters, and on the contrary, those for the tandem mooring are selected as 30 m and 50 m. Motion RAOs as varying the distance apart from each other for the side-by-side mooring are compared as shown in Figures 7.4 to 7.5 for heave and roll motions in beam sea state. For the different mooring systems, the longitudinal drift forces are compared as shown in Figures 7.6 and 7.7 for the head sea condition.

The distance effect on the longitudinal drift force is shown in Figure 7.8 for the head sea condition.

The drift forces in the lateral direction for the side-by-side moored vessels are shown in Figures 7.9 and 7.10 in different heading condition. For more clear comparison, the calculated RAOs and drift forces for a single body of the FPSO and a single body of the shuttle tanker in the same condition are depicted in the above figures. The whole trends show good agreement to the experiments.

The shielding effects on heave and roll motion RAO are well investigated in the lee side vessel of the side-by-side mooring vessels as shown in Figures 7.4 and 7.5. They are very clear over the whole frequency range. As is well known, the effects are large enough to pay attention to the matter for solving the interaction problem more accurately.

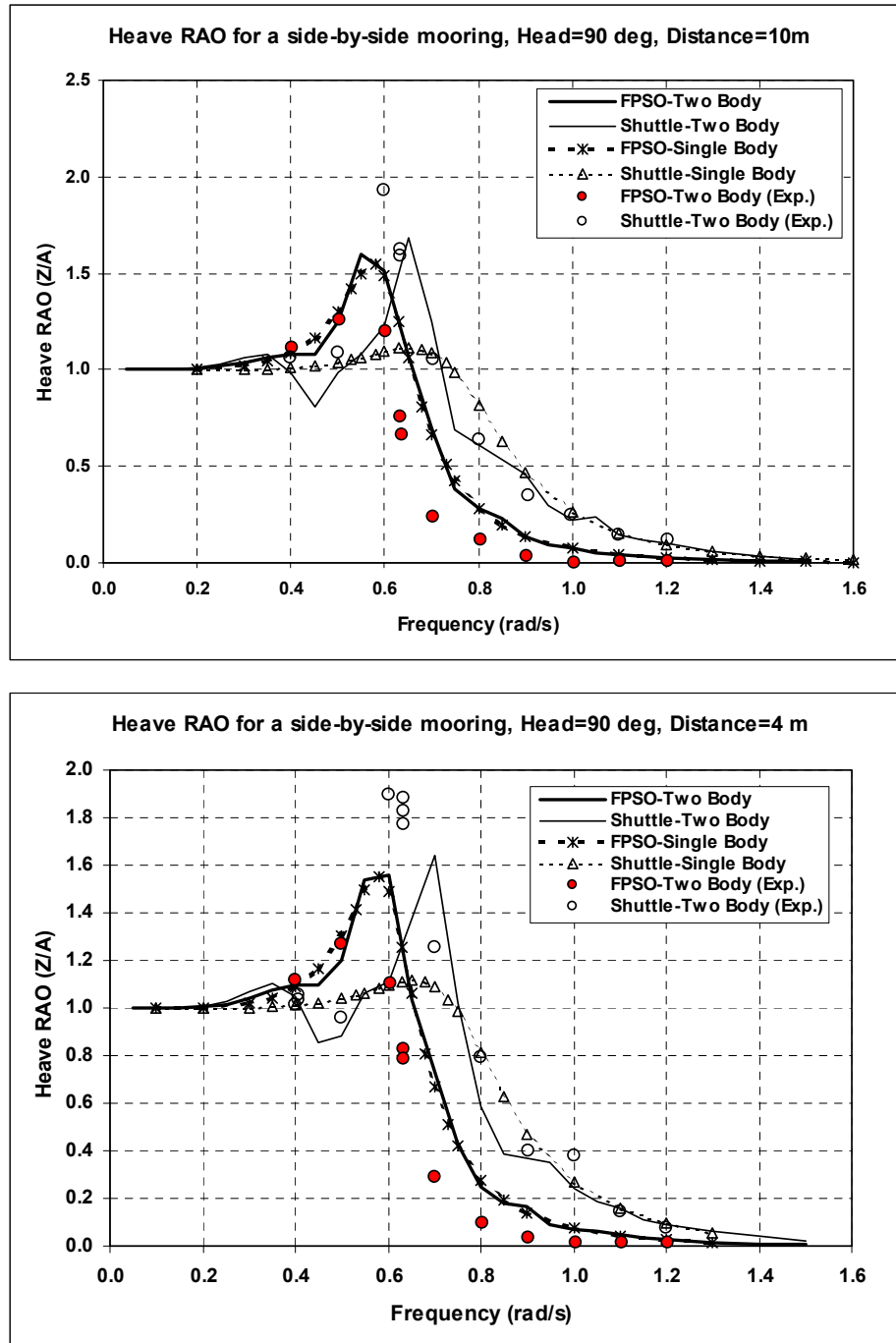


Figure 7.4 Heave response operators of side-by-side moored vessels in the beam Sea

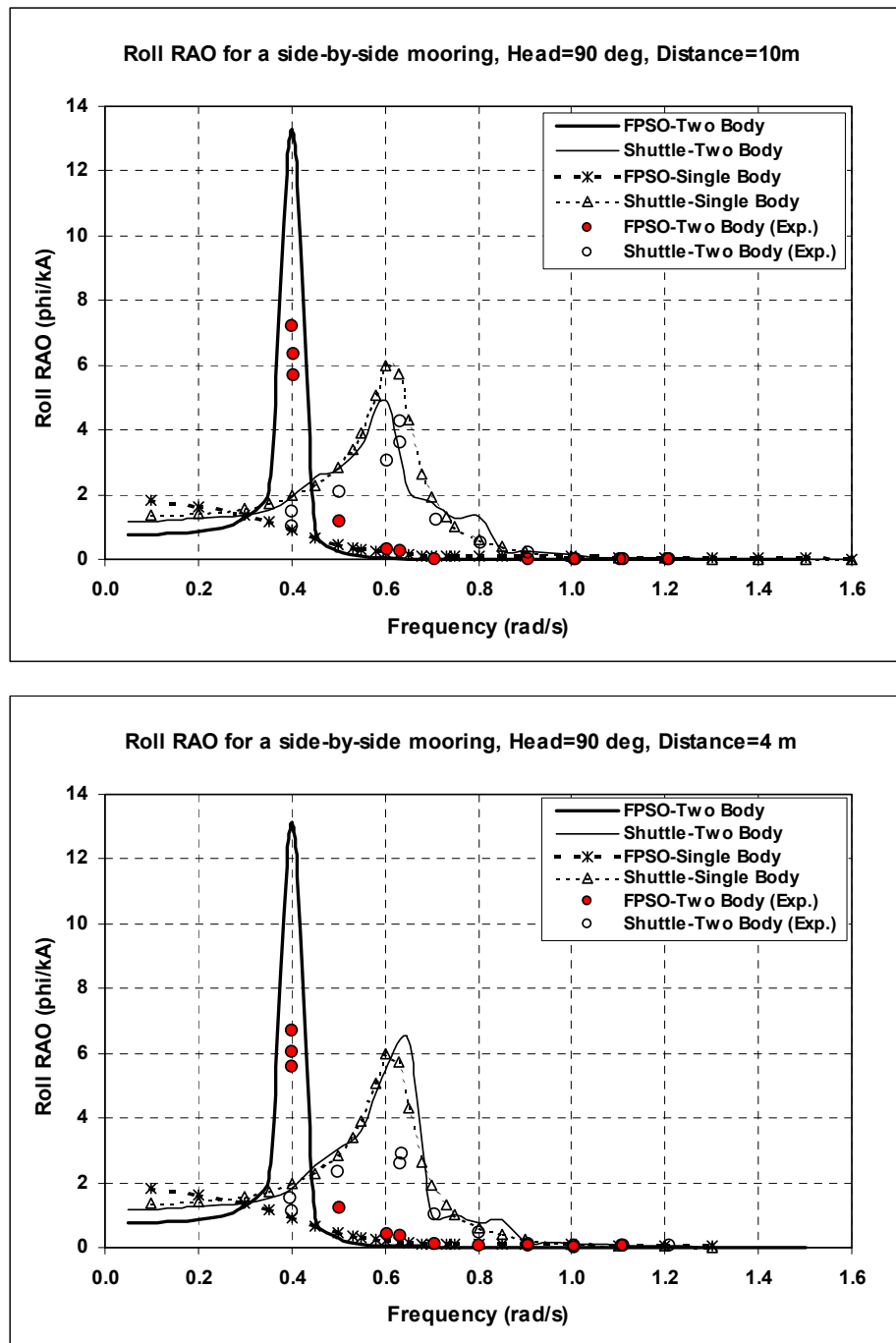


Figure 7.5 Roll response operators of side-by-side moored vessels in the beam sea

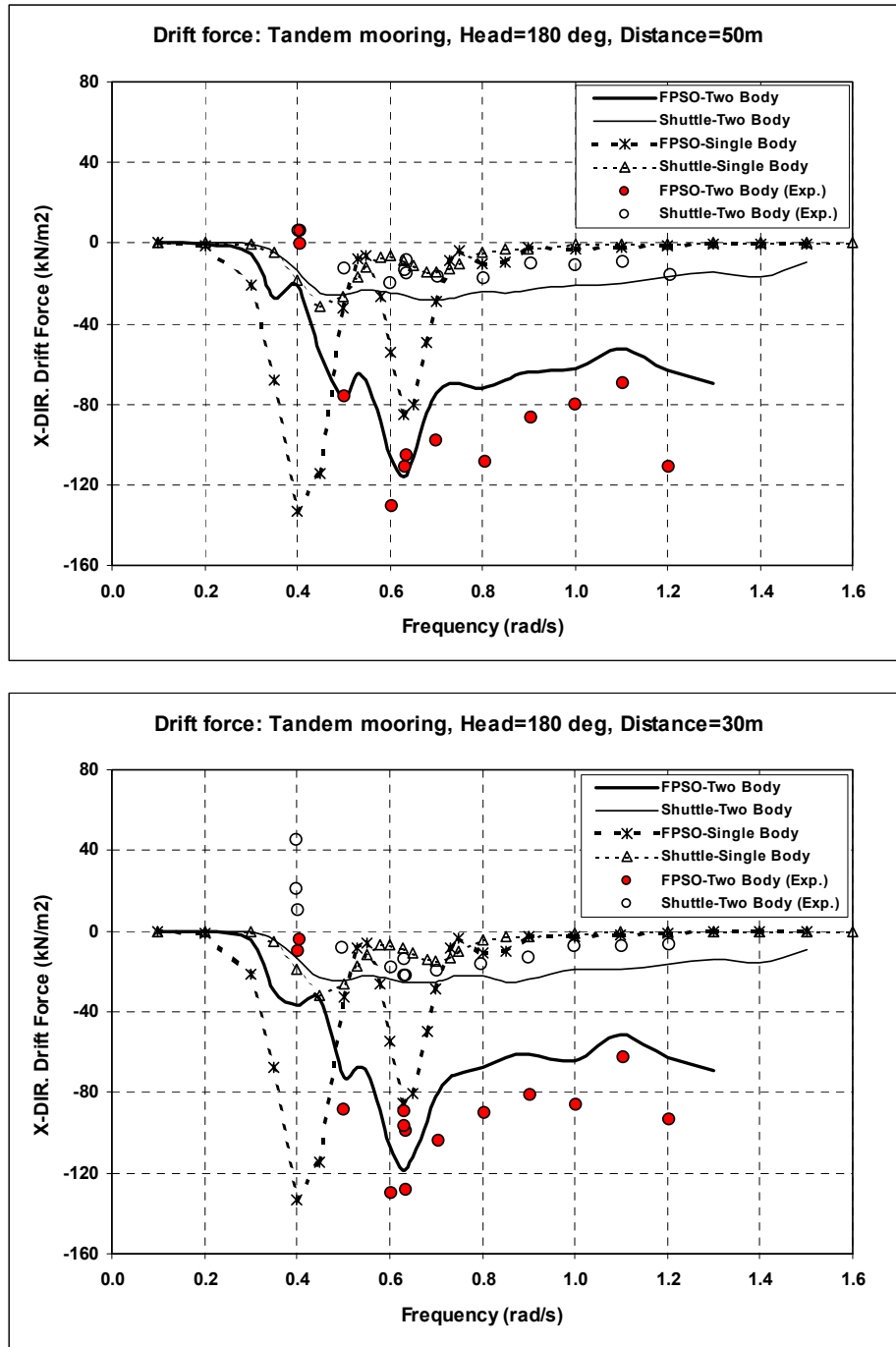


Figure 7.6 Longitudinal wave drift force of tandem moored vessels in the head sea

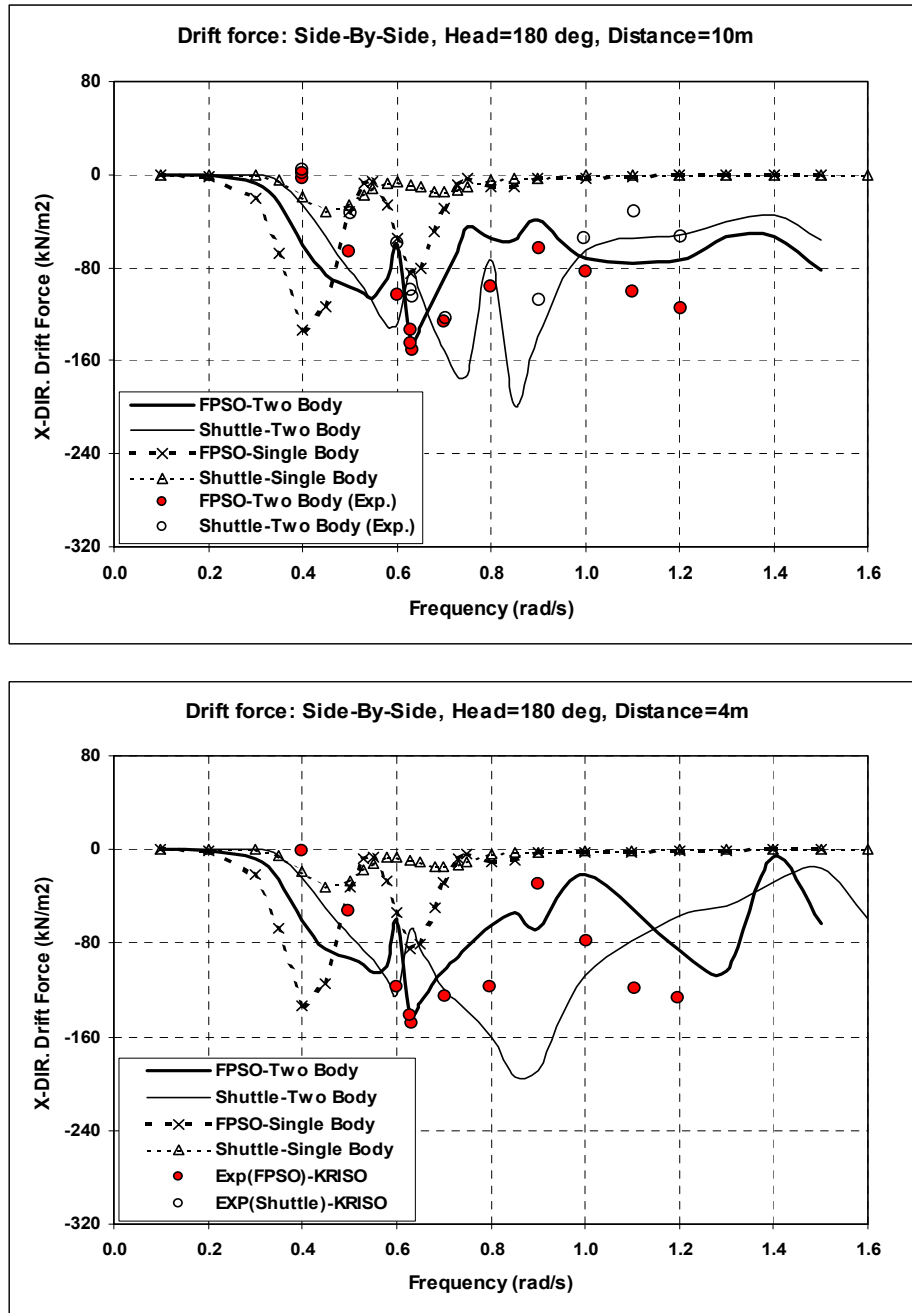


Figure 7.7 Longitudinal wave drift force of side-by-side moored vessels in the head sea

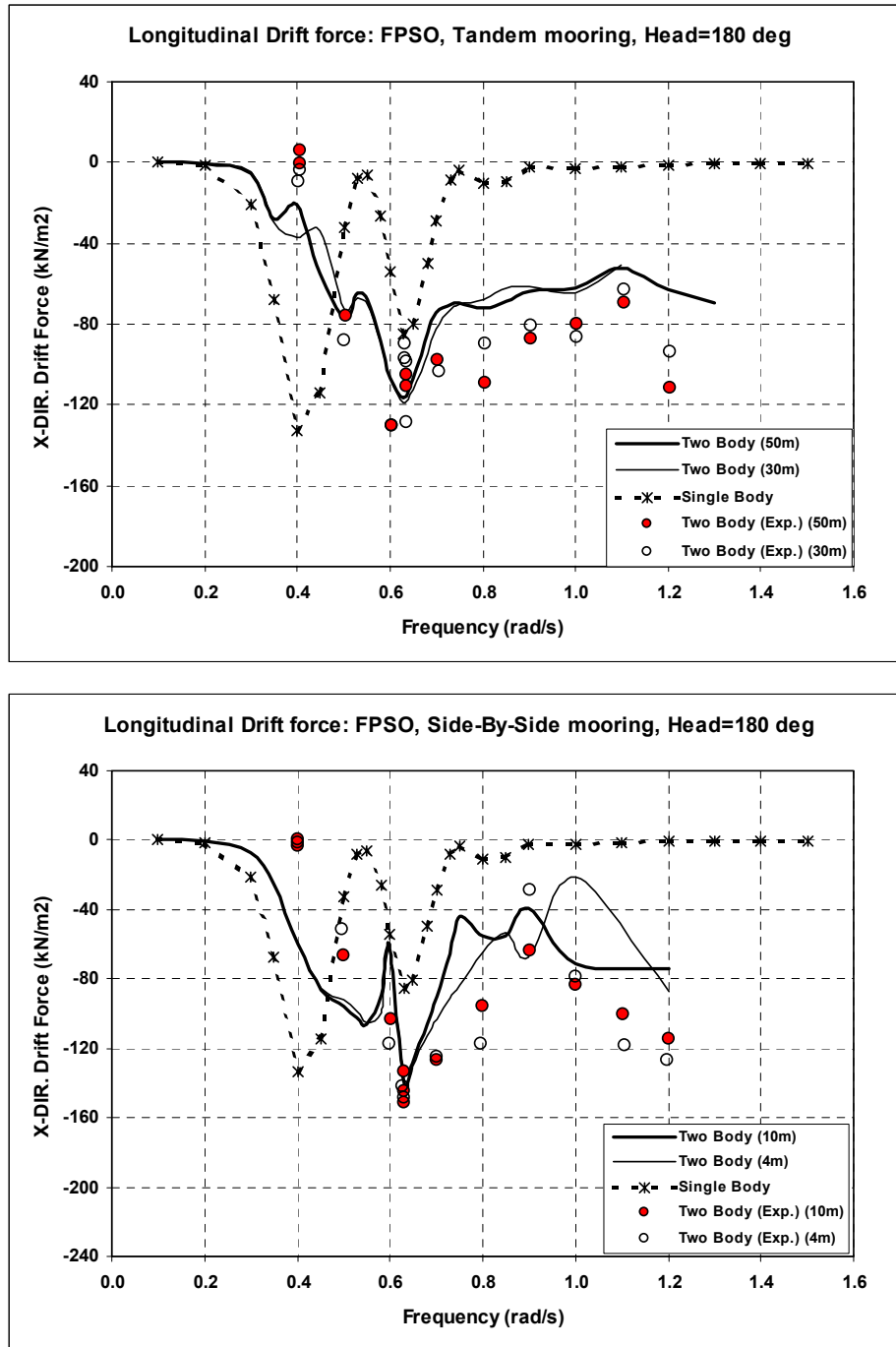


Figure 7.8 The distance effect on the longitudinal wave drift force for a two-body and a single body model in the head sea

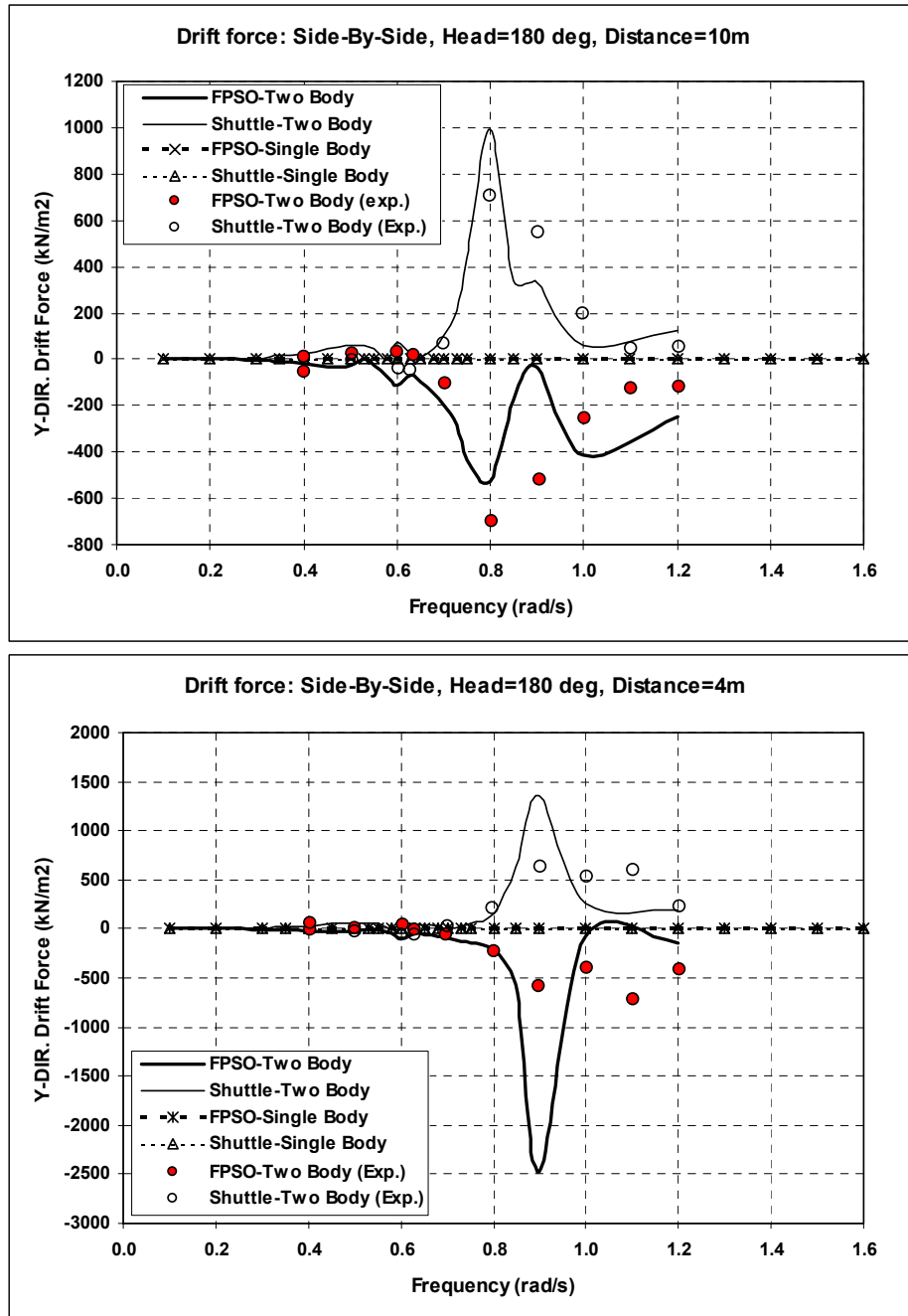


Figure 7.9 Lateral wave drift force of side-by-side moored vessels in the head sea

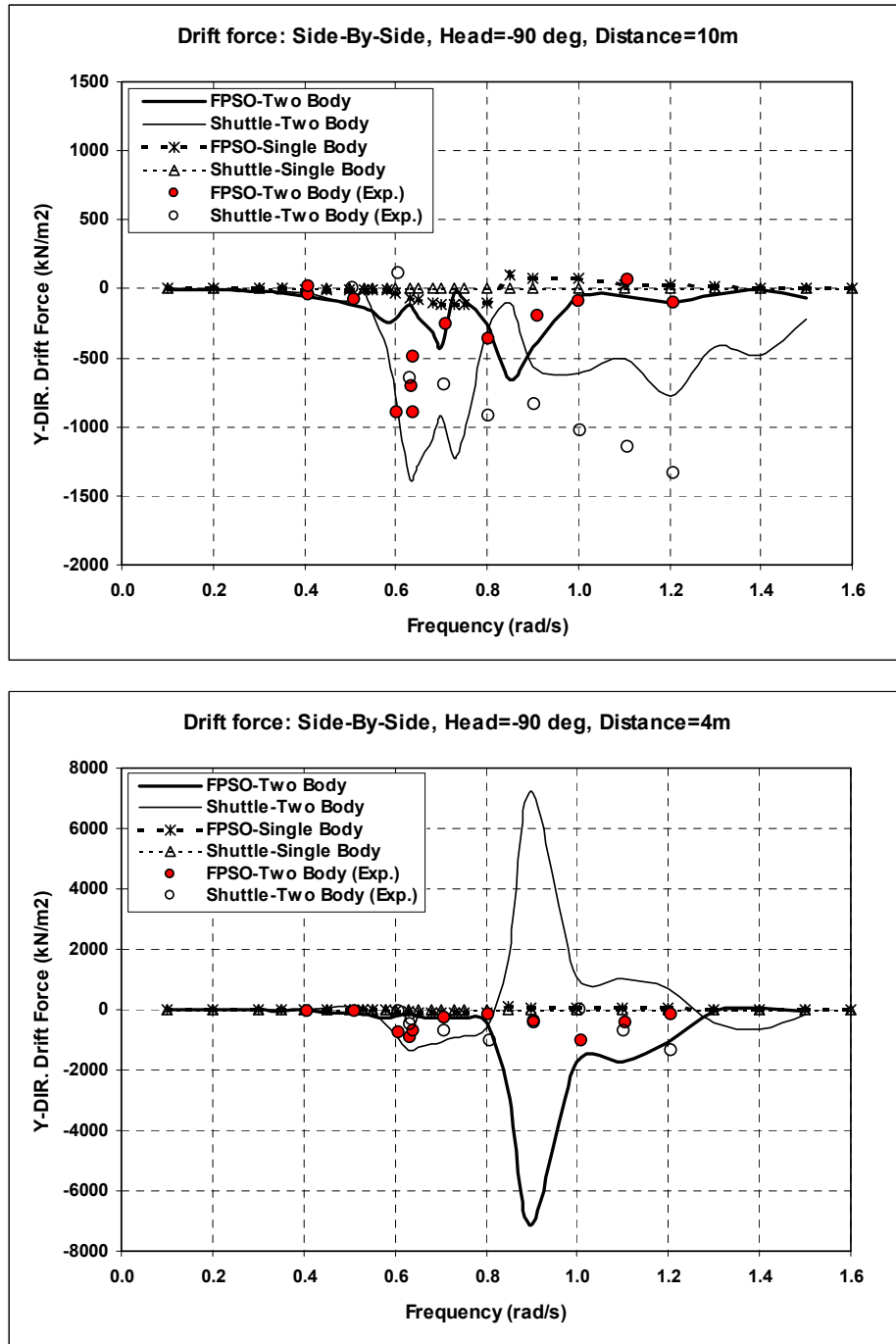


Figure 7.10 Lateral wave drift force of side-by-side moored vessels in the beam sea

As shown in Figures 7.6 and 7.7, the shielding effects on the longitudinal drift forces for the head sea conditions are investigated, and are also remarkable in the tandem moored vessel, but are not clear in the side-by-side moored vessels. The distance effect on the drift force is not significant. The lateral drift force of side-by-side moored vessels in head sea and in beam sea are quite different. As the distance gets closer, the blockage effect on the lateral drift force increases. It causes the force to be magnified as the lee side vessel approaches the weather side vessel, as shown in Figure 7.9 and 7.10.

7.5 Summary and Conclusions

The hydrodynamic interaction effects for the multi-body system are investigated by a comparative study for the numerical calculations and experiments. The LNG FPSO and a shuttle tanker are taken as the multi-body system, and the side-by-side and tandem mooring are considered. The distance effects on the motions and drift forces of the two vessels are also reviewed.

In tandem mooring, the shielding effect is noticeable on the drift force. The distance has no great effect on the longitudinal force. In side-by-side mooring, the shielding effect of the lee side vessel is significant on the drift force and motion RAO. In lateral, the lee side ship acts as a block to disturb the flow pattern of the wave. Furthermore, when the distance between both vessels gets closer, the magnitude of the lateral drift seems to be reciprocally amplified against the distance. With comparing the experiment, the WAMIT gives the fairly reasonable results, so that the conclusion is drawn that the program can be applied to that kind of interaction problem.

CHAPTER VIII

CASE STUDY 4:

DYNAMIC COUPLED ANALYSIS FOR A TWO-BODY SYSTEM COMPOSED OF SPAR AND SPAR

8.1 Introduction

In this study, the dynamic coupled analysis for two-body structures is performed to verify the program (WINPOST-MULT) for the dynamic coupled analysis of the multiple-body floating platforms and the results are compared with the analysis results using the idealized model of a two-mass-spring model. The multiple body system is composed of two identical spars. The conventional tandem moorings have been taken for the multiple-body connection in many cases. For the multiple-body model of spar structures, the side-by-side mooring and the tandem mooring have no difference, since the structure is symmetric about the x- and y-axis. The simplified mass-spring model will give a compatible result to judge the validity of the multiple-body program.

In this study, the body motions and line tensions are mainly reviewed with the numerical calculations performed by WINPOST-MULT, the dynamic coupled analysis program for multiple-body platforms. The hydrodynamic coefficients in consideration of the multiple-body interaction are calculated by the WAMIT. The two-body interaction problem of the fluid was studied in the previous chapter. The WAMIT program has the module to solve the fluid interaction problem based on multiple body interaction theory, as explained before. The analysis results by the program are compared with the analysis

results of the two-body spar model connected by a hawser with and without the hydrodynamic interaction effect, and also compared with the results by the linear spring model replaced for the hawser. Especially, for the linear spring modeling, the program is modified slightly. From this study, the effect of the hawser to connect the two structures can also be clarified. For this verification, the models with a hawser and without a hawser are made and analyzed.

For the mooring system, the tandem mooring is taken into account since this type of mooring system has been used for many years for offloading operations to transfer the oil from one platform to other structures. The distance is kept as close as possible. Thus, the distance is determined to be 30 meter to allow the maximum surge or sway motion, since the expected maximum surge motion is about 30 meters and the maximum sway motion about 10 meters. It can be said that the side-by-side mooring should be identical to the tandem mooring due to the symmetry of the structure.

8.2 Particulars of Models and Arrangements for the Analyses

The main particulars including the principle data of spar are listed in Table 8.1. The arrangement of the tandem is shown in Figure 8.1. The distance between the two spars in tandem mooring is taken as 30 m. The mooring lines are fixed at the sea floor. For the calculation of the hydrodynamic coefficients, the WAMIT program is. For the validity of the numerical modeling, Static offset test and free decay tests are performed and compared with the target values, which are given from experiments conducted by other institute.

Table 8.1 Main particulars of moored spar

| Description | Symbol | Unit | Quantity |
|---|------------------|---------------|---------------|
| Water depth | | <i>m</i> | 914.4 |
| Production level of oil | | <i>bpd</i> | 55,000 |
| Production level of gas | | <i>mmscfd</i> | 72 |
| Length | | <i>m</i> | 214.88 |
| Draft | T | <i>m</i> | 198.12 |
| Hard tank depth | H | <i>m</i> | 67.06 |
| Well bay dimension (25 slots) | | <i>m</i> | 17.68 x 17.68 |
| Center of buoyancy center above base line | KB | <i>m</i> | 164.59 |
| Center of gravity above base line | KG ⁻ | <i>m</i> | 129.84 |
| KG (based on total displacement) | KG | <i>m</i> | 95.71 |
| Displacement | ∇^- | <i>mT</i> | 53,600 |
| Total displacement | ∇ | <i>mT</i> | 220,740 |
| Pitch radius of gyration in air | R_{xx} | <i>m</i> | 67.36 |
| Yaw radius of gyration in air | $R_{\zeta\zeta}$ | <i>m</i> | 8.69 |
| Drag force coefficient | Cd | | 1.15 |
| Wind force coefficient | Cw | $N/(m/s)^2$ | 2671.6 |
| Center of pressure above base line | | <i>m</i> | 220.07 |

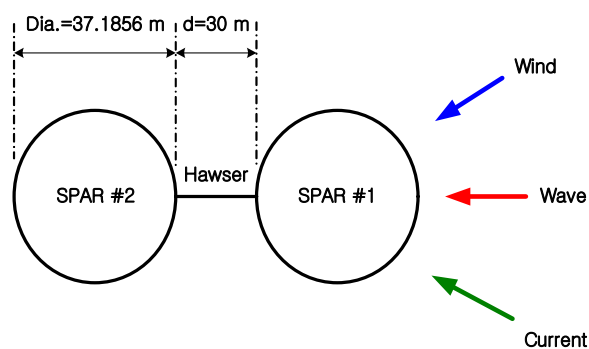


Figure 8.1 Configuration of the mooring system and the environmental loads (Tandem arrangement, $d=30m$)

In Figures 8.2 and 8.3, the numerical models are shown. In Table 8.2, the particulars of the mooring systems are tabulated.

Table 8.2 Particulars of the mooring systems

| Description | Unit | Quantity |
|---|-------------|----------|
| Pretension | <i>kN</i> | 2,357 |
| Number of lines | | 14 |
| Scope ratio | | 1.41 |
| Length of mooring line | <i>m</i> | 1,402.08 |
| Firlead location above base line | <i>m</i> | 91.44 |
| Segment 1 (ground position): chain | | |
| Length at anchor point | <i>m</i> | 121.92 |
| Diameter | <i>mm</i> | 24.5 |
| Weight in air | <i>kg/m</i> | 287.8 |
| Weight in water | <i>kg/m</i> | 250.3 |
| Stiffness, AE | <i>kN</i> | 1.03E+06 |
| Minimum breaking load, MBL | <i>kN</i> | 1.18E+04 |
| Added mass | <i>kg/m</i> | 37.4 |
| Current force coefficient | | 2.45 |
| Segment 2: wire | | |
| Length | <i>m</i> | 2347.44 |
| Diameter | <i>mm</i> | 21.0 |
| Weight in air | <i>kg/m</i> | 36.52 |
| Weight in water | <i>kg/m</i> | 7.77 |
| Stiffness, AE | <i>kN</i> | 3.18E+05 |
| Mean breaking load, MBL | <i>kN</i> | 1.28E+04 |
| Added mass | <i>kg/m</i> | 28.8 |
| Current force coefficient | | 1.20 |
| Segment 3 (hang-off position): chain | | |
| Length | <i>m</i> | 91.44 |
| <i>Other parameters are the same as those of segment 1.</i> | | |

8.3 Environmental Conditions

The environmental conditions to be used in this analysis correspond to the 100-year storm conditions in Gulf of Mexico. The wind velocity is 41.12 m/s at 10 m of reference height for 1 minute sustained. For wind force calculation, API RP2T is used. For wave, irregular waves are taken for the calculation of the head sea condition. The range of the wave frequencies is from 0.5 rad/s to 1.2 rad/s with 50 intermediate intervals. The wave spectrum used here is the JONSWAP spectrum, as shown in Figure 8.3, which has the significant wave height of 12.192 meters, the peak period of 14 seconds, and the overshooting parameter of 2.5. The current velocity is 1.0668 m/s at the free surface, and it is kept 60.96 m under the water surface. After that, it varies from 1.0668 m/s to 0.0914 m/s from 60.96 m to 91.44 m under the water surface. Under the water depth of 91.44 m, the current speed becomes uniform as 0.0914 m/s. In Table 8.3, the environmental conditions are summarized.

Table 8.3 Environmental conditions

| Description | Unit | Quantity |
|-----------------------------|--|-------------------|
| Wave | | |
| Significant wave height, Hs | <i>m</i> | 12.19 |
| Peak period, Tp | <i>sec</i> | 14 |
| Wave spectrum | <i>JONSWAP ($\gamma=2.5$)</i> | |
| Direction | <i>deg</i> | 180 ¹⁾ |
| Wind | | |
| Velocity | <i>m/s</i> | 41.12 m/s @ 10m |
| Spectrum | <i>API RP 2A-WSD</i> | |
| Direction | <i>deg</i> | 210 ¹⁾ |
| Current | | |
| Profile | | |
| at free surface (0 m) | <i>m/s</i> | 1.0668 |
| at 60.96 m | <i>m/s</i> | 1.0668 |
| at 91.44 m | <i>m/s</i> | 0.0914 |
| on the sea bottom | <i>m/s</i> | 0.0914 |
| Direction | <i>deg</i> | 150 ¹⁾ |

Remarks: 1) The angle is measured from x-axis (the East) in the counterclockwise.

8.4 Calculation of Hydrodynamic Coefficients Using WAMIT 1st and 2nd Order

In Figures 8.2 and 8.3, the numerical models are shown. The hydrodynamic coefficients are calculated by WAMIT. For the single body analysis, the 2nd order wave force coefficients are calculated with free surface modeling. For the two-body analysis, the 1st order wave force coefficients and wave drift force coefficients are calculated. The hydrodynamic coefficients of added mass, wave damping, linear transfer function (LTF) of diffraction potential force and the sum- and difference-frequency quadratic transfer function (QTF) of diffraction potential force are calculated by the WAMIT 1st order module and the 2nd order module. In Figure 8.2, the model for the 2nd order wave force coefficients is shown. The body has 1024 elements, and the free surface has 576 panel elements. In Figure 8.3, the two-body model for the 1st order wave force coefficients is shown. Here, for the purpose of comparison, the 1st order model is used for the single body analysis and also for the two-body analysis, so that for both analyses Newman's Approximation Method is adopted for conforming the full QFT when the wave force coefficients are considered. The hawser connecting each spars to the other is taken to have 1/100 of the mooring stiffness and 1/10 of the mooring pre-tension.

The hydrodynamic interaction effect is calculated with the 1st order model. All coupling terms are considered for the two-body analysis. The program WINPOST-MULT can treat the numerical calculation with the fully coupled system matrices composed by multiple bodies. The added mass, the linear wave damping, the system stiffness and the resorting coefficient matrix are fully coupled with each other due to the interaction effects of both structures. Especially, if the hawser or the fluid transfer lines

are connected, they will cause to make the stiffness matrix coupled so that the whole system stiffness matrix composed by the body and line stiffness and restoring coefficients comes to a huge sparse matrix.

As mentioned above, the analysis of the two-body system is performed using the 1st order model with and without interaction effects. In the case of no interaction effects, the coupling terms of the hydrodynamic coefficients are set as zero.

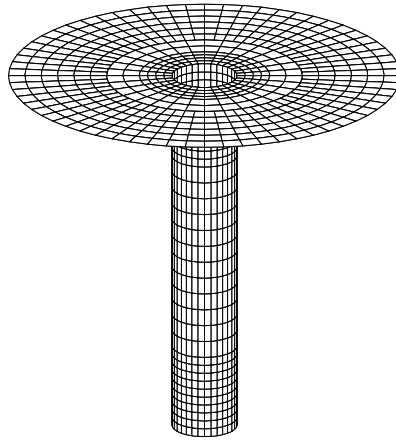


Figure 8.2 Configuration of the modeling of a single spar

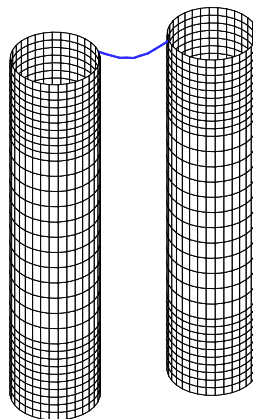


Figure 8.3 Configuration of the modeling of a two-body spar

8.5 Linear Spring Modeling

The hawser for connecting the two spars can be replaced by a linear spring. For verifying the numerical analysis results by the full numerical model, a linear spring for the hawser is considered by putting the linear spring constant as a restoring coefficient in surge direction into the body system matrix of the restoring force coefficients inside the program. Furthermore, the WINPOST-MULT program is modified slightly since the replaced spring can work only when two bodies move in the opposite direction against each other out of phase. At every time step, the distance between both spars is checked in the modified program, and then the spring works only when spars are moving over 30 m in surge direction.

8.6 Results and Discussion

The analysis results using the two-body spar model with a hawser connection and a linear spring model between two spars are compared with the results of a single spar as shown in Table 8.4. In the table, the spar-spring-spar model is considered an ideal case so that the responses of both spars are identical. The corresponding case to this is the spar-hawser-spar model with no interaction effect. These models show a good agreement to each other. The results of the interaction case and the no-interaction case with no cable reveal that the fluid interaction effect makes the rear side structure move a little less in all directional motion except the sway motion. However, the effect makes the sway motion of the lee side structure amplified a little. It means that the weather side structure acts as a protector for the lee-side structure.

When one hawser is used for the connection, it also forces the second body to move in a more restricted way and less than the first body in the front side of the wave, wind and current. The cable can be imagined to limit the motion of the second body, since the hawser has the rigidity in the surge direction and so it will go to the opposite direction against the second body movement when they are in an out-of-phase state. The magnitude of the compensating reaction will vary according to the stiffness of the hawser. To get some clues for the reason of the sudden increases in surge and yaw motion RMS in the case of interaction effect with one hawser, the surge motion RAO is illustrated in Figure 8.4.a. The heave motion RAO and the roll motion RAO are shown in Figures 8.4.b and 8.4.c. As shown in Figure 8.4.a, the surge motion RAO for the two-body model has a similar trend to that for the single-body model. As shown in Figures 8.4.b and 8.4.c, the heave and roll motion RAOs for the two-body model have similar trends to those for the single-body model. But, the surge drift force for the two-body model has twice large than that for a single body model. It can make the differences between the analysis results for the single-body model and the two-body model in surge, heave and roll dynamic motions. In Figure 8.5, the surge mean drift forces for a single body and those for two-body by the pressure integration method are shown for comparison purpose. In the figure, the two-body interaction effect can be seen.

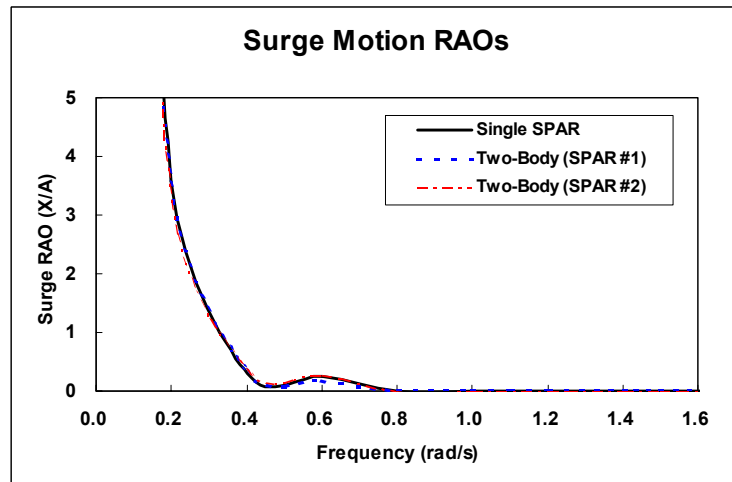


Figure 8.4.a Comparison of the surge motion RAOs

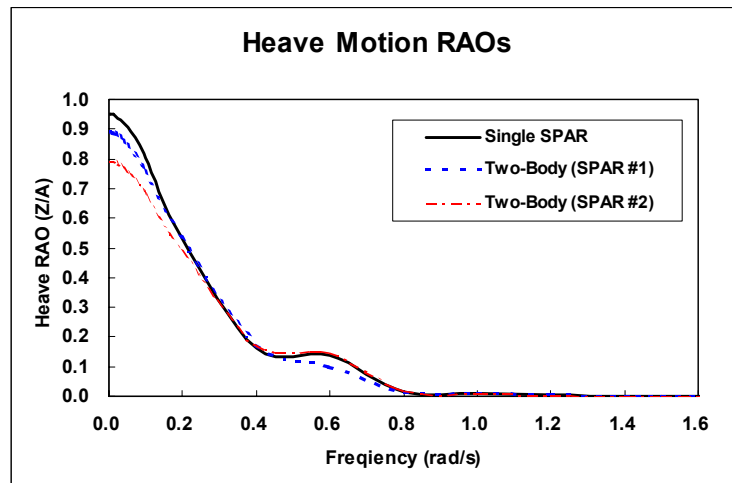


Figure 8.4.b Comparison of the heave motion RAOs

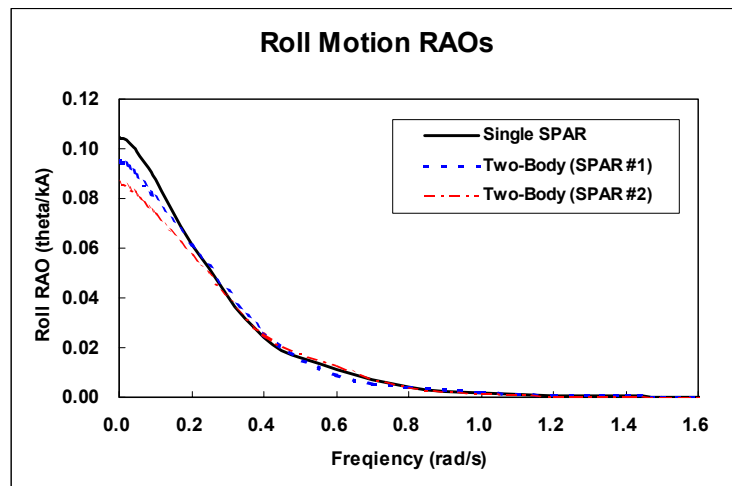


Figure 8.4.c Comparison of the roll motion RAOs

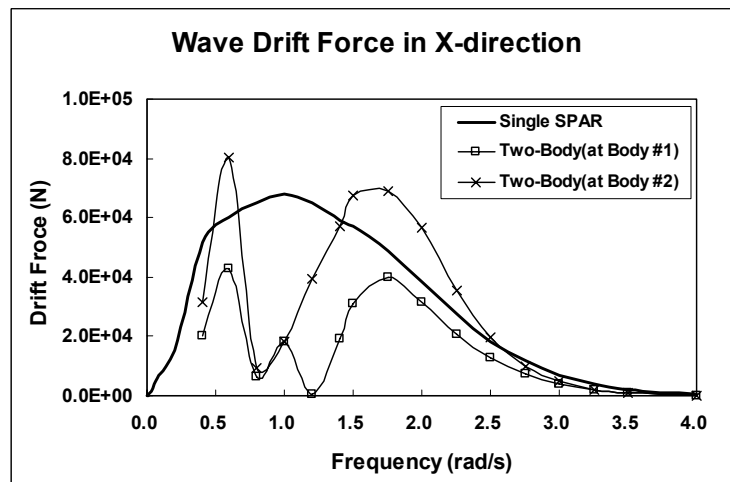


Figure 8.5 Comparison of the surge drift force

Table 8.4 The analysis results for two-body model composed of two spars

| | | Single SPAR | SPAR+SPAR ¹⁾ | | | | | | | | SPAR+SPRING+SPAR ²⁾ | |
|----------------------|------|-------------|-------------------------|--------|-------------|--------|------------------|--------|-------------|--------|--------------------------------|--------|
| | | | w/o interaction | | | | with interaction | | | | w/o interaction | |
| | | | w/o hawser | | with hawser | | w/o hawser | | with hawser | | with a linear spring | |
| | | | SPAR 1 | SPAR 2 | SPAR 1 | SPAR 2 | SPAR 1 | SPAR 2 | SPAR 1 | SPAR 2 | SPAR 1 | SPAR 2 |
| Body Motion | | | | | | | | | | | | |
| surge (m) | mean | -24.60 | -24.32 | -25.45 | -24.40 | -25.41 | -23.84 | -24.57 | -23.75 | -24.46 | -23.81 | -24.16 |
| | min. | -31.54 | -30.63 | -33.66 | -30.71 | -33.59 | -30.73 | -31.69 | -29.73 | -31.45 | -30.48 | -30.95 |
| | max. | -18.36 | -18.40 | -18.55 | -18.54 | -18.49 | -18.29 | -17.89 | -18.72 | -17.54 | -18.63 | -19.44 |
| | rms. | 2.33 | 2.18 | 2.82 | 2.18 | 2.66 | 2.17 | 2.57 | 2.05 | 2.73 | 2.25 | 2.40 |
| sway (m) | mean | -6.36 | -6.46 | -5.71 | -6.46 | -5.80 | -6.44 | -5.91 | -5.86 | -5.56 | -6.37 | -6.47 |
| | min. | -9.85 | -9.88 | -9.59 | -9.87 | -9.60 | -9.89 | -10.16 | -11.22 | -10.73 | -10.57 | -10.62 |
| | max. | -2.78 | -2.91 | -1.91 | -2.90 | -1.91 | -3.18 | -1.47 | 0.04 | 0.20 | -3.73 | -3.78 |
| | rms. | 1.40 | 1.40 | 1.64 | 1.40 | 1.53 | 1.40 | 1.60 | 1.96 | 2.03 | 1.50 | 1.49 |
| heave (m) | mean | 0.22 | 0.23 | 0.19 | 0.22 | 0.19 | 0.26 | 0.23 | 0.27 | 0.24 | 0.26 | 0.24 |
| | min. | -0.54 | -0.49 | -0.46 | -0.49 | -0.60 | -0.31 | -0.24 | -0.19 | -0.65 | -0.15 | -0.26 |
| | max. | 0.83 | 0.80 | 0.78 | 0.79 | 0.78 | 0.93 | 0.54 | 0.97 | 0.93 | 0.63 | 0.64 |
| | rms. | 0.18 | 0.17 | 0.18 | 0.17 | 0.19 | 0.14 | 0.11 | 0.15 | 0.24 | 0.12 | 0.13 |
| roll (deg) | mean | 0.67 | 0.67 | 0.64 | 0.67 | 0.64 | 0.67 | 0.34 | 0.65 | 0.63 | 0.67 | -0.68 |
| | min. | -0.43 | -0.49 | -0.33 | -0.49 | -0.38 | -0.48 | -0.19 | -1.06 | -0.95 | -0.22 | -0.23 |
| | max. | 1.82 | 1.83 | 1.70 | 1.83 | 1.74 | 1.85 | 1.48 | 2.78 | 1.89 | 1.50 | 1.53 |
| | rms. | 0.43 | 0.45 | 0.39 | 0.45 | 0.41 | 0.44 | 0.34 | 0.57 | 0.39 | 0.38 | 0.39 |
| pitch (deg) | mean | -2.17 | -2.14 | -2.27 | -2.16 | -2.26 | -2.07 | -2.17 | -2.04 | -2.16 | -2.19 | -2.01 |
| | min. | -6.54 | -6.31 | -6.36 | -6.31 | -6.73 | -6.04 | -4.57 | -5.87 | -4.46 | -5.23 | -5.03 |
| | max. | 2.00 | 2.00 | 1.52 | 1.96 | 1.56 | 1.60 | -0.11 | 1.36 | 0.49 | 0.05 | 0.28 |
| | rms. | 1.19 | 1.16 | 1.16 | 1.16 | 1.19 | 1.09 | 0.69 | 1.01 | 0.67 | 0.96 | 0.98 |
| yaw (deg) | mean | 0.05 | 0.04 | 0.05 | 0.04 | 0.04 | 0.04 | 0.04 | 0.13 | 0.09 | 0.04 | 0.04 |
| | min. | -0.04 | -0.04 | -0.04 | -0.05 | -0.05 | -0.05 | -0.15 | -6.94 | -3.72 | -0.07 | -0.04 |
| | max. | 0.16 | 0.15 | 0.17 | 0.15 | 0.16 | 0.16 | 0.27 | 7.05 | 3.85 | 0.18 | 0.16 |
| | rms. | 0.03 | 0.03 | 0.04 | 0.03 | 0.04 | 0.03 | 0.09 | 2.85 | 1.48 | 0.05 | 0.04 |
| Line Tension | | | | | | | | | | | | |
| Mooring line #1 (kN) | mean | 16,339 | 16,070 | 17,152 | 16,162 | 17,071 | 15,768 | 16,350 | 15,672 | 16,279 | 15,784 | 16,024 |
| | min. | 10,587 | 10,678 | 11,374 | 10,686 | 10,629 | 11,423 | 12,196 | 11,117 | 12,170 | 12,173 | 12,092 |
| | max. | 27,045 | 25,223 | 29,225 | 26,377 | 29,717 | 24,792 | 24,711 | 23,876 | 24,079 | 23,987 | 25,040 |
| | rms. | 2,421 | 2,260 | 2,958 | 2,259 | 2,839 | 2,003 | 2,095 | 1,882 | 2,022 | 1,958 | 2,090 |
| Mooring line #2 (kN) | mean | 9,807 | 9,815 | 9,710 | 9,823 | 9,723 | 9,823 | 9,745 | 9,743 | 9,702 | 9,817 | 9,831 |
| | min. | 9,280 | 9,304 | 9,132 | 9,304 | 9,131 | 9,322 | 9,160 | 8,937 | 8,821 | 9,431 | 9,441 |
| | max. | 10,389 | 10,393 | 10,375 | 10,391 | 10,377 | 10,382 | 10,436 | 10,629 | 10,597 | 10,568 | 10,578 |
| | rms. | 215 | 237 | 245 | 215 | 228 | 215 | 238 | 292 | 290 | 236 | 236 |
| Mooring line #3 (kN) | mean | 7,207 | 7,222 | 7,165 | 7,216 | 7,168 | 7,244 | 7,220 | 7,251 | 7,222 | 7,246 | 7,232 |
| | min. | 6,093 | 6,382 | 6,214 | 6,152 | 6,217 | 6,113 | 6,778 | 6,333 | 6,769 | 6,553 | 6,638 |
| | max. | 7,871 | 7,863 | 7,759 | 7,859 | 7,833 | 7,823 | 7,633 | 7,964 | 7,619 | 7,660 | 7,669 |
| | rms. | 224 | 218 | 235 | 215 | 229 | 203 | 136 | 193 | 132 | 164 | 161 |
| Mooring line #4 (kN) | mean | 8,356 | 8,354 | 8,412 | 8,348 | 8,403 | 8,351 | 8,395 | 8,403 | 8,426 | 8,356 | 8,348 |
| | min. | 8,081 | 8,085 | 8,095 | 8,086 | 8,094 | 8,088 | 8,072 | 7,996 | 8,033 | 8,021 | 8,018 |
| | max. | 8,678 | 8,658 | 8,774 | 8,658 | 8,774 | 8,650 | 8,790 | 8,978 | 9,119 | 8,579 | 8,573 |
| | rms. | 116 | 125 | 137 | 115 | 128 | 115 | 133 | 166 | 174 | 121 | 120 |
| Riser (kN) | mean | 45,368 | 45,368 | 45,369 | 45,368 | 45,369 | 45,368 | 45,368 | 45,368 | 45,368 | 45,368 | 45,368 |
| | min. | 45,360 | 45,360 | 45,360 | 45,360 | 45,360 | 45,360 | 45,361 | 45,360 | 45,361 | 45,610 | 45,361 |
| | max. | 45,392 | 45,388 | 45,393 | 45,389 | 45,393 | 45,385 | 45,380 | 45,392 | 45,381 | 45,380 | 45,850 |
| | rms. | 4 | 3 | 4 | 4 | 4 | 4 | 3 | 4 | 3 | 3 | 4 |
| Hawser (kN) | mean | | | | | 66 | | | | 66 | | |
| | min. | | | | | 31 | | | | 29 | | |
| | max. | | | | | 171 | | | | 207 | | |
| | rms. | | | | | 21 | | | | 25 | | |

Remarks: 1) Both SPARs have 4 equivalent mooring lines and 1 equivalent central riser.

2) A linear spring of the same stiffness as the hawser is put directly in the system stiffness matrix.

8.7 Summary and Conclusions

The multiple body interaction effects on the two-body model of two spars due to the hawser connection and the hydrodynamic interaction effects are investigated by comparative study using two numerical models.

When a linear spring is used, the results must be an ideal case. So, the statistical results of the motions of two bodies are shown to be identical. With comparing this, the results of the hawser connection model make the two bodies move a little differently. It shows that the hawser acts as a compensator for the second body in the lee side. When the second body tends to move out of phase against the first body motion, it makes the second body move to the opposite direction. Therefore, the second body will be able to move within a certain range.

The hydrodynamic interaction effect is exhibited well in the six DOF motions as the motions of the second body, except the sway motions are a little bit smaller than those of the other. It is why the flow route of the external forces of wind, wave and current is restricted by the protection effect of the front structure. However, for the sway motion, it is hard to say that the second body will move less than the first body. On the whole point of view, the fluid interaction effect is clearly illustrated in the leeward structure, and the front structure acts as a protector for the rear structure when the environmental loads are applied to the first structure collinearly with the direction of the body connection.

CHAPTER IX

CASE STUDY 5:

DYNAMIC COUPLED ANALYSES FOR TWO-BODY SYSTEM COMPOSED OF AN FPSO-FPSO AND AN FPSO-SHUTTLE TANKER

9.1 Introduction

In this chapter, an FPSO-FPSO and an FPSO-Shuttle tanker are taken as the multiple-body models for the verification of the program (WINPOST-MULT) for the dynamic coupled analysis of the multiple-body floating platforms, and the results are compared with the exact solution using a two-mass-spring model. An FPSO-FPSO model consists of two identical FPSOs. The other two-body model is composed of an FPSO and a shuttle tanker. The conventional tandem moorings have been used for the multiple-body connections in many cases of the operation of offloading in the sea. For the multiple-body model of the FPSO-shuttle tanker, the tandem mooring is considered to investigate the interaction effect. The simplified mass-spring model will give a compatible result to judge the validity of the multiple-body program.

In this study, the interaction characteristics for the tandem-moored vessels are calculated in regular waves at several frequencies by using WAMIT. The body motions and line tensions are mainly reviewed with the numerical calculations performed by WINPOST-MULT, the dynamic coupled analysis program for multiple-body platforms. The coupled analysis results for the model of two identical FPSOs by the WINPOST-MULT program are compared with the exact solution for the two-mass-spring model.

From this study, the effect of the hawser to connect two structures is also specified. For this verification, models both with a hawser and without a hawser are made and analyzed. The interaction effect is studied as well for this model.

For the mooring system, a tandem mooring is taken into account. The tandem mooring has been used for many years. The distance of the tandem mooring system is taken as 30 meters, which is the same as in the previous chapter.

9.2 Particulars of Models and Mooring Arrangements

The main particulars, including the principle data of spar, are listed in Table 9.1. The main particulars and dimensions of the shuttle tanker are taken as the same as the FPSO's. The arrangement of the tandem is shown in Figure 9.1. The water depth is 6,000 ft (1828.8 m). The distance between the two FPSOs in the tandem mooring is taken as 30 meters. The original FPSO studied in Chapter V has 12 taut mooring lines and 13 steel catenary risers(SCR). Here, for simplification, they are equivalently combined as 4 groups for mooring lines and 1 group for risers. Each mooring line group has 3 legs, and one riser group is composed of all (13) risers. The riser group is centralized on the geometrical center of the turret. The configuration for the mooring of the equivalent mooring lines is shown in Figure 9.2. The mooring lines are fixed at the sea floor. The WAMIT program is used for the calculation of the hydrodynamic coefficients of the vessels. The validity of the numerical modeling was already proven in the previous chapters by the static offset test and free decay tests. The numerical models and the particulars of the mooring systems are the same as the FPSO's reviewed in

Chapter V. The hawser connecting the two FPSOs and the FPSO-Shuttle tanker has the stiffness of 1/100 of the mooring stiffness and the pre-tension of 1/10 of the mooring pre-tension. Main particulars of the mooring systems are summarized in Table 9.2.

Table 9.1 Main particulars of the turret moored FPSO

| Description | Symbol | Unit | Quantity |
|--|-----------|-------------|-----------|
| Production level | | <i>bpd</i> | 120,000 |
| Storage | | <i>bbls</i> | 1,440,000 |
| Vessel size | | <i>kDWT</i> | 200 |
| Length between perpendicular | L_{pp} | <i>m</i> | 310.0 |
| Breadth | B | <i>m</i> | 47.17 |
| Depth | H | <i>m</i> | 28.04 |
| Draft (in full load) | T | <i>m</i> | 18.09 |
| Displacement (in full load) | | <i>MT</i> | 240,869 |
| Length-beam ratio | L/B | | 6.57 |
| Beam-draft ratio | B/T | | 2.5 |
| Block coefficient | C_b | | 0.85 |
| Center of buoyancy forward section 10 | FB | <i>m</i> | 6.6 |
| Water plane area | A | m^2 | 13,400 |
| Water plane coefficient | C_w | | 0.9164 |
| Center of water plane area forward section 10 | FA | <i>m</i> | 1.0 |
| Center of gravity above keel | KG | <i>m</i> | 13.32 |
| Transverse metacentric height | MG_t | <i>m</i> | 5.78 |
| Longitudinal metacentric height | MG_l | <i>m</i> | 403.83 |
| Roll radius of gyration in air | R_{xx} | <i>m</i> | 14.77 |
| Pitch radius of gyration in air | R_{yy} | <i>m</i> | 77.47 |
| Yaw radius of gyration in air | R_{zz} | <i>m</i> | 79.30 |
| Frontal wind area | A_f | m^2 | 1,012 |
| Transverse wind area | A_b | m^2 | 3,772 |
| Turret in center line behind F_{pp} (20.5 % L_{pp}) | X_{tur} | <i>m</i> | 63.55 |
| Turret elevation below tanker base | Z_{tur} | <i>m</i> | 1.52 |
| Turret diameter | | <i>m</i> | 15.85 |

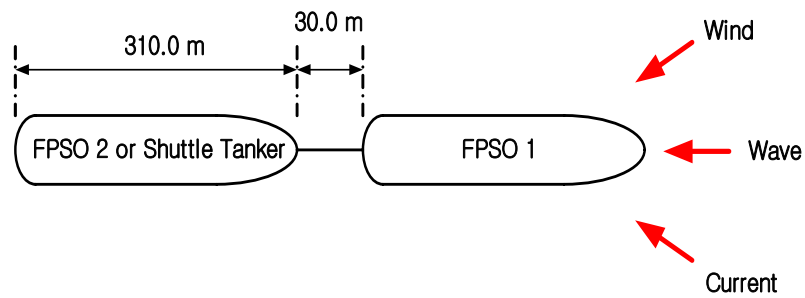


Figure 9.1 Configuration of the mooring systems (Tandem mooring system)

Table 9.2 Main particulars of the mooring systems

| Description | Unit | Quantity |
|--|-------------|----------|
| Pretension | <i>kN</i> | 1,201 |
| Number of lines | | 4*3 |
| Degrees between 3 lines | <i>deg</i> | 5 |
| Length of mooring line | <i>m</i> | 2,087.9 |
| Radius of location of chain stoppers on turn table | <i>m</i> | 7.0 |
| Segment 1 (ground position): chain | | |
| Length at anchor point | <i>m</i> | 914.4 |
| Diameter | <i>mm</i> | 88.9 |
| Weight in air | <i>kg/m</i> | 164.9 |
| Weight in water | <i>kg/m</i> | 143.4 |
| Stiffness, AE | <i>kN</i> | 794,841 |
| Mean breaking load, MBL | <i>kN</i> | 6,515 |
| Segment 2: chain | | |
| Length | <i>m</i> | 1127.8 |
| Diameter | <i>mm</i> | 107.9 |
| Weight in air | <i>kg/m</i> | 42.0 |
| Weight in water | <i>kg/m</i> | 35.7 |
| Stiffness, AE | <i>kN</i> | 690,168 |
| Mean breaking load, MBL | <i>kN</i> | 6,421 |
| Segment 3 (hang-off position): chain | | |
| Length | <i>m</i> | 45.7 |
| Diameter | <i>mm</i> | 88.9 |
| Weight in air | <i>kg/m</i> | 164.9 |
| Weight in water | <i>kg/m</i> | 143.4 |
| Stiffness, AE | <i>kN</i> | 794,841 |
| Mean breaking load, MBL | <i>kN</i> | 6,515 |

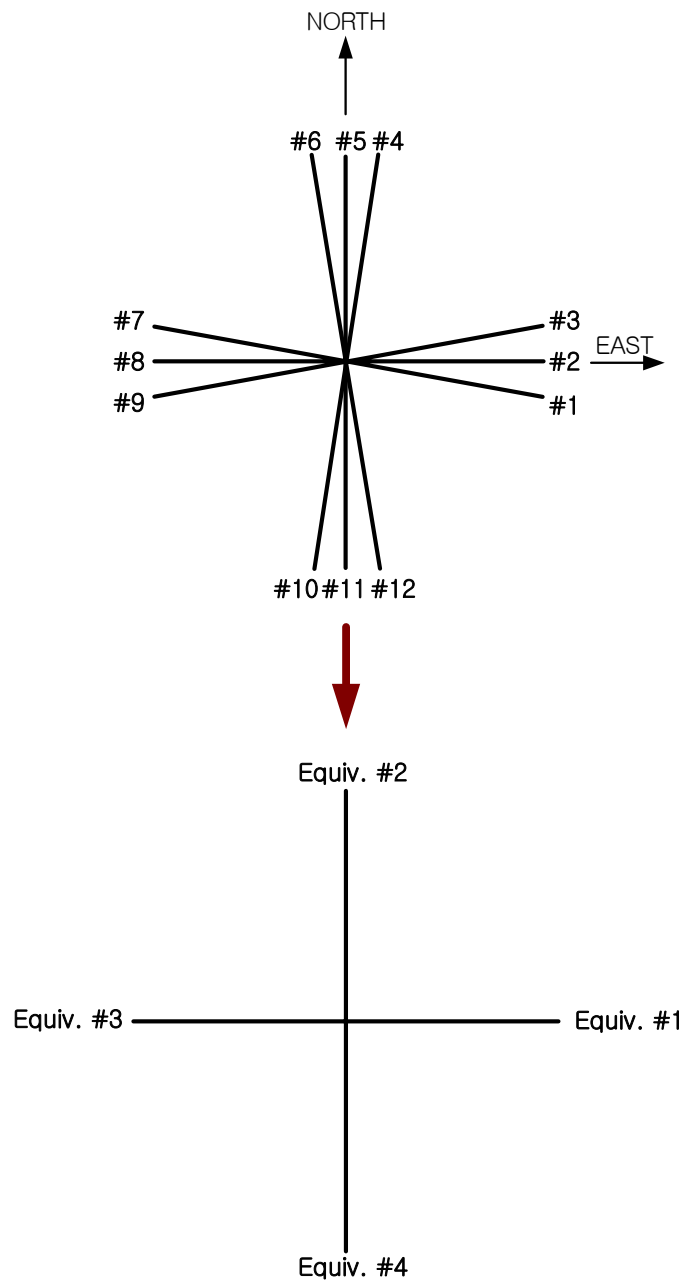


Figure 9.2 Configuration of the arrangement of the mooring line groups

9.3 Environmental Conditions

The environmental conditions correspond to the 100-year storm conditions in GoM and the sea condition of West Africa. The 100-year storm conditions are used in the case of tandem moored vessels of the two body model of an FPSO and an FPSO. For the wind force, API RP 2T is referred to obtain the wind velocity spectrum. For the wave force, JONSWAP spectrum is used. The wave frequencies are taken account of the range from 0.5 rad/s to 1.2 rad/s. The wave is calculated at every frequency, dividing the range by 100 intervals, and it is summed up with a random phase at every time. The current velocity is 1.0668 m/s at the free surface, and it is reduced as 0.0914 m/s at the sea floor. It varies linearly to the sea floor. The environmental conditions at GOM and at the west Africa sea are summarized in Tables 9.3.a and 9.3.b, respectively. The incident wave heading in hurricane conditions is 180° when the x-coordinate is set to the East and y-axis is set to the North.

The west Africa sea conditions are used for the two-body model of an FPSO and a shuttle tanker. The API wind velocity spectrum is also used, but the wind speed is slower than that in the 100-yr. storm condition. The current speed in the West Africa is less than that in GoM. The reason that the mild condition is taken for the FPSO-Shuttle tanker model is that the tandem mooring system for transferring oil or gas from the FPSO to the shuttle tanker in the real open sea has been tried in a rather mild sea condition for the safety. The wave heading of this condition is 180° when the x-coordinate is set to the East and y-axis is set to the North.

Table 9.3.a Environmental conditions (100-year storm condition at GOM)

| Description | Unit | Quantity |
|-----------------------------|--|-------------------|
| Wave | | |
| Significant wave height, Hs | <i>m</i> | 12.19 |
| Peak period, Tp | <i>sec</i> | 14.0 |
| Wave spectrum | <i>JONSWAP ($\gamma=2.5$)</i> | |
| Direction | <i>deg</i> | 180 ¹⁾ |
| Wind | | |
| Velocity | <i>m/s</i> | 41.12 m/s @ 10m |
| Spectrum | <i>API RP 2T</i> | |
| Direction | <i>deg</i> | 210 ¹⁾ |
| Current | | |
| Profile | | |
| at free surface (0 m) | <i>m/s</i> | 1.0668 |
| at 60.96 m | <i>m/s</i> | 1.0668 |
| at 91.44 m | <i>m/s</i> | 0.0914 |
| on the sea bottom | <i>m/s</i> | 0.0914 |
| Direction | <i>deg</i> | 150 ¹⁾ |

Remark: 1) The angle is measured counterclockwise from the x-axis (the East).

Table 9.3.b Environmental conditions (west Africa sea condition)

| Description | Unit | Quantity |
|-----------------------------|--|-------------------|
| Wave | | |
| Significant wave height, Hs | <i>m</i> | 2.70 |
| Peak period, Tp | <i>sec</i> | 16.5 |
| Wave spectrum | <i>JONSWAP ($\gamma=6.0$)</i> | |
| Direction | <i>deg</i> | 180 ¹⁾ |
| Wind | | |
| Velocity | <i>m/s</i> | 5.0 m/s @ 10m |
| Spectrum | <i>API RP 2A-WSD</i> | |
| Direction | <i>deg</i> | 210 ¹⁾ |
| Current | | |
| Profile | | |
| at free surface (0 m) | <i>m/s</i> | 0.150 |
| at 60.96 m | <i>m/s</i> | 0.150 |
| at 91.44 m | <i>m/s</i> | 0.050 |
| on the sea bottom | <i>m/s</i> | 0.050 |
| Direction | <i>deg</i> | 150 ¹⁾ |

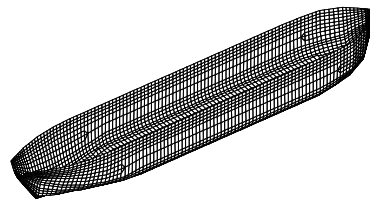
Remark: 1) The angle is measured counterclockwise from the x-axis (the East).

9.4 Calculation of Hydrodynamic Coefficients Using WAMIT

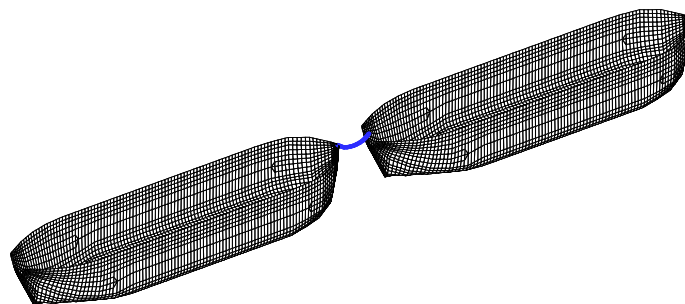
The hydrodynamic coefficients are calculated by WAMIT. For the two-body analysis, the wave force coefficients and wave drift force coefficients are calculated. The hydrodynamic coefficients of added mass, wave damping and linear transfer function (LTF) of diffraction potential force are calculated by WAMIT. In Figure 9.3, the model for the wave force coefficients is shown. The modeling is made only for the port side, and the number of elements is 1684.

A turret-moored FPSO has been designed to weathervane in the sea so that the mooring lines and risers are only connected at the bottom of turret. Under the circumstances of applying the environmental conditions associated with wave, wind and current load, it will pursue the dynamical equilibrium position corresponding to the neutral location for the sum of the environmental loads to be zero and trace the path by itself. After that, she will move and rotate freely. For a two-body model composed of FPSO and FPSO, the mooring lines and risers are connected as what they are, and the 100-year storm conditions at GoM are applied. But, for a two-body model composed of FPSO and a shuttle tanker, the mooring lines and risers are installed only for FPSO, and the shuttle tanker has no mooring line and riser. FPSO and the shuttle tanker are connected with one hawser. For FPSO and shuttle tanker model, the West Africa sea condition is applied. It is well known that the range of yaw angle in which she may move in the 100-year storm condition will be about 10~20 degrees. Accordingly, the hydrodynamic coefficients at every angle should be calculated for the dynamic analysis. However, in the time-domain simulation, it is not practical to calculate the coefficients at

every time step. In this study, at every 5-degree interval, the coefficients are calculated prior to the coupled analysis. So, when the coupled analysis of the body and the mooring system is performed, at every time step the yaw angle is checked. If the yaw angle is beyond 5 degrees from the starting position, the other coefficients are read from the pre-made files.

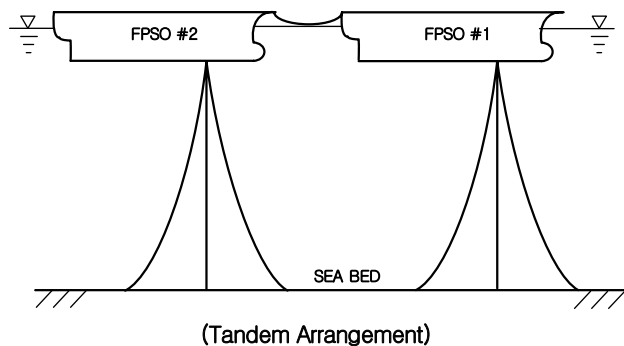


(a) A single-body FPSO model

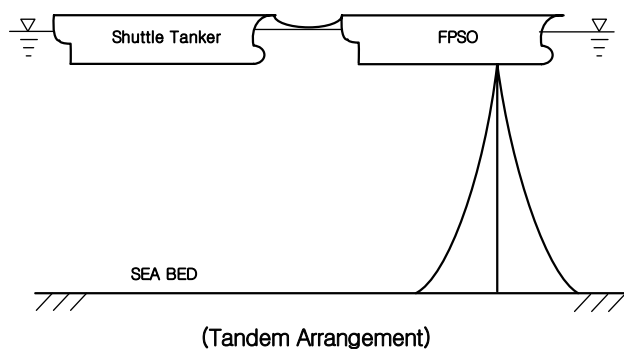


(b) Two-body model of FPSO and FPSO (or Shuttle tanker) in tandem arrangement

Figure 9.3 Configuration of single-body, two-body models and the mooring system



(c) Configuration of moorings for two-body model of FPSO and FPSO



(d) Configuration of moorings for two-body model of FPSO and Shuttle tanker

Figure 9.3 Continued

9.5 Two-Mass-Spring Modeling

The two-mass-spring model is devised to get an exact solution for the idealized two-body FPSO model and is used for verifying the numerical analysis results by the WINPOST-MULT program. The idealized model is shown in Figure 9.4. The environmental loads are calculated using Morison's equation for the wind and current forces and the JONSWAP spectrum formula for the wave force. The masses are

determined to add the FPSO body mass and the added mass at around surge natural frequency. Spring constants are calculated by considering the total top tension of the mooring lines and risers in the horizontal direction. The hawser stiffness can be directly converted to the linear spring in the middle of the idealized model.

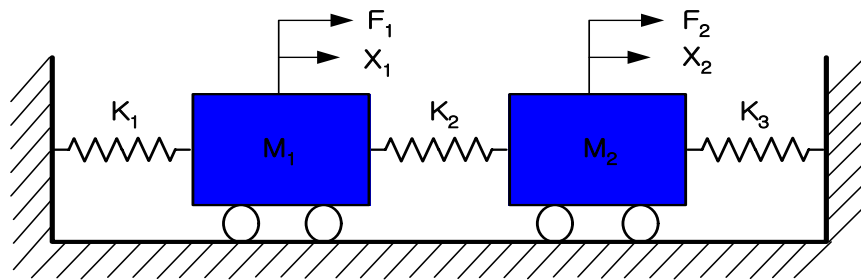


Figure 9.4 Two-mass-spring model

The wind force in x-direction, F_{xw} , is obtained from Morison's formula and OCIMF wind coefficient as:

$$F_{xw} = \frac{1}{2} C_{xw} \rho_w A_T V_w^2 \quad (9.1)$$

where C_{xw} is the wind force coefficient that can be read from the OCIMF document, ρ_w is the water density, A_T denotes the projected area in the lateral direction of the vessel against wind, and V_w is the wind velocity. The wind force by API RP 2T, $F_{ww}(1)$, represents the force per unit area in the normal direction to the wind blowing, and is given by:

$$F_{ww}(1) = \frac{1}{2} \rho_w V_w^2 \quad (9.2)$$

Here, in this study, the unit wind force, $F_{ww}(1)$, is calculated by a separate program, and the resultant wind force is computed in the WINPOST program, since the force varies according to the wind blowing direction. In WINPOST, the yaw angle of the body at every time step is checked, and the wind force coefficient is interpolated by using the reading data from the OCIMF document. A_T is given by a user as an input data. In y-direction, the wind force is obtained in the same way by the following formula:

$$F_{yw} = C_{yw} A_L F_{ww}(1) \quad (9.3)$$

where C_{yw} is the wind force coefficient in y-direction obtained from the OCIMF document, and A_L denotes the projected area in the longitudinal direction to be normal to the wind. As the initial wind direction is considered to be 210° counterclockwise from the x-axis (true East), the coefficients of C_{xw} and C_{yw} are evaluated as 0.73 and 0.30, respectively, in the full load condition.

The current forces, F_{xc} in x-direction and F_{yc} in y-direction, are also calculated from Morison's formula as follows:

$$\text{In x-direction:} \quad F_{xc} = \frac{1}{2} C_{xc} \rho_c V_c^2 L_{pp} T \quad (9.4)$$

$$\text{In y-direction:} \quad F_{yc} = \frac{1}{2} C_{yc} \rho_c V_c^2 L_{pp} T \quad (9.5)$$

Where L_{pp} and T are the same as in Table 9.1, ρ_c is the water density, and V_c is the current velocity, and here current speed is used at the free surface. The current

coefficients, C_{xc} and C_{yc} are evaluated as 0.024 and 0.922, respectively, by considering the initial current direction of 150° from the x-axis counterclockwise.

The formula of the JONSWAP wave spectrum was written in Chapter V (equation (5.1)). If the significant wave height, H_s , the peak period, T_p , and overshooting parameter, γ , are taken in Tables 9.3.a and 9.3.b, the wave can be estimated at any time with random phases.

$$F_\phi(t_i) = \sum_j A(\omega_j) \cos(\omega_j t_i + \phi_j) \quad (9.6)$$

where i and j are the indices for representing the time instant and the frequency of any wave component, ω_j is the frequency of the incident wave component j , $A(\omega_j)$ is the wave amplitude, and ϕ_j is the random phase between wave components. The total force is determined as the linear sum of the equation (9.2) ~ (9.6) as:

$$F_1(t) = F_2(t) = F_w + F_c + F_\phi \quad (9.7)$$

where $F_1(t)$ and $F_2(t)$ are the applied forces to the mass M_1 and M_2 in the idealized model, and M_1 and M_2 represent the virtual masses made of the mass weights and the added masses of the FPSOs.

The body mass and stiffness are obtained by considering the mass weight of FPSO, m , the added mass, m_a , and the line top tension as follows:

$$M_1 = M_2 = m + m_a \quad (9.8)$$

$$K_1 = K_3 = \text{stiffness of mooring lines and risers} \quad (9.9)$$

$$K_2 = \text{stiffness of the hawser} \quad (9.10)$$

Table 9.4 The system parameters for two-mass-spring model

| ITEM | Symbol | Unit | Magnitude |
|--------------------------|--------|------|-----------|
| Added mass | m_a | kg | 1.466E+07 |
| FPSO weight in mass | m | kg | 2.397E+08 |
| Mass of FPSO #1 | M_1 | kg | 2.543E+08 |
| Mass of FPSO #2 | M_2 | kg | 2.543E+08 |
| Stiffness of mooring #1 | K_1 | N/m | 2.389E+05 |
| Stiffness of hawser | K_2 | N/m | 1.868E+03 |
| Stiffness of mooring #2 | K_3 | N/m | 2.389E+05 |
| Natural period (Mode #1) | | sec | 16.34 |
| (Mode #2) | | sec | 205.02 |

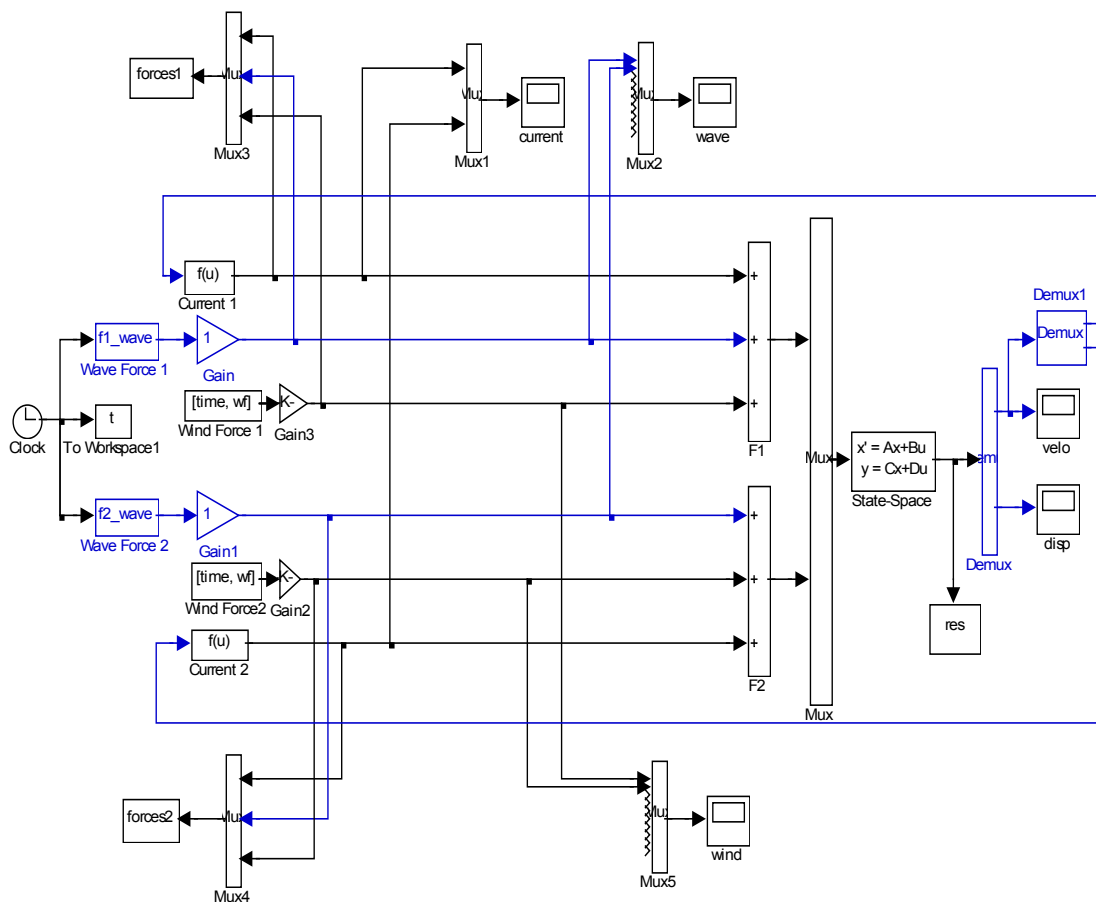
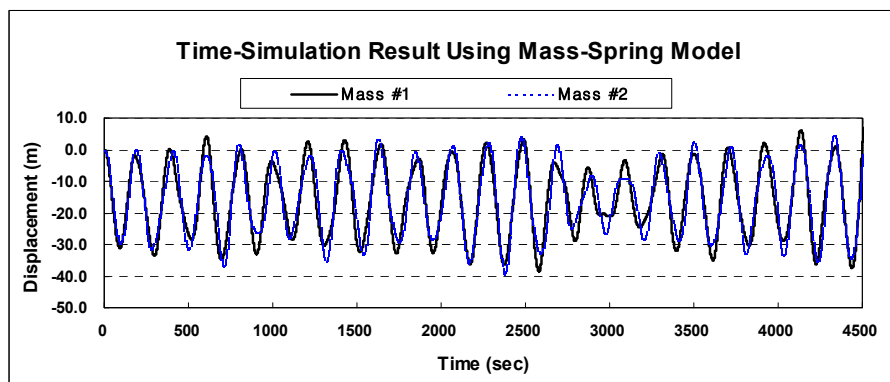
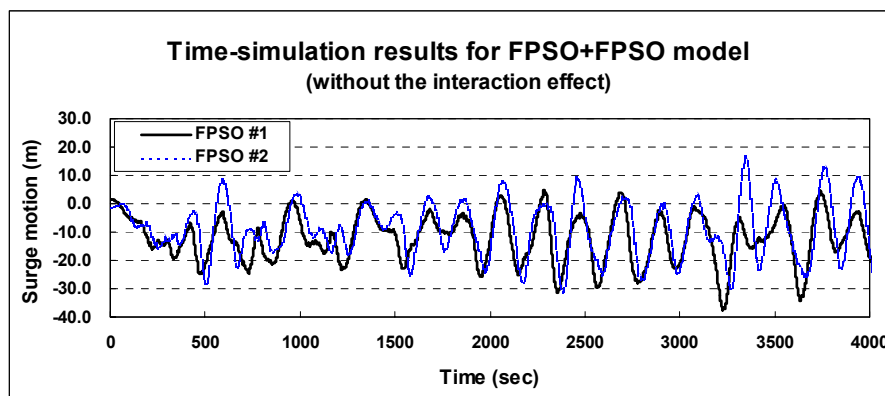


Figure 9.5 The diagram of the time simulation in SIMULINK of MATLAB

The calculated results to get the idealized two-mass-spring model are summarized in Table 9.4. For the validity of the model data, the eigenvalues are checked using MATLAB. The time simulation for the mass-spring model is performed using MATLAB. The calculation diagram in MATLAB is depicted in Figure 9.5.

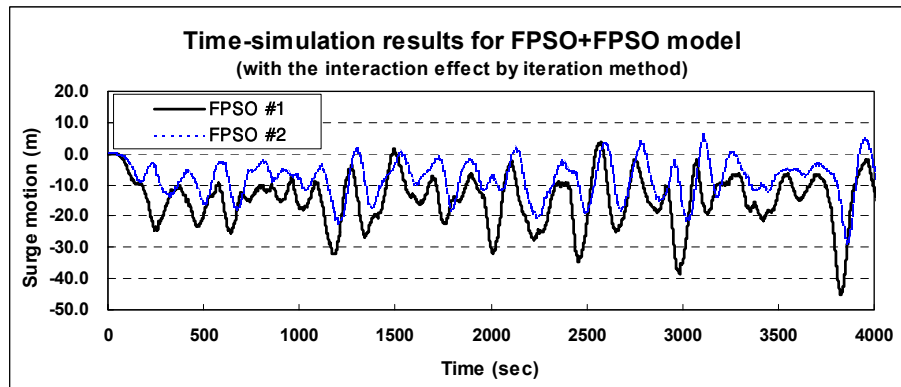


(a) The displacements at mass #1 and #2 of the mass-spring model by MATLAB

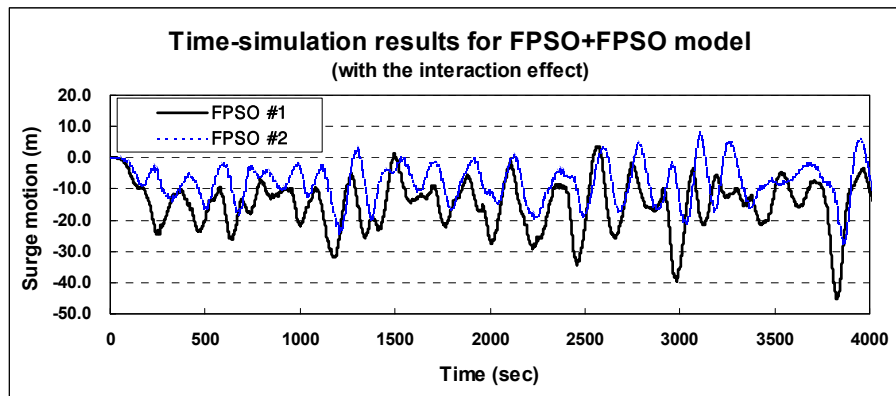


(b) The surge motion of FPSO+FPSO model by WINPOST-MULT (without the interaction effect)

Figure 9.6 The surge motion of the FPSO and FPSO model by MATLAB for mass-spring model and by WINPOST-MULT for two-body model



(c) The surge motion of FPSO+FPSO model by WINPOST-MULT (with the interaction effect by iteration method)



(d) The surge motion of FPSO+FPSO model by WINPOST-MULT (with the interaction effect by combined method)

Figure 9.6 Continued

Table 9.5 Analysis results of mass-spring model: displacement at mass #1 and #2

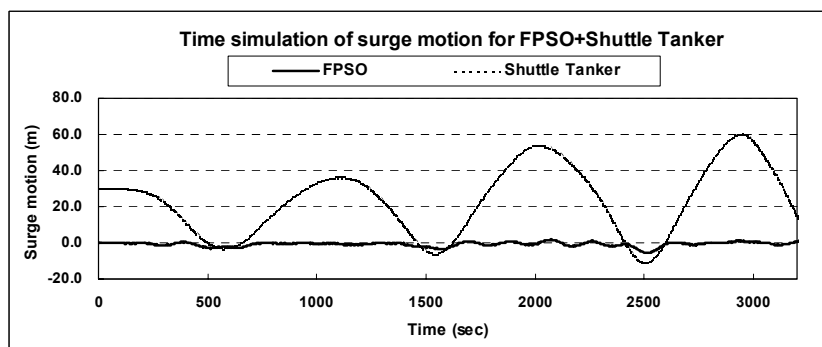
(unit: m)

| | Mean | Min. | Max. | RMS |
|----------------|--------|--------|-------|-------|
| Mass #1 | -15.47 | -38.99 | 11.71 | 14.46 |
| Mass #2 | -15.45 | -42.97 | 8.55 | 14.08 |

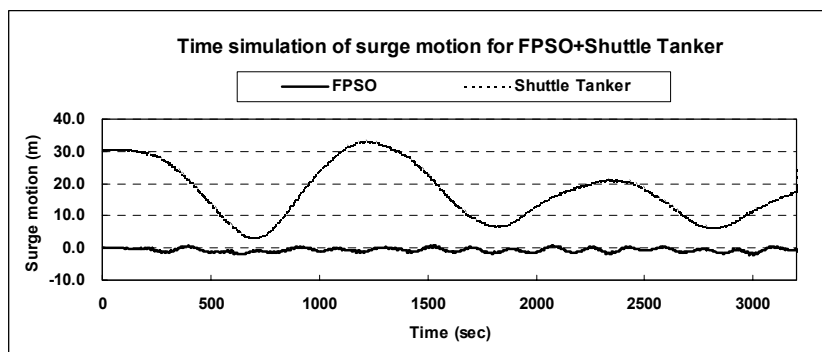
Table 9.6 Summary of the analysis results for two body FPSO+FPSO

| | | Single FPSO | FPSO+FPSO ¹⁾ | | | | | | | | | | | |
|----------------------|------|-------------|-------------------------|---------|-------------|---------|--|---------|-------------|---------|---------------------------------------|---------|-------------|---------|
| | | | w/o interaction | | | | with interaction (by iteration method) | | | | with interaction (by combined method) | | | |
| | | | w/o hawser | | with hawser | | w/o hawser | | with hawser | | w/o hawser | | with hawser | |
| | | | FPSO 1 | FPSO 2 | FPSO 1 | FPSO 2 | FPSO 1 | FPSO 2 | FPSO 1 | FPSO 2 | FPSO 1 | FPSO 2 | FPSO 1 | FPSO 2 |
| Body Motion | | | | | | | | | | | | | | |
| surge (m) | mean | -14.63 | -14.19 | -13.98 | -13.70 | -13.36 | -13.86 | -10.95 | -14.97 | -7.89 | -14.72 | -10.34 | -13.24 | -9.32 |
| | min. | -35.57 | -34.51 | -33.36 | -37.45 | -37.55 | -33.15 | -20.09 | -34.78 | -22.53 | -34.38 | -24.64 | -36.30 | -21.49 |
| | max. | 3.07 | 3.55 | 3.25 | 7.89 | 7.50 | -1.37 | -1.98 | 3.63 | 4.07 | 0.50 | -2.18 | 6.24 | 1.81 |
| | rms. | 8.01 | 8.55 | 8.59 | 9.23 | 9.20 | 7.25 | 4.06 | 8.05 | 5.93 | 7.27 | 4.19 | 8.06 | 4.40 |
| sway (m) | mean | 4.41 | 4.59 | 4.19 | 3.65 | 4.06 | 3.76 | 4.07 | 1.81 | 1.43 | 4.56 | 3.34 | 3.23 | 3.51 |
| | min. | -0.91 | -0.98 | -0.56 | -1.13 | -1.48 | -2.35 | -1.73 | -3.03 | -5.53 | -2.84 | -3.13 | -3.09 | -3.53 |
| | max. | 12.59 | 13.93 | 10.74 | 8.77 | 10.88 | 11.43 | 12.23 | 7.04 | 10.94 | 13.89 | 9.82 | 11.61 | 14.41 |
| | rms. | 2.68 | 2.87 | 2.47 | 1.42 | 1.88 | 2.81 | 3.33 | 2.17 | 3.61 | 2.98 | 2.96 | 2.11 | 3.01 |
| heave (m) | mean | -1.32 | -1.31 | -1.30 | -1.27 | -1.28 | -1.18 | -0.71 | -1.19 | -0.67 | -1.29 | -0.69 | -1.24 | -0.70 |
| | min. | -9.58 | -10.30 | -9.95 | -9.44 | -9.65 | -8.68 | -3.29 | -8.26 | -3.22 | -9.43 | -3.41 | -10.42 | -3.83 |
| | max. | 5.79 | 6.39 | 6.37 | 5.52 | 5.72 | 5.50 | 1.25 | 5.26 | 1.37 | 5.91 | 1.52 | 6.49 | 2.01 |
| | rms. | 2.60 | 2.57 | 2.54 | 2.47 | 2.51 | 2.32 | 0.72 | 2.28 | 0.62 | 2.55 | 0.67 | 2.43 | 0.72 |
| roll (deg) | mean | 0.00 | -0.01 | -0.01 | 0.00 | 0.00 | -0.01 | -0.07 | 0.04 | 0.02 | -0.03 | 0.00 | 0.00 | -0.04 |
| | min. | -4.87 | -4.54 | -5.35 | -2.97 | -5.15 | -5.93 | -3.15 | -1.38 | -1.83 | -8.11 | -3.12 | -4.83 | -4.09 |
| | max. | 4.70 | 4.36 | 5.66 | 2.95 | 5.08 | 6.02 | 2.91 | 1.54 | 1.57 | 7.53 | 2.85 | 4.67 | 3.20 |
| | rms. | 1.50 | 1.45 | 1.34 | 0.90 | 1.34 | 1.76 | 0.83 | 0.37 | 0.53 | 2.42 | 0.66 | 1.38 | 0.82 |
| pitch (deg) | mean | 0.45 | 0.45 | 0.45 | 0.43 | 0.44 | 0.41 | 0.25 | 0.40 | 0.23 | 0.44 | 0.24 | 0.42 | 0.24 |
| | min. | -3.12 | -3.44 | -3.55 | -3.36 | -3.45 | -2.82 | -0.79 | -2.89 | -0.78 | -3.09 | -0.87 | -3.40 | -0.97 |
| | max. | 4.93 | 5.48 | 5.41 | 5.08 | 5.18 | 4.47 | 1.18 | 4.20 | 1.15 | 4.87 | 1.23 | 5.25 | 1.44 |
| | rms. | 1.45 | 1.44 | 1.42 | 1.39 | 1.41 | 1.28 | 0.31 | 1.28 | 0.26 | 1.40 | 0.29 | 1.34 | 0.31 |
| yaw (deg) | mean | 9.52 | 9.85 | 8.65 | 6.56 | 8.46 | 12.92 | 18.75 | 1.82 | 12.48 | 11.47 | 18.59 | 9.33 | 16.67 |
| | min. | 0.80 | 3.79 | 0.47 | 2.53 | 2.45 | 3.65 | 10.73 | -2.37 | 5.61 | 3.52 | 14.83 | 0.62 | 8.24 |
| | max. | 17.85 | 17.23 | 16.14 | 11.49 | 13.57 | 21.87 | 26.46 | 5.53 | 16.86 | 20.19 | 21.72 | 16.77 | 23.20 |
| | rms. | 4.08 | 2.82 | 3.61 | 1.56 | 2.29 | 5.18 | 4.07 | 1.99 | 2.41 | 4.26 | 1.68 | 3.43 | 2.75 |
| Line Tension | | | | | | | | | | | | | | |
| Mooring line #1 (kN) | mean | 6,399 | 6,349 | 6,313 | 6,271 | 6,216 | 6,285 | 5,873 | 6,477 | 5,413 | 6,416 | 5,780 | 6,193 | 5,619 |
| | min. | 3,516 | 3,480 | 3,373 | 3,041 | 3,025 | 4,001 | 4,369 | 3,543 | 3,634 | 3,859 | 4,312 | 3,330 | 3,802 |
| | max. | 10,570 | 10,430 | 9,757 | 10,480 | 10,490 | 10,110 | 7,601 | 10,080 | 7,932 | 10,330 | 8,263 | 10,700 | 7,818 |
| | rms. | 1,306 | 1,377 | 1,373 | 1,470 | 1,466 | 1,167 | 654 | 1,297 | 927 | 1,184 | 673 | 1,291 | 701 |
| Mooring line #2 (kN) | mean | 3,537 | 3,506 | 3,553 | 3,617 | 3,565 | 3,621 | 3,642 | 3,872 | 3,994 | 3,512 | 3,728 | 3,679 | 3,710 |
| | min. | 1,759 | 1,884 | 2,098 | 2,286 | 2,033 | 2,102 | 2,455 | 2,805 | 2,631 | 1,788 | 2,604 | 1,989 | 2,237 |
| | max. | 4,768 | 4,889 | 4,968 | 4,783 | 4,734 | 4,685 | 4,672 | 5,350 | 5,098 | 5,040 | 4,784 | 4,923 | 4,792 |
| | rms. | 488 | 496 | 460 | 383 | 409 | 473 | 440 | 435 | 500 | 500 | 405 | 427 | 405 |
| Mooring line #3 (kN) | mean | 2,585 | 2,634 | 2,662 | 2,704 | 2,730 | 2,639 | 2,847 | 2,556 | 3,208 | 2,554 | 2,929 | 2,700 | 3,019 |
| | min. | 570 | 535 | 608 | 558 | 530 | 785 | 1,868 | 622 | 1,798 | 693 | 1,754 | 668 | 1,828 |
| | max. | 4,853 | 5,085 | 5,051 | 5,724 | 5,704 | 4,496 | 3,879 | 4,857 | 4,780 | 4,562 | 3,995 | 5,284 | 4,455 |
| | rms. | 767 | 866 | 878 | 913 | 920 | 677 | 417 | 766 | 669 | 709 | 431 | 815 | 484 |
| Mooring line #4 (kN) | mean | 4,765 | 4,809 | 4,751 | 4,667 | 4,728 | 4,701 | 4,796 | 4,411 | 4,419 | 4,803 | 4,691 | 4,609 | 4,711 |
| | min. | 3,349 | 3,193 | 3,194 | 3,326 | 3,345 | 3,384 | 3,697 | 2,887 | 3,404 | 2,937 | 3,625 | 3,328 | 3,677 |
| | max. | 6,906 | 7,073 | 6,613 | 6,224 | 6,704 | 6,747 | 6,335 | 5,550 | 5,900 | 7,231 | 5,956 | 6,580 | 6,598 |
| | rms. | 561 | 591 | 542 | 430 | 483 | 563 | 513 | 462 | 534 | 619 | 452 | 492 | 462 |
| Riser (kN) | mean | 109,800 | 109,800 | 108,700 | 107,300 | 108,100 | 102,900 | 75,360 | 103,700 | 73,270 | 110,500 | 73,870 | 106,400 | 74,360 |
| | min. | 0 | 0 | 0 | 0 | 0 | 0 | 0 | 0 | 0 | 0 | 0 | 0 | 0 |
| | max. | 676,700 | 724,600 | 721,900 | 655,700 | 671,900 | 663,300 | 255,100 | 638,900 | 254,800 | 703,200 | 274,300 | 734,500 | 316,400 |
| | rms. | 132,300 | 131,100 | 130,300 | 127,000 | 128,400 | 120,000 | 5,006 | 120,100 | 45,060 | 131,000 | 48,330 | 125,300 | 49,850 |
| Hawser (kN) | mean | | | | | 101 | | | | 101 | | | | 102 |
| | min. | | | | | 100 | | | | 100 | | | | 100 |
| | max. | | | | | 103 | | | | 104 | | | | 106 |
| | rms. | | | | | 0 | | | | 1 | | | | 1 |

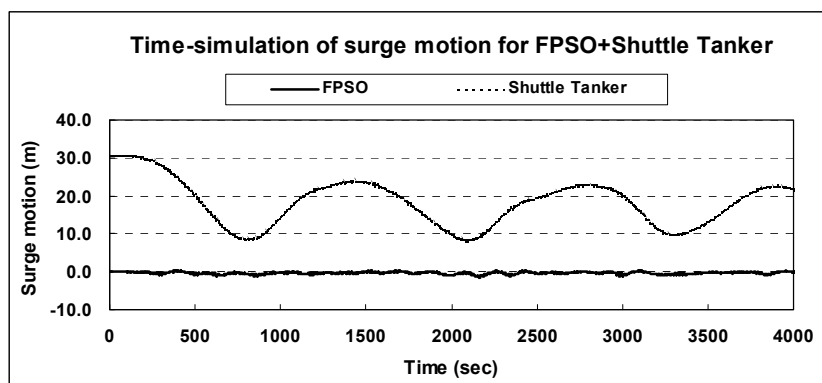
Remarks: 1) Both FPSOs have 4 equivalent mooring lines and 1 equivalent central riser.



(a) The time simulation results of FPSO+shuttle tanker model (without the interaction effect)



(b) The time simulation results of FPSO+shuttle tanker model by the iteration method (with the interaction effect)



(c) The time simulation results of FPSO+shuttle tanker model by the combined method (with the interaction effect)

Figure 9.7 The time simulation results of the FPSO and shuttle tanker model

Table 9.7 Summary of the analysis results for the two-body FPSO+shuttle tanker

| | | Single FPSO | FPSO+Shuttle Tanker ²⁾ | | | | | |
|----------------------|------|----------------|-----------------------------------|---------|--|---------|---|---------|
| | | | w/o interaction | | with interaction by the iteration method | | with interaction by the combined method | |
| | | | with hawser | | with hawser | | with hawser | |
| | | | FPSO | Shuttle | FPSO | Shuttle | FPSO | Shuttle |
| Body Motion | | | | | | | | |
| surge (m) | mean | -0.46 | -0.91 | 21.72 | -0.67 | 16.86 | -0.39 | 17.51 |
| | min. | -2.01 | -5.74 | -6.13 | -2.23 | 6.11 | -1.52 | 8.14 |
| | max. | 0.81 | 1.81 | 54.15 | 0.80 | 33.16 | 0.41 | 24.26 |
| | rms. | 0.51 | 1.54 | 17.69 | 0.62 | 8.10 | 0.35 | 5.09 |
| sway (m) | mean | 0.12 | 0.03 | -0.12 | 0.05 | 2.50 | 0.01 | 3.50 |
| | min. | -0.65 | -0.79 | -8.57 | -1.16 | -2.59 | -1.26 | -2.81 |
| | max. | 0.85 | 0.84 | 5.44 | 1.38 | 8.74 | 1.41 | 9.25 |
| | rms. | 0.28 | 0.39 | 3.62 | 0.48 | 3.70 | 0.47 | 4.11 |
| heave (m) | mean | -0.60 | -0.60 | 0.77 | -0.60 | 0.77 | -0.60 | 0.77 |
| | min. | -1.58 | -1.48 | -2.66 | -1.40 | -1.62 | -1.44 | -1.73 |
| | max. | 0.43 | 0.27 | 4.19 | 0.23 | 3.34 | 0.28 | 3.41 |
| | rms. | 0.27 | 0.26 | 1.15 | 0.27 | 0.86 | 0.26 | 0.87 |
| roll (deg) | mean | 0.00 | 0.00 | 0.00 | 0.00 | 0.00 | 0.00 | 0.00 |
| | min. | -0.47 | -0.26 | -0.66 | -0.11 | -0.23 | -0.32 | -0.34 |
| | max. | 0.51 | 0.28 | 0.65 | 0.10 | 0.23 | 0.33 | 0.34 |
| | rms. | 0.14 | 0.05 | 0.13 | 0.01 | 0.06 | 0.11 | 0.08 |
| pitch (deg) | mean | 0.21 | 0.21 | -0.27 | 0.21 | -0.27 | 0.21 | -0.27 |
| | min. | -0.51 | -0.39 | -1.66 | -0.36 | -1.28 | -0.33 | -1.31 |
| | max. | 0.97 | 0.84 | 1.16 | 0.81 | 0.69 | 0.79 | 0.73 |
| | rms. | 0.20 | 0.20 | 0.48 | 0.20 | 0.34 | 0.19 | 0.35 |
| yaw (deg) | mean | 0.98 | 0.48 | 3.20 | -0.38 | 5.02 | -5.71 | 10.62 |
| | min. | -1.21 | -2.99 | -2.46 | -2.56 | 0.62 | -7.67 | 4.50 |
| | max. | 2.52 | 2.72 | 7.54 | 2.34 | 10.17 | -0.07 | 14.75 |
| | rms. | 1.11 | 0.16 | 3.11 | 1.13 | 2.69 | 1.68 | 2.84 |
| Line Tension | | | | | | | | |
| Mooring line #1 (kN) | mean | 4,268 | 4,339 | | 4,298 | | 4,257 | |
| | min. | 4,086 | 3,944 | | 4,094 | | 4,122 | |
| | max. | 4,487 | 5,050 | | 4,509 | | 4,428 | |
| | rms. | 74 | 232 | | 89 | | 51 | |
| Mooring line #2 (kN) | mean | 4,174 | 4,187 | | 4,184 | | 4,189 | |
| | min. | 3,974 | 4,018 | | 3,946 | | 3,965 | |
| | max. | 4,350 | 4,375 | | 4,408 | | 4,397 | |
| | rms. | 57 | 67 | | 78 | | 75 | |
| Mooring line #3 (kN) | mean | 4,115 | 4,051 | | 4,086 | | 4,126 | |
| | min. | 3,811 | 3,374 | | 3,779 | | 3,918 | |
| | max. | 4,367 | 4,508 | | 4,375 | | 4,353 | |
| | rms. | 93 | 225 | | 104 | | 74 | |
| Mooring line #4 (kN) | mean | 4,210 | 4,197 | | 4,200 | | 4,195 | |
| | min. | 4,041 | 4,019 | | 3,967 | | 3,991 | |
| | max. | 4,422 | 4,353 | | 4,449 | | 4,433 | |
| | rms. | 54 | 67 | | 78 | | 78 | |
| Riser (kN) | mean | 69,550 | 69,530 | | 69,490 | | 69,560 | |
| | min. | 0 | 0 | | 0 | | 0 | |
| | max. | 164,900 | 150,600 | | 146,600 | | 151,300 | |
| | rms. | 24,730 | 24,170 | | 24,410 | | 23,730 | |
| Hawser (kN) | mean | | 254 | | 119 | | 79 | |
| | min. | | 5 | | 6 | | 6 | |
| | max. | | 844 | | 296 | | 252 | |
| | rms. | | 254 | | 86 | | 77 | |

2) The loading condition is changed for this calculation, which is intended to investigate the difference with the results by three methods in a mild loading condition (West Africa sea condition). The wind velocity is 10 m/s at 10 m height, the current speed is 0.15 m/s at free surface, and the wave has Hs of 2.7 m, Tp of 16.5 sec, and gamma of 6.0.

9.6 Results and Discussion

In Table 9.5, the statistics of the analysis results for the mass-spring model is shown. The analysis results for the FPSO and FPSO model are summarized in Table 9.6. The two tables show that the statistical results are well matched with each other. In Figure 9.6(a)~(d), the displacements in x-direction (surge motion) by the time simulation analyses for the mass-spring model and the FPSO and FPSO model when the mooring is in tandem arrangement are depicted. The hawser stiffness used for this analysis was $1/100^{\text{th}}$ of the mooring stiffness, and the top tension of the hawser was taken as $1/10^{\text{th}}$ of the mooring line tension. The surge motion amplitude for each case is very similar, so that the validity of the program WINPOST-MULT for the two-body analysis with one hawser is proved. However, whether the interaction effect is considered or not affects the shape and the phase difference between surge motions of two bodies in the time simulation. The time simulation results are shown for the purpose of comparison in Figure 9.7.

In Table 9.7, the analysis cases for the two-body model of an FPSO and a shuttle tanker are summarized for three different cases. The hawser stiffness used for this analysis was $1/1000^{\text{th}}$ of the mooring stiffness, and the top tension of the hawser was taken as $1/10^{\text{th}}$ of the mooring line tension. In the case of “no interaction”, the hydrodynamic coefficients induced by wave, the body stiffness matrix and mass matrix have only the terms for the single body, and the interaction terms are set to zero. That means, in this case, the interaction effect between two vessels of the fluid and the structures is not considered. In the case of the “with the interaction effect by iteration

method” for the two-body model, the self-coupling terms in the hydrodynamic coefficients, the two-body stiffness matrix and the two-body mass matrix are only considered. Thus, the interaction terms between two bodies are set to zero. In the case of the “with the interaction effect by the combined method”, the fully coupled matrices are used for the analysis. The purpose of this study is to compare the analyzed results by the developed program with the results produced by the methods used in the industry. The program WINPOST-MULT has the kind function of performing the above three cases by handling the system matrix or the hydrodynamic coefficient matrices. In Table 9.7, to review the results of all cases can make some clues drawn about the hawser connection effect and the hydrodynamic interaction effect between two bodies. In all motions at the rear side vessel, the interaction and hawser effects are clearly illustrated. In the two-body model of the FPSO and shuttle tanker, the analysis results for the case of “with interaction by the iteration method” give medium values among the results for the cases of “with no interaction” and “with interaction by the combined method”. It means that it is significant to consider the fully coupled interaction effect for the two-body analysis.

From Figures 9.8a through 9.10d, the time histories and the motion amplitude spectra are shown for all analysis cases. To review the motion amplitude spectrum for each case, the vessels have almost the same characteristics in their dynamic behaviors.

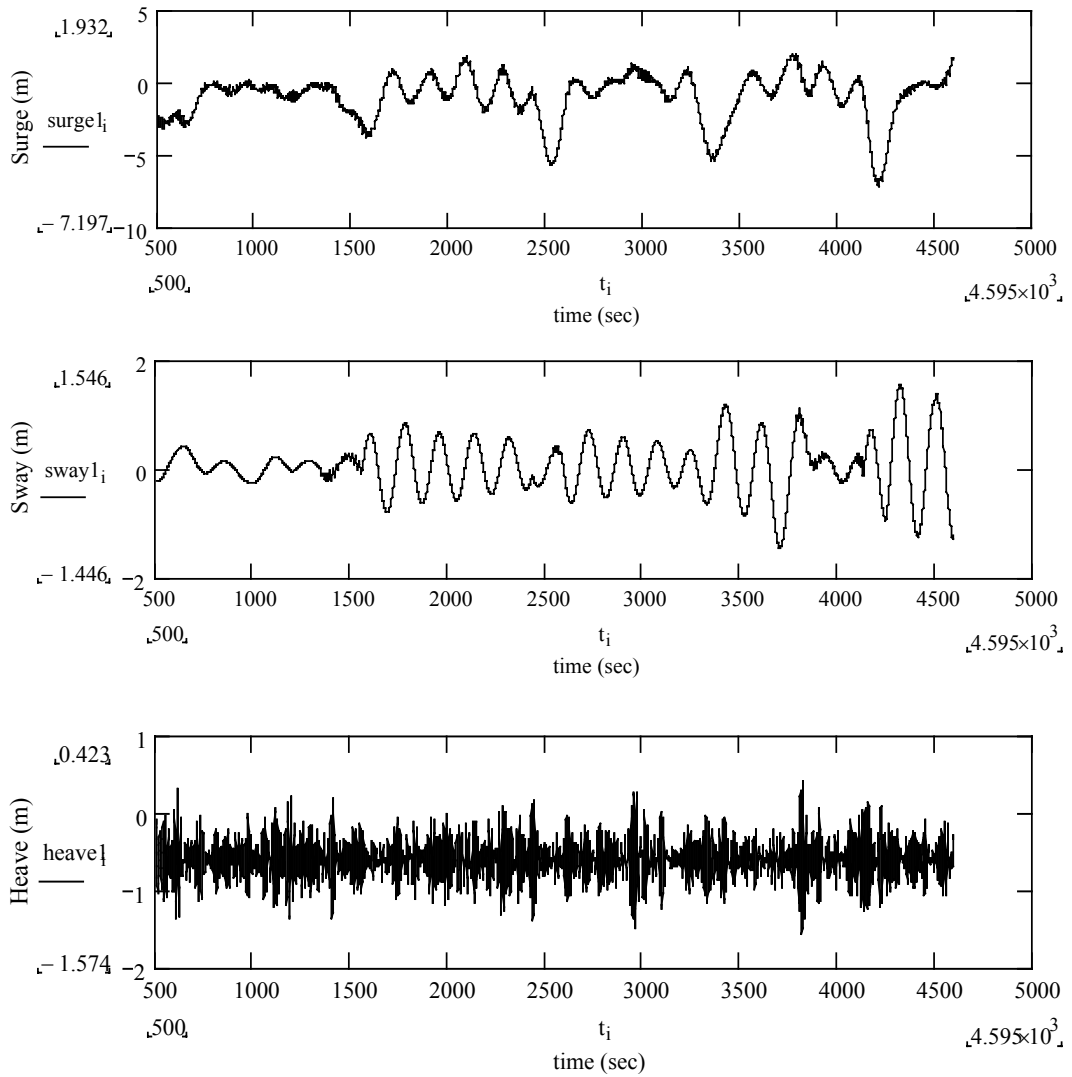


Figure 9.8.a Time simulation for the two body model of the FPSO and shuttle tanker (at body #1=FPSO; tandem; without interaction effect)

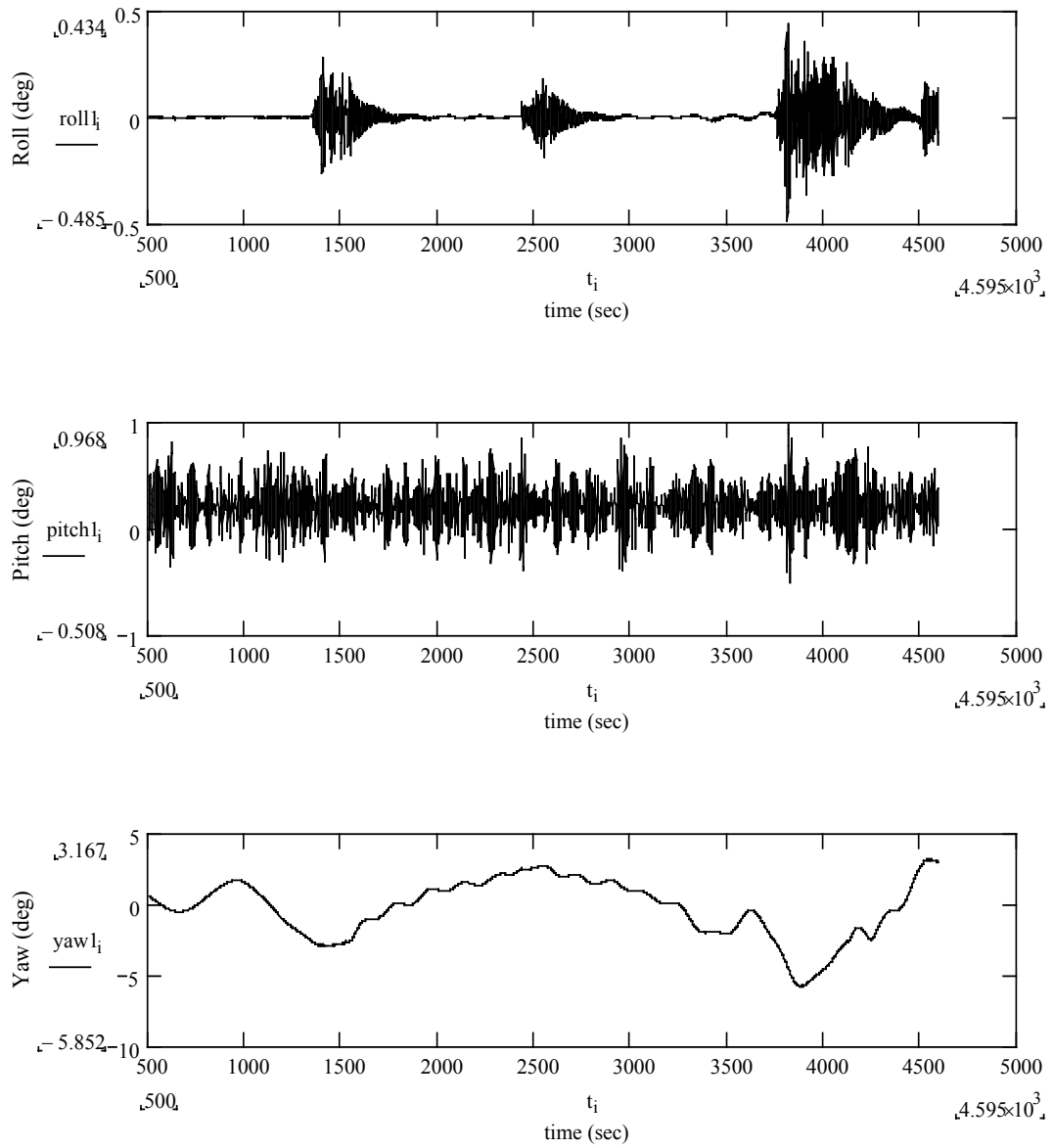


Figure 9.8.a Continued

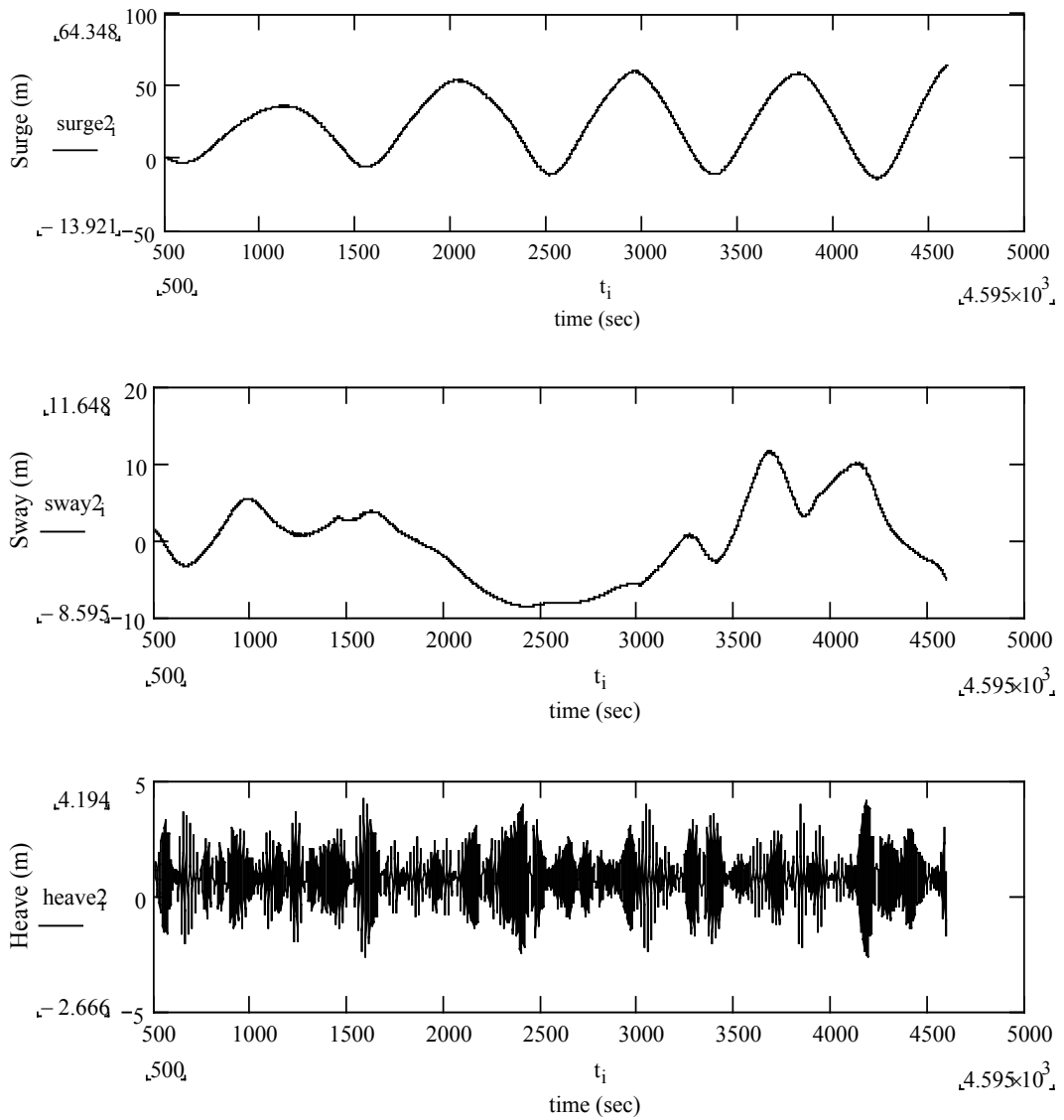
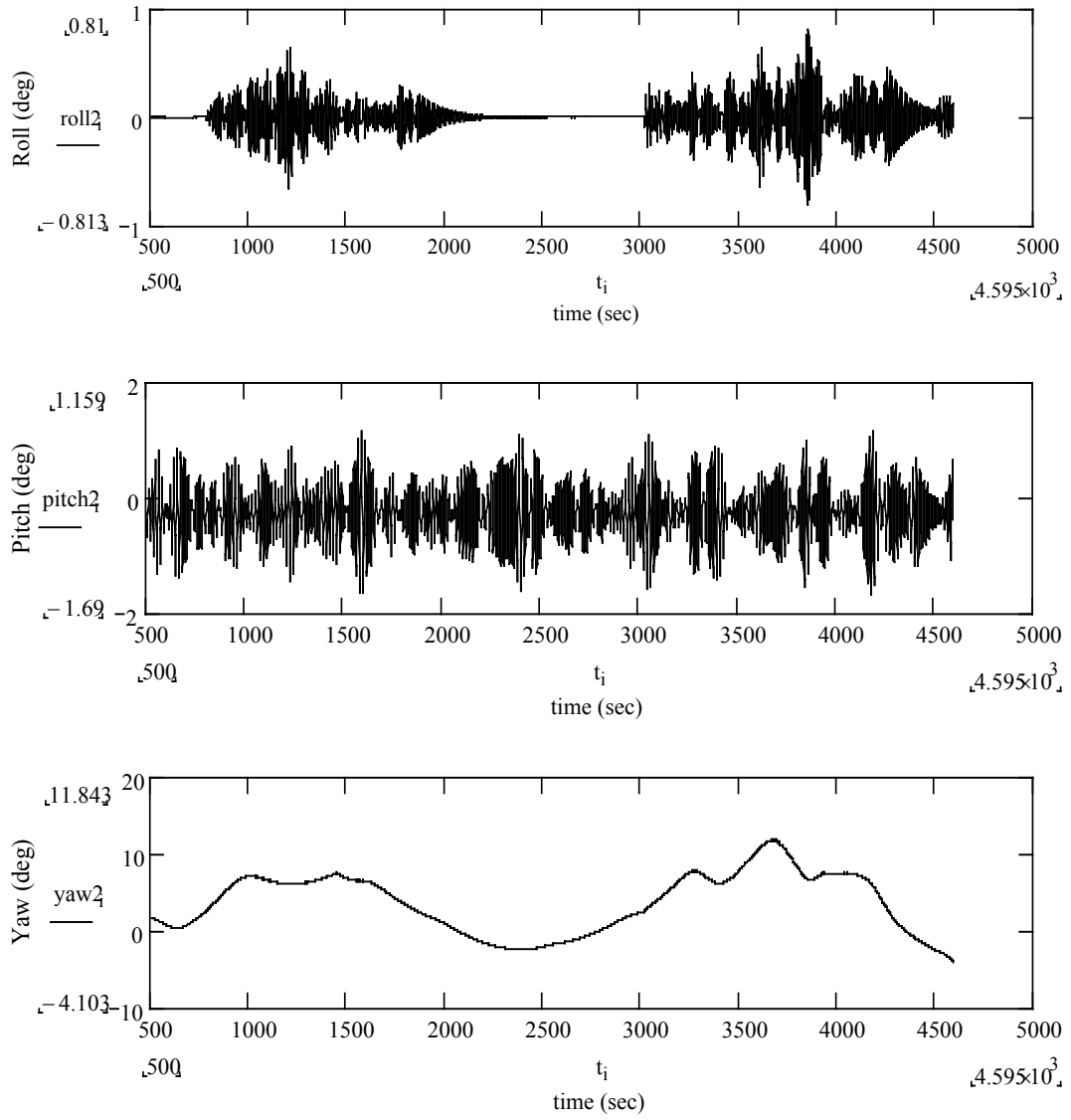


Figure 9.8.b Time simulation for the two body model of the FPSO and shuttle tanker (at body #2=shuttle tanker; tandem; without interaction effect)

**Figure 9.8.b Continued**

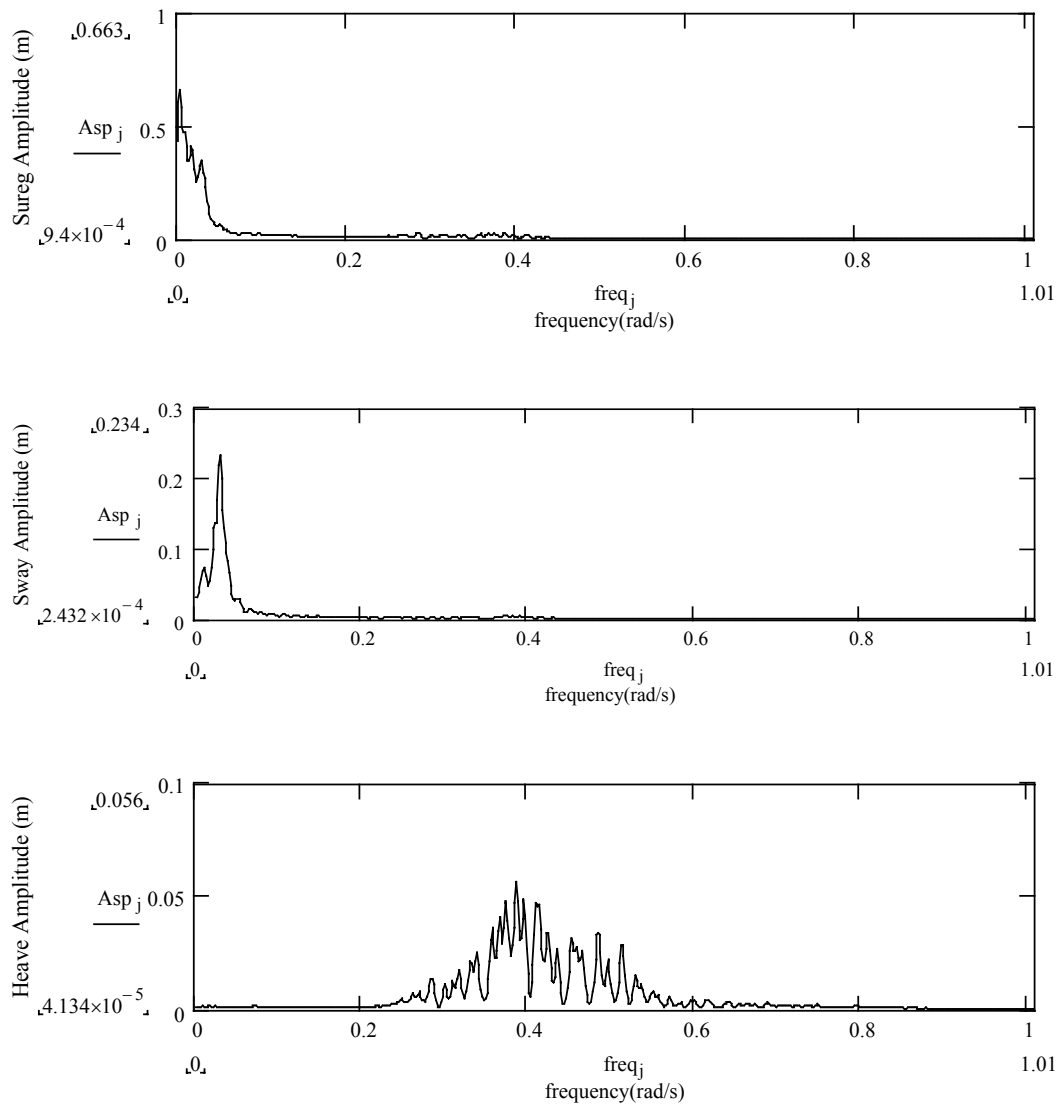


Figure 9.8.c Amplitude spectrum density curve of the motion responses for the two body model of the FPSO and shuttle tanker (at body #1=FPSO; tandem; without interaction effect)

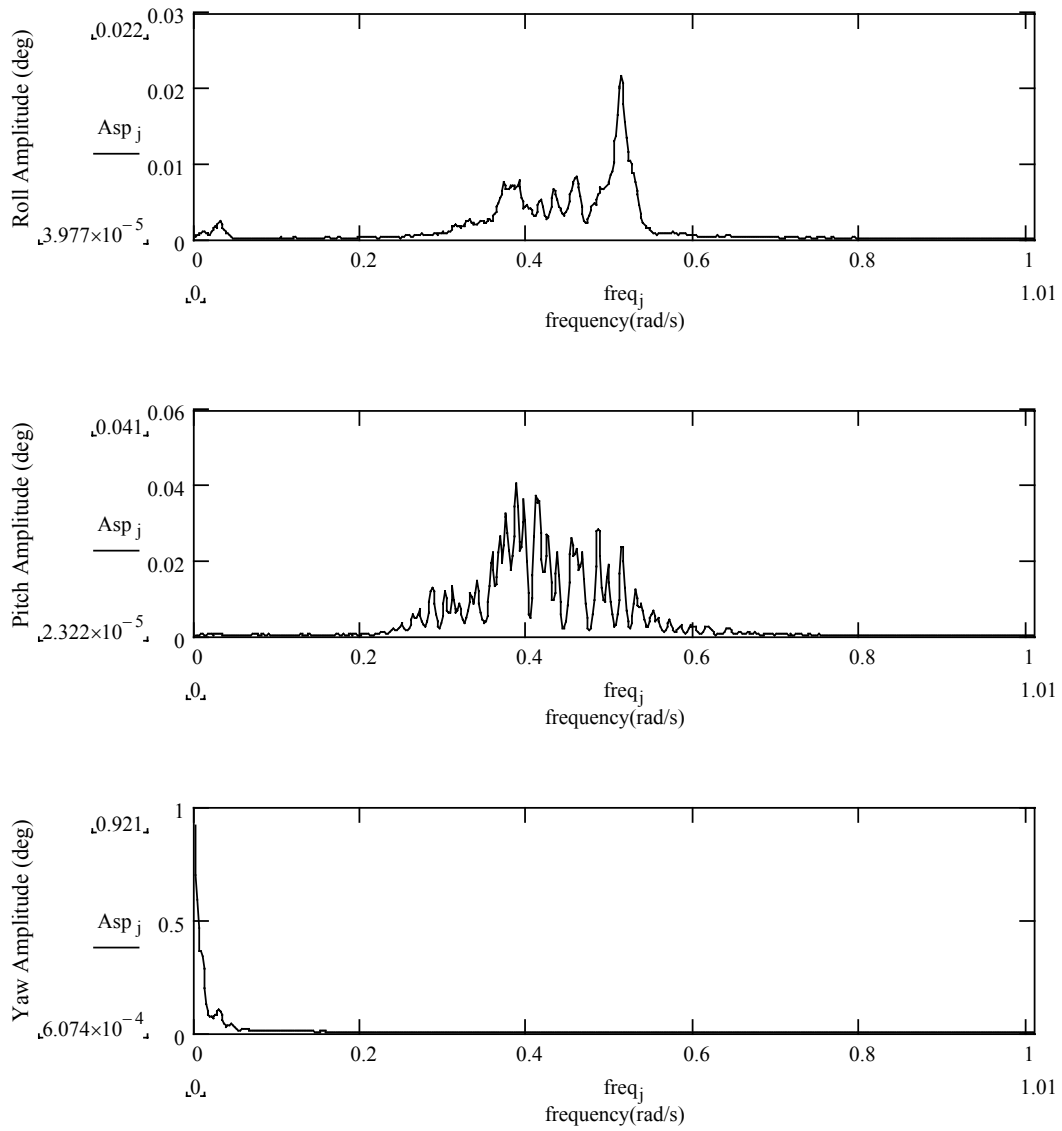


Figure 9.8.c Continued

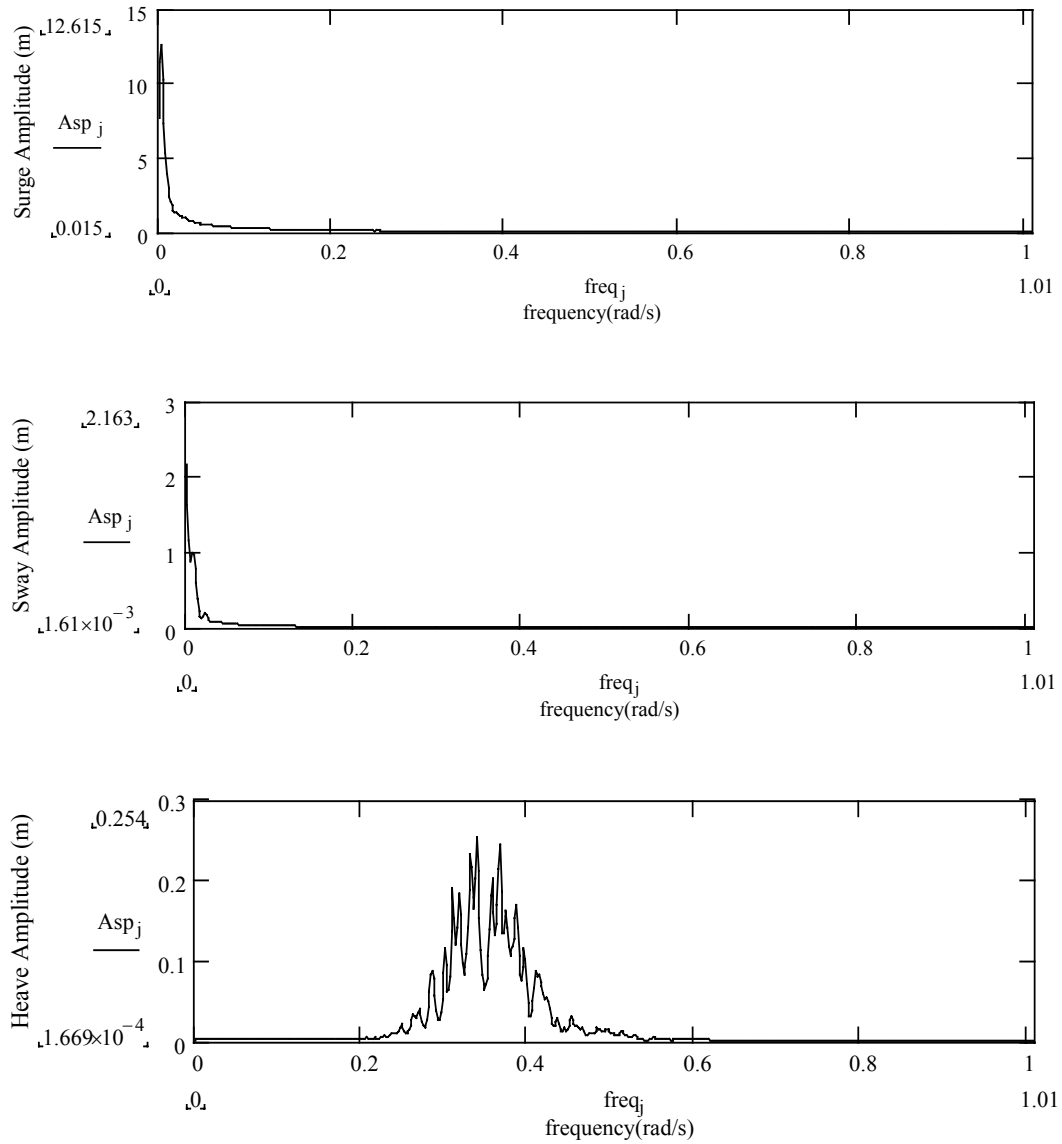


Figure 9.8.d Amplitude spectrum density curve of the motion responses for the two body model of the FPSO and shuttle tanker (at body #2=shuttle tanker; tandem; without interaction effect)

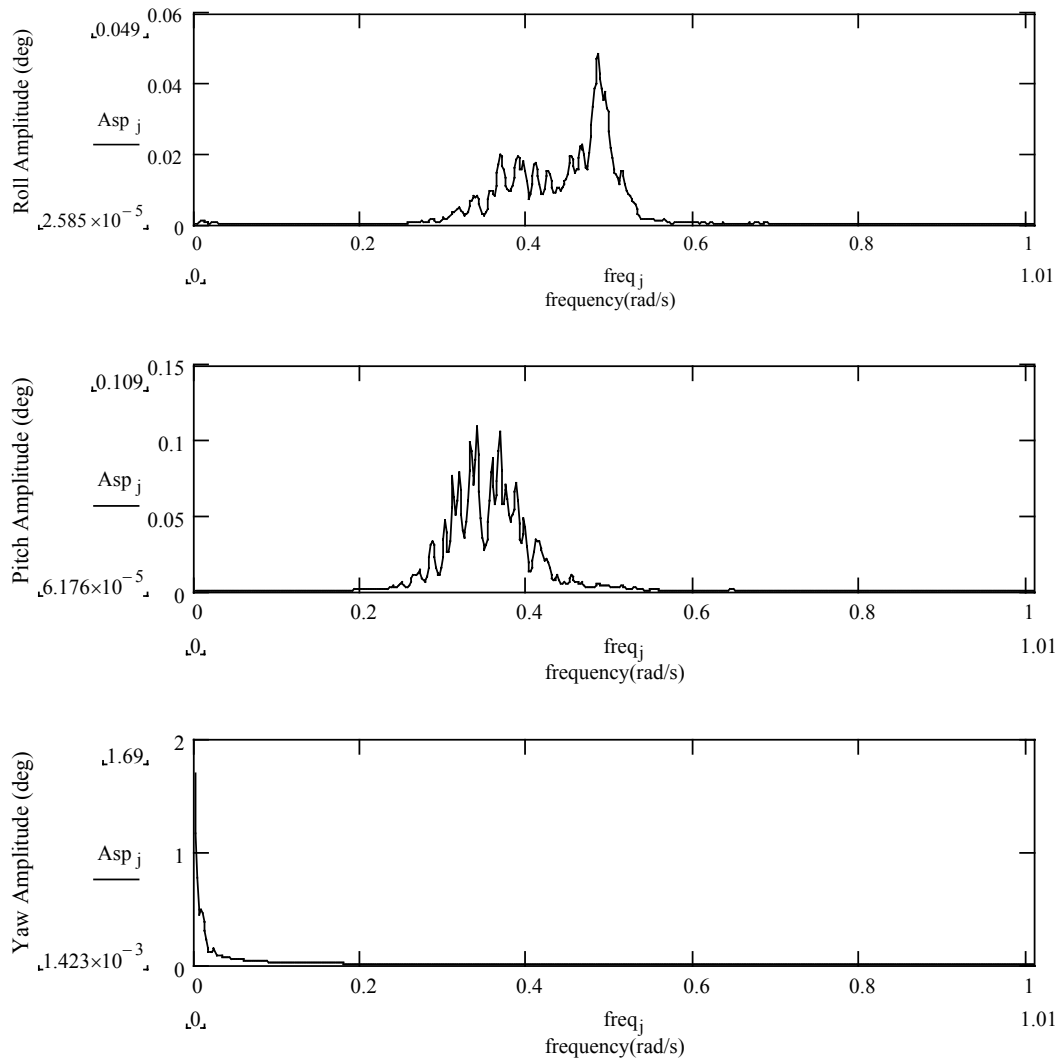


Figure 9.8.d Continued

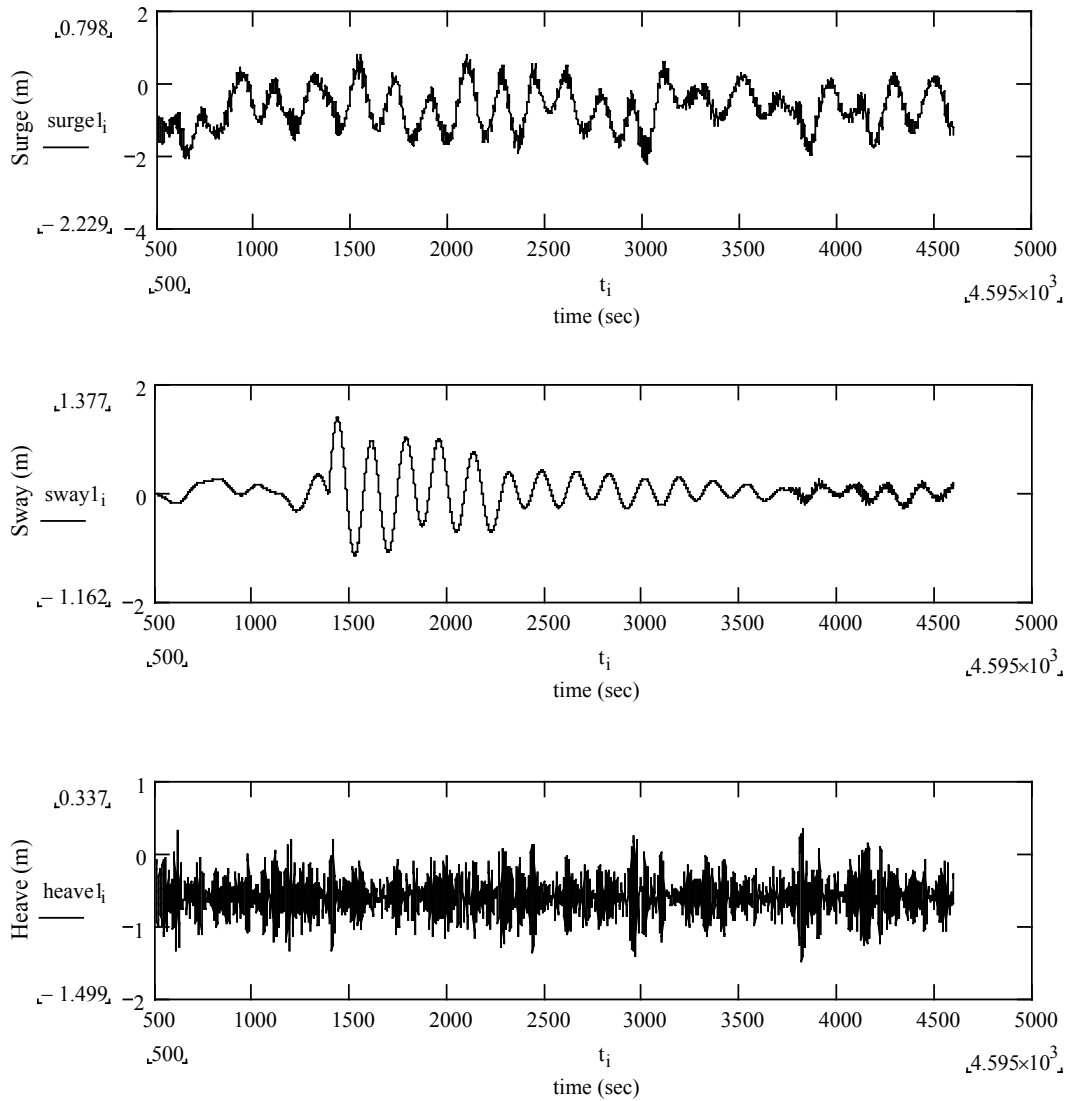


Figure 9.9.a Time simulation the for two body model of the FPSO and shuttle tanker (at body #1=FPSO; tandem; with interaction effect by iteration method)

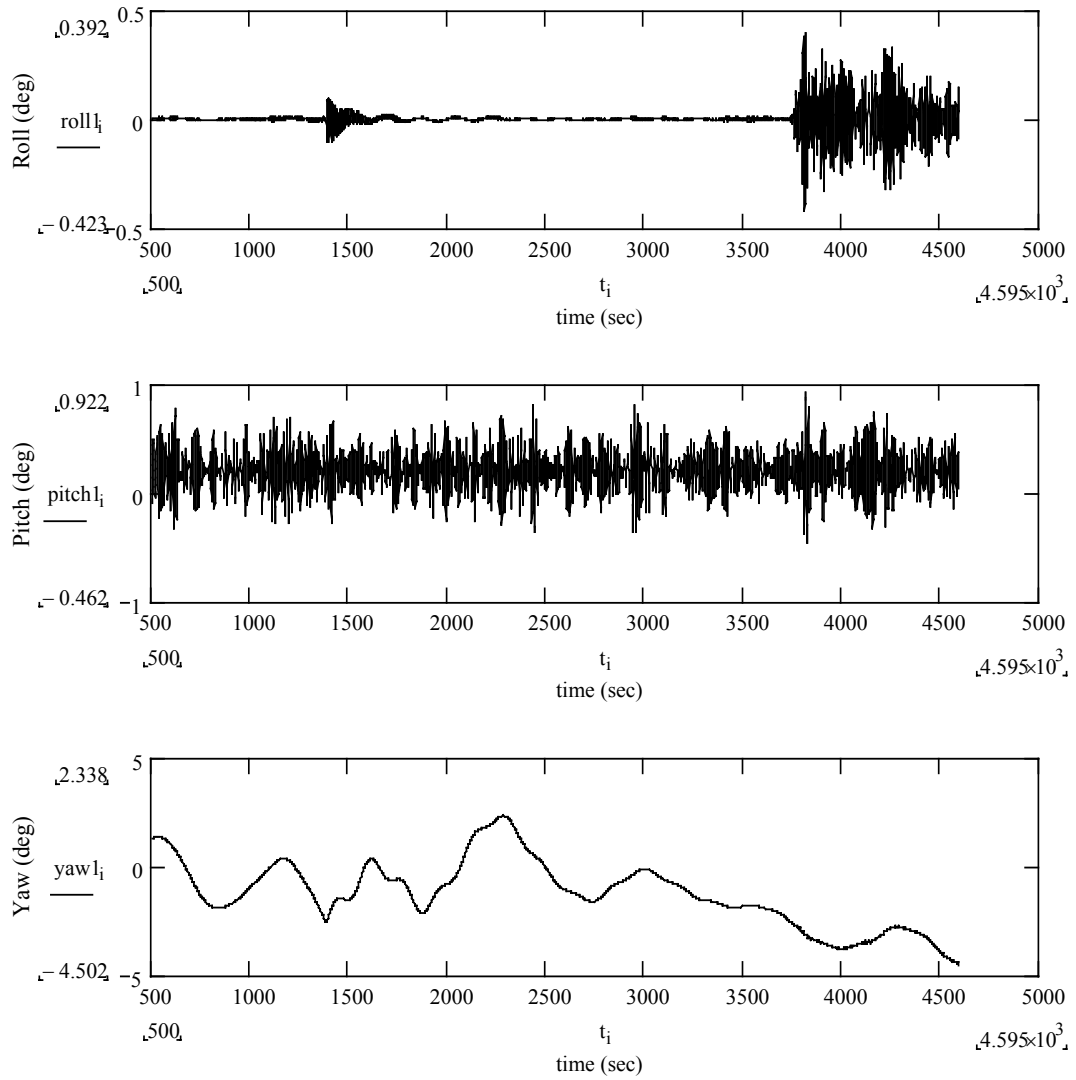
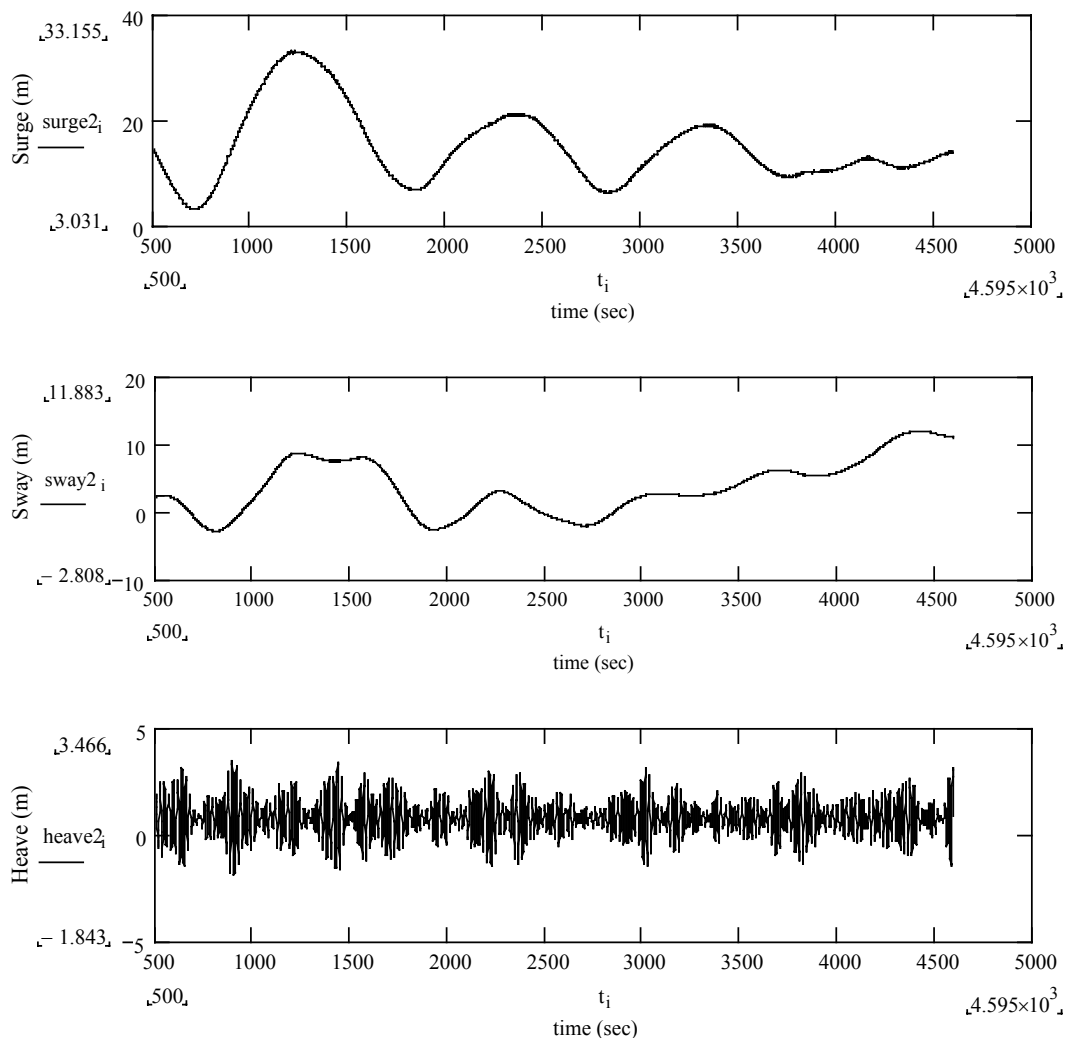


Figure 9.9.a Continued



**Figure 9.9.b Time simulation for the two body model of the FPSO and shuttle tanker
(at body #2=shuttle tanker; tandem; with interaction effect by iteration method)**

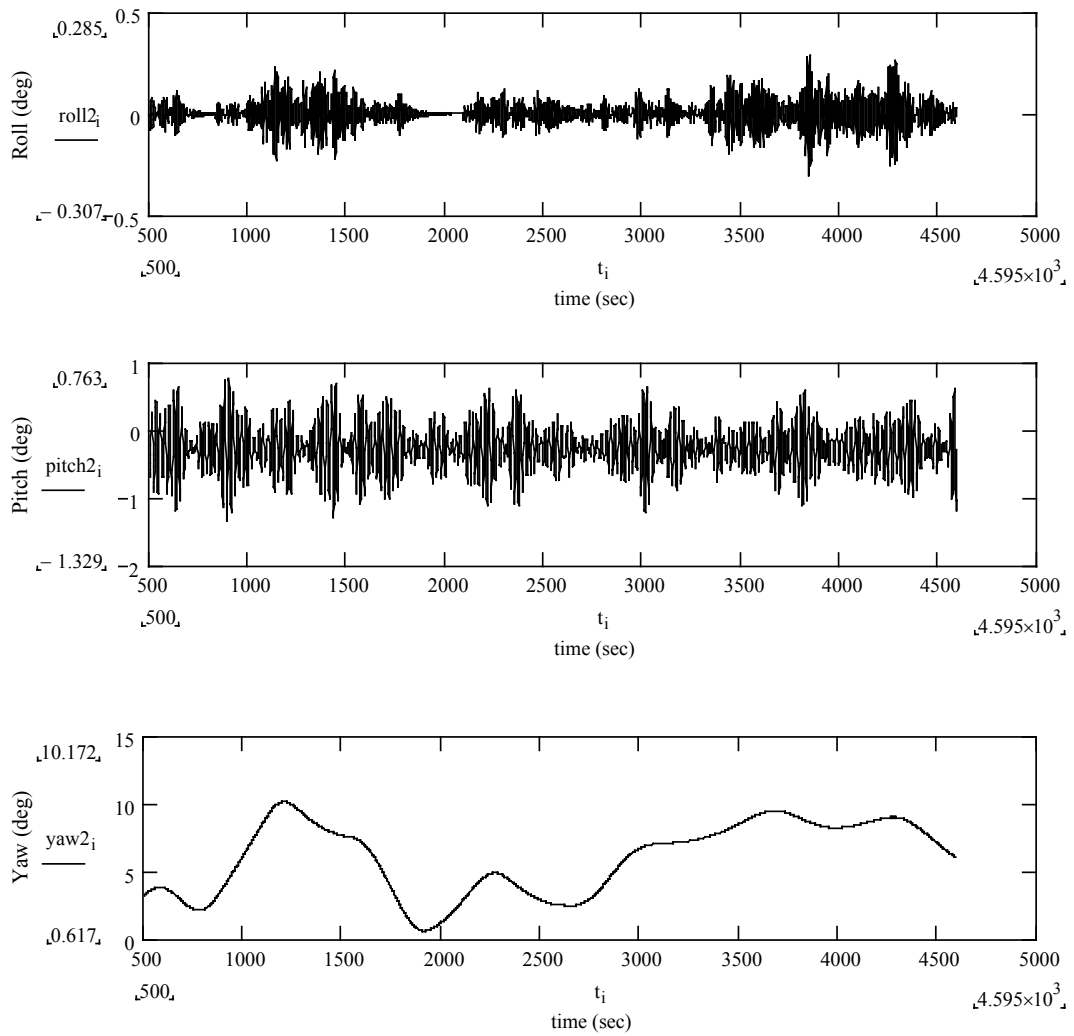


Figure 9.9.b Continued

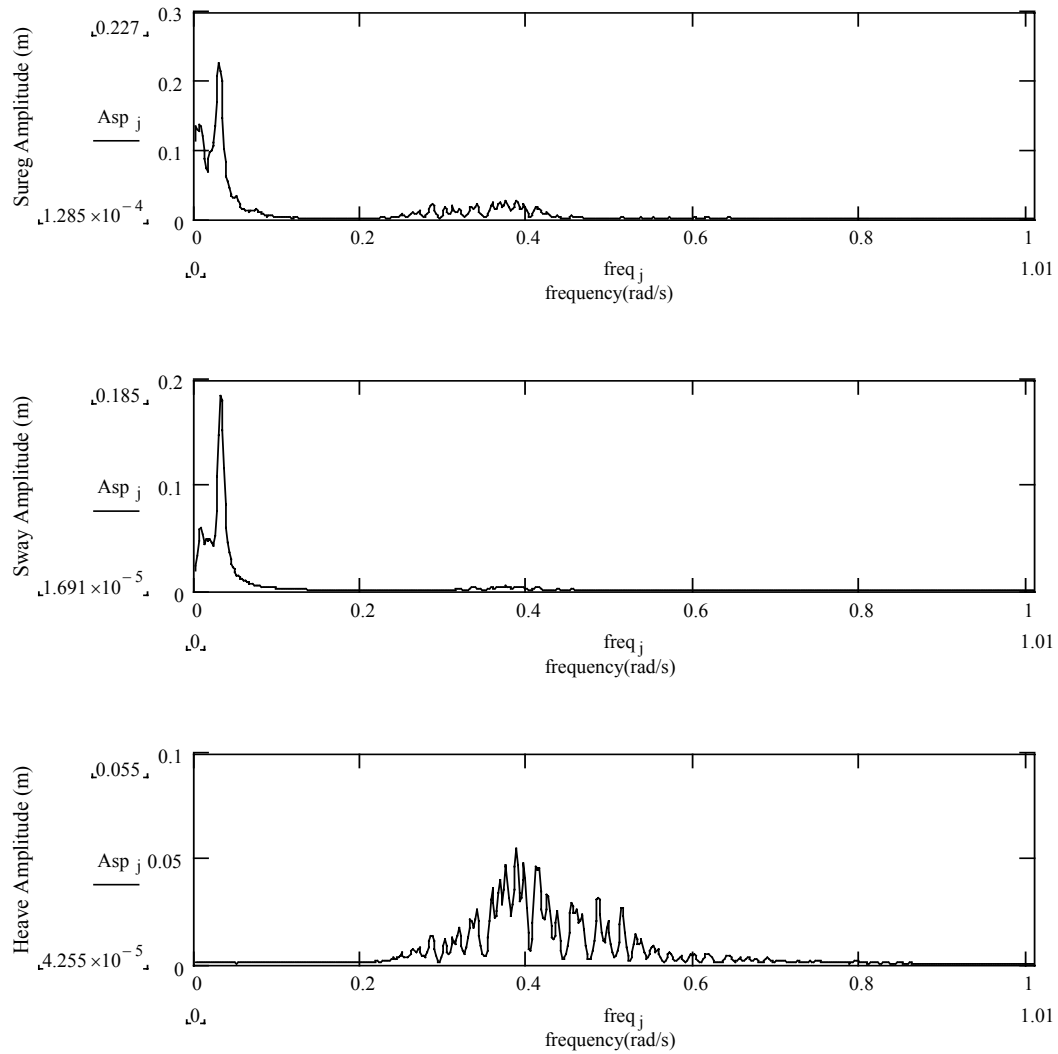


Figure 9.9.c Amplitude spectrum density curve of the motion responses for the two body model of the FPSO and shuttle tanker (at body #1=FPSO; tandem; with interaction effect by iteration method)

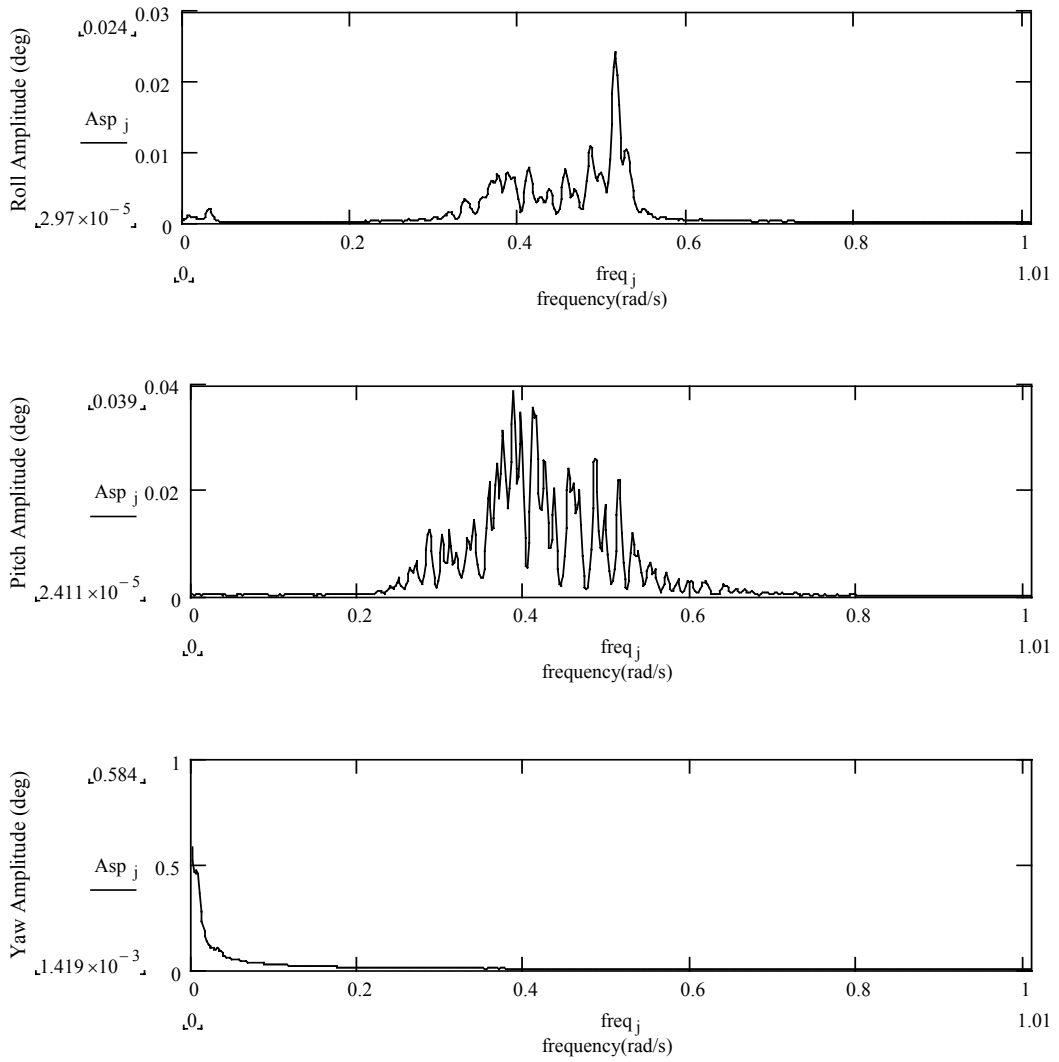


Figure 9.9.c Continued

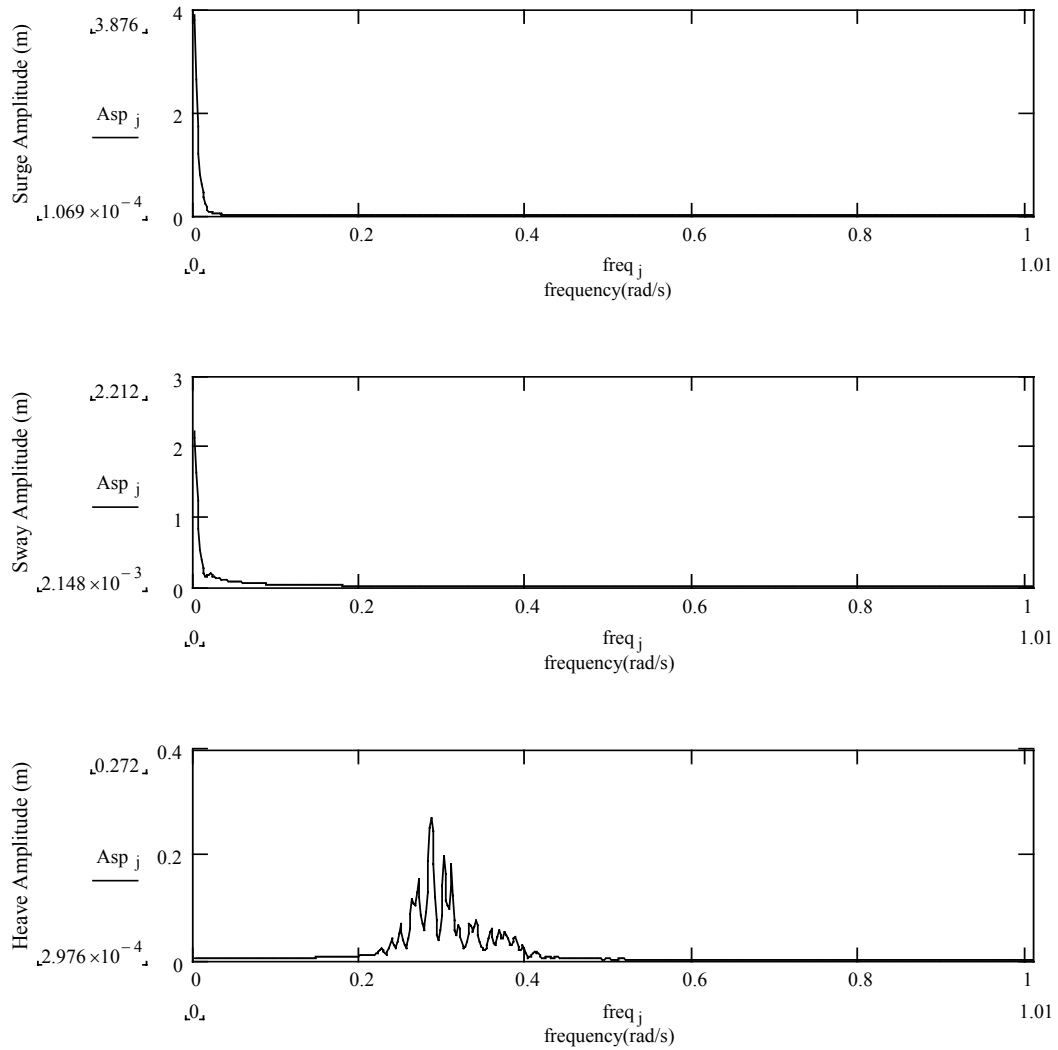


Figure 9.9.d Amplitude spectrum density curve of the motion responses for the two body model of the FPSO and shuttle tanker (at body #2=shuttle tanker; tandem; with interaction effect by iteration method)

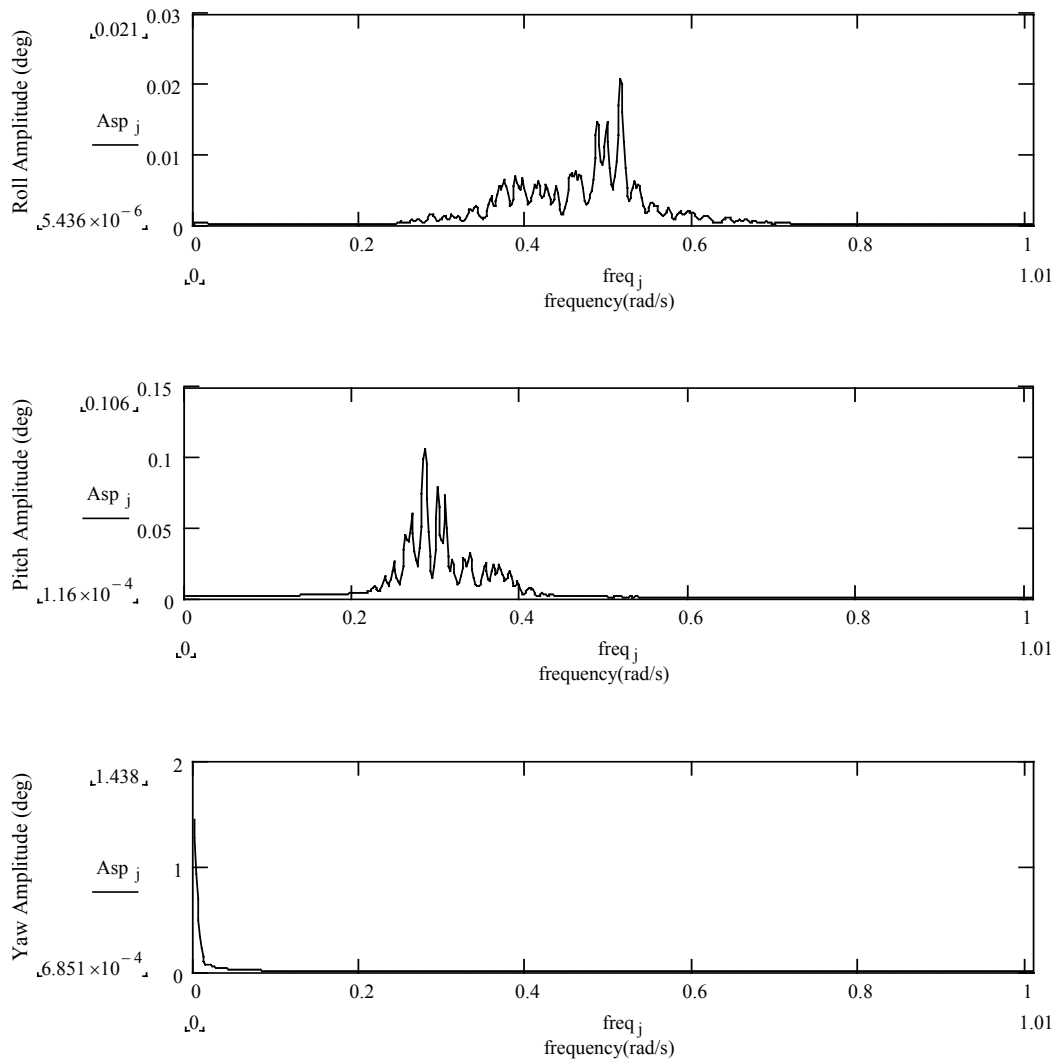
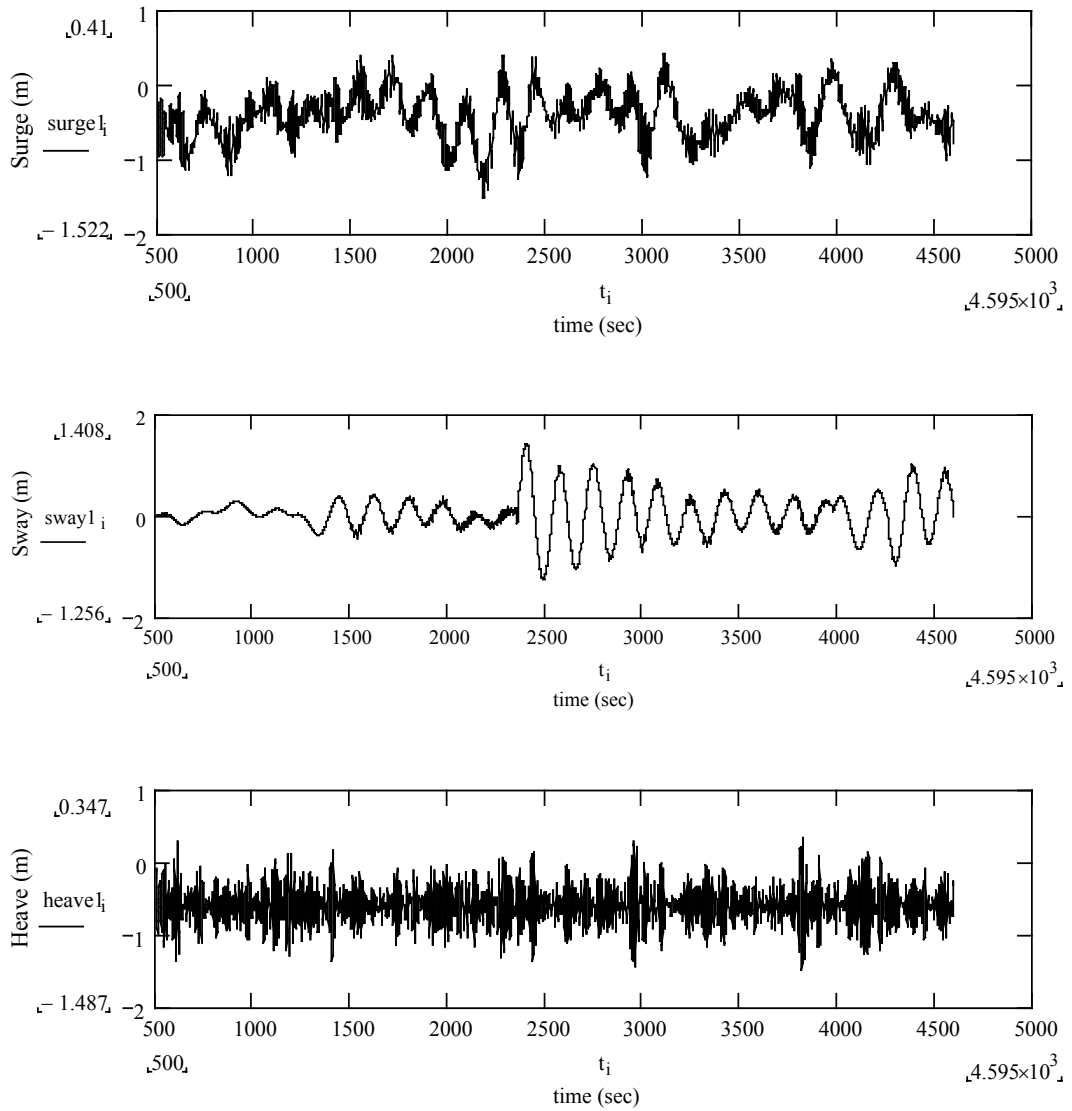


Figure 9.9.d Continued



**Figure 9.10.a Time simulation for the two body model of the FPSO and shuttle tanker
(at body #1=FPSO; tandem; with interaction effect by combined method)**

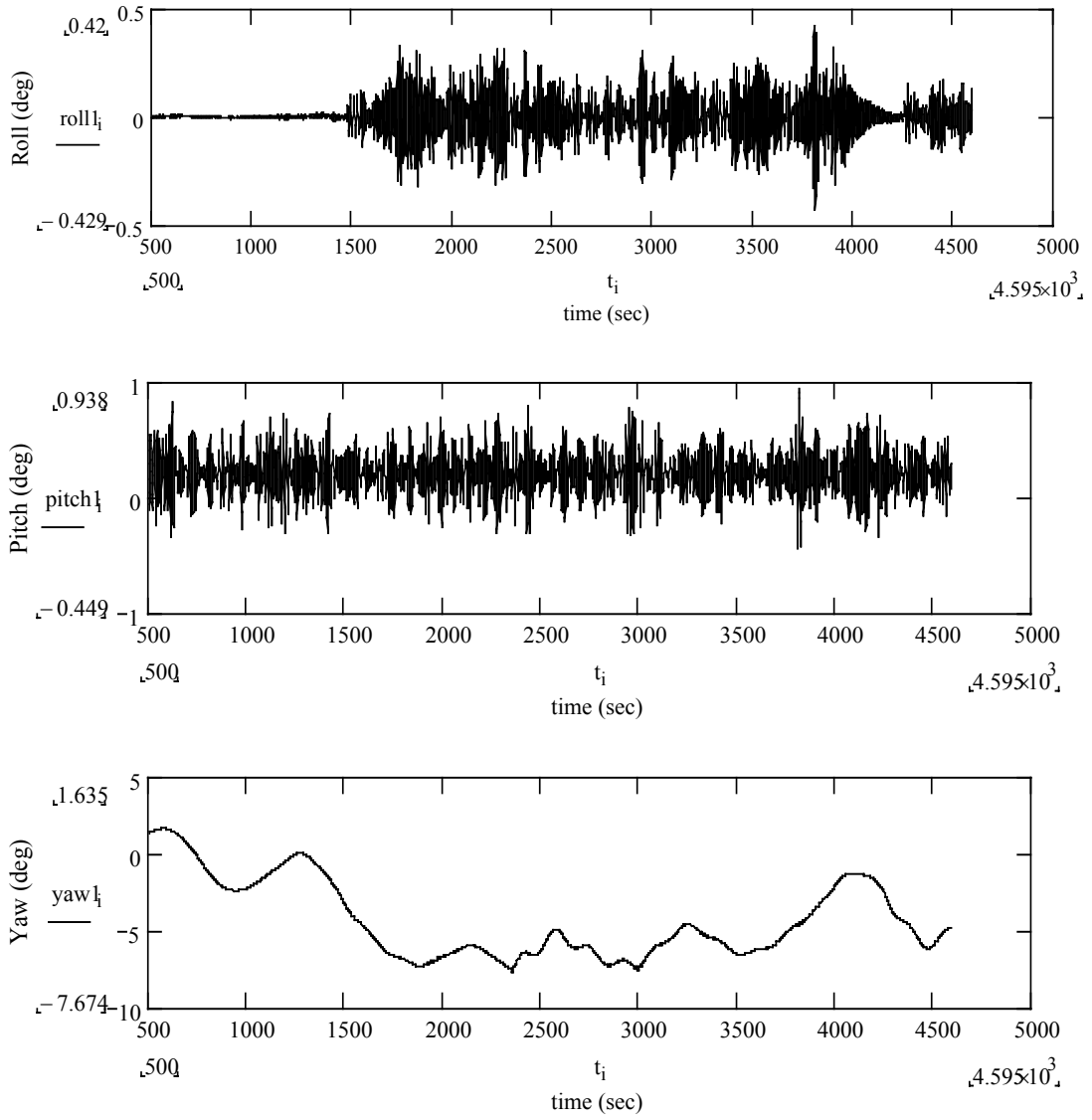


Figure 9.10.a Continued

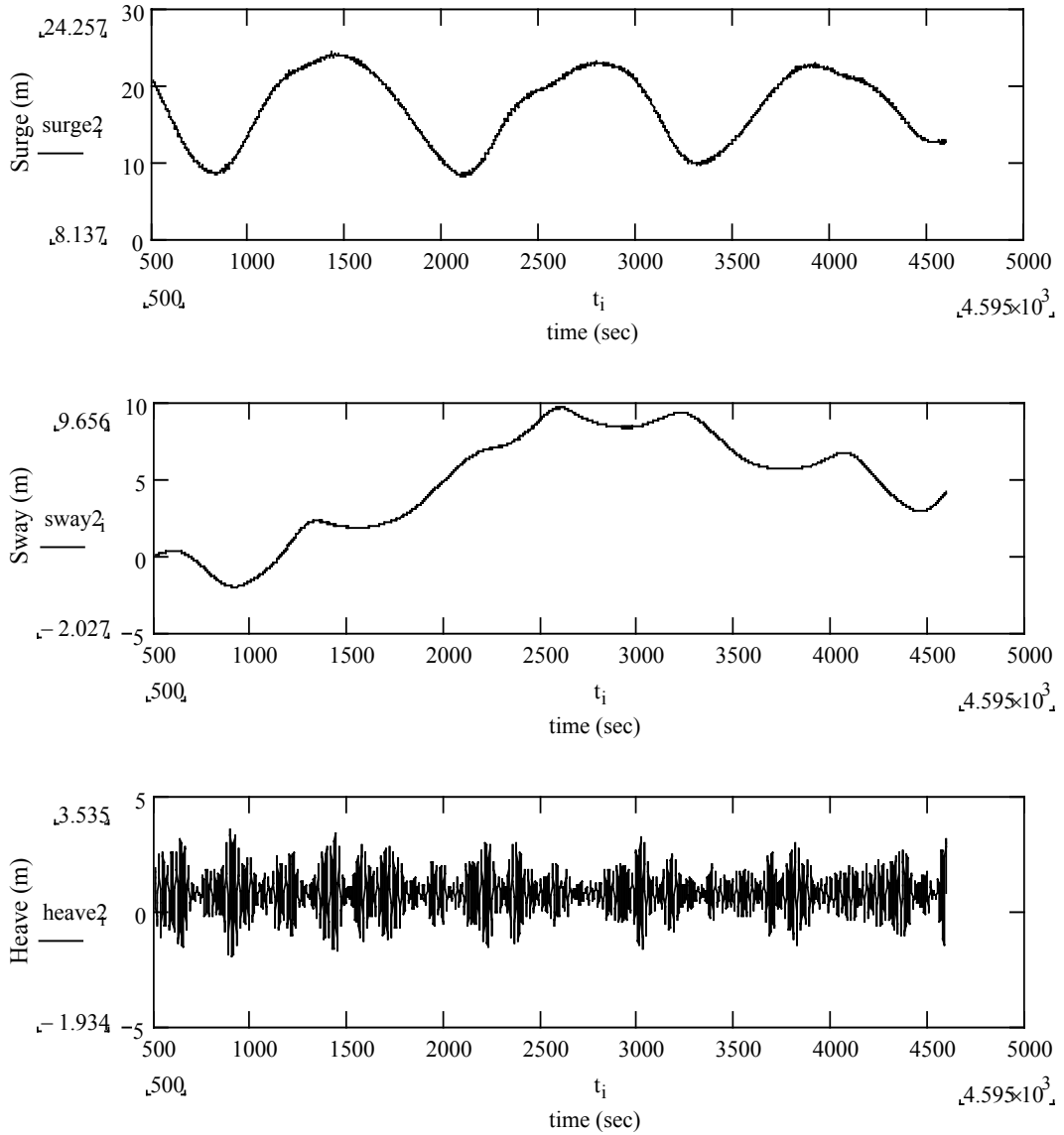


Figure 9.10.b Time simulation for the two body model of the FPSO and shuttle tanker (at body #2=shuttle tanker; tandem; with interaction effect by combined method)

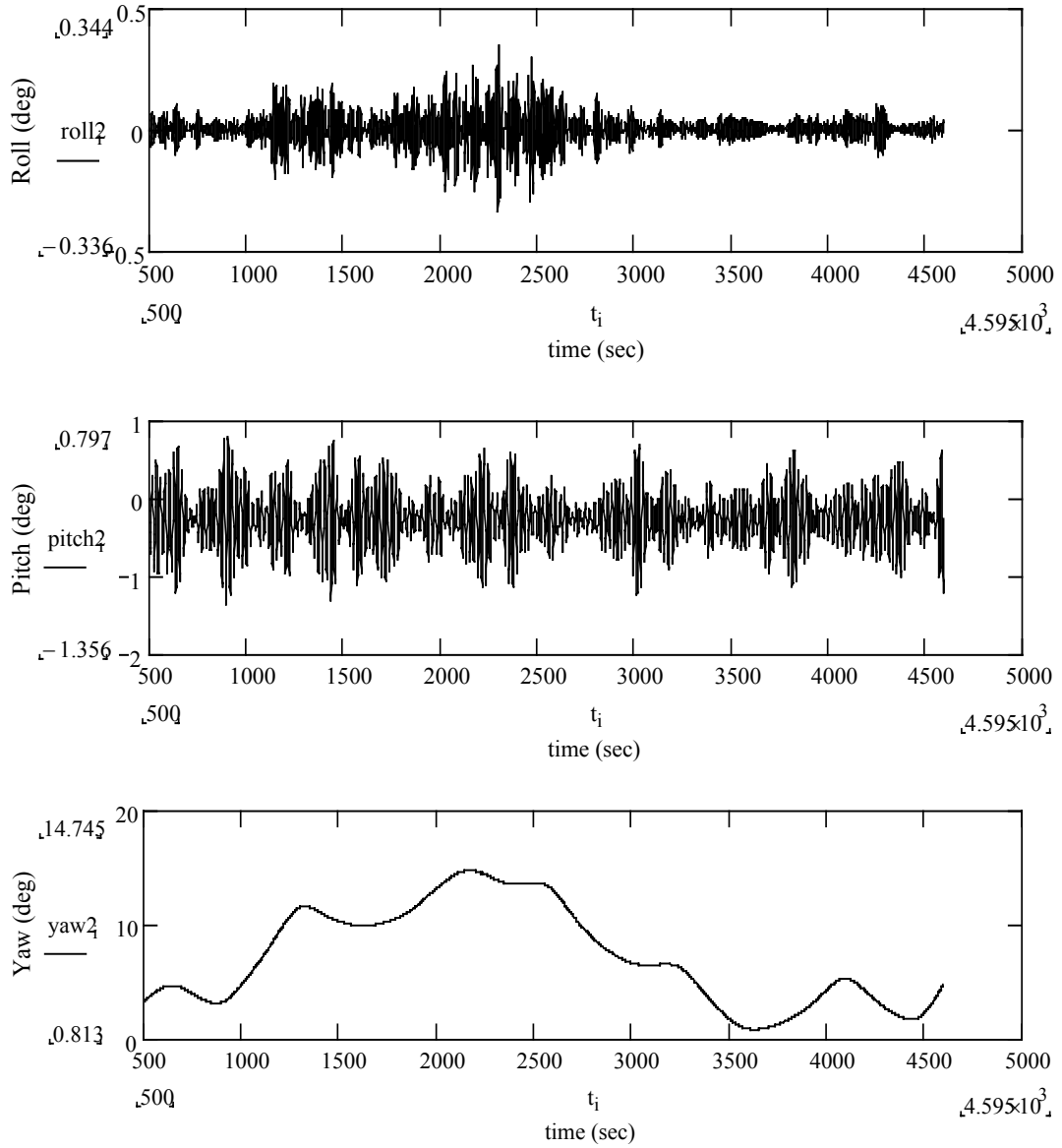


Figure 9.10.b Continued

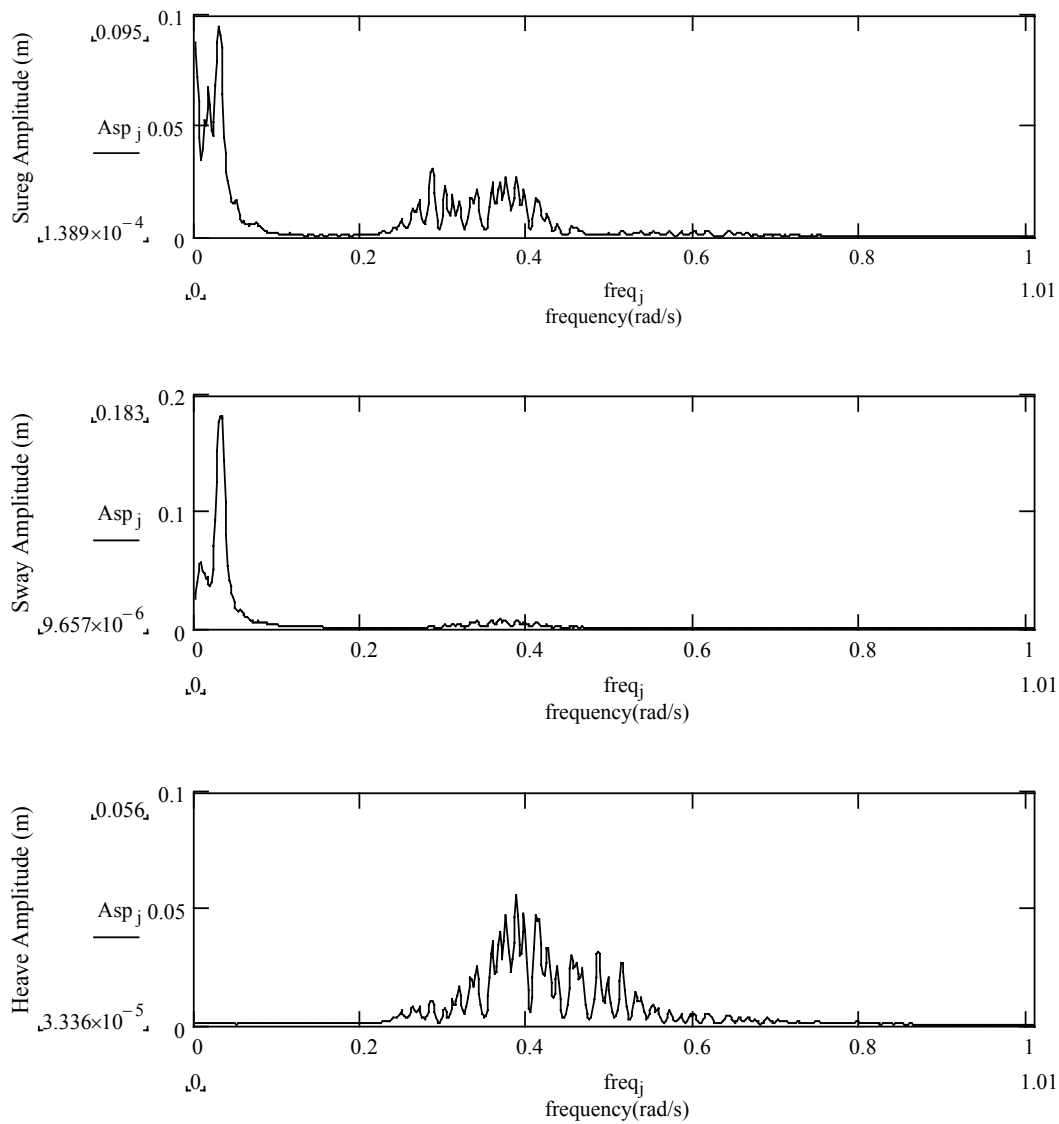


Figure 9.10.c Amplitude spectrum density curve of the motion responses for the two body model of the FPSO and shuttle tanker (at body #1=FPSO; tandem; with interaction effect by combined method)

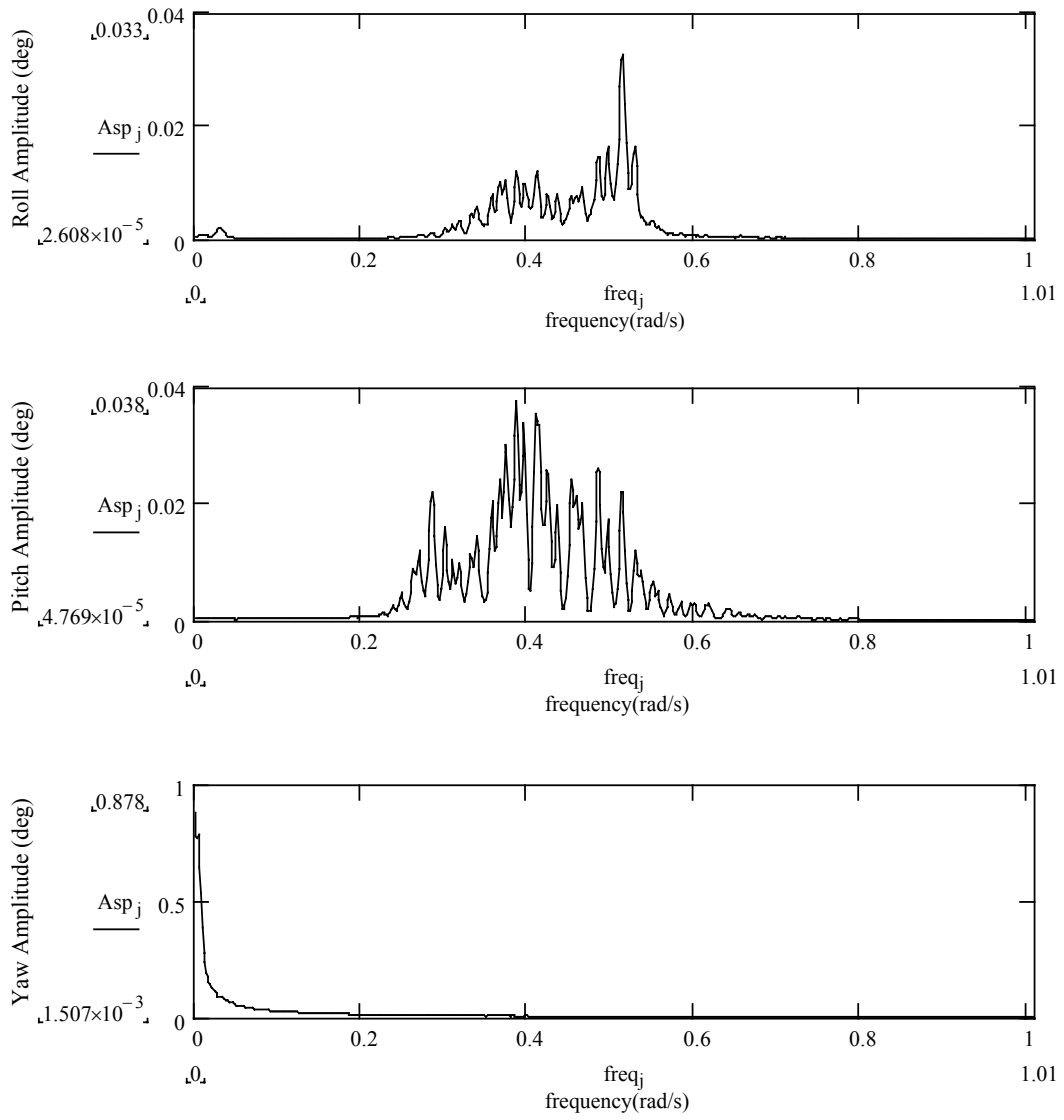


Figure 9.10.c Continued

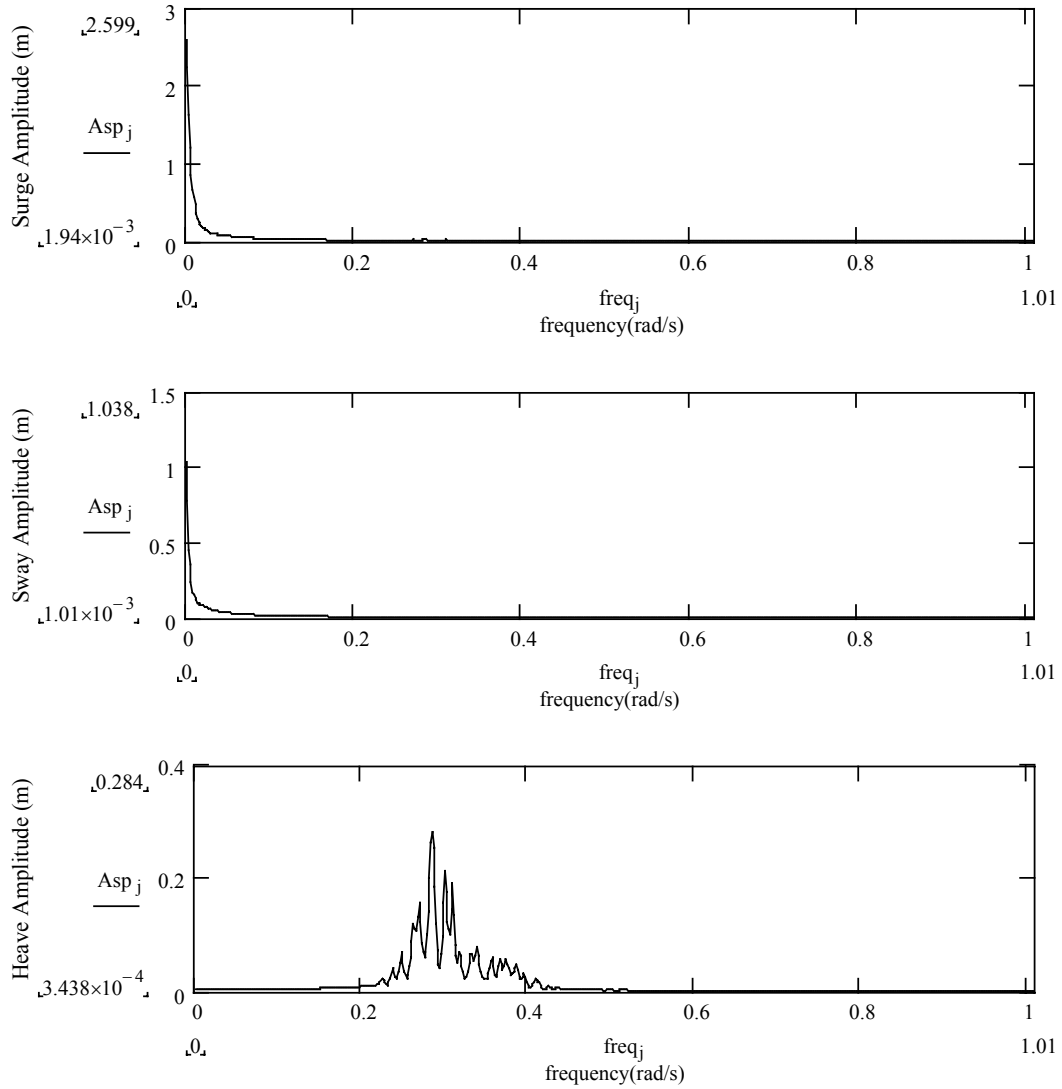


Figure 9.10.d Amplitude spectrum density curve of the motion responses for the two body model of the FPSO and shuttle tanker (at body #2=shuttle tanker; tandem; with interaction effect by combined method)

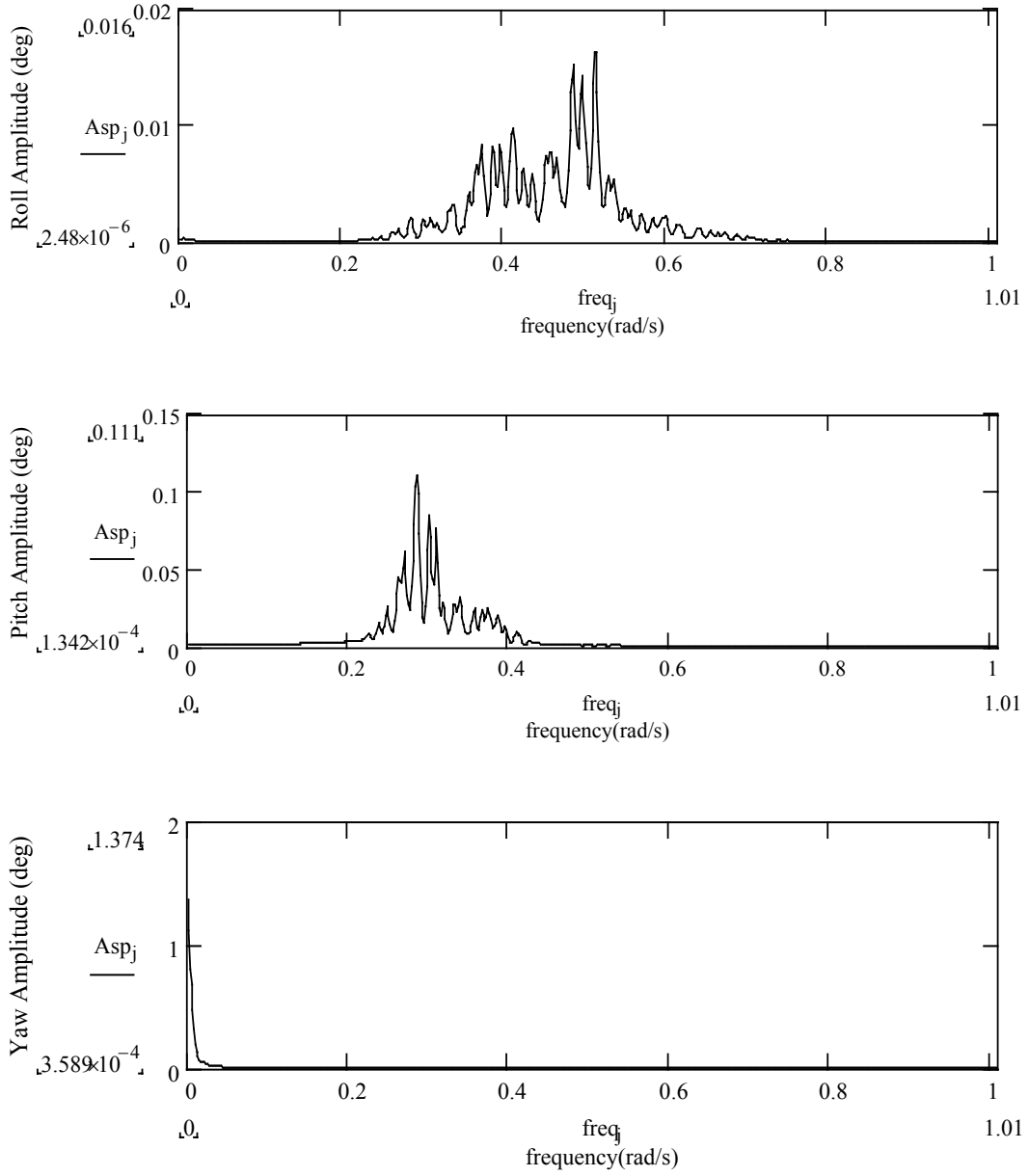


Figure 9.10.d Continued

9.7 Summary and Conclusions

The hydrodynamic interaction effects and the hull/mooring/riser/hawser coupling for the multiple body system are investigated by numerical simulations. A simplification by the mass-spring model is also considered. An LNG FPSO and a shuttle tanker are taken as a multiple body system, and the tandem mooring is considered. The distance effects on motions and drift forces of two vessels are already reviewed in Chapter VII. The coupling and interaction effects are studied using the two-body model of an FPSO and a shuttle tanker.

The comparison of the analysis results for the FPSO and FPSO model and the mass-spring model has the validity of the program WINPOST-MULT. The comparative study of an FPSO and a shuttle tanker illustrates the importance of including the interaction effect between multiple bodies.

CHAPTER X

CONCLUSIONS FOR ALL CASE STUDIES

WINPOST program was developed for the hull/mooring/riser coupled dynamic analysis of floating structures, such as SPAR, TLP, and FPSO. In this study, the program was extended to multiple body problems, including hydrodynamic interactions.

5 case studies are presented for the verification of the developed program WINPOST-MULT. The first two cases are for single FPSOs. The first one is a turret-moored FPSO in full load or ballast condition. In the second case, the intermediate loading conditions and the simulated results are compared with OTRC experiment. In the OTRC experiment, several platform parameters are not clearly identified. Thus, the missing parameters are deduced from the free decay test. Even though the adjustment is made, there exist several uncertainties to be clarified. For example, the wind force, current force and the truncated mooring lines with buoys and springs may well not match with our numerical modeling. Despite the uncertainties mentioned, the trend of the numerical simulations follows that of experimental results.

The third case is to review the hydrodynamic characteristics of two-body interaction. For the two-body model, an FPSO and a shuttle tanker are selected. They are moored in a tandem arrangement and a side-by-side arrangement. Both mooring systems are considered for this study. The interaction effect is much stronger in the side-by-side mooring system than in the tandem mooring system. For example, if the distance closes to a half of the original distance, the motion RAOs double.

The fourth case is for the two-body analysis with two identical SPARs. For the validity of this analysis, the connecting hawser is modeled as a spring. The spring stiffness is directly input in the system matrix in the program. The spring is programmed to work in taut state, but not to work in slack state. The analysis results using the simplified mass-spring model and two-spar model show a reasonable agreement with each other.

For the verification of the two-body module of the program WINPOST-MULT, several cases are considered, i.e., FPSOs with and without hawsers and an FPSO and a shuttle tanker with and without hawser. To verify the results, the connecting hawser, mooring lines and two FPSOs are modeled as a simple two-mass-spring system, and an approximate solution is obtained. The environmental loads are calculated in a simplified form to apply to the mass-spring model. These analyses are conducted for the tandem mooring system. When multiple floated dynamics are solved, a typical approach in offshore industry is one of them, either completely neglecting or partially including the hydrodynamic interaction effects. The existing methods used in the industry are reviewed with the more sophisticated WINPOST-MULT program, which includes the full hydrodynamic interactions. From the analysis results, the conclusion is drawn that the interaction effects of the two-body problem can be very important. The WINPOST-MULT program is proved to be a useful tool for solving multiple-body interaction problems.

REFERENCES

- API RP 2T 1997 *Recommended Practice for Planning, Designing, and Consulting Tension Leg Platforms*. 2nd Edition, American Petroleum Institute, N.W., Washington D.C.
- Arcandra, T. 2001 Hull/Mooring/Riser Coupled Dynamic Analysis of a Deepwater Floating Platform with Polyester Lines. Ph.D. Dissertation, Texas A&M University.
- Arcandra, T., Nurtjahyo, P. & Kim, M.H. 2002 Hull/Mooring/Riser Coupled Analysis of a Turret-Moored FPSO 6000 ft: Comparison between Polyester and Buoy-Steel Mooring Lines. *Proc. 11th Offshore Symposium The Texas Section of the Society of Naval Architects and Marine Engineers, SNAME*, 1-8.
- Baar, J.J.M, Heyl, C.N. & Rodenbusch, G. 2000 Extreme Responses of Turret Moored Tankers. *Proc. Offshore Technology Conference, OTC 12147 [CD-ROM]*, Houston, Texas.
- Buchner, B, van Dijk, A. & de Wilde, J.J. 2001 Numerical Multiple-Body Simulations of Side-by-Side Moored to an FPSO. *Proc. 11th Int. Offshore and Polar Eng. Conference, ISOPE*, **1**, 343-353.
- Choi, Y.R. & Hong, S.Y. 2002 An Analysis of Hydrodynamic Interaction of Floating Multi-Body Using Higher-Order Boundary Element Method. *Proc. 12th Int. Offshore and Polar Eng. Conference, ISOPE*, **3**, 303-308.

Dean, R.G. & Dalrymple, R.A. 1992 *Water Wave Mechanics for Engineers and Scientists*. Advanced Series on Ocean Engineering. **2**, World Scientific Press, Dover, D.E.

Faltinsen, O.M. 1998 *Sea Loads on Ships and Offshore Structures*. The Cambridge University Press, Cambridge.

Garrett, D.L. 1982 Dynamic Analysis of Slender Rods. *J. of Energy Resources Technology, Trans. of ASME*, **104**, 302-307.

Garrison, C.J. 2000 An Efficient Time-Domain Analysis of Very Large Multi-Body Floating Structures. *Proc. 10th Int. Offshore and Polar Eng. Conference, ISOPE*, **1**, 65-71.

Huijsmans, R.H.M., Pinkster, J.A. & de Wilde, J.J. 2001 Diffraction and Radiation of Waves Around Side-by-Side Moored Vessels. *Proc. 11th Int. Offshore and Polar Eng. Conference, ISOPE*, **1**, 406-412.

Hong, S.Y., Kim, J.H., Kim, H.J. & Choi, Y.R. 2002 Experimental Study on Behavior of Tandem and Side-by Side Moored Vessels. *Proc. 12th Int. Offshore and Polar Eng. Conference, ISOPE*, **3**, 841-847.

Inoue, Y. & Islam, M.R. 2001 Effect of Viscous Roll Damping on Drift Forces of Multi-Body Floating System in Waves. *Proc. 11th Int. Offshore and Polar Eng. Conference, ISOPE*, **1**, 279-285.

Kim, M.H. 1992 *WINPOST V3.0 Users Manual*. Dept. of Ocean Engineering, Texas A&M University.

Kim, M.H., Arcandra, T. & Kim, Y.B. 2001a Validability of Spar Motion Analysis against Various Design Methodologies/Parameters. *Proc. 20th Offshore Mechanics and Arctic Eng. Conference, OMAE01-OFT1063 [CD-ROM]*, L.A., California.

Kim, M.H., Arcandra, T. & Kim, Y.B. 2001b Validability of TLP Motion Analysis against Various Design Methodologies/Parameters. *Proc. 12th Int. Offshore and Polar Eng. Conference, ISOPE, 3*, 465-473.

Kim, M.H. & Ran, Z. 1994 Response of an Articulated Tower in Waves and Currents. *International Journal of Offshore and Polar Engineering, 4*, (4), 298-231.

Kim, M.H., Ran, Z. & Zheng, W. 1999 Hull/Mooring/Riser Coupled Dynamic Analysis of a Truss Spar in Time-Domain. *Proc. 9th Int. Offshore and Polar Eng. Conference, ISOPE*, Brest, France, **1**, 301-308.

Kim, M.H. & Yue, D.K.P. 1989a The Complete Second-Order Diffraction Solution for an Axisymmetric Body. Part 1. Monochromatic Incident Waves. *J. of Fluid Mechanics, 200*, 235-264.

Kim, M.H. & Yue, D.K.P. 1989b The Complete Second-Order Diffraction Solution for an Axisymmetric Body. Part 2. Bichromatic Incident Waves. *J. of Fluid Mechanics, 211*, 557-593.

- Lee, C.H. 1999 *WAMIT User Manual*. Dept. of Ocean Engineering, Massachusetts Institute of Technology, Cambridge, M.A.
- Ma, W., Lee, M.Y., Zou, J. & Huang, E. 2000 Deep Water Nonlinear Coupled Analysis Tool. *Proc. Offshore Technology Conference, OTC 12085 [CD-ROM]*, Houston, Texas.
- Nordgen, R.P. 1974 On Computation of the Motions of Elastic Rods. *ASME Journal of Applied Mechanics*, 777-780.
- OCIMF 1994 *Prediction of Wind and Current Loads on VLCCs*. 2nd Edition, Witherby & Co. Ltd, London, England.
- Pauling, J.R. & Webster, W.C. 1986 A Consistent Large-Amplitude Analysis of the Coupled Response of TLP and Tendon System. *Proc. 5th OMAE Conf.*, Tokyo, **3**, 126-133.
- Ran, Z. & Kim, M.H. 1997 Nonlinear Coupled Responses of a Tethered Spar Platform in Waves. *International Journal of Offshore and Polar Engineering*, **7**, (2), 27-34.
- Ran, Z., Kim, M.H. & Zheng, W. 1999 Coupled Dynamic Analysis of a Moored Spar in Random Waves and Currents (Time-Domain versus Frequency-Domain Analysis). *Journal of Offshore Mechanics and Arctic Engineering*, **121**, (2), 194-200.
- Teigen, P. & Trulsen, K. 2001 Numerical Investigation of Nonlinear Wave Effects Around Multiple Cylinders. *Proc. 11th Int. Offshore and Polar Eng. Conference, ISOPE*, **3**, 369-378.

Ward, E.G., Irani, M.B. & Johnson, R.P. 2001 The Behavior of a Tanker-Based FPSO in Hurricane Waves, Winds, and Currents. *Proc. 11th Int. Offshore and Polar Eng. Conference, ISOPE, 4*, 650-653.

Wichers, J.E.W. 1988 A Simulation Model for a Single Point Moored Tanker. Ph.D. Dissertation, Delft University of Technology, Delft, The Netherlands.

Wichers, J.E.W. & Develin, P.V. 2001 Effect of Coupling of Mooring Lines and Risers on the Design Values for a Turret Moored FPSO in Deep Water of the Gulf of Mexico. *Proc. 11th Int. Offshore and Polar Eng. Conference, ISOPE, 3*, 480-487.

Wichers, J.E.W. & Ji, C. 2000a On the Coupling Term in the Low-Frequency Viscous Reaction Forces of Moored Tankers in Deep Water. *Proc. Offshore Technology Conference, OTC 12086 [CD-ROM]*, Houston, Texas.

Wichers, J.E.W. & Ji, C. 2000b DeepStar-CTR 4401- Theme Structure Benchmark Analysis for Tanker Based FPSO-GoM. *Technical Rep. No. 15629-1-OE*, MARIN, Wageningen, The Netherlands.

Wichers, J.E.W., Voogt, H.J., Roelofs, H.W. & Driessen, P.C.M. 2001 DeepStar-CTR 4401- Benchmark Model Test. *Technical Rep. No. 16417-1-OB*, MARIN, Wageningen, The Netherlands.

VITA

Young-Bok Kim was born in Incheon in the Republic of Korea on September 9, 1958. He graduated from Inha University with a Bachelor of Science degree in naval architecture and ocean engineering in February 1981. After he served in the Korean Army about for 10 months, he was employed by the Daewoo Ship Building and Heavy Industry Co. Ltd. (DWSH) on Keoje Island, Korea. There he worked as a structural engineer and also as a ship vibration analysis engineer. He was involved in ship design, vibration analyses and measurements for newly built ships. After working for seven years for DWSH, he moved to the Korean Register of Shipping (KR) in Seoul, Korea. While he worked at KR, he entered the graduate school of Seoul National University in 1992. He majored in naval architecture and ocean engineering, and two years later he received his Master of Science degree in February 1994. After that, he went abroad to pursue the doctoral degree at Texas A&M University in January 1999. In May 2003, he received his Ph.D. in the field of ocean engineering. He married Deock-Seung Seo in 1983 and has two sons, Hayong and Harin. His permanent address is: 459-6, Chowon Villa 102, Jeonmin-Dong, Yuseong-Ku, Taejeon, Republic of Korea, 305-810.